Identifying biophysical determinants of virus-cell fusion through live-cell imaging

Charles A. Coomer

Magdalen College

Supervisors:

Dr. Alex Compton

Dr. Ewaldus Compeer

Dr. Sergi Padilla-Parra

Wellcome Trust Centre for Human Genetics
Nuffield Department of Medicine

National Cancer Institute
National Institutes of Health

NIH Oxford-Cambridge Scholars Program

A thesis submitted for the degree of
Doctor of Philosophy
Hillary Term 2021

Acknowledgements

I often find myself living in two worlds. One is a world as seen through the lens of a virus—epitomised by an evolutionary civil war where we, as scientists, are privileged to observe the underpinnings of pathology, immunology and medicine clash. Through this world, I have tracked single viruses surf the plasma membrane of a cell, watched how a virus alters the metabolic flux of its host in real-time, and quantified the oligomeric state of molecules with spatiotemporal resolution I never thought possible. It is a rewarding, fascinating world, but my second one is by far superior. My second world is populated with other organisms who are, although slightly less eccentric and are only approximately 8% retrovirus, are supremely real, full of kindness and who undoubtedly are my inspiration throughout my life.

It is to these people I dedicate this dissertation, which its completion would have not been possible without their support and mentorship. Pursuing a PhD provides ample time to create an exceptionally long list of people to thank. Consequently, it will be very difficult to name each person individually here. However, to those who I have missed, please know this: from the bottom of my heart, you have my humblest thanks and gratitude.

To my mentors—Alex Compton, Ewoud Compeer, and Sergi Padilla-Parra—who are enthusiastic, inspiring people that have been exceptionally supportive and gracious to accept and train me in such a complicated, fast-paced program. All three are brilliant scientists, whose kindness and patience are seemingly endless, and their steady guidance both inside and outside the lab has been nothing short of paramount. I would not be here without them. I can only hope to emulate their qualities as mentors as I move to the clinic and hope that I make you proud.

To the mentors I had in undergraduate school—Drs. Audra Jennings, Melinda Grimsley, Craig Cobane and Lester Pesterfield—who not only shaped my undergraduate education with unparalleled support and enthusiasm, but also provided me with an outlet to chase my dreams.

To Dr. Rodney King, who was the first investigator to introduce me to the intricacies, challenges and rewards of wet-lab virology research. The impact of his willingness to let me explore the scientific process early as an undergraduate student cannot be understated. His enthusiasm in teaching virology is the reason why I pursued a PhD in the first place.

To my lab-mates: Dr. Irene Carlon-Andres, Dr. Rory Nolan, Maro Iliopoulou from the Padilla-Parra lab, and Dr. Saliha Majdoul, Dr. Kazi Rahman and Dr. Scarlett Shi of the Compton lab, who fostered supportive, creative and friendly laboratory homes on either side of the Atlantic Ocean. Additionally, to my colleagues at the HIV Dynamics and Replication Program (DRP), particularly Dr. Melissa Fernandez, Dr. Alice Duchon, Demetria "Meech" Harvin, Dr. Tomas Kroupa, Dr. Connie Rink, Dr. Sid Datta, and Dr. Bahni Biswas, who also helped make the DRP community such a pleasant, warm and communal place to study. It has been such a joy to work alongside each of you for the last four years and learning from your endless expertise. I wish each of you the best.

To my parents, Don and Evell Coomer, who are without a doubt the most patient, kind and generous people I could ever know and have influenced me more than I could possibly describe. They are my twin pillars, without whom I could not stand. Both of them unwaveringly encouraged me that I could pursue whatever career I chose and be whomever I wanted to be, even when the

greatest source of doubt came from myself. I would not be here today without their support, love and reassurance.

Finally, to my best friend, my husband, Chris. Ever since the beginning of my PhD course, he has filled our lives and home with love, excitement, friends and family that I am indescribably grateful to be immersed. He continually pushed me to learn, grow and become a better person, even in the face of the mountains of papers, ImageJ files, drafts and worries that I have carried these last four years. He has laughed at my corny jokes, offered patience and an outlet for me to express my frustrations and concerns when things (quite often) went wrong at the bench, lent a shoulder to cry on when I could no longer believe in myself and celebrated with me in the brief, but cherished moments of success. As he has guided me though these last four years, I do not know if he ever realised that the person I most wanted to be most like is him. Thank you, Chris: you are my guidepost for everything. In a career path that can seem so incredibly intricate and complicated, you make it so indescribably simple.

Vita

2014..... B.S. Biology, B.S. Chemistry, Western Kentucky University

2015..... MSc. Infection and Immunity, University College London

2015 to present.....Medical Student, University of Kentucky College of Medicine

2015 to present.....Graduate Fellow, University of Oxford

Publications

C. Coomer*, K. Rahman*, A. Compton (2020). The CD225 proteins: a family portrait of fusion regulators. Trends in Genetics. *In press.* https://doi.org/10.1016/j.tig.2021.01.004

C. Coomer I. Carlon-Andres, S. Padilla-Parra (2020). Advanced Light and Correlative Microscopy in Virology. Reference Module in Life Sciences. https://doi.org/10.1016/B978-0-12-814515-9.00108-9.

K. Rahman*, **C. Coomer***, S. Majdoul, S. Ding, S. Lockett, S. Padilla-Parra, A. Compton (2020). A conserved motif functionally links the antiviral activity of IFITM3 with its oligomeric state in membranes. eLife. 9:e58537 DOI: 10.7554/eLife.58537

C. Coomer, I. Carlon-Andres, M. Iliopoulou, M. Dustin, E. Compeer, A. Compton, S. Padilla-Parra (2020). Single-cell glycolytic activity regulates membrane tension and HIV-1 fusion. PLoS Pathogens. https://doi.org/10.1371/journal.ppat.1008359

M. Iliopoulou, R. Nolan, L. Alvarez, Y. Watanabe, **C. Coomer**, G. Maria Jakobsdottir, T. Bowden, S. Padilla-Parra (2018). A dynamic three step mechanism drives the HIV-1 prefusion reaction. Nature Structural and Molecular Biology. https://doi.org/10.1038/s41594-018-0113-x.

M.F. Kearney, E.M. Anderson, **C. Coomer**, L. Smith, W. Shao, N. Johnson, C. Kline, J. Spindler, J.W. Mellors, J.M. Coffin, Z. Ambrose. (2015) Well-mixed plasma and tissue viral populations in RT-SHIV-infected macaques implies a lack of viral replication in the tissues during antiretroviral therapy. Retrovirology 12: 93.

*indicates equal contribution

Dedication:

The dedication of this dissertation is divided in seven ways:

To Otis, my cat, who keeps Chris and I on our toes.

To my course mates, who provided endless sources of laughter.

To my siblings, Brad and Nicole, who keep me grounded.

To my in-laws, Karen, Hayley, Melissa, and Pauline, who graciously welcomed an eccentric American into their lives.

To my parents, who are my source of unconditional love and encouragement.

To my husband, who makes every day such a gift.

And to every graduate student who told himself or herself that they “can’t do it”. You can.

Declaration

I declare that the work presented in this D.Phil thesis entitled, "Identifying biophysical determinants of virus-cell fusion through live-cell imaging approaches" is entirely my own work except for where the contributions of my collaborators have been clearly acknowledged. No part of this thesis has been submitted for any degree of other qualification at the University of Oxford or elsewhere.

Hilary Term 2021

Charles Coomer

Magdalen College
Wellcome Trust Centre for Human Genetics
HIV Dynamics and Replication Program-National Institutes of Health

Abstract:

The biophysical properties of both enveloped virus and cell membranes must be favourable for successful fusion and entry of the virus into its host. Characterising these properties in cells and virions is critical for understanding and manipulating target cell susceptibility to infection, as well as blocking infection by cell-autonomous antiviral proteins. To characterise such properties, we developed imaging assays multiplexing genetically-encoded biosensors concomitant with single virus tracking in live cells to uncover a link between the host cell membrane biophysical landscape, host metabolic state, and virus fusion. Expanding the utility of these assays, we characterised a conserved GxxxG oligomerisation motif in antiviral protein interferon-inducible transmembrane 3 (IFITM3), linking the oligomeric state of IFITM3 and its antiviral activity to its ability to rigidify host cell membranes. Interestingly, the GxxxG motif is not intact in human IFITM5, and this IFITM protein is traditionally not associated with antiviral immunity. Therefore, we restored the GxxxG motif in IFITM5 to determine if its oligomerisation capacity and antiviral activity was potentiated. Collectively, the results described in this dissertation connects the fusion of viruses with the biophysical properties of membranes of the host cell, which are dependent on host metabolic state and the ability of IFITM proteins to oligomerise and rigidify membranes.

Table of Contents

List of Figures

Page

Chapter 1:

Chapter 2:

Chapter 3:

Chapter 4:

Appendices:

Chapter 1: Introduction

1.1 Interferon-mediated restriction of virus infection

Human cells are armed with an arsenal of genes which act as either sentinels of or barriers to viral infection. In particular, a portion of these genes encode proteins designed to detect conserved pathogen-associated molecular patterns (PAMPs), which are shared amongst viral pathogens, via pattern recognition receptors (PRRs). The PAMPs sensed by PRRs range from viral nucleic acids—(e.g. cytoplasmic DNA or double-stranded RNA) to viral proteins [1–3]. In response to PAMP detection by PRRs, pro-inflammatory cytokines and chemokines are expressed and released in an autocrine and paracrine fashion (Figure 1.1.1). Importantly, PAMP detection indirectly leads to robust restriction of virus infection by upregulating viral restriction factors via the induction of type I or type II interferon [4–7].

All nucleated cells produce and secrete pro-inflammatory type I interferons (IFNs) in response to viral infection [4]. Interferons, once bound to autologous or non-autologous interferon receptors, signal through the JAK- (Janus kinase) or TYK (tyrosine-specific kinase)- STAT pathway to upregulate thousands of interferon-stimulated genes (i.e. ISGs) which vary widely in their capabilities to thwart infection of a diverse array of viruses (Figure 1.1.1) [3,8]. Ultimately, these genes create an antiviral state where cells are resistant to virus infection. Importantly, even though the first ISGs were discovered decades ago, many of these proteins have uncharacterised functions.

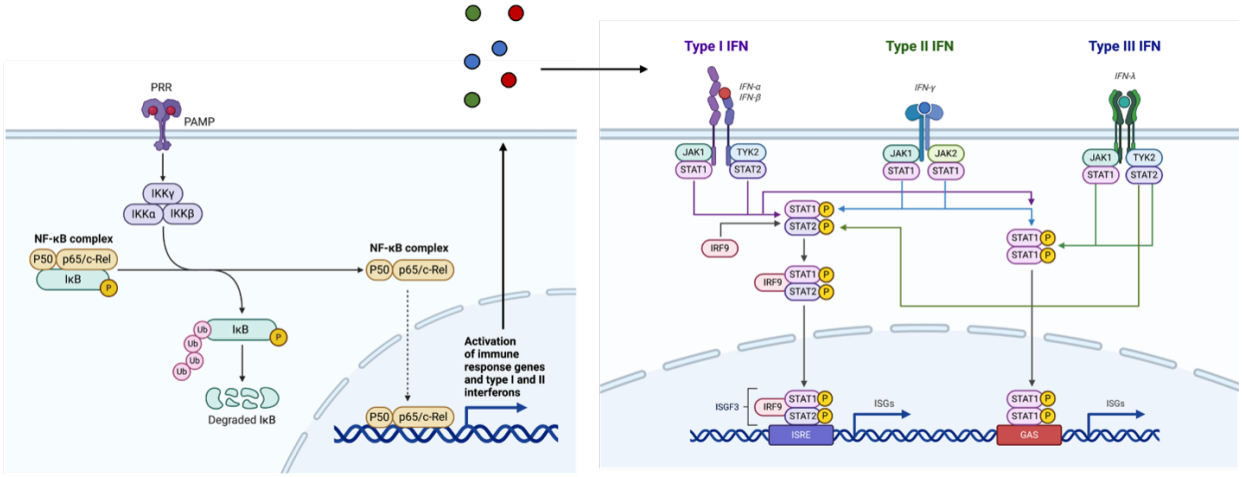

Figure 1.1.1: PAMP recognition by PRRs triggers the release of cytokines and interferons. (Left) Pathogen-associated molecular patterns (PAMPs) are recognized by pattern recognition receptors to activate the IκB kinase (IKK) complex. IKKβ-dependent phosphorylation of IκBα or IκBβ leads to their degradation via the proteosome, releasing p50/p65 heterodimers to enter the nucleus and bind κB DNA sites to transcriptionally-activate numerous genes encoding several cytokines, including type I, II or III interferons (IFNs). (Right) Type I IFNs (IFNα or IFNβ), type II IFNs (IFN γ) or type III IFNs (IFN λ) cytokines bind to their cognate receptor and activate Janus activated kinase (JAK)-signal transducer and activator of transcription (STAT) complexes to translocate directly, or assist interferon regulatory factors (IRFs) to translocate to the nucleus to transcriptionally activate interferon stimulated genes (ISGs) by binding to IFN-stimulated response elements (IRSEs). Created with BioRender.

A plethora of these ISGs fall into the category of restriction factors, which vary widely in their level of expression and their extent to be upregulated by interferon [9]. These genes were initially described to underpin variation in intra- and inter-species susceptibility to retroviral infection [10]. Unlike PRRs, which merely act to block viral infection by inducing interferon expression (Figure 1.1.1), restriction factors block viral replication immediately and directly (Figure 1.1.2). Ultimately, the battalion of host restriction factors work in concert to thwart virus infection via blocking multiple stages of the viral lifecycle (Figure 1.1.2). Studying these restriction factors, which have been optimised by evolution, may inspire cutting-edge antiviral therapeutics. In turn, information acquired from these investigations may also be used to inform key host requirements necessary for the specific stages of viral infection to occur.

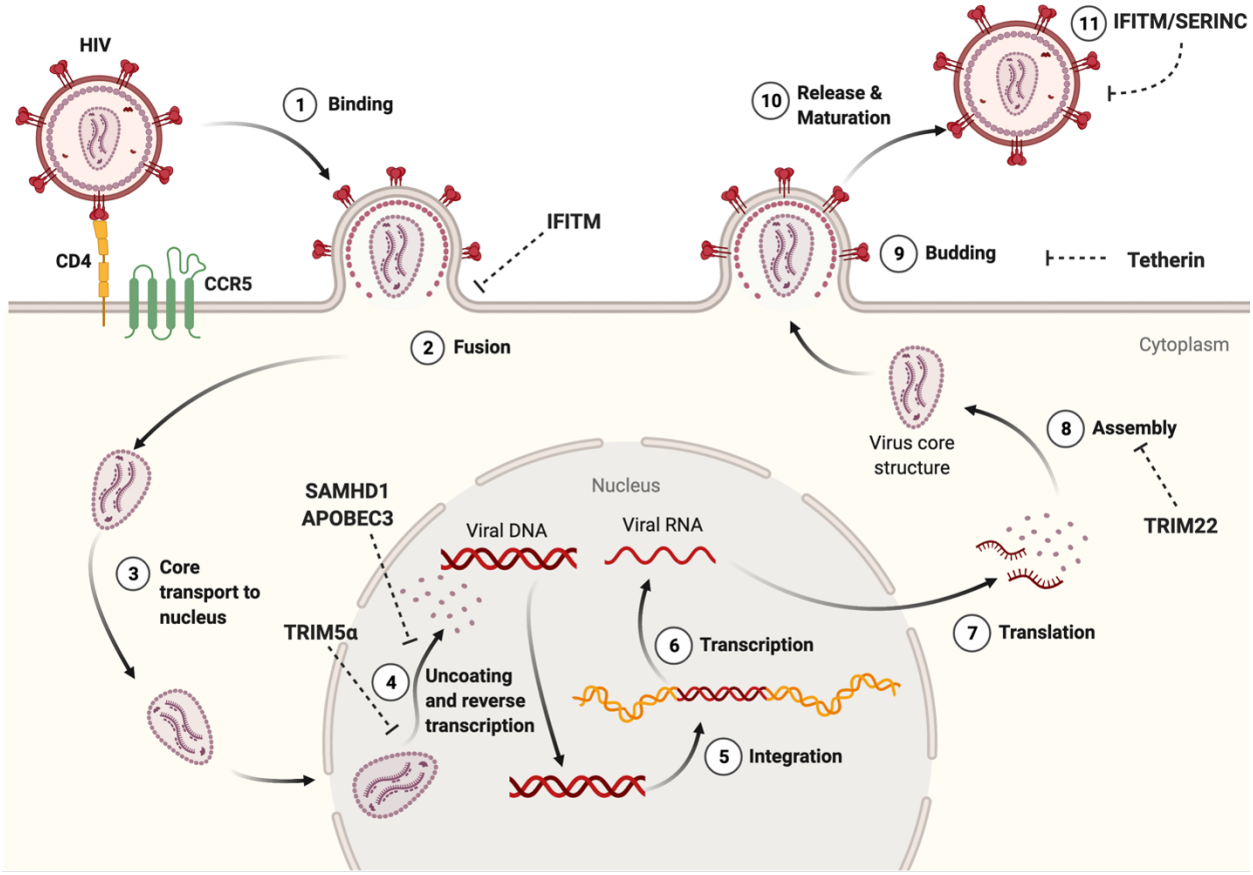

Figure 1.1.2: The cell-intrinsic immune system blocks multiple steps in the HIV-1 lifecycle. After binding of HIV-1 envelope (Env) to host cell receptor CD4 and co-receptor CCR5 (**1**), HIV-1 virions fuse with the plasma membrane (**2**). This process may be blocked by the interferon-induced transmembrane proteins (IFITMs) by rigidifying and bending membranes. Following fusion, the HIV-1 conical core is transported to the nucleus (**3**) where the core uncoats (**4**) near the site of viral integration into the host chromatin (**5**). The uncoating process is deterred by tripartite motif (TRIM) TRIM5α interception in such a way that reverse transcription is blocked. Additionally, the dNTPase SAMHD1 depletes deoxynucleotide pools in resting CD4+ T cells such that reverse transcription is blocked. Furthermore, apolipoprotein B mRNA-editing enzyme, catalytic polypeptide-like 3 (APOBEC3) cytidine deaminases introduce overwhelming numbers of lethal mutation into reverse transcription products, leading to replication-incompetent virions. During productive infection, following integration, viral transcription (**6**) proceeds the splicing and export of viral RNAs, such that translation (**7**) and virus assembly (**8**), directed by HIV-1 Gag-RNA interactions, occurs in the cytoplasm. TRIM22 blocks virus assembly by disrupting proper Gag trafficking. New virus particles bud from the plasma membrane (**9**) and become infectious after maturation by the viral protease (**10**). Budding of virions is blocked by the antiviral restriction factor tetherin. Importantly, the members of the IFITM and SERINC family may incorporate into nascent virions during assembly and release, dramatically reducing virus infectivity (**11**). Created with BioRender.

1.2 The IFITM protein family

Some of the most potent restriction factors in the cell-autonomous immune arsenal are the interferon-induced transmembrane proteins (IFITMs). The IFITM family encompasses many members, including several pseudogenes and species-specific orthologs. It is likely that this gene family was horizontally transferred from bacteria to unicellular eukaryotes (e.g. metazoans).

Consequently, *IFITM* genes are present in a vast range of vertebrates [11,12]. Indeed, most vertebrate animals possess at least two *IFITM* genes in their *IFITM* repertoire. Furthermore, as these genes have been subjected to duplication and divergence events over time, this accordion-like pattern of evolution has generated diverse species-specific *IFITM* portfolios in terms of sequence and copy number [13,14]. In primate species, the *IFITM* locus often contains multiple copies of *IFITM3*-like genes resulting from gene duplication. For example, the African Green Monkey *IFITM* locus harbours eight copies of the *IFITM3* gene [14]. Importantly, these gene expansion and diversification events are consistent with cell-intrinsic factors undergoing adaptive evolution to thwart viral infection.

In humans, located on chromosome 11, the members of the IFITM protein family include interferon-inducible *IFITM1, IFITM2* and *IFITM3,* as well as *IFITM5* and *IFITM10*, of which the latter two have to date no known role in immunity. Indeed, *IFITM5* has been described to play a role in bone-mineralisation and point mutations within *IFITM5* have been associated with osteogenesis imperfecta type V [15,16]. Contrastingly, *IFITM10* has been suggested to play a role in adaptation to aquatic environments, yet how IFITM10 facilitates this process has been undetermined [11]. Based on protein function and sequence similarity, the human *IFITM* genes are organised into two of the three clades of *IFITM* genes in vertebrates [11]. In contrast to single-member clade *IFITMs*, members located within the third clade have antiviral activity, respond to interferons, and are thus deemed the immune-related IFITMs. Within this clade, IFITM members 1-3 are considered the core antiviral IFITM proteins in mammals, as all other derivatives are likely IFITM 1-3 orthologs [17]. IFITM2 and 3 are homologous with minimal sequence differences. In contrast, IFITM1 has diverged from these two members, particularly at the N terminus.

Interestingly, comparative genomics studies have illustrated that *IFITM3* is the most ancient member in the *IFITM* family and *IFITM2* has only recently emerged in humans [14]. Owing to their antiviral properties, much of our current knowledge regarding the *IFITM* family has centred on these three IFITM members.

IFITM genes contain one intron flanked by two coding exons and are associated with an interferon-stimulated response element (IRSE) in their promotor regions [18]. These promoters serve as scaffolds for a plethora of transcription factors, including MYC, STAT1, STAT2, STAT3, IRF1, TBP, CTCF which facilitate IFITM protein expression [18]. Nevertheless, although the immune-related *IFITM* genes are interferon-inducible, they may still be constitutively expressed at moderate to high levels in several tissue types. For example, it has been demonstrated that IFITM3 and a plethora of other ISGs are highly expressed in hematopoietic stem cells (HSCs) yet are lost following increasing differentiation, likely a protective mechanism against viral infection [19]. Interestingly, it was serendipitously discovered that treatment with mTOR inhibitors, such as rapamycin, and other rapalogs could enhance gene delivery by lentiviral vectors in both human and murine HSCs and other progenitor cells [20]. Importantly, this investigation showed that rapamycin treatment enhanced lentivector fusion with HSC target membranes, suggesting a previously uncharacterized connection between mTOR and virus–cell fusion. Only recently however, was it discovered that mTOR inhibitors, down-regulate endogenous IFITM3 in HSCs by lysosomal degradation [21]. Consequently, understanding the cellular distribution and expression of the *IFITM* genes may catalyse our implementation of future gene delivery therapeutics to correct a variety of human diseases reliant on vector delivery.

1.3 Initial characterisation of IFITM protein antiviral activity

The antiviral activities of both IFITM1 and IFITM3 were documented early *in vitro*. Although referred to initially as either 9-27 or Leu-13, preliminary reports indicated that IFITM1 was an interferon-inducible gene [22] which could restrict cell growth in human peripheral blood mononuclear cells [22,23]. Shortly thereafter, studies of IFITM1 antiviral activity began to surface, where it was demonstrated that IFITM1 could abrogate vesicular stomatitis (VSV) infection, but not influenza A virus (IAV), when overexpressed in murine cell lines [24]. Nearly a decade later, Zhu and colleagues demonstrated that interleukin-1 (IL-1) and IFNα induced high levels of IFITM3 (referred to as 1-8U) expression, and that this antiviral protein could diminish hepatitis C virus replication in the FCA1 cell line [25].

Although these initial reports suggested that some IFITM proteins are interferon-inducible and possess antiviral activity, it would take many years for the broad-spectrum antiviral activity of IFITM proteins to be fully realised. Until then, most investigations devoted to IFITM proteins concentrated on their role in germ cell development. In particular, these studies created murine single-cell gene expression profiles indicating that cells expressing high levels of IFITM proteins may demarcate germ cells from their somatic neighbours [26] and track with germ cell differentiation [27]. However, multiple *in vivo* studies of IFITM knockout (KO) mice subsequently demonstrated that mice lacking IFITM proteins displayed normal viability, development and reproductive capability [28]. Indeed, any abnormalities noted in the IFITM KO mice were limited to littermates being overweight [29] or subtle changes in bone morphology in IFITM5 KO mice

[15]. Fortunately, generating IFITM and IFITM3 KO mice would catalyse future investigations characterising the role of the immune-related IFITM proteins in restricting virus infection *in vivo*.

1.4 Characterisation of IFITM3 as an antiviral protein *in vitro* and *in vivo*

Owing to the selection, expansion and conservation of the vertebrate immune-related *IFITMs*, it would not be long before the broad antiviral role of IFITM proteins would be uncovered. Indeed, a functional genomic screen utilizing an siRNA panel in U2OS cells discovered that IFITM1, IFITM2 and IFITM3 restrict an early step in IAV replication and that IFITM3 expression critically repressed IAV infection *in vitro* [30]. Importantly, by utilising knockdowns of IFITM3 in HeLa cells and primary lung fibroblasts, IFITM3 was shown to be responsible for a substantial proportion of type I and II IFN antiviral activity. Furthermore, by employing a broad panel of virus pseudoparticles, IFITM3's ability to block virus infection was localized to the virus entry step. This is because the lifecycles of the pseudoviruses tested differ only by their glycoproteins, and thus their means of entry. Moreover, this study began to reveal the broad antiviral action of IFITM proteins by illustrating that IFITM1, IFITM2 and IFITM3 overexpression also reduced infection of a panel of flaviviruses, including Dengue (DENV), West Nile (WNV), Yellow Fever (YFV) and Omsk haemorrhagic fever (OHFV) viruses. Importantly, the authors also demonstrated that some enveloped viruses, particularly the retrovirus murine leukaemia virus (MLV) and the arenaviruses Lassa virus (LASV), Machupo virus (MACV), and lymphocytic choriomeningitis virus (LCMV) were resistant to IFITM3 antiviral activity. Overall, this study illustrated for the first time the broad antiviral scope of IFITM proteins and primed future work to investigate the role of IFITM proteins in viral infection *in vivo*.

Indeed, the production of IFITM KO mice for germ cell development studies later catalysed investigations reporting on the role of IFITM3 in limiting viral infections *in vivo*. Shortly after the report described above from Brass and colleagues, multiple investigations reported almost simultaneously that IFITM3 KO mice quickly succumbed to fulminant viral pneumonia when challenged with low-pathogenic strains of IAV compared to their WT littermates [31,32]. Both studies indicated that the IFITM3 KO mice had drastically increased pathological features characterised by severe oedema, lung lesions, and higher viral loads during H3N2 [31] or H1N1 IAV infection [32]. Extending their results to humans, the former study also analysed *IFITM3* alleles of patients hospitalized with H1N1/09 influenza, demonstrating that hospitalised subjects were enriched for a minor *IFITM3* allele (discussed below) that allegedly altered IFITM3 splicing and reduced IAV restriction *in vitro* [31]. Interestingly, the latter study utilized experiments harnessing the *IFITMdel* mouse line, which lacks the entire mouse IFITM locus on chromosome 7, in combination with IFITM3 KO mice to show that IFITM3 is the primary restriction factor against pathogenic IAVs *in vivo* [32]. In particular, the *IFITMdel* mice and the *IFITM3* KO exhibited the same drastic increase in morbidity and mortality during IAV challenge, indicating IFITM3 is the dominant acting restriction factor in *in vivo* IAV infection [32]. Together, these studies identified that IFITM3 profoundly alters the course of influenza virus infections in both mouse and humans and drastically reduces IAV infection morbidity and mortality.

1.5 Human IFITM3 polymorphisms in health and disease

Multiple reports have linked several genetic markers with severe viral IAV infection in humans [33–35]. Similarly, after the initial characterisation of its ability to alter the course of influenza infection *in vivo*, IFITM3's role in human viral infection quickly emerged. In particular,

various SNPs within the IFITM3 promotor or open reading frame have been linked to increased susceptibility to severe IAV infection. Initially, the rs12252 synonymous SNP, commonly found in Asian populations and located within the first exon of IFITM3, was shown to be associated with not only severe influenza infection [31,36] but also faster progression to AIDS in HIV-infected patients [37]. Follow-up investigations suggested that this SNP may generate an alternative splicing site, subsequently resulting in a protein product with an N-terminal truncation removing a YXXΦ motif essential for endocytic localisation [14,38,39]. As other investigations indicated that IFITM3 with an N-terminal 21 amino acid truncation translocates to the plasma membrane, it was assumed that this variant fails to restrict IAV as its entry occurs within endosomes.

Nevertheless, this conjecture was not uncontested as other reports demonstrated that the rs12252 produces N-terminally truncated IFITM3 only at negligible levels [40]. Therefore, these data suggest that the association of severe influenza A infections with the rs12252 allele is not due to an N-terminally truncated IFITM3 product. Furthermore, other case-control and retrospective cohort investigations have indicated the association between rs12252 and IAV infection severity was unfounded [40–42]. However, the null conclusions purported by these studies likely stem from several shortcomings, such as low numbers of included rs12252 patients and the narrow focus on white European patients. Supporting this notion is a recent meta-analysis confirming association between severe influenza infection and the rs12252 allele [43]. Therefore, the mechanism detailing how the rs12252 variant leads to severe IAV infection outcomes remains to be described, yet studies dissecting the mechanism of IFITM3 virus restriction will assist this investigation.

Two other SNPs of IFITM3 have also been detected relatively recently. One SNP variant, rs34481144, is located in the IFITM3 promoter region, has been mapped to European populations and is linked to severe IAV infection [44]. Interestingly, recent reports have revealed that this SNP enhances binding of the transcriptional factor CTCF and increased methylation of the *IFITM3* locus, both repressing the expression of IFITM3. The other, rs6598045, was also enriched in patients suffering from adverse H1N1/09 IAV infection. Preliminary investigations have revealed that this SNP may reduce transcriptional efficiency of IFITM3 owing to diminished binding of the transcription factor TFII-I and thus diminished promoter activity via a transcriptional luciferase assay [45]. Nevertheless, further investigations will be needed to consolidate this preliminary report, including *in vitro* and *in vivo* data confirming decreased IFITM3 mRNA and protein expression as well as transcription factor binding.

1.6 IFITM3 topology

Although the ability of IFITM3 to restrict IAV infection *in vitro* and *in vivo* was well-established early, the topology of IFITM3 has been only recently solidified. Nevertheless, determining the topology of IFITM3 was critical to predict IFITM3's interactions with host and viral membranes as well as other cellular proteins in order to characterise its mechanism of restriction. Initially, it was thought that IFITM3 possessed two transmembrane (TM) domains with a cytoplasmic intracellular loop (CIL) as initial investigations revealed that antisera against the CIL could only bind after cell permeabilization, confirming its intracellular location [46].

However, less clear were the locations and orientation of the TM domains as well as the N and C termini. Preliminary reports alleged that antibodies against the IFITM1 N-terminus enhanced human T cell aggregation [47] and cell-surface radiolabelling could recover IFITM1 in human B lymphoma cell lines [48], suggesting an extracellular location for the N-terminus of IFITM1. These results were supported by flow cytometry assays showing that IFITM proteins tagged at their N terminus could be labelled extracellularly [49–51]. Additionally, the identification of three conserved S-palmitoylated cysteines and their positioning was consistent with a dual transmembrane topology [52]. Together, these studies suggested that IFITM proteins, including IFITM3, held a type III dual-pass transmembrane structure (Figure 1.1.3).

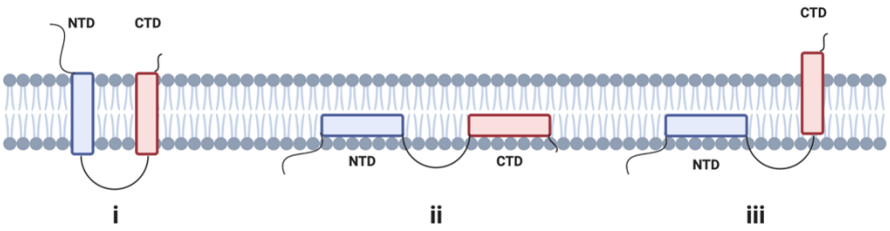

Figure 1.1.3. Different topological models proposed for IFITM3. Several different topologies have been proposed for IFITM3. In chronological order, IFITM3 was first proposed to be a type III dual-pass transmembrane protein (**i**) with both hydrophobic regions of the CD225 domain spanning the membrane (hence the name "Dispanins" for CD225-containing proteins). Following this, several investigators indicated that both the N (blue) and C (red) terminus of IFITM3 had access to the cytoplasm, indicating both hydrophobic segments were intramembrane domains (**ii**). Finally, several labelling and structural studies have indicated a type II transmembrane topology for IFITM3, where the first hydrophobic segment is an intramembrane domain containing an amphipathic helix, whereas the second hydrophobic domain traverses the membrane (**iii**). Created with BioRender.

Nevertheless, other investigators soon reported contradictory data indicating both the N and C termini could be cytosolic. In particular, two studies indicated that the N-terminus of IFITM3 could be post-translationally modified by cytosolic enzymes, implying cytoplasmic access to the N-terminus [38,53]. For example, one study showed that IFITM3 phosphorylation at Tyr20 via cytoplasmic kinase Fyn regulates IFITM3 endosomal localisation promoted by adapter protein 2 (AP2) association to IFITM3's ^{20}YEML^{23} motif [38]. Similarly, Yount and colleagues demonstrated that the Lys24 residue could be ubiquitinated by cytosolic ubiquitin ligases, further suggesting N terminus access to the cytosol [53]. Furthermore, the same study reported no glycosylation of IFITM3 at the N terminus despite the insertion of glycosylation motifs, suggesting IFITM3 is not exposed to glycosylation machinery in the endoplasmic reticulum lumen [53]. Interestingly, this report also indicated that the IFITM3 C terminus may be localised to the cytosol. In particular, the authors modified a palmitoylation-deficient IFITM3 construct by adding myristylation and prenylation motifs to the N and C termini, and subsequently used cytoplasmic chemical reporters to confirm N and C terminal access to the cytosol. Together, these studies pointed to an intramembrane topology of IFITM3, where both N and C termini face the cytosol (Figure 1.1.3).

Although more recent reports have confirmed the cytosolic N terminal orientation of IFITM3, the C terminus has been brought back under scrutiny. In particular, Bailey and colleagues utilised murine IFITM3 to show its C terminus localizes to the ER lumen by analysing antibody labelling efficiency of the N and C termini via flow cytometry and immunofluorescence in permeabilized and non-permeabilized cells [54]. Their results illustrated that the C terminus, but not the N terminus, was readily accessible to the cell surface. Moreover, by utilizing a C-terminal

KDEL IFITM3-tagged construct, the authors showed that the IFITM3 C-terminus was oriented towards the ER lumen, as C terminal KDEL motifs are bound by chaperones in the ER lumen, halting their secretion [55]. Therefore, a type II transmembrane protein topology was asserted by the authors (Figure 1.1.3). This notion was confirmed by employing a Myc-IFITM3-C9 construct and demonstrating both biochemically and by immunofluorescence microscopy that C-terminal, but not N-terminal, epitope tags were also degraded within lysosomes, consistent with type II transmembrane topology. Collectively, this study for the first time purported that IFITM3 adopted a type II transmembrane topology, with a cytosolic N-terminus, a luminal/extracellular C-terminus, an intramembrane domain and a transmembrane domain.

Since this landmark study, several reports have solidified this topological model of IFITM3. Indeed, Chesarino and colleagues identified a conserved amphipathic helix within IFITM3's first hydrophobic domain that is critical for its antiviral activity [56]. As amphipathic helices wedge into one leaflet of the membrane, this previously unappreciated stretch of residues within this hydrophobic domain corroborated prior reports that this region of IFITM3 could be an intramembrane domain. Additionally, a structural-based electron paramagnetic resonance and NMR analyses of IFITM3 in detergent micelles confirmed the C-terminal TM domain and an N-terminal hydrophobic intramembrane domain [57]. Together, these results support that IFITM3 is a type II transmembrane protein.

1.7 IFITM3 post-translational modifications

IFITM3's broadly acting antiviral activity is regulated by numerous post-translational modifications (PTMs). These PTMs affect IFITM3 localisation, stability and thus its antiviral action. Of note, major IFITM3 PTMs that have been characterised are palmitoylation, phosphorylation, and ubiquitination.

IFITM3 harbours three palmitoylated cysteine residues, which were initially identified in a chemical proteomics screen and were shown to be highly conserved in vertebrates as well as other antiviral IFITMs [52,53]. Palmitoylation is a modification whereby a 16-carbon acyl chain is appended to cysteine residues and increases protein hydrophobicity, membrane localisation, and association with lipid rafts [58]. The first two (Cys71 and Cys72) are located within the intramembrane domain, whereas the third (Cys105) is less conserved and resides at the junction of the CIL and TM domains. Importantly, site-directed mutagenesis studies changing these cysteine residues to alanine resulted in diffusely-spread IFITM3 devoid of antiviral activity [52,53]. Recently, an overexpression study determined that likely most zinc finger DHHC domain-containing (ZDHHC) palmitoyltransferase enzymes are redundantly responsible for the palmitoylation of IFITM3, yet the primary ZDHHCs palmitoylating this protein were ZDHHC3, 7 and 20 [59]. Interestingly, as IFITM3's amphipathic helix is located proximally to C71 and C72 [56], it is possible PTM may direct this conserved amphipathic helix to membranes to exert IFITM3's antiviral function [60].

Tyrosine phosphorylation and lysine ubiquitination have both been shown to regulate IFITM3's antiviral activity. As mentioned previously, IFITM3's Y20 residue was purported to be phosphorylated by protein kinase Fyn [38], which masks a Yxxϕ motif ("x" is any amino acid and ϕ is either a leucine, valine or isoleucine) [61,62]. As Yxxϕ is an AP2-mediated endocytic motif [63] required for proper IFITM3 localisation and antiviral activity, phosphorylation or disruption of Y20 retains IFITM3 within the plasma membrane and unable to perform its antiviral function [61,62]. Interestingly, Chesarino and colleagues determined that IFITM3 Y20 phosphorylation also decreases its propensity to be ubiquitinated. Almost immediately following these reports, a follow-up study revealed that IFITM3 is ubiquitinated by the E3 ubiquitin ligase NEDD4 and that this PTM requires a PPxY motif [64], which overlaps with the Yxxϕ motif [65]. Interestingly, these studies primed a report which showed that non-human primate IFITM3 orthologs can harbour mutations in both the PPxY and Yxxϕ motifs, resulting in natural IFITM3 variants with tailored antiviral activity against specific viruses entering at the cell surface or within endosomes based on IFITM3 localisation determined jointly by these regions [14].

Several investigations have also demonstrated that IFITM3 contains four lysine residues (Lys24, Lys48, Lys63, and Lys88) which may be ubiquitinated when IFITM3 is overexpressed [53,62]. Alanine mutagenesis studies indicated that ubiquitination could occur at any lysine position, yet Lys24 and Lys63 are likely the most strongly modified [53]. These results were corroborated by anti-ubiquitin blotting of immunoprecipitated IFITM3 and large-scale mass spectrometry studies which defined multiple IFITM proteins as ubiquitinated substrates [66,67]. As polyubiquitin linkages notably regulate protein turnover and trafficking, these PTMs indicated that ubiquitination of IFITM3 could have substantial effects on its antiviral function. Indeed, Yount

and colleagues demonstrated by pulse-chase experiments that the lysine-deficient IFITM3 mutant had increased stability, IAV restriction, and localisation to endolysosomal compartments [53]. Interestingly, single lysine mutations resulted in minimal reductions in antiviral activity and localisation, suggesting that other lysine residues compensate for each other [53].

1.8 IFITM3 restricts a broad range of viral pathogens

Although initial reports of IFITM3's antiviral activity were primarily limited to IAV infection *in vitro* and *in vivo*, multiple investigations that followed were quick to document its broad-spectrum antiviral function. Indeed, IFITM3 has been shown to be capable of restricting every IAV strain studied [17]. Furthermore, IFITM3 has been shown to able to restrict several enveloped RNA viruses, including flaviviruses [30,68], filoviruses [68], bunyaviruses [69], paramyxoviruses [70], human immunodeficiency virus (HIV-1) [53,71–74], and respiratory syncytial virus [75] through knockdown and overexpression studies.

Interestingly, although the restrictive properties of the IFITM proteins was alluded to in the context of VSV-G infection [24], rhabdoviruses seem to only be modestly restricted by IFITM3 [30]. Corroborating these observations, reports overexpressing human IFITM proteins showed moderate restriction against rabies virus and Lagos virus [76]. Although rhabdoviruses typically undergo "back fusion" when penetrating the host cell, whereby the viral membrane first fuses with the intraluminal vesicles and then the limiting membrane of its resident endosome to release its contents, it is unclear if this contributes to the stunted restriction of IFITM proteins.

Coronaviruses offer a unique pattern of restriction by the IFITM proteins. Indeed, although severe acute respiratory syndrome coronavirus 1 (SARS-CoV1) has been shown to be sensitive to IFITM1 [68], human IFITM2 and IFITM3 have been shown to be essential host factors facilitating entry of coronavirus OC43 [77,78]. Interestingly, Middle Eastern Respiratory Syndrome coronavirus (MERS-CoV) entry was shown to be moderately diminished in IFITM3 overexpression studies [79]. Contrastingly, SARS-CoV2 has been shown to be restricted by both human and mouse IFITM1, IFITM2 and IFITM3. Interestingly, IFITM3 could restrict SARS-CoV2 infection in an amphipathic helix-dependent, yet S-palmitoylation independent manner, suggesting a restrictive function that is perhaps yet unidentified [80]. Importantly, mutation of the Yxxϕ motif and redirection of IFITM3 to the cell surface converted human IFITM3 into an enhancer of SARS-CoV2 [80]. Surprisingly, reports investigating structural motifs within IFITM1 or IFITM3 found differential effects of these mutations in modulating the entry of five human coronaviruses [78]. In particular, overexpression studies utilizing several IFITM mutants converted their restrictive function to potent enhancers of both SARS-CoV1 and MERS-CoV [78]. Together, these studies suggest that IFITM proteins may act as determinants of entry of human coronaviruses by likely enhancing or disrupting interactions between viral and host cellular components or the fusion machinery functionality at sites of virus fusion.

Although IFITM3 has been shown to restrict primarily enveloped RNA viruses, IFITM3 has been reported to act against non-enveloped RNA viruses and DNA virus as well. In particular, IFITM3 has been shown to restrict two strains of reovirus, a non-enveloped double-stranded RNA virus [81]. Entering via late endosomal membranes, reovirus strain type 1 and type 3 were shown to be sensitive to IFITM3 restriction in overexpression and knockdown approaches. Interestingly,

similar to SARS-COV1, reovirus particles treated with exogenous proteases (e.g. trypsin) bypass IFITM3 restriction. These reports may suggest that IFITM3 targets a process central to enveloped and non-enveloped viruses, such as endosomal trafficking or endolysosomal maturation [82]. Finally, IFITM3 has been shown to abrogate entry of Vaccinia virus (VACV) [83]. However, later reports indicate that VACV superinfection may overwhelm IFITM-mediated restriction mechanisms VACV entry [83].

Although IFITM3 has been shown to restrict a host of viruses and pseudoviruses, many are resistant. These IFITM3-resistant viruses include arenaviruses, such as LASV, MACV, and LCMV; alphaviruses, such as Venezuelan encephalitis virus, Sindbis virus, chikungunya virus and Crimean Congo Hemorrhagic Fever Virus; some retroviruses, such as MLV; and several DNA viruses, including human cytomegalovirus, human papillomavirus, and adenovirus. Discussed in section 1.10, several live cell imaging studies have demonstrated that resistant viruses and pseudoviruses do not localize with IFITM3-laden compartments during entry, suggesting a proximity-based mechanism of restriction [82,84].

1.9 IFITM3 restricts bacterial pathogens

Owing to IFITM3's ability to restrict a broad range of viruses, many studies have sought to determine whether IFITM3 could also affect the course of bacterial infections as well. Interestingly, initial reports purported that IFITM3 failed to inhibit infection of a variety of bacteria [75]. In particular, these reports utilized an IFITM3 KO mouse model to show that compared to their WT littermates, IFITM3 KO mice displayed no difference in disease course or bacterial load

when challenged with either *Salmonella typhimurium, Citrobacter rodentium,* or *Mycobacterium tuberculosis* (MTb) infection [75]. In contrast, later studies reported the immune-related IFITMs, when overexpressed, could diminish intracellular growth of MTb *in vitro* in monocytes and that knockdown of the IFITM proteins could enhance this process [85]. Although this study linked restriction of bacterial growth to IFITM-mediated enhancement of endosomal acidification, several investigations have shown that IFITM3 overexpression does not alter the acidic profile of the endolysosomal compartment [51,84,86,87]. Overall, these studies indicate that IFITM3 is unable to restrict the majority of bacterial infections yet may have a limited effect on MTb *in vitro*. Therefore, further investigation into IFITM3's role in restriction of MTb and other bacterial species may be warranted.

1.10 Mechanism of IFITM3

Since the discovery of the antiviral IFITM proteins their mechanism of restriction has been sought but remains incompletely understood. Nevertheless, even in their initial characterisation, it was clear that IFITM proteins likely carried out their antiviral action at the point of viral entry [30]. Indeed, Brass and colleagues demonstrated that IFITM3 restricted IAV, DENV, WENV and retroviral particles pseudotyped with these same glycoproteins, narrowing its restrictive mechanism to the entry step. Solidifying this notion, retroviral particles pseudotyped with arenavirus glycoproteins LCMV, LASV, MACH were not affected by IFITM3 expression, indicating that the viral entry machinery acts as a primary determinant to IFITM3 sensitivity.

Probing this entry-based mechanism of restriction, investigations shortly thereafter illustrated that IFITM3 did not affect host receptor expression or localisation [30,68], endosomal acidification [51,84,86,87], or endosomal trafficking [68,81,88]. Nevertheless, further study began to suggest a proximity-based mechanism of IFITM3 antiviral activity. In particular, confocal imaging showed IFITM3 was present in late endosome/lysosomal compartments where labelled viruses were prevented from endosomal escape [88]. This notion was corroborated by other reports which showed that viruses incorporating envelopes that drive fusion at higher pH (i.e. in early endosomes), such as the IAV H5 and H7 strains, are increasingly resistant to IFITM3 restriction [89]. Along similar lines, VSV infection, which relies on virus-cell fusion in early endosomes, is less sensitive to IFITM3 activity [30,90].

More recently, the implementation of confocal and super-resolution microscopy techniques in combination with advances in endogenous protein and virion labelling helped confirm the proximity-based mechanism of IFITM3. Spence and colleagues utilised a site-specific fluorophore labelling strategy incorporating amber-codon-suppression-mediated unnatural amino acid mutagenesis to evaluate IFITM3 trafficking and restriction activity in live mammalian cells during IAV and LASV pseudovirus entry [82]. Concomitantly, Suddala *et al*. created a functional IFITM3 tagged with eGFP to enable live-cell imaging of virus co-trafficking and fusion within endosomal compartments harbouring labelled IFITM3 [84]. Importantly, both labelled IFITM3 proteins retained restriction activity, and demonstrated that sensitive (e.g. IAV), but not resistant (e.g. LASV) viruses are trapped within IFITM3-laden endosomes. These results suggest that resistant viruses escape IFITM3 restriction by trafficking through endocytic pathways devoid of this restriction factor [82,84]. To further define this proximity-based mechanism of restriction,

Kummer *et al.* harnessed stimulated emission-depletion microscopy to detect endogenous IFITM3 interactions with IAV in cell lines and primary human airway epithelial cells [91]. Corroborating the previous two studies, the authors illustrated that IFITM3 proteins reorganise into clusters in endosomal vesicles early in the course of IAV infection, beginning within hours.

Although these observations support a proximity-based mechanism of action of IFITM3 restriction, further work was required to characterise this process. Previous investigations have reported that IFITM family members could block cell-cell fusion mediated by all three classes of viral fusion proteins, indicating that IFITM blocks to virus entry could be isolated to the fusion step [51]. Using a pharmacologic-based assay, this study additionally reported that IFITM proteins block virus-cell fusion at hemifusion, or when the outer membrane leaflets of the virus and cell have merged [51]. Specifically, the authors demonstrated that cells over-expressing IFITM proteins and treated with oleic acid (OA) were able to support virus-cell fusion, whereas cells treated with chlorpromazine (CPZ) were unable to alleviate this restriction barrier. As OA has been shown to promote hemifusion, whereas CPZ was known to promote the transition from hemifusion to full fusion, the authors concluded that IFITM3 may block the hemifusion step [51,92,93]. This hypothesis however, was quickly revised when single-virus tracking of double-labelled virus particles indicated that it was fusion pore expansion, not hemifusion, which was blocked by IFITM3 [86].

Further supporting a proximity-based mechanism of restriction, several studies have indicated that IFITM proteins perform an antiviral function which impacts the late stages of the virus lifecycle, particularly for HIV-1 [94]. Stemming from the utilisation of several cell co-culture

experiments, it was shown that IFITM overexpression in HIV-1 infected donor cells led to potent decreases in the infection of target cells owing to an inhibition of virion fusion [95]. Importantly, IFITM3 was shown to be incorporated into the viral lipid bilayer, and redirection of IFITM3 to HIV-1 sites of assembly (i.e. the plasma membrane) increased its antiviral function. Although one study indicated that IFITM3 exerted its late-stage antiviral activity against virions by primarily hindering Env maturation and decreasing virion-associated gp120 in 293T cells [96], this phenomenon was not reproducible in T cell lines or primary T cells [95]. Additionally, it was later shown that IFITM3 could reduce the infectivity of several DNA and RNA viruses with no impact on their respective glycoproteins [97]. Consequently, it is unlikely that Env antagonism is solely responsible for the inhibition of HIV-1 virion infectivity. However, it seems that Env and IFITM3-mediated virion restriction must be linked to some degree, as Env variants (e.g. AD8) is insensitive to IFITM3 overexpression in virus-producing cells, and this insensitivity is mapped to the V3 loop of gp120 [98]. Combined with the knowledge that IFITM proteins may inhibit fusion pore expansion by altering target cell membranes, as described above, these results may support the notion that IFITM proteins similarly disturb the viral lipid bilayer to ablate virion infectivity. Together, these studies clearly indicated that IFITM3 performs at least two antiviral activities against virus entry, for which there may be mechanistic overlap.

As these investigations showed that IFITM3 restricted virus-cell fusion via a proximity-based mechanism, it is possible that IFITM3 could alter the properties of membranes in which it resides. In line with this hypothesis, Li *et al.* initially reported via fluorescent lifetime imaging microscopy that Laurdan-labelled 293T cells stably overexpressing IFITM proteins contained increased membrane rigidity and positive curvature [51]. Furthermore, IFITM3 was shown to

contain a juxtamembrane amphipathic helix which is vital for its antiviral function [56]. Amphipathic helices have been well-known to bind to, bend, and modulate the fluidity of membranes [99,100]. More recently, Guo and colleagues have shown that the amphipathic helix of IFITM3 is sufficient to increase the rigidity and negative curvature of artificial membranes [101]. In line with these observations and supporting a proximity-based mechanism as described above, IFITM3 incorporated into enveloped viruses also impairs virion fusion within target cells [73,74,102]. Therefore, IFITM3 may act proximally to restrict virus-cell fusion by altering the properties of membranes (i.e. increasing membrane rigidity). Supporting this notion is the observation that membrane remodelling polyenes, such as amphotericin B and nystatin, counteract the activity of IFITM3, rendering cells permissive to virus invasion [103]. Nevertheless, a mechanistic view of IFITM3 is incompletely resolved owing to studies lacking mutants devoid of antiviral function and membrane altering properties, such that these properties could be linked. However, using a homology guided approach, we recently identified a new determinant of IFITM3 oligomerisation and antiviral function, linking these properties to IFITM3's ability to enhance membrane rigidity such that virus-cell fusion is restricted (Chapter 3).

Furthermore, characterisation of the antiviral IFITM proteins provides evidence that several determinants of IFITM antiviral function are located within its conserved CD225 domain (described below) [104,105]. Interestingly, recent investigations suggest that this nominal domain, located in several biologically diverse proteins, is responsible for regulating membrane fusion events in several physiological contexts. Importantly, disruption of key motifs within the CD225 domain of these proteins thwarts proper function of both the IFITMs and these protein family

members, resulting in human disease, suggesting that these determinants work synergistically to provide the foundation upon which IFITM antiviral function and CD225 functionality is laid.

1.11 CD225 proteins: a portrait of membrane fusion regulators

The IFITM family of proteins fits within a larger and more diverse group of membrane proteins: the Dispanins/CD225 proteins. As our work in Chapters 3 and 4 discuss members of this superfamily, the shared features within their CD225 domain, and their diverse functions as fusion regulators, I briefly review them here.

CD225 proteins are transmembrane proteins harbouring an evolutionarily conserved, yet poorly understood CD225 domain. This domain is characterized by two hydrophobic regions separated by a cytoplasmic intracellular loop (Figure 1.1.4). Although originally thought to adopt a double-pass transmembrane topology, as it was thought for IFITM3, it is now accepted that CD225 proteins contain a single-pass hydrophobic helix and a second intramembrane region.

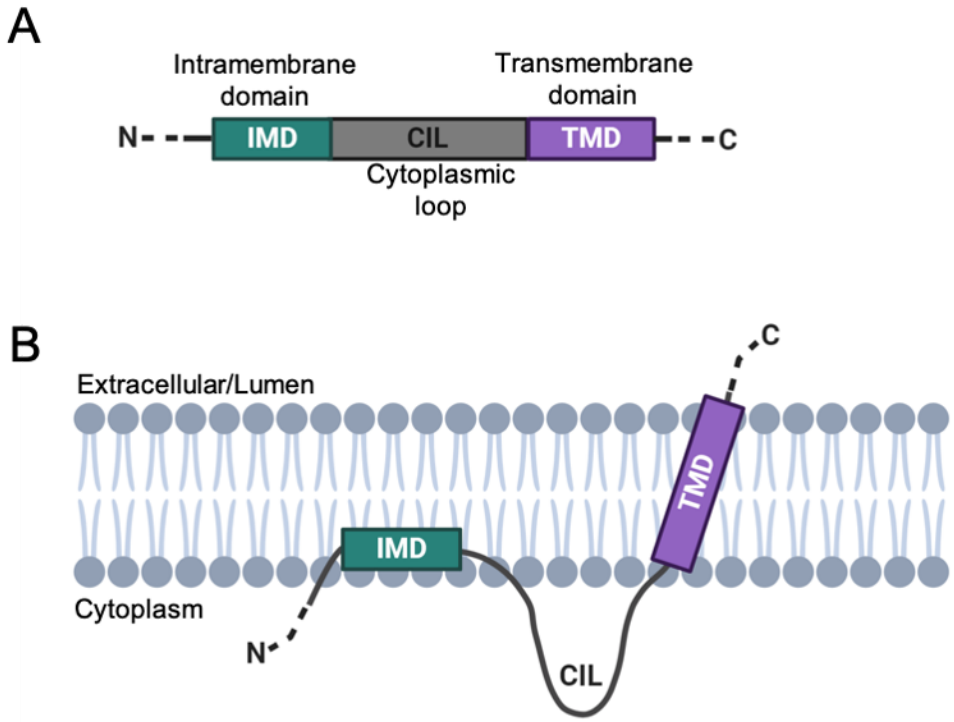

Figure 1.1.4: CD225 domain structure and membrane topology. (A) The CD225 domain is comprised of three key regions: an intramembrane domain (IMD), cytoplasmic intracellular loop (CIL) and a transmembrane domain (TMD). This domain is flanked by an N-terminus facing the cytoplasm and a C-terminus facing the extracellular space/lumen, and the length of both termini are variable among CD225 proteins. The IMD in IFITM3 was found to be discontinuous and is amphipathic in nature. **(B)** The CD225 family members for which structural information is available conform to a type II, single-pass transmembrane topology. Reproduced with permission from *Trends in Genetics*.

Originating in bacteria, this family was introduced to some metazoan ancestors via horizontal gene transfer, where it subsequently underwent gene expansion and diversification [12,13]. Consequently, the CD225 family contains many proteins with various functions, yet numerous conserved features. In humans, members include the interferon-inducible transmembrane (IFITM) proteins (IFITM1, IFITM2, IFITM3, IFITM5/BRIL and IFITM10), PRRT1/SYNDIG4, PRRT2, TUSC5, TMEM90A, TMEM90B/SYNDIG1, TMEM91, TMEM233, TMEM265, and PMIS2. In addition, a plethora of related pseudogenes as well as several mammalian CD225 family members which are not orthologous in humans also exist. Finally,

several CD225 family members contain gene copy variation amongst closely related species (e.g. the *IFITM* locus). Collectively, this oscillating evolution of the CD225 family has generated several members which operate in distinct biological contexts yet perform similar mechanistic functions [106].

For example, several well-characterized CD225 proteins play roles in neurotransmission, metabolism, antiviral immunity, or bone formation, and their loss of function is linked to human disease. Interestingly, these same members in mice and humans have been shown to be regulators of membrane fusion events in these biological contexts. Furthermore, recent investigations have identified shared features amongst CD225 proteins necessary for their fusion regulatory activity. Consequently, it is likely that CD225 proteins evolved as membrane fusion regulators.

1.12 CD225 proteins regulate exocytosis of cellular cargo

Several CD225 family members are integral in regulating exocytic processes, such as neurotransmission and insulin secretion. One such member, proline-rich transmembrane protein-2 (PRRT2) is a neuron-specific protein which maintains synaptic integrity by abrogating fusion of neurotransmitter-containing vesicles at neuronal synapses. Importantly, SNPs within *PRRT2* are linked to several convulsive neurological disorders caused by dysregulated, unchecked neurotransmission [107–111].

For example, basic research has linked multiple mutations within PRRT2 enriched in patients to disrupted interactions between PRRT2 with the soluble N-ethylmaleimide-sensitive

factor attachment protein receptor (SNARE) complex [109]. SNARE proteins collectively work to facilitate vesicle exocytosis at the pre-synaptic terminal. As PRRT2 binds to and negatively regulates the assembly of the SNARE complex, is likely that convulsive disease in patients with SNPs in PRRT2 is due to disrupted interactions between PRRT2 and the SNARE proteins, therefore allowing SNARE complex assembly and unchecked neurotransmitter release (Figure 1.1.5). Interestingly, one SNP (i.e. G305W/R) located within the CD225 domain of PRRT2 disrupts this function (Figure 1.1.5) [109]. Consequently, it is possible that because PRRT2 indirectly controls membrane fusion events by modulating SNARE complex assembly, that other CD225 proteins may perform similar roles as well.

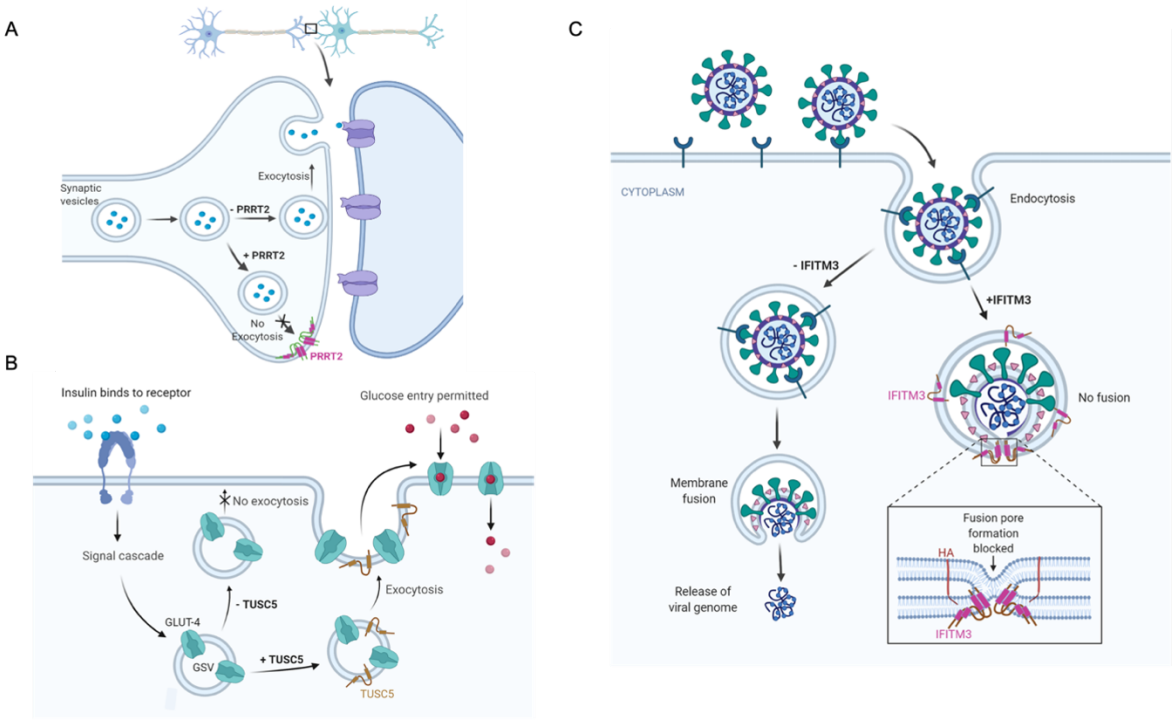

Figure 1.1.5: CD225 proteins regulate membrane fusion in diverse biological contexts. (A) An action potential in the pre-synaptic neuron initiates the exocytosis of neurotransmitter-containing vesicles in the pre-synaptic neuron. PRRT2 disrupts SNARE complex assembly at the pre-synaptic neuron to prevent the fusion of neurotransmitter-containing vesicles with the plasma membrane of thus inhibiting neurotransmission. **(B)** The insulin signalling cascade in adipocytes leads to the fusion and exocytosis of GLUT4 storage vesicles (GSV) at the cell surface, consequently increasing glucose transport into adipocytes. TUSC5, present within the GSVs, facilitates fusion of GSVs with the plasma membrane. **(C)** Several enveloped viruses fuse with the plasma membrane or the endosomal membrane to access the host cell cytoplasm to initiate genome replication. IFITM3, when present at these sites of virus-cell fusion pore formation, restricts this process due to altering host cell membrane rigidity and curvature. Reproduced with permission from *Trends in Genetics*.

In fact, this notion appears to be true. Closely-related tumour suppressor candidate 5 (TUSC5), a CD225 family member whose expression is predominately in adipocytes, has been previously demonstrated to regulate exocytosis of glucose transporter 4 (GLUT4)-laden vesicles, mediating insulin-dependent glucose uptake in adipocytes *in vitro* and *in vivo* [112]. Interestingly, GLUT4-laden vesicle fusion with the plasma membrane is a SNARE dependent process and recent evidence suggests that TUSC5 alters SNARE complex formation within GLUT4-containing vesicles. However, unlike PRRT2, TUSC5 may promote SNARE complex assembly in order to facilitate this process. Supporting this idea, *TUSC5* knockout mice are prone to diabetes, high

blood glucose, and insulin resistance, phenocopying the loss of SNARE components required for GLUT4 exocytosis at the plasma membrane [112]. Collectively, data surrounding CD225 family members PRRT2 and TUSC5 suggests that alteration of SNARE fusogens may be an ancient function of the CD225 protein family, enabling them to either promote or deter specific membrane fusion events.

1.13 CD225 proteins regulate intracellular trafficking and fusion outside the context of viral infection

Recently, the immune-related IFITMs have also been shown to play pivotal roles in host cell physiology outside the context of viral infection, particularly endocytic trafficking. Recently, it was demonstrated that IFITM3 overexpression accelerates the lysosomal degradation of epidermal growth factor receptor (EGFR) following EGF treatment [82]. It remains to be determined whether this phenomenon is linked to membrane fusion or an earlier stage of endolysosomal trafficking. Nevertheless, these results suggest that IFITM proteins may inhibit fusion through an additional indirect mechanism involving trafficking. This function may extend to the rest of CD225 protein family. Accordingly, family member TUSC5 has also been linked to endosomal recycling, and therefore, a broader role for CD225 proteins and intracellular membrane trafficking may remain to be uncovered [112].

An increasing body of literature has also linked the antiviral IFITM proteins with tumorigenesis [113–115]. Silencing IFITM proteins in certain cancers decreased tumour size and metastatic potential, and IFITM overexpression is linked to progressive tumour grading and

staging [113]. Although it is likely multiple mechanisms exist, IFITM proteins may be linked to tumorigenesis owing to their ability to modify membrane properties. For example, IFITM expression and mis-localisation amplifies intracellular signals (e.g. PI3K) integral to cell growth, division, and progression of B cell malignancies [115]. In particular IFITM3 binds surface phospholipid PIP3 and locally increases membrane rigidity to amplify CD19-mediated PI3K signalling during B cell receptor engagement [115]. Consequently, it is likely that IFITM proteins have a larger role in maintaining membrane properties to modify signal transduction.

Unlike the immune-related IFITM proteins, IFITM10 currently lacks an ascribed function and IFITM5 has a poorly defined role in bone mineralisation. Current evidence indicates that IFITM5 is strongly expressed in osteoblasts and knockdown of *IFITM5 in vitro* cell culture models has been shown to deter bone mineralisation [116]. Nevertheless, *in vivo* studies analysing bone structure of *Ifitm5*-deficient mice illustrated little if any skeletal abnormalities [15]. These results suggest that either IFITM5 has redundant function with other proteins or that physiological compensatory mechanisms are in place if its function is inhibited. However, several SNPs in human *IFITM5* have been linked to osteogenesis imperfecta (OI) type V, a disease resulting in fragile bones, hearing loss, and joint laxity [117]. Interestingly, a recurrent mutation in humans which is commonly associated with OI type V introduces a start codon shifted upstream into the untranslated region of *IFITM5*, creating a five amino acid residue MALEP extension at its N-terminus [117]. Although future investigations are needed, it is possible that IFITM5-mediated bone mineralisation is linked to an unidentified fusion process. In support of this notion, transient overexpression of human IFITM5 blocks IAV infection, although to a lesser extent than IFITM3 [68]. Furthermore, fluorescently-tagged IFITM5 has been shown to oligomerise by a FRET flow

cytometry assay, albeit to a lesser extent than the immune-related IFITMs [118]. Finally, IFITM5 has also been shown to facilitate CD9-CD81 immune complex association to increase gene expression and may also accomplish this by increasing membrane order to sustain intracellular signalling [119].

1.14 Family roots: shared motifs and modifications suggest ancestral fusion regulatory roles

Owing to their evolutionary duplication and expansion, it is little surprise that CD225 family members share multiple features which provide a foundation for their divergent functions. In particular, post-translational modifications, especially lipidation, play a crucial role in regulating CD225 domain activity. Supporting this notion is the observation that nearly all CD225 proteins of both eukaryotes and prokaryotes which have been examined are able to be palmitoylated. As palmitoylation is a conserved feature amongst all of the IFITM proteins studied to date, PRRT2, PRRT1/SynDIG4 and TMEM90B/SynDIG1, it is likely this modification was critical to CD225 domain evolution.

Another shared feature amongst CD225 proteins is that all characterized members adopt a type II or type IV transmembrane conformation. This is particularly interesting as the variable cytosolic N terminal domain (NTD) of CD225 proteins have been shown to contain functional residues readily accessible to intracellular protein partners. As mentioned above, IFITM3 localisation and turnover is directed by overlapping NTD PPxY ubiquitination and YxxΦ internalisation motifs [14,38,65]. Additionally, the cytosolic NTD comprises most of PRRT2 and PRRT1 structure, and therefore sites within this domain likely interact with several addition

partners in order to modulate their function. It is tempting to speculate that other regulatory residues in other CD225 members may be located within their NTD and have yet to be characterised.

A third commonality shared amongst CD225 proteins that is only beginning is to be revealed is self-oligomerisation. As discussed in Chapter 3, we recently identified a GxxxG oligomerisation motif in IFITM3 that drives self-association in membranes and is integral to antiviral function [105]. Importantly, a homologous motif also mediates oligomerisation of CD225 member PRRT2, and the G305W/R mutation within in this motif is enriched in patients suffering from convulsive neurological diseases [105,109]. Furthermore, as the ability for PRRT2 to bind SNARE fusogens is also impacted by the G305W/R mutation, it is likely that PRRT2 oligomerisation is necessary to interact with other proteins as well. Additionally, TMEM90B/SynDIG1 was shown to oligomerise, and its oligomerisation is required for excitatory synaptogenesis [120]. Collectively, these studies suggest an ancestral CD225 protein may have oligomerised to perform an ancient function in membranes, and that several, if not all CD225 proteins oligomerise to perform their biological function.

Finally, although amphipathic helices have only been formally identified within IFITM proteins, it is tempting to speculate that other CD225 proteins also harbour areas with at least some amphipathicity to enable direct modification of membrane properties, such as rigidity and curvature. Alteration of any of these functional properties thwarts proper function of the antiviral IFITMs, suggesting that these determinants work synergistically to provide the foundation upon which CD225 functionality is laid. Ultimately, future research is necessary to further uncover

additional mechanisms of CD225 proteins to regulate membrane fusion. It is just as likely that these efforts will also uncover additional roles for the CD225 domain which do not involve fusion.

1.15 Fluorescence microscopy to characterise virus fusion

Understanding the dynamic nature and determinants of virus fusion and its restriction demands methodologies that reveal lipid- and protein-induced membrane alterations in living systems without compromising spatiotemporal resolution. Traditionally, *in vitro* genetic, structural and biochemical techniques have been implemented to characterise membrane protein interactions and lipid binding partners [121]. However, these approaches are unable to evaluate these events in live cells, in real-time. The more recent development of several live-cell fluorescent probes, along with advances in microscopic techniques, has opened several avenues for visualising key events in virus entry in living cells in real-time. Specifically, the ability to concomitantly tag and track both viral lipids and proteins, as well as host cell receptors or restriction factors has enabled detailed visualisation of the virus fusion process and its restriction. Moreover, as viruses are smaller than the diffraction limit of light, the rise of super-resolution fluorescence microscopy platforms have generated powerful tools that can resolve single virions, their substructures and virus-cell interactions with high-throughput and exquisite detail.

Several fluorescence microscopy techniques were used in the preparation of this dissertation. Consequently, to provide more context for the upcoming results chapters (i.e. Chapters 2-4), I will describe several approaches used here.

1.16 Förster-Resonance Energy Transfer

Förster resonance energy transfer (FRET) [122] has been exploited to determine several virus-host interactions both *in vitro* and *in vivo* [123,124]. Additionally, the advances made in fluorescent proteins have made FRET microscopy a common useful tool in virology [123,124]. FRET is a non-radiative energy transfer process which occurs when specific proximity, spectral overlap, and orientation requirements are met between donor and acceptor fluorophores, such that dipole-dipole coupling occurs from an excited state donor to a ground state acceptor (Figure 1.1.6).

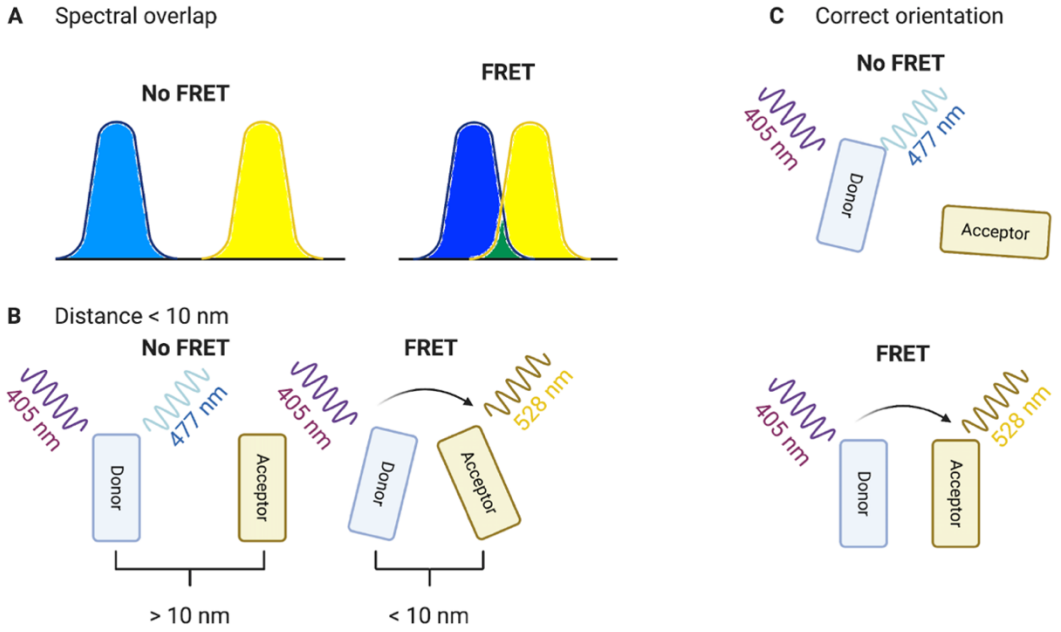

Figure 1.1.6: Förster resonance energy transfer depends on several fluorophore properties. Several properties influence the efficiency of energy transfer between donor (blue) and acceptor (yellow) fluorophores. (**A**) It is critical that the donor emission spectrum (blue) is at a wavelength (or energy) that the acceptor is able to absorb. Therefore, the donor fluorophore emission spectrum and the acceptor fluorophore excitation spectrum must overlap. (**B**) Donor and acceptor fluorophore distance is potently determines energy transfer efficiency. Consequently, if the FRET donor and acceptor are greater than 10 nm apart, then very little energy transfer occurs, and the emitted fluorescence is that of the donor fluorophore. However, if the donor and acceptor are less than ~10 nm from each other, energy transfer occurs from the donor (e.g. eCFP) to the acceptor (e.g. mVenus). (**C**) The donor and acceptor fluorophore must have properly oriented dipoles for efficient energy transfer. Therefore, if the FRET pair dipoles are perpendicularly arranged, then very little FRET occur. However, if the dipoles are arranged parallel to one another, the efficiency of FRET increases and FRET will occur. Created with BioRender.

In terms of proximity, FRET efficiency (Equation 1), or the proportion of energy transferred to the acceptor fluorophore via donor excitation, is inversely related to the distance between donor and acceptor fluorophores by the sixth-power, and consequently is a useful tool to determine molecular distance on the nanoscale, on the order of 1-10nm [125]

$$E_{FRET} = \frac{1}{1+\frac{r^6}{R_0^6}} \qquad \text{(Equation 1)}$$

where E_{FRET} is the FRET efficiency, r is the distance between the donor and acceptor fluorophores, and R_0 is the Förster distance, or the donor-acceptor distance where energy transfer is fifty-percent efficient. Provided spectral overlap (J) between the donor emission spectrum ($F_D(\lambda)$) and acceptor excitation spectrum ($E_A(\lambda)$) at donor wavelength λ (Equation 2),

$$J = \int_0^\infty F_D(\lambda) \times E_A(\lambda) \times \lambda^4 \, d\lambda \qquad \text{(Equation 2)}$$

FRET efficiency is primarily dependent on the fluorophore dipole orientation (κ^2) and the quantum efficiency of the donor (Q_D), reflected in the Förster radius (R_0) calculation

$$R_0 = [2.8 \times 10^{17} \times \kappa^2 \times Q_D \times E_A \times J]^{1/6} \qquad \text{(Equation 3)}$$

Because the restrictions for FRET between donor and acceptor fluorophores are manoeuvrable, with readily available tools to match donor and acceptor fluorophores [126], FRET is able to provide accessible and physiologic measurement of protein-protein interactions, conformational changes, and macromolecular concentrations [125].

In the context of viral infection, protein-protein interactions facilitating virus entry can be directly monitored by FRET. For example, the β-lactamase assay has offered a wide breadth of knowledge regarding the kinetics and dynamics of HIV-1 fusion [127]. This assay relies on the packaging of β-lactamase enzyme into nascent HIV-1 virions, where fusion-positive cells are able to cleave the cytoplasmic-loaded FRET-based CCF2 dye, therefore altering the FRET profile. Having been widely implemented, this assay has been able to quantify virus fusion events in bulk cell populations, but most recently approximated the number of viruses fused in individual cells [128]. FRET may also be harnessed to reveal restriction factor antagonism or function. For example, recent investigations used FRET to map key residues in the TMD of HIV-1's accessory protein Vpu and characterise its interactions with other target proteins (e.g. tetherin) [129]. Most recently, it was shown via a FRET-based flow cytometry assay that IFITM3 oligomerisation does not require residues F75 and F78 residues, indicating that the determinants of IFITM3 oligomer formation are still unknown [118]. Ultimately, these FRET microscopy studies can be utilised at the bulk or single-cell level to characterise key events in virus fusion or its restriction.

1.1.17 Fluorescent Lifetime Imaging Microscopy

FRET microscopy is a particularly quantitative analysis owing to the quantum yield of the energy transfer. Interestingly, the FRET donor fluorescence lifetime, or the time the donor fluorophore in a FRET pair exists in the highest unoccupied molecular orbital during excitation, decreases in proportion to the efficiency of FRET. One platform which exploits this phenomenon is fluorescence lifetime imaging microscopy (FLIM), which is a microscopy-based technique that has gained considerable popularity owing to its high sensitivity to molecular environment and

changes in molecular confirmation [130,131]. Advantageously, the FRET efficiency calculation acquired by lifetime measurements in living cells is independent of the fluorophore concentration and the light excitation path [130]. Broadly, there are two distinct methods for FLIM acquisition: the time domain, and the frequency domain. Time-domain acquisitions require the excitation of the sample with a rapid pulsed-laser, and a fluorescence decay is calculated from binned histograms recording the time-of-arrival of thousands of photons (Figure 1.1.7). Alternatively, frequency-domain methods harness the phase delay of fluorescence photon relative to the excitation photon, where subsequently the phase distribution is analysed in Fourier space to extract modulation and demodulation parameters.

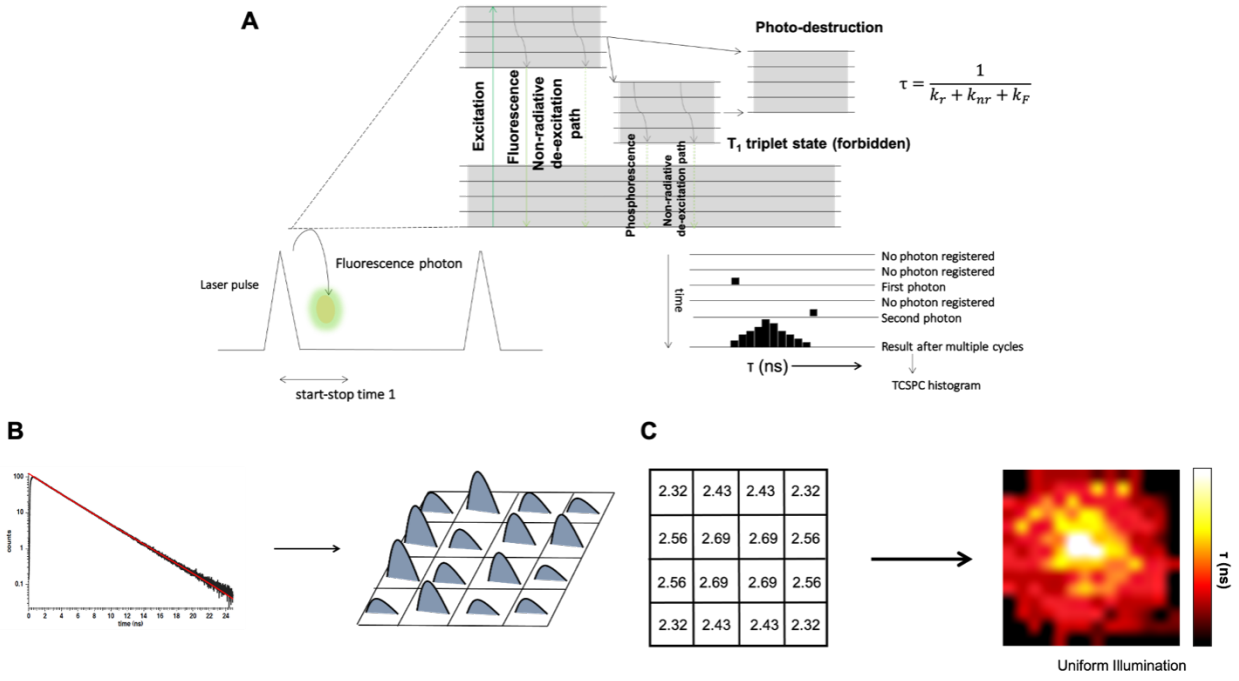

Figure 1.1.7: A fundamental overview of time-correlated single photon counting fluorescence lifetime imaging microscopy. (**A**) A pulse laser is used as an excitation source to excite the fluorophore. This excitation enables the transition of an electron from the highest occupied molecular orbital to the lowest unoccupied molecular orbital. This excitation to an excited state is shortly followed by the emission of a photon with a given start-stop time. This is illustrated with the Perrin-Jablonksi diagram, along with the various de-excitation paths the excited electron can take after excitation. The rate of de-excitation down each excitation path contributes to the fluorophore lifetime (τ). Notably, the time between the laser pulse and detection of the fluorescence photon is recorded in a histogram. The repetition of many cycles leads to the construction of a TCSPC histogram. (**B**). The histogram is fitted with an exponential decay curve to extract the fluorescence lifetime from the slope. Notably, this process happens for each pixel in the recorded image. (**C**) Consequently, each pixel is assigned a lifetime value that is used to construct a lifetime image.

One of the most commonly implemented time-domain platforms is time-correlated single photon counting (TCSPC) (Figure 1.1.7). In this setup, a pulsed laser is used as an excitation source such that less than one photon is detected per laser pulse (i.e. one photon per 100 excitation pulses) [130,132]. During acquisition, time is measured between the excitation pulse and the detected photon (Δt), stored in a histogram, and will construct the fluorescence decay waveform (Figure 1.1.7). The slope of this decaying waveform reports the donor fluorophore lifetime.

However, in practice, three curves are used to construct this decay: the instrument response function (IRF), the measured data $N(t_k)$, and the calculated decay $N_c(t_k)$. Briefly, the IRF is the response of the instrument to a zero lifetime sample (i.e. $\tau = 0$), and thus is the shortest lifetime detectable by the instrument and varies per instrument [130]. $N(t_k)$ is the actual histogram of photons detected at a time interval Δt. Lastly, $N_c(t_k)$ is the fitted function that represents a convolution of the IRF with the impulse decay function $I(t)$, represented by the general equation

$$I(t) = a_1 e^{\frac{-t}{\tau 1}} + a_2 e^{\frac{-t}{\tau 2}} + \cdots + a_i e^{\frac{-t}{\tau n}} \text{ (Equation 4)}$$

such that t is time following excitation, a_i is a pre-exponential factor corresponding to the fractional amount of fluorophore in each environment n (e.g. in the presence or absence of a FRET acceptor), and τ_n represents the lifetime corresponding to the fluorophore in n environment. Ultimately, the pre-exponential factors a_i and lifetimes τ_n are extracted from FLIM analysis software [133].

The measured lifetime decay function thus is a convolution integral with the IRF $L(t_k)$ summating impulse decay functions created by individual excitation pulses occurring until t_k such that

$$N_{t_k} = \sum_{t=0}^{t=t_k} L(t_k)\, I\,(t - t_k)\, \Delta t \qquad \text{(Equation 5)}$$

and for infinitesimal values of Δt can be represented by

$$N(t) = \int_0^t L\,(t_k)\, I(t - t_k) dt_k \qquad \text{(Equation 6)}$$

There are several advantages to using FLIM microscopy over intensity-based methods. For example, intensity-based measurements which are commonly used to discriminate between fluorophores are often complicated by overlapping spectra. Furthermore, unique molecular environments surrounding each fluorophore often are indistinguishable [134]. In contrast, FLIM may exploit a fluorophore's lifetime to discriminate fluorophores which spectrally overlap. A classic example is NAD(P)H, where its various molecular species are only distinguishable in different cellular contexts (e.g. protein bound or free) when visualised by FLIM imaging [135]. Additionally, FLIM-based measurements are uniquely independent of fluorophore concentration, light path and nonuniform illumination. Furthermore, lifetime is a self-referenced measurement, meaning that FLIM experiments need not require calibration steps that are often required of intensity-based measurements [134]. Therefore, lifetime measurements may be acquired across multiple commercial devices with increased reproducibility. Moreover, although time-resolved fluorescent lifetime measurements typically acquire long acquisition times, recent commercial

developments have shortened the acquisition times of FLIM images to seconds, enabling the visualisation of fast biological events, such as alterations in membrane tension during virus-cell fusion [136,137].

Several studies have taken advantage of FLIM imaging to visualise key steps in virus entry with unparalleled spatial resolution. For example, Jones *et al.* utilised FLIM microscopy to ascertain the oligomeric state of dynamin-driven HIV-1 fusion pore formation [138]. Additionally, we have utilised FLIM to visualise favourable host membrane order and tension parameters that support HIV-1 fusion in live cells, connecting biophysical properties of host membranes with the metabolic activity of the cell [137]. We envision that soon FLIM microscopy will be utilised to unveil key mechanisms of restriction of cell-intrinsic antiviral proteins. Already, we have utilized FLIM microscopy to link a conserved motif in IFITM3 with its ability to oligomerise and rigidify membranes [105], supporting previous reports which utilised FLIM to show that IFITM proteins alter membranes rigidity and curvature of the host cell to prevent virus-cell fusion [51].

1.18 Fluorescence Fluctuation Spectroscopy

Understanding virus fusion and its restriction at the single-molecule level integrates an intricate understanding between structure, dynamics and function which must be probed with high spatial (e.g. nanometer) and temporal (e.g. microsecond) resolution under *in vivo* conditions. Nevertheless, spatial and temporal resolution are often mutually exclusive requirements [139]. For example, high-resolution nanoscopy measurements often come at the cost of temporal resolution [140]. Fortunately, the analysis of fluorescence intensity fluctuation to infer molecular processes,

a technique known as fluorescence fluctuation spectroscopy (FFS), enables the resolution of molecular dynamics over the course of nanosecond to milliseconds.

In general, fluorescence fluctuation methods can be categorised into two flavours based on the statistical analyses employed to analyse the detected intensity fluctuations of fluorescent molecules in space and time [141]. The first and most common analysis method is fluorescence correlation spectroscopy (FCS) [142]. In this approach, the fluorescence signal of a labelled molecule is recorded in a small observation volume over time, and this intensiometric information is used to infer the mechanism underpinning the recorded fluctuations, such as diffusion, chemical reactions, excited state transitions and bleaching [139]. Additionally, a two-coloured FCS approach called fluorescence cross-correlation spectroscopy (FCCS), can be used to study molecular interactions [143]. Nevertheless, FCS and FCCS are limited in multiple ways. In particular, the autocorrelation function, which is calculated to extract information about the molecular processes underlying the intensity trace fluctuations, cannot be easily extracted with high accuracy [139]. Additionally, FCS has been implemented as a method that observes only a single spot in space [139].

Alternatively, number and brightness (N&B) analysis [144,145] extracts the first and second moments (i.e. mean and variance) from recorded intensity fluctuations at every pixel from a series of images to compute the mean number of entities (i.e. fluorescent molecules) within each pixel (*n)* and the mean number of photon detector counts per unit time, or brightness (ε) (Figure 1.1.8). From this information, the number of mobile particles can be obtained to infer molecular aggregation and binding states. The calculation was first described by Digman and colleagues

[144]. Assuming zero background and all particles are mobile, the mean signal $<I>$ in a pixel in a stack of images is proportional to its apparent number of particles. Additionally, the apparent brightness of these particles is proportional to the squared variance σ^2 of the recorded intensity. The ratio of these two values computes the particle brightness. The mean intensity can then be divided by particle brightness to extract the number of mobile particles in a pixel. That is, we have

$$N = \frac{<I>^2}{\sigma^2} = \frac{\varepsilon n}{1+\varepsilon} \qquad \text{(Equation 7)}$$

$$B = \frac{\sigma^2}{<I>} = 1 + \varepsilon \qquad \text{(Equation 8)}$$

where N and B are referred to as the "apparent number" and "apparent brightness" respectively. This gives

$$n = \frac{<I>^2}{\sigma^2 - <I>} \qquad \text{(Equation 9)}$$

$$\varepsilon = \frac{\sigma^2}{<I>} - 1 \qquad \text{(Equation 10)}$$

One clear advantage of this approach is that N&B has minimal requirements of labelled protein concentration, often in the nanomolar range [146]. Furthermore, the stack of images acquired to extract these values can be acquired with a simple laser scanning microscope or a camera-based fluorescence microscope [138,147,148].

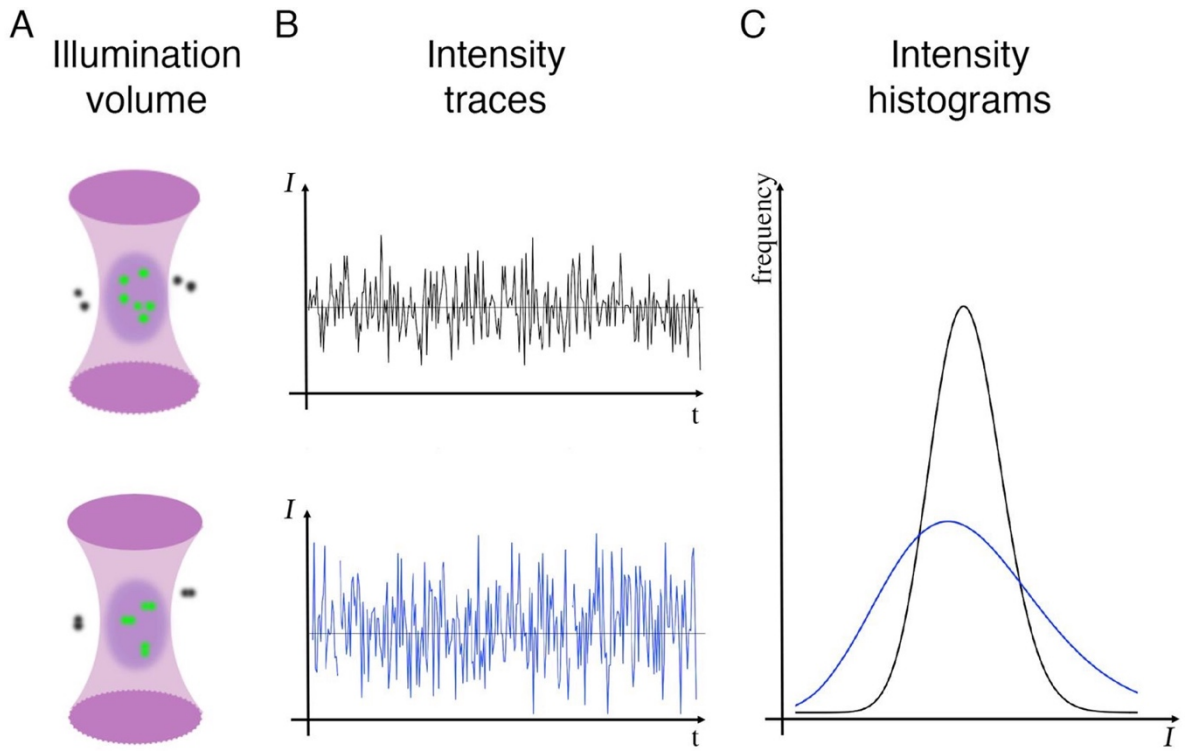

Figure 1.1.8. The basis of number and brightness fluorescence fluctuation analysis. (**A**) Here is a system in which monomeric proteins (Top Row) undergo dimerization (Bottom Row) in the confocal volume. Prior to dimerization, a mean number of monomers were excited in the confocal volume. However, upon dimerization, a mean number of dimers are excited in the confocal volume. (**B**) Notably, the same concentration of fluorophores, and therefore mean intensity will be the same in both conditions. Nevertheless, after dimerization, the condition containing dimers has recorded a higher variance in intensity, owing to the fact that the labelled protein is entering and leaving the confocal volume in pairs. (**C**) Intensity histograms can be used to visualise the constant mean and increase in variance (monomers, black; dimers, blue), with the wide blue histogram indicating the increase in variance when dimers are present. The mean intensity and its variance are used to calculate the brightness and oligomeric state of the protein. Reproduced with permission from [153].

One clear caveat of N&B measurements is that photobleaching may confound any calculated result and therefore must be corrected for appropriately [149]. Additionally, this analysis can only calculate the number of mobile particles, meaning a subpopulation of immobile particles in the sample can confound the results [144,145,148]. This is because the for immobile particles, $B = 1$, and therefore ε cannot be computed from B. Importantly, however, if an illuminated pixel contains a mixture of both mobile and immobile particles, B must be between its mobile and immobile value and will increase proportionally with its oligomeric state. Therefore, one can detect changes in oligomeric state, but not identify the oligomeric state.

N&B analysis requires specific acquisition parameters, particularly in regard to the pixel dwell time (t_{dwell}) and the frame rate (t_{frame}). As N&B analysis requires mobile particles, is theoretically possible to acquire a frame that is too slow or too fast [144,145]. If a frame rate is too quick, then the mobile particles may not move out of a pixel by the next frame capture, and therefore will appear as immobile, rendering ε incalculable. Additionally, the pixel dwell time must be short enough such that only one configuration of particles in the confocal volume is sampled. Therefore, for the average time a particle remains in a confocal volume (τ_D), then the t_{frame} and t_{dwell} must be set such that:

$$t_{frame} \gg \tau_D \gg t_{dwell} \qquad \text{(Equation 11)}$$

Interestingly, N&B analysis has been extended to a two-coloured version, denoted cross-correlation number and brightness (cc-N&B), which can be used to investigate the stoichiometry of multimolecular complexes provided that different proteins are labelled with different fluorophores [145]. However, difficulties of fluorophore bleed-through can confound results from such analysis and therefore must be closely monitored. For example, the wide emission spectra of GFP-based fluorophores may lead to photons from the green channel to be counted in the red channel as well, artificially leading to false conclusions about protein-protein interactions. Nevertheless, multiple sequential scanning approaches can avoid this problem [150].

Recently, FFS approaches, particularly N&B, have been implemented to quantify molecular interactions to elucidate critical steps within the lifecycle of several viruses. Initially, N&B analysis was first utilised to uncover mechanisms of IAV polymerase assembly and nuclear import by quantifying the stoichiometry of the H1N1 polymerase subunits PB1, PB2, and PA,

ultimately showing the PB1 and PA heterodimerize in the cytoplasm before being imported into the nucleus to form a heterotrimer with PB2 [151]. Shortly thereafter, Adu-Gyamfi and colleagues utilized N&B to quantify the stoichiometry of Ebola matrix protein VP40 at sights of virus egress within plasma membrane protrusions, further expanding this approach to studying important steps of viral assembly and release in live cells [152].

N&B has also been pivotal in describing key steps of the HIV-1 lifecycle, particularly in HIV-1 assembly and entry. For example, Ferrer *et al.* illustrated that dimerization of HIV-1 genomic RNA first occurs in the cytosol of infected cells and that HIV-1 Gag is a key player in this process [153]. These results were obtained by utilising a ccN&B approach harnessing eGFP and mCherry labelled HIV-1 RNA binding proteins to visualise large amounts of bright, co-diffusing complexes in the cytosol and mapping dimerization and co-trafficking to virion assembly sites. Similarly, Hendrix and colleagues incorporated several FFS approaches to provide direct proof for the existence of two different HIV-1 Gag species in the cytosol: fast-diffusive monomers and slow-diffusive Gag oligomers [154]. These results suggest that HIV-1 assembly initiates in the cytosol with Gag-RNA and Gag-Gag interactions before anchoring into the plasma membrane.

Number and Brightness analysis has also been harnessed to describe HIV-1 entry and its restriction. Indeed, Iliopoulou and colleagues were first to apply N&B analyses to determine the stoichiometric relationships of receptors and co-receptors required for HIV-1 entry. In particular, using a combination of SPT of labelled virus particles and fluorophore-tagged CD4, CCR5, or CXCR4, they showed that mature HIV-1 entry requires a specific stoichiometry of receptors and coreceptors which is tropism dependent [155]. Shortly before, Chojnacki and others combined

nanoscopy with FFS to determine the molecular mobility of HIV-1 Env in mature and immature particles [156]. Finally, we have utilised N&B imaging of mCherry-labelled IFITM3 to show that a GxxxG motif is critical to support self-oligomerisation of this restriction factor, which is required to rigidify membranes and thwart HIV-1 entry (Chapter 3). Similar approaches can be applied to answer outstanding questions regarding the mechanisms of action of IFITM proteins and other restriction factors. For example, although IFITM3 has been shown to act as higher order oligomers to restrict inbound virus particles, can IFITM proteins hetero-oligomerise to accomplish the same task? Do IFITM proteins interact with other host factors to prevent virus fusion? Furthermore, as IFITM3 has been shown to increase membrane rigidity, can it do so in virions and thus alter the mobility of HIV-1 Env? Future studies will provide answers to such questions.

1.19 Super-resolution microscopy

The resolution of traditional fluorescence microscopy is physically restrained due to the diffraction limit of visible light, represented by Equation 12,

$$d = \frac{\lambda}{2NA} \qquad \text{(Equation 12)}$$

where *d* is the distance between which two labelled molecules can be identified as separate, *NA* is the numerical aperture of the objective, and λ is the wavelength of light [157]. Therefore, the theoretical resolution limit of conventional fluorescence microscopy is approximately 200nm in the xy focal plane and 600nm along the optical z axis [157]. Several viruses, including HIV-1 and IAV, are smaller than 200nm. Therefore, the diffraction limit of light complicates the analysis of

virus architecture or virus-host interaction dynamics at the molecular scale. Importantly, although the observation and characterisation of virus particles and their interactions with host cells have been visualised *in vitro* by electron microscopy for decades, this technology suffers from sample preparation requirements which distort both viral and cellular architecture [158] and cannot be performed in living cells [159].

The dawn of super-resolution fluorescence microscopy has made the visualisation of fluorescently-tagged molecules in live cells with a resolution of 10-100nm routine [159]. In particular, STED [160] and PALM/dSTORM [161] techniques allow the reconstruction of virus architecture or virus-cell interactions with exquisite detail and in real-time. Both of these techniques employ targeted switching of fluorescent labels between bright and dark states, with only a small fraction of fluorophores fluorescing at any moment, allowing their resolution below the diffraction limit. These two techniques differ primarily based on how the fluorophore position is recorded. STED microscopy employs an intense laser targeted to outer regions of the excitation focus to return molecules to the ground state, thus allowing only the excited molecules in the centre of the excitation focus to be detected. In contrast, PALM/dSTORM utilises photoswitchable fluorophores tagged to molecules of interest and stochastically switches them on in the entire field of view to localise them, photobleach them, and repeat the process many times.

The recent implementation of nanoscopy-based approaches in studies of virus entry and its restriction have expanded our general understanding of these events. In particular, STED microscopy was utilised to analyse HIV-1 Env glycoprotein distribution during virus assembly and maturation in nascent virions, revealing that virus maturation enables the formation of an HIV-

1 entry claw, consisting of multiple mobile Env trimers on virion surfaces [162]. In particular, Chojnacki and colleagues demonstrated through STED nanoscopy that although Env trimers are initially recruited to virus sites of assembly and egress in a random distribution, the underlying Gag lattice restricted their movement via interaction with the cytoplasmic tail of Env [162]. Subsequent proteolytic cleavage of HIV-1 Gag initiates Env mobility, driving the formation of a single Env focus within individual virions.

Additionally, studies concomitantly implementing both STED and FCS have shown that this critical Env mobility relies on virion lipid composition and membrane order [156]. Indeed, alteration of lipid content may immobilise Env in nascent HIV-1 virions, and excessive lipid packing may negatively impact HIV-1 infectivity [156]. This comes as little surprise owing to the fact that HIV-1 actively incorporates specific lipidic components during egress such as PI(4,5)P2 and cholesterol, as shown by nanoscopy studies which incorporated STED-FCS to analyse the mobility of fluorescent lipid analogues HIV-1 assembly sites in HIV-1 infected CD4+ T cells [163]. Since we and others have demonstrated that IFITM3 oligomers increases membrane order in cells, it would be tempting to determine if IFITM3 oligomers also perform this function in virions and whether this reduces Env mobility. Furthermore, additional investigations could also determine if IFITM3 will form higher order oligomers in membranes serving as virus assembly sites and in nascent virions. Nanoscopy-based platforms such as STED, PALM/dSTORM will be able to reveal answers to such questions. Indeed, the utility of super resolution microscopy methods to delineate key virus-host interactions to mediate entry of pathogenic viruses, such as HIV-1 [155] or its restriction [91], is only in its infancy.

1.20 The fundamentals of enveloped virus-cell fusion

All viruses must traverse the cell's membrane barrier to release their contents into the cell to initiate genome replication. Enveloped viruses accomplish this generally by merging their lipid envelope with either the host cell's plasma or endosomal membrane through membrane fusion, facilitated by viral fusion machinery. This fusion reaction is likened to the stalk-hemifusion-pore model which proposes that virus-cell membrane fusion proceeds through a series of lipidic intermediates [164]. In particular, the fusion reaction is initiated by the deformation of virus and cell membranes, facilitated by conformational changes in viral surface glycoproteins as a result of receptor binding (Figure 1.1.9). These deformations in virus and host membranes forms a lipid connection between them, likened to a bridge formed by the outer leaflets of the fusing bilayers. This lipid connection is commonly referred to as a hemifusion stalk. Subsequently, this stalk undergoes radial expansion to create a conserved hemifusion intermediate where the outer monolayers the fusing bilayers are merged, but the inner leaflets are intact. Ultimately, this hemifusion diaphragm transforms into a fusion pore, where both bilayers are merged into one, and will expand until fusion is completed [165]. Interestingly, super-resolution studies have recently visualised this fusion pore hypothesis and have shown fusion pores to be dynamic and metastable, dramatically varying in in size, rate of expansion, and propensity to collapse [166]. Consequently, this stalk-hemifusion-pore model now describes many different cellular events, not only viral fusion, but exocytosis and cell-cell fusion as well [93,167].

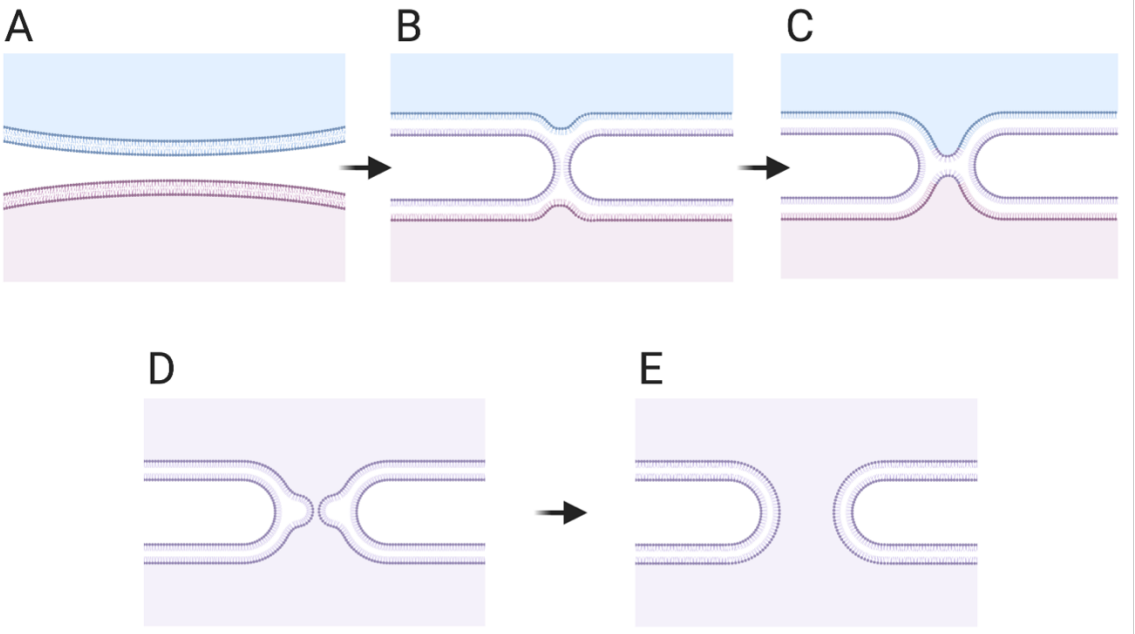

Figure 1.1.9. The stalk-hemifusion-pore model of fusion. (**A**) Generally facilitated by a viral fusogen after binding to its cognate receptor, lipid bilayers of the virus (blue) and host (pink) bend into close proximity to one another. (**B**) Once the virus and host cell membranes initially contact, the lipid bilayers move apart to enable local close contact between the outer leaflets of the two membrane bilayers such that a hemifusion stalk is created. (**C**) The hemifusion stalk will expand into a small hemifusion diaphragm as more lipid surface area between the virus and host outer membrane leaflets merge. (**D**) From the hemifusion diaphragm, an initial fusion pore is opened, although can collapse. (**E**) This initial fusion pore expands and eventually creates an hourglass fusion pore of various sizes, enabling release of virus contents into the cytoplasm. Created with BioRender.

Enveloped viruses utilise transmembrane fusion proteins or "fusogens" to drive the fusion reaction between virus and host cell membranes. These proteins have adapted to undergo conformational changes when they are triggered (e.g. by low pH or cell-receptor binding) to expose hydrophobic fusion peptides or loops which embed themselves within the host cell membrane, catalysing membrane fusion. The conformations of these proteins post-fusion form a hairpin-like

structure, and preliminary conformational changes of these fusion proteins often results in their inactivation. Overall, there are three classes (I-III) of viral fusion proteins utilised by enveloped viruses [168]. Class I fusion proteins, exemplified by HIV-1 gp41 or influenza hemagglutinin (HA), are identified by a characteristic helical hairpin trimer with a central coiled-coil structure post-fusion conformation. In contrast, class II fusion proteins, such as Dengue or Hepatitis C virus fusion proteins, are characterized by a post-fusion hairpin trimer which lacks the central coiled-coil structure. Class III fusion proteins, typified by the VSV-G glycoprotein, combine structural similarities found in class I and II fusogens.

The structural characterisation of several class I fusion proteins has been paramount in identifying key steps of entry for several pathogenic viruses, such as HIV-1. In particular, retrovirus Env protein trimers had proven particularly complicated for structural studies due to their extensive glycosylation, conformational flexibility and tendency of their N and C terminal subunits to spontaneously dissociate [169]. Nevertheless, engineered HIV Env constructs which stabilise the Env trimer and generate an antigenic profile similar to that of native Env (e.g. SOSIP), helped catalyse the reconstruction of HIV Env to inform both immunologic and structural studies [169–171].

The HIV-1 envelope (Env) spike, synthesised as precursor gp160 trimer, catalyses the fusion of viral and target cell membranes. This precursor is cleaved into two fragments by furin-like proteases to form the receptor binding subunit (gp120) and the fusion transmembrane subunit (gp41). Interestingly, unlike several other type I fusion viral glycoproteins, the HIV-1 fusion

peptide appears to point away from the core of the trimer, extending past its HR2 helical domain [170,172].

During HIV-1 entry, gp120 binding to receptor CD4 and either coreceptor CCR5 or CXCR4 induces a series of refolding events of the prefusion gp41, enabling its N-terminal insertion into the target cell membrane and subsequent formation of the extended gp41 conformation. This state, where the gp41 fusion peptide is embedded within the target cell membrane and the transmembrane segment in the viral membrane, is referred to as the pre-hairpin intermediate. Importantly, this conformational state is the target of the antiretroviral salvage therapy enfuvirtide as well as several broadly neutralizing antibodies (bnAbs) (e.g. 10E8, 4E10 and 2F5) [171]. Immediately thereafter, the gp41 subunit refolds into a hairpin conformation, creating the canonical six-helix bundle termed the metastable post-fusion conformation, which brings the virus and host cell membranes in close proximity and facilitates their fusion, ultimately reducing the energy required for this reaction occur. Importantly, the full fusion peptide has recently been resolved but only in the presence of bnAbs (PGT151 and VRC34) [170]. In these structures, it appears that the fusion peptide is fully exposed and constitutes a major component of the epitopes. Therefore, the fusion peptide is accessible to antibodies and has become a target for HIV vaccine design.

The fusion process driven by viral fusogens is regulated by key biophysical properties of the viral and host membranes, including membrane curvature, membrane order, and membrane tension. In particular, membrane bending has been shown to regulate the transition from hemifusion to full fusion [93,165] and the directionality of the curved membrane, either toward

(i.e. “negative” curvature) or away (i.e. “positive” curvature) relative to the compartment or volume contained by the membrane, regulates the process. Specifically, positive membrane curvature has been shown to deter the hemifusion to fusion transition, whereas negative membrane curvature has been shown to promote this transition [51,173]. Multiple membrane components influence membrane curvature, including lipid composition and membrane proteins [99,173]. For example, lipidic components which have a small polar headgroup to acyl chain ratio, such as cholesterol, diacyl glycerol, and phosphatidylserine promote negative membrane curvature, whereas lysophospholipids and phosphatidylinositol phosphates promote positive membrane curvature as they possess large headgroup to acyl chain ratio [174]. Likewise, amphipathic helices from membrane remodelling proteins have been shown to positively bend membranes [99].

Additionally, negative-curvature inducing lipids, such as cholesterol, have been shown to facilitate fusion pore formation, confirming the importance of membrane bending in virus-cell fusion [175]. Importantly, depletion of these lipids disrupts virus fusion and entry into the host cell [176]. Furthermore, given that host cell membranes may act as capacitors for cell lipid metabolites [177] and that metabolic sensors, membrane composition, and membrane biophysical properties are interlinked [178,179], it is likely that host cell metabolism may indirectly regulate several fusion processes. Nevertheless, the connection between host metabolism, membrane biophysics and their impact on virus-cell fusion has not been investigated until recently [137].

Intertwined with membrane curvature is membrane order, a property which quantifies the rigidity of the membrane. Several investigations have shown that increases in membrane rigidity potently block fusion pore formation and expansion [92,180,181]. Consequently, it is tempting to

speculate that membrane properties, such as membrane order, may be intentionally perturbed by the host cell in order to thwart virus-cell fusion.

In addition, membrane tension has been shown to drive fusion pore expansion [93]. Specifically, tension generated by either osmotic pressure, lipid reservoirs, or cytoskeletal proteins have been shown to drive fusion pore expansion in the context of cell-cell fusion initiated by influenza hemagglutinin [181–183]. Nevertheless, high membrane tension often collapses hemi-fusion intermediates [184,185], suggesting that an appropriate balance of membrane order, curvature, and tension are required to support the fusion between virus and host.

Importantly, these biophysical regulators of membrane fusion are not confined to the host cell, but the viral membrane as well. For example, the membranes of many enveloped viruses, including HIV-1, have been shown to be increasingly ordered when compared to the host cell [163]. Importantly, decreases in HIV-1 membrane fluidity have been shown to disrupt virus-cell fusion [186,187]. These results are in line with reports showing that depletion of lipid-ordered cholesterol has been shown to also decrease the infectivity of IAV [188] and Dengue [189] and HIV-1 [190,191].

Collectively, these results suggest that the fusion process necessary for a virus to penetrate host membranes requires a balanced biophysical landscape, where too rigid or too fluid membranes in either the virus or host cell could disrupt the fusion reaction. Therefore, although viral fusogens facilitate the creation and expansion of a fusion pore to initiate infection, the biophysical properties of the two participating membranes are inevitably critical in mediating this reaction. Importantly,

employing biological systems where these membrane properties can be altered (i.e. membrane order and membrane tension) provides a unique strategy to identify and characterise novel biophysical regulators of virus-cell fusion, specifically those which can be monitored by non-invasive, live-cell imaging approaches.

1.21 Aims of thesis

This dissertation describes the development and implementation of several microscopy techniques to identify, quantify and characterise membrane properties, such as order and tension, and their regulating factors in the context of virus entry, particularly HIV-1 (Chapter 2). The application of these advanced imaging tools is then extended to characterising the mechanism of action of IFITM3 (Chapter 3), offering evidence to suggest that CD225-containing proteins employ a shared oligomerisation motif to alter host membrane rigidity to block virus-cell fusion. Incorporating the tools and conclusions developed from Chapters 2 and 3, preliminary data describing how introduction of this oligomerisation motif enhances the restriction activity of a non-canonically antiviral human IFITM is presented in Chapter 4. We conclude with a discussion describing the future of advanced imaging techniques to inform key regulators of virus-cell fusion, as well as an updated mechanism of action of IFITM3 restriction in host cells and in virions (Chapter 5). Ultimately, this work provides significant new insight into the mechanism of virus fusion and its inhibition by IFITM3, and catalyses new discussions expanding the known roles of CD225 proteins in regulating fusion processes in a variety of biological contexts.

1.22 Acknowledgements

The sections of this introduction highlighting the role of CD225 proteins (i.e. sections 1.11 to 1.14) were written with Kazi Rahman and Alex Compton. This work was originally published in *Trends in Genetics*.

Coomer CA, Rahman K, Compton, AC (2021) CD225 proteins: A Family Portrait of Fusion Regulators. *Trends in Genetics. In press.*

Chapter 2: Single-cell glycolytic activity regulates membrane tension and HIV-1 fusion

2.1 Introduction

HIV-1 infects target cells via engagement of its Envelope (Env) glycoprotein with host receptor CD4 [192] and co-receptors CCR5 [193] or CXCR4 [194]. Interaction between Env, CD4, and either co-receptor triggers conformational changes in the Env gp41 transmembrane subunit, catalysing virus-cell fusion [195]. Characterising the earliest stages of HIV-1 infection is a priority in devising novel treatment strategies [196]. Recently, multiple reports have identified host cell metabolism as a key player in shaping both T cell-mediated antiviral responses as well as the course of HIV-1 infection [197,198]. Nevertheless, the role of host cell metabolic activity and its relationship to cellular susceptibility to HIV-1 infection has only begun to be described.

To mitigate the strenuous energy demand associated with an immune response, T cells have been shown to increase rates of glycolytic flux following activation [199] and upregulate cell-surface glucose transporter GLUT1 [199]. Furthermore, end-products from glycolysis in activated T cells function as biosynthetic intermediates which regulate several biophysical properties of host-cell membranes. In particular, activated T cells harbour elevated levels of citrate and NAD+ [200], which are precursors of key components utilised in the biosynthesis of cholesterol, a major determinant of cell membrane fluidity and tension [201,202]. Moreover, as the activated T cell metabolic program relies on increased rates of aerobic glycolysis, T cells support upregulated levels of fatty acid synthesis and mevalonate metabolism via the increased flux of pyruvate into

the mitochondria, subsequently feeding acetyl-CoA and citrate into lipogenic pathways (Appendix Figure 5.11) [203].

Interestingly, HIV-1 replication also requires GLUT1 expression in T cells and may increase the sensitivity of infected CD4+ T cells to virus-induced cytopathic effects [204–206]. More recently, the basal glycolytic activity of CD4+ T cell subsets has been shown to track with HIV-1 susceptibility and glycolysis inhibition has been shown to diminish HIV-1 infection in these cells [207]. However, it was unclear which stage of HIV-1 infection was affected. Consequently, the role of glycolytic flux in modulating key regulators of cellular membrane architecture (e.g. cholesterol) and its impact on early-steps of HIV-1 infection have not been characterised.

Host cell cholesterol content and membrane biophysical properties have become increasingly relevant in the context of virus infection, including HIV-1 [93,208]. In addition to locally reducing membrane tension, cholesterol facilitates the formation and maintenance of liquid-ordered (Lo) domains [202,209]. These Lo domains form a discontinuity within the lipid bilayer which has been recently shown to be critical for the HIV-1 fusion reaction [210–212]. These boundaries between Lo and liquid-disordered (Ld) microdomains are well-established to facilitate successful entry for a range of viruses, including HIV-1, owing to the ability for these boundaries to drive membrane bending required for the fusion reaction [210–213]. Importantly, membrane order and tension regulate each other in addition to membrane curvature. Together, these properties influence the hemifusion reaction specific to lipid membranes of the virus and target cell [92,93,167]. Specifically, positive membrane curvature has been shown to disfavour fusion pore formation, whereas negative membrane curvature facilitates this process [92,174].

Furthermore, increased membrane cholesterol content may generate negative membrane curvature and locally decrease membrane tension in support of fusion, whereas local cholesterol depletion increases tension and promotes positive membrane curvature, disfavouring the fusion reaction [202,211,214–216].

Previous investigations have reported reduced plasma membrane cholesterol content of dendritic cells, macrophages, and T cells in HIV-1-infected long-term non-progressors compared to those of rapid progressors [217]. Furthermore, cellular cholesterol content has been shown promote HIV-1 *trans*-infection from macrophages to CD4+ T cells [218]. These data, in combination with previous investigations characterising biophysical regulators of virus-cell fusion, suggest an unexplored relationship may exist between the host metabolic state, membrane cholesterol content, and HIV-1 entry into target cells.

Recent investigations have applied fluorescence-lifetime imaging microscopy (FLIM) to visualise cellular metabolic processes in single-cells that are often overlooked by population-based or spectral methods [219,220]. In this chapter, we utilised a FLIM-based approach to observe that higher rates of HIV-1 fusion and infection occur in cells with notably higher glycolytic activity. We subsequently observed that targeted inhibition of glycolysis with 2-deoxy-d-glucose (2-DG) diminished both HIV-1 fusion and infection. Visualisation of HIV-1 entry with multicolour, real-time single virus tracking (SVT) revealed that HIV-1 pseudoparticles are arrested at hemifusion when attempting fusion with target cells pre-treated with 2-DG. When evaluating for membrane irregularities in response to inhibition of glycolysis, we discovered a loss of membrane-associated cholesterol in 2-DG-treated cells, and that supplementation with water-soluble cholesterol in 2-

DG-treated cells rescued HIV-1 fusion. Owing to cholesterol's influential role on host cell membrane order and tension, we expanded these results by utilising FLIM of FRET-based probes of membrane order and tension. Strikingly, 2-DG-treated cells displayed decreased membrane rigidity and increased tension. To further probe the connection between membrane tension and HIV-1 entry, we implemented a novel assay that multiplexes FLIM and SVT to visualise HIV-1 entry and membrane tension fluctuations with high spatiotemporal resolution in single cells. Through this approach, we report HIV-1 particles generate increased flux in global host-cell membrane tension that is, at least in part, driven by HIV-1 engagement with co-receptor CCR5. Importantly, we show that HIV-1 entry requires local decreases in membrane tension during virus-cell fusion, which is absent during 2-DG treatment of TZM-bl cells yet rescued via cholesterol supplementation. Collectively, our results reveal a link between host cell glycolytic activity and HIV-1 virus-cell fusion, highlighting a potentially critical role for host cell membrane cholesterol content to establish a biophysical environment supportive of HIV-1 entry.

2.2 Material and Methods

2.2.1 Cell culture

TZM-bl (a kind gift from Quentin Sattentau) and Lenti-X-293T cells (Takara Bio, France) were cultured in Dulbecco's Modified Eagle Medium (DMEM) or DMEM F-12 (Gibco) supplemented with 10% foetal bovine serum (FBS), 1% Penicillin-Steptomycin (PS) and 1% L-glutamine (LGlut). Cells were routinely passaged with the aid of Trypsin-EDTA 0.05% (Gibco) and maintained at 37 C and 5% CO_2. MT4 cells (a kind gift from Alex Compton) were cultured in RPMI medium (Gibco) complemented with 10% FBS), 1% PS, and 1% LGlut.

Healthy donors provided peripheral blood which was utilized to isolate CD4 T cell lymphoblasts, as previously described (Levine et al. 1997). Briefly, CD4 T cells were isolated by negative selection according to the manufacturer's protocol (RosetteSep Human CD4+ T cell Enrichment Kit, StemCell Technologies). Following isolation, CD4 T cells were activated for 2 days using anti-CD3/anti-CD28 T-cell activation and expansion beads (Dynabeads, ThermoFisher Scientific) in complete RPMI medium complemented with 100U/mL of recombinant human IL-2 (PeproTech). 48 hours post-treatment, CD4+ T cells were separated from the beads and incubated for 72 hours in fresh IL2-containing RPMI medium at a concentration of 1 x 10^6 cells/mL prior to use.

2.2.2 Reagents and antibodies

The LiveBlazer FRET B/G Loading Kit for performing the β-lactamase assay was purchased from Life Technologies (Carlsbad, CA, USA). 2-deoxy-d-glucose (2-DG), methyl-β-cyclodextrin (MBCD) and water-soluble cholesterol was purchased from Sigma-Aldrich (St. Louis, MO, USA). Simvastatin and low-density lipoprotein from human plasma (BODIPY) complex were acquired from ThermoFisher. Antibodies against CD4 conjugated to PercP Cy5.5 (ab161a1) and CCR5 conjugated to FITC (ab11466) were obtained from BioLegend (San Diego, CA, USA) and Abcam (Cambridge, UK), respectively. The FliptR probe was purchased from Spirochrome (Geneva, Switzerland). The FliptR probe was purchased from Spirochrome (Geneva, Switzerland).

2.2.3 Plasmid transfections

Perceval (number 21737) and Laconic (number 44238) plasmids were obtained from Addgene. MSS and KMSS sensors were provided from Bo Liu (Dalian University of Technology). Plasmids encoding HIV-1 JR-FL or HIV-1 NL4.3 were provided by James Binley (Torrey Pines Institute for Molecular Studies) and Alex Compton (National Cancer Institute), respectively. pR8ΔEnv, pcRev, Vpr-BlaM, Gag-eGFP and VSV-G were kind gifts from Greg Melikyan (Emory University). Transient transfections of Perceval, Laconic, MSS and KMSS were performed with GeneJuice (Novagen) according to the manufacturer's protocol.

2.2.4 Virus production

HIV-1 virus particles pseudotyped with JR-FL or VSV-G containing Vpr-BlaM were produced via transfection of 60-70% confluent Lenti-X-HEK-293T cells seeded in T175 flask via GeneJuice (Novagen) according to the manufacturer's protocol. 2 μg pR8ΔEnv, 1 μg pcRev, 3 μg of the required viral envelope (i.e. VSV-G, HIV-1 JR-FL, or HIV-1 NL4.3), and either 2 μg Vpr-BlaM or 3 μg of eGFP-GagΔEnv if to be used for β-lactamase or flow cytometry experiments, respectively. If to be used for SVT experiments without MSS lifetime acquisition, virus particles were generated from transfection of 2 μg pR8ΔEnv, 1 μg pcRev, 3 μg of eGFP-GagΔEnv, and 3 μg of the required viral envelope. Virus particles produced from transfection with 2 μg pR8ΔEnv, 1 μg pcRev, 2 μg mCherry-2xCL-YFP-Vpr, and 3 μg of the required viral envelope were utilized for SVT experiments whilst recording MSS lifetimes. All transfection mixtures were added to cells sustained in DMEM F12 supplemented with 10% FBS, 1% PS, and 1% LGlut at 37 °C and 5% CO_2. The medium was replaced with fresh, phenol-red free, complete DMEM-F12 supplemented with 10% FBS, 1% PS, and 1% LGlut after washing with PBS 12 hours post-transfection and allowed to grow for a further 24 hours at 37 °C and 5% CO_2. However, if viruses to be generated were to be utilised for SVT, cells were supplemented with DMEM F12 medium containing 10 μM 1,1-dioctadecyl-3,3,3,3-tetramethylindodicarbocyanine (DiD) (Life Technologies) for 4 hours at 37 °C and 5% CO_2 after washing with PBS. Following incubation, the staining mixture was removed, the virus-producing cells were washed twice with PBS, and phenol-red free DMEM F12 was added such that cells were allowed to incubate for a further 24 hours at 37 °C and 5% CO_2. For all produced viruses, 48 hours post-transfection, the supernatant containing virus particles was

harvested, filtered with a 0.45 μm syringe filter (Sartorius Stedim Biotech), aliquoted and stored at -80 °C.

2.2.5 Virus tittering

As Vpr-BlaM-containing or double-labelled JR-FL and VSV-G pseudotyped viral particles additionally contained the β-galactosidase gene in the pr8ΔEnv construct, a β-galactosidase assay was performed for virus titration as follows: 2 x 10^4 TZM-bl cells were seeded in triplicate in complete DMEM in 96-well round-bottom plates (Falcon) and grown for 24 hours at 37 °C and 5% CO_2. Subsequently, the media was replaced with 10-fold serially diluted pseudoviruses in complete DMEM and cells were allowed to grow for an additional 48 hours at 37 °C and 5% CO_2. 48 hours post-infection, TZM-bl cells were washed with PBS, fixed with 2% paraformaldehyde for 15 minutes, and washed with PBS once more prior to staining with a solution comprised of 50 mg/mL X-gal (i.e. BCIG, or 5-bromo-4-chloro-3-indoyl-β-D-galactopyranoside), 500mM $K_3[Fe(CN)_6]$, 250mM $K_4[Fe(CN)_6]$, 1M $MgCl_2$ diluted in PBS, for 2 hours at 37 °C protected from light. After staining, cells were washed with PBS and imaged with a continuous 630 nm laser excitation while capturing the emission via a 650-750 nm emission window using a Leica SP8-X-SMD microscope in order to count infected cells for each 10-fold dilution to calculate the virus titre.

2.2.6 Single virus tracking: spun vs. non-spun cells

TZM-bl cells were exposed to generated HIV-1 particles concurrently labelled with membrane-associated DiD and Gag-eGFP and pseudotyped with JR-FL Env and either incubated at 4 °C or spun for 30 minutes at 2100 x g in a refrigerated centrifuge at 4 °C in order to facilitate virus attachment. Following this step, TZM-bl cells were then washed with cold PBS to remove unprimed HIV pseudoparticles. Observation chambers holding the TZM-bl cells harbouring primed HIV-1 pseudoparticles were then placed under an incubation-supported SP8-X-SMD confocal microscope set at 37 °C and the cold medium was immediately replaced by pre-warmed medium set at 37 °C to initiate both the HIV-1 fusion reaction and image acquisition. To acquire single-virus tracking images, cells were selected with a 63x/1.4 NA and subjected to both a white laser tuned to 488 nm and an argon laser tuned to 633nm via alternating lines to excite Gag-eGFP and DiD, respectively, whilst avoiding emission bleed-through. The emission photons from both fluorescent markers were captured using internal HyD photon-counting detectors and a PMT was used to recover transmission light concurrently.

2.2.7 β-lactamase assay

TZM-bl cells transiently expressing Perceval or Laconic were incubated with pseudotyped virus particles harbouring Vpr-BlaM for 4 hours at the specified MOI before being washed twice with PBS, supplemented with virus-free complete DMEM, and allowed to grow at 37 °C and 5% CO_2. Cells were then washed with PBS, loaded with CCF2-AM from the LiveBlazer FRET-B/G Loading Kit (Life Technologies), and allowed to incubate at room temperature in the dark for 2

hours. Following this, the CCF2 solution was removed, the cells were washed with PBS, and maintained in 2% FBS-containing, phenol-red free DMEM prior to imaging.

2.2.8 β-lactamase assay spectral analysis

Transiently transfected TZM-bl cells or primary rested CD4+ T cells loaded with CCF2 were selected under a 20X air-immersion objective and subjected to continuous laser excitation at 405 nm. Emitted fluorescence was captured via two channels: blue (440-488 nm) and green (500-540 nm), representing cleaved and uncleaved CCF2, respectively, using internal HyD detectors in a SP8-X-SMD microscope. The ratio of the blue to green emission was calculated pixel-by-pixel in Image J. If to be analysed for infection via the β-galactosidase assay, cells were allowed to grow for a further 24 hours in phenol-red free, complete DMEM at 37 °C and 5% CO_2.

2.2.9 β-galactosidase assay

Transiently-transfected TZM-bl cells infected with pseudoviruses were washed with PBS and fixed with 2% paraforlmaldehyde for 10 minutes. After fixation, cells were washed once more with PBS and stained with an X-gal solution described above for 2 hours at 37 °C, protected from light. Following X-gal staining, cells were washed with PBS and infected cells were subsequently visualised via a 20x air-immersion objective with a 630 nm continuous laser while capturing emission with a 650-750 nm emission window via a SP8-X-SMD microscope.

2.2.10 Filipin fluorescence staining

TZM-bl, MT4, or PBMCs adhered to poly-l-lysine coated Ibidi 35 mm gridded dishes were treated with indicated concentrations of MBCD, water-soluble cholesterol, 2-DG, or a mock control for 2 hours. After drug-treatment, these cells were fixed with 4% PFA for 15 minutes at room temperature. Following fixation, cells were washed three times with cold PBS and the fixative was quenched by treatment with 1.5 mg/mL glycine for 15 minutes at room temperature. Cells were subsequently washed again with PBS and stained with filipin at a concentration of 50 μg/mL for 2 hours at room temperature in the dark. Following staining, cells were washed with PBS three times and imaged using a SP8-X-SMD confocal microscope. If cells were to be analysed for endosomal cholesterol content, before fixation, cells were treated with 10 μg/mL LDL-Bodipy and allowed to incubate at 37 °C and 5% CO_2 for 2 hours. Following incubation, the LDL-Bodipy complex was removed and cells were washed with PBS three times, followed by drug treatment and fixation as described above. For all conditions, z-stacks were acquired with a 0.3 μm step-size and the median 5-10 slices in each stack for each image were analysed.

2.2.11 Fluorescence lifetime imaging microscopy

Live TZM-bl cells transiently expressing Perceval, Laconic, or stained with FliptR were selected under either a 20x air-immersion or 63x oil-immersion objective using a SP8-X-SMD Leica Microscope (Manheim, Germany) 48 hours post-transfection. However, for live TZM-bl cells transiently expressing MSS or KMSS, cells of interest were selected under a 100x/1.4 NA oil immersion objective using a Leica SP8-X-SMD microscope with the FALCON module (Manheim, Germany) 48 hours post-transfection. For FLIM imaging of Perceval-expressing cells,

a 488 nm pulsed-laser tuned to 40 MHz was coupled to single photon counting electrons (PicoHarp 300) was used for excitation and single photons were detected by external hybrid detectors in photon counting mode. Similarly, Laconic-expressing cells were subjected to a 470 nm pulsed laser tuned to the same frequency. FliptR-stained cells were subjected to excitation with a 488 nm pulsed laser tuned to 20MHz. To remove photobleaching artifacts or poor signal to noise, only cells with negligible photobleaching and at least 250-1000 photon counts per pixel were included in analysis. For cells transiently expressing Perceval, Laconic, or stained with FliptR, we used Symphotime 64 software (Picoquant) to generate the fluorescence decay of each pixel in single cells. The fluorescence decays were deconvoluted with the instrument response function (IRF) and fitted by a Marquandt non-linear least-square algorithm with a two-exponential model. The mean fluorescence lifetime (τ) in addition to short and long lifetimes (i.e. τ_1 and τ_2), as well as their associated amplitudes (i.e. a_1 and a_2) were calculated using Symphotime. All statistical analysis of the lifetime data was performed using a two-tailed t-test (Origin, Northhampton, MA, USA).

In contrast, cells transiently expressing MSS or KMSS were subjected to a 440nm picosecond pulsed diode laser PDL 800-B (PicoQuant) tuned to 40MHz for excitation of CFP. Emitted photons were captured via a 450-480nm emission filter and were subsequently detected using internal hybrid detectors in photon counting mode. For MSS- or KMSS-expressing cells, FLIM experiments were performed via a time-domain single photon counting approach operated by the FALCON module (Leica Microsystems, Manheim, Germany) incorporated within the Leica SP8-X-SMD microscope.

2.2.12 Label-free NAD(P)H two photon fluorescent lifetime imaging microscopy

To capture NAD(P)H autofluorescence in live MT4 and TZM-bl cells we used a two-photon SP8 DEEP DIVE FALCON FLIM microscope (Leica Microsystems) equipped with three non-descanned photon-counting detectors as previously described [221]. Cells of interest were selected under a 100x/1.4 NA objective corrected for IR and subjected to 730 nm excitation. Autofluorescence emission was captured with an emission window set to 450-500 nm. To remove photobleaching artifacts or poor signal-to-noise, only cells with negligible photobleaching and at least 100-1000 photon. Using the embedded FALCON FLIM software, ROIs were selected as single cells and a two-exponential fluorescence decay from all pixels in the ROI was constructed to extract the ratio of protonated and non-protonated NAD(P)H. Phasor FLIM diagrams [222] were constructed in LASX (Leica Microsystems) to illustrate the shift in intracellular NAD(P)H concentration when comparing MT4 or TZM-bl cells in either vehicle or 2-DG-treated conditions.

2.2.13 Extrapolating the ATP:ADP ratio and relative lactate concentrations and MSS lifetimes

We used Symphotime software (Picoquant) to select individual cells expressing either Perceval or Laconic as regions of interest (ROIs). For cells transiently expressing Perceval, after identifying the ROI with the smallest lifetime (τ_{int}), which was indicative of high levels of ATP relative to ADP, the short lifetime component (τ_1) was utilized as a fixed value in subsequent ROIs examined when acquiring the TCSPC fluorescence decay. The corresponding amplitude (a_1) was used as a numerical representation of the relative intracellular ATP concentration. Simultaneously, the long lifetime (τ_2) was attributed to the relative contribution of ADP binding to the Perceval sensor, and therefore its amplitude (a_2) was utilized to extract the relative ADP concentration. The

resulting two-exponential decay, which was deconvoluted with the IRF and fitted as described above, contained two amplitudes a_1 and a_2. Consequently, the ratio (i.e. a_1/a_2) of these two extrapolated amplitudes were used as a marker of the intracellular ATP:ADP ratio. To compute the relative intracellular lactate concentration of Laconic-expressing cells, a similar approach was utilised. In particular, the associated amplitude a_1 of long lifetime component τ_1 was divided by the sum of the amplitudes of both the long and short (a_2) components from the calculated two-component exponential decay to generate relative intracellular lactate concentrations.

For cells transient expressing the MSS probe, we utilized the internal FALCON module integrated within the Leica SP8-X-SMD microscope to perform FLIM analysis. Region of interests were selected as either whole cells expressing the MSS probe or 3 x 3 pixel-by-pixel regions (corresponding to ~2μm^2) of the MSS-labelled membrane which overlapped with mCherry-labelled virions. We binned 5 x 5 pixels in addition to grouping frames of 10 from our acquisition to increase photon counts per pixel such that sufficient signal-to-noise was ensured spatiotemporally. During analysis, we used a three-exponential decay deconvoluted with the IRF and Marquandt nonlinear least-squared algorithm as described above to extract three amplitudes and three lifetimes. The third long lifetime component was fixed to the average of all cells analysed in order to extract a short (τ_1) and intermediate (τ_2) components. Subsequently, the intermediate (τ_2) lifetime component was used to represent the MSS donor lifetime and therefore, membrane tension. We used a single-exponential decay to generate τ_1 to accommodate low photon counts when analysing 3 x 3 pixel-by-pixel regions off MSS-labelled regions overlapping with mCherry-labelled virions.

2.2.14 Flow cytometry

HIV-1_{VSV-G} or HIV-$1_{NL4.3}$ eGFP-Gag pseudoparticles were used for single round infections of 1 x 10^5 MT4 T cells at the indicated MOI. 48 hours post-infection, HIV-1 infection was detected by flow cytometry (BD LSR II, BD Bioscience) and reported as the percentage of eGFP-expressing, live MT4 cells. Dead cells were excluded by Live/Dead Fixable Near-IR Dead Cell Stain as per manufacturer's protocol (Invitrogen).

2.2.15 Statistics

All calculations (i.e. ANOVA, t-test, standard deviation, and standard error) were computed in OriginLab Software (Northhampton, USA)

2.3. Results

2.3.1 Host basal metabolic state influences HIV-1 infection in T cells and TZM-bl cells

Different T cell subsets require unique metabolic signatures to perform their immunologic function. Recently, it was reported that T cell subset metabolic requirements strongly correlate with their hierarchical susceptibility to HIV-1 infection [207]. Similar to activated CD4 T cells, TZM-bl HeLa and MT4 T cell lines homogenously sustain high glycolytic activity. Importantly, TZM-bl and MT4 T cells are susceptible to R5-tropic HIV-1_{JR-FL} and X4 HIV-$1_{NL4.3}$ infection, respectively, whereas both are susceptible to HIV-1_{VSV-G} infection.

As prior reports have purported that host glycolytic activity tightly correlates with HIV-1 susceptibility and pathogenicity, we assessed if glycolysis inhibition abrogated MT4 T cell susceptibility to HIV-1 infection by pre-treatment with 2-DG, an inhibitor of hexokinase. Acute pre-treatment (i.e. 2 hours) with 2-DG prior to infection with either HIV-1_{VSV-G} or HIV-$1_{NL4.3}$ diminished infection of both pseudoviruses in MT4 T cells (Figure 2.3.1A and Figure 2.3.2A). These results suggest a dependence of HIV-1 infection in MT4 T cells on host glycolytic activity. Importantly, as the pseudoviruses tested differ only by their glycoproteins, and thus their means of entry, these data suggest that this infection arrest may be arrested to the virus entry step. To determine whether inhibition of oxidative phosphorylation, rather than reductions in glycolysis abrogates HIV-1 infection, we pre-treated MT4 T cells with oligomycin. Oligomycin is an inhibitor of the F_0 proton channel of ATP synthase and reduces ATP levels in T cells. Pre-treatment of MT4 cells with oligomycin failed to inhibit HIV-1_{VSV-G} infection (Figure 2.3.2B). These results

indicate that deficiency of upstream biosynthetic intermediates derived from glycolysis, rather than a decrease in ATP production by inhibition of oxidative phosphorylation, diminishes HIV-1 infection.

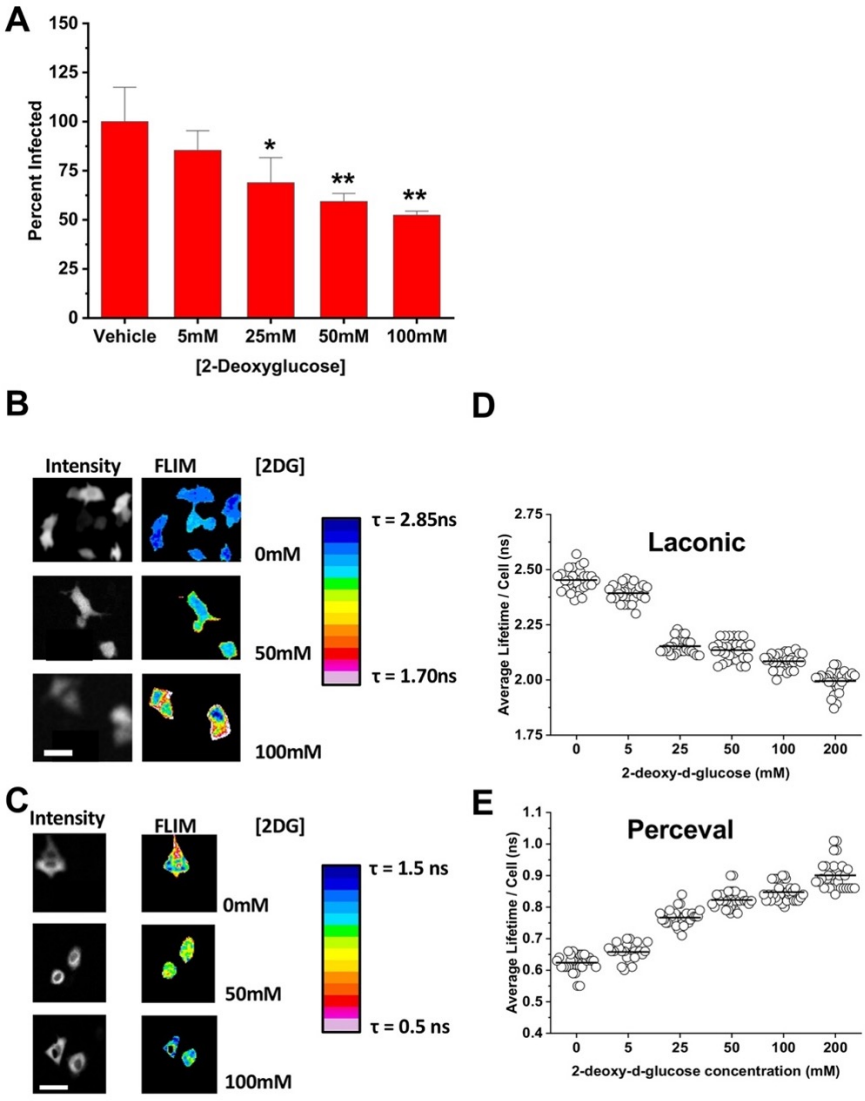

Figure 2.3.1. Acute 2-DG treatment diminishes HIV-$1_{NL4.3}$ infection in MT4 cells and induces fluorescence lifetime changes in Laconic and Perceval. (**A**) MT4 cells were challenged with HIV-$1_{NL4.3}$ pseudovirions harbouring the eGFP construct. In the conditions indicated, MT4 cells were pre-treated with the indicated concentration of 2-DG for two hrs. Cells were fixed at 48 hours post-infection, and infection was scored by GFP expression using flow cytometry. Statistical analysis was performed using one-way ANOVA. Bar charts represent mean percent infected cells of three independent experiments normalized to a vehicle-treated control. (**B**) Representative intensity (left) and fluorescent lifetime imaging (right) of single TZM-bl cells transiently expressing intracellular lactate biosensor Laconic with increasing concentrations of 2-DG; scale bar, 50 μm. (**C**) Representative intensity (left) and fluorescent lifetime imaging (right) of single TZM-bl cells transiently expressing intracellular ATP:ADP ratio biosensor Perceval with increasing concentrations of 2-DG; scale bar, 50 μm. (**D**) Scatter plots representing lifetimes of intracellular lactate biosensor Laconic extracted from live, single TZM-bl cells post-treatment with increasing concentrations of 2-DG. Line represents the mean lifetime. (**E**) Dot plots representing lifetimes of intracellular ATP:ADP ratio biosensor Perceval extracted from live, single TZM-bl cells as regions of interest post-treatment with increasing concentrations of 2-DG. Line represents the mean lifetime.

As our results in MT4 cells suggested a correlation between HIV-1 infection and glycolytic activity, we attempted capture the influence of glycolytic flux on HIV-1 infection at the single-cell

level. FLIM imaging enables the quantification of metabolic activity via measuring the lifetime of fluorescent reporters for specific metabolites [135]. Importantly, FLIM captures a metabolic readout that is independent of the biosensor concentration [223] and allows a broad dynamic range to be reported by the fluorescent probe (Figure 2.1.1B-2.1.1D) [132]. Therefore, we transiently expressed Perceval [224], a ratiometric reporter of intracellular ATP:ADP ratios, or Laconic [225], an intracellular lactate reporter, to monitor glycolytic flux in TZM-bl cells via FLIM and correlated these markers of glycolytic flux with HIV-1 infection in single cells (Figure 2.3.2C and Figure 2.3.2D). Treatment of transiently-transfected cells with increasing concentrations of 2-DG led to drastic changes in the fluorescence lifetime of both Perceval and Laconic (Figure 2.3.1B-Figure 2.3.1E). Higher ATP:ADP ratios corresponded to lower Perceval lifetimes [224] and higher intracellular lactate concentrations corresponded with higher Laconic lifetimes [225]. Importantly, 2-DG treatment in these cells did not result in drastic intracellular pH changes, a factor known to distort the lifetime of metabolic fluorescent reporters (Figure 2.3.3B) [226]. To confirm our FLIM approach in transiently-transfected cells, we utilized two-photon FLIM to assess NAD(P)H metabolism in live, non-transfected cells [227]. Both 2-DG-treated MT4 cells and TZM-bl cells illustrated potent decreases in their $NAD(P)H_{free}$ vs. $NAD(P)H_{bound}$ ratio, indicating diminished glycolytic flux (Figure 2.3.3A and Figure 2.3.3D). In line with Figure 2.3.2B, MT4 cells subjected to oligomycin treatment did not lead to appreciable changes in the redox ratio, most likely owing to their pre-activated state (Figure 2.3.3C).

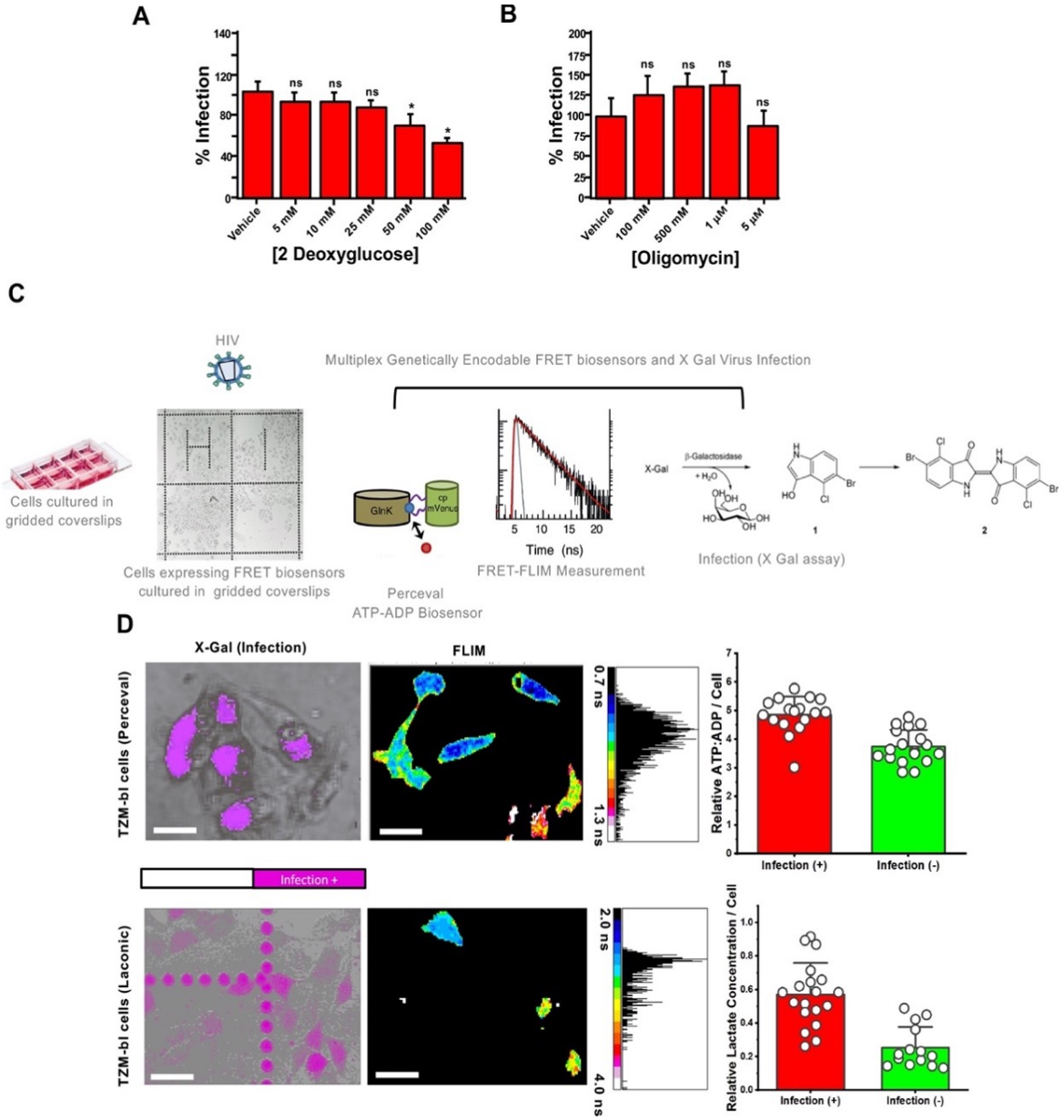

Figure 2.3.2. Relative lactate and ATP/ADP concentrations in single cells correlate with HIV-1 infection. (**A**) MT4 cells were challenged with HIV-1_{VSV-G} pseudovirions harbouring the eGFP construct. In the conditions indicated, MT4 cells were pre-treated with the indicated concentration of 2-DG for two hrs. Cells were fixed at 48 hr post-infection, and infection was scored by GFP expression using flow cytometry. Statistical analysis was performed using one-way ANOVA. Bar charts represent mean percent infected cells of three independent experiments normalized to a vehicle-treated control. (**B**) MT4 cells were challenged with HIV-1_{VSV-G} pseudovirions harbouring the eGFP construct. In the conditions indicated, MT4 cells were pre-treated with the indicated concentration of oligomycin for two hrs. Cells were fixed at 48 hr post-infection, and infection was scored by GFP expression using flow cytometry. Statistical analysis was performed using one-way ANOVA. Bar charts represent mean percent infected cells of three independent experiments normalized to a vehicle-treated control. (**C**) Cartoon diagram describing our approach to record glycolytic flux and HIV-1_{JR-FL} infection in TZM-bl cells concomitantly. TZM-bl cells were seeded onto an Ibidi 8-well gridded dish and transiently transfected with Laconic or Perceval. FLIM images of biosensor-positive cells were recorded along with their location on the grid. These cells were then challenged with HIV-1_{JR-FL}. 48 hours post-infection, cells were fixed,, permeabilized and subjected to β-galactosidase assay to score infection. (**D**) (Top row) Representative images of β-galactosidase-scored cells recorded 48 hours after HIV-1_{JR-FL} infection (left) and basal FLIM images of Perceval-expressing TZM-bl cells taken before infection (right). Cells with higher intracellular ATP:ADP ratios concentrations (cool colours) in this assay were more likely to be infected by HIV-1_{JR-FL}; scale bar 50 µm. (Bottom Row) Representative images of β-galactosidase-scored cells recorded 48 hours after HIV-1_{JR-FL} infection (left) and basal FLIM images of Laconic-expressing TZM-bl cells taken before infection (right) illustrating cells with higher intracellular lactate concentrations (warm colours) were more likely to be infected by HIV-1_{JR-FL}; scale bar 50 µm. Infected (purple) and un-infected (grey) TZM-bl cells expressing either biosensor were recorded and their relative ATP:ADP ratio of lactate concentration were recorded in bar charts (right), and represent three independent experiments. Dots represent individual cells. Error bars indicate standard deviation.

Employing lifetime measurements of Perceval- and Laconic-expressing TZM-bl cells enabled the extrapolation of relative ATP:ADP ratios and lactate concentrations prior to HIV-1 infection. Consequently, we could determine if this surrogate of host cell glycolytic flux is predictive permissivity to HIV-1 infection. HIV-1 infection was reported by β-galactosidase activity as previously described [228]. Importantly, β-galactosidase activity could be detected and spectrally unmixed from Perceval or Laconic fluorescence owing to their non-overlapping emission spectra. Furthermore, as we seeded the TZM-bl cells onto gridded coverslips, we could track transiently transfected TZM-bl cells throughout the experiment. Strikingly, TZM-bl cells which were calculated to have higher relative lactate (Figure 2.3.2D, bottom row) or ATP:ADP ratios (Figure 2.3.2D, top row) were more likely to support HIV-1_{JR-FL} infection. Collectively, these results suggest that in TZM-bl cells glycolytic flux and HIV-1 infection susceptibility are linked at both bulk cell populations and individual cells.

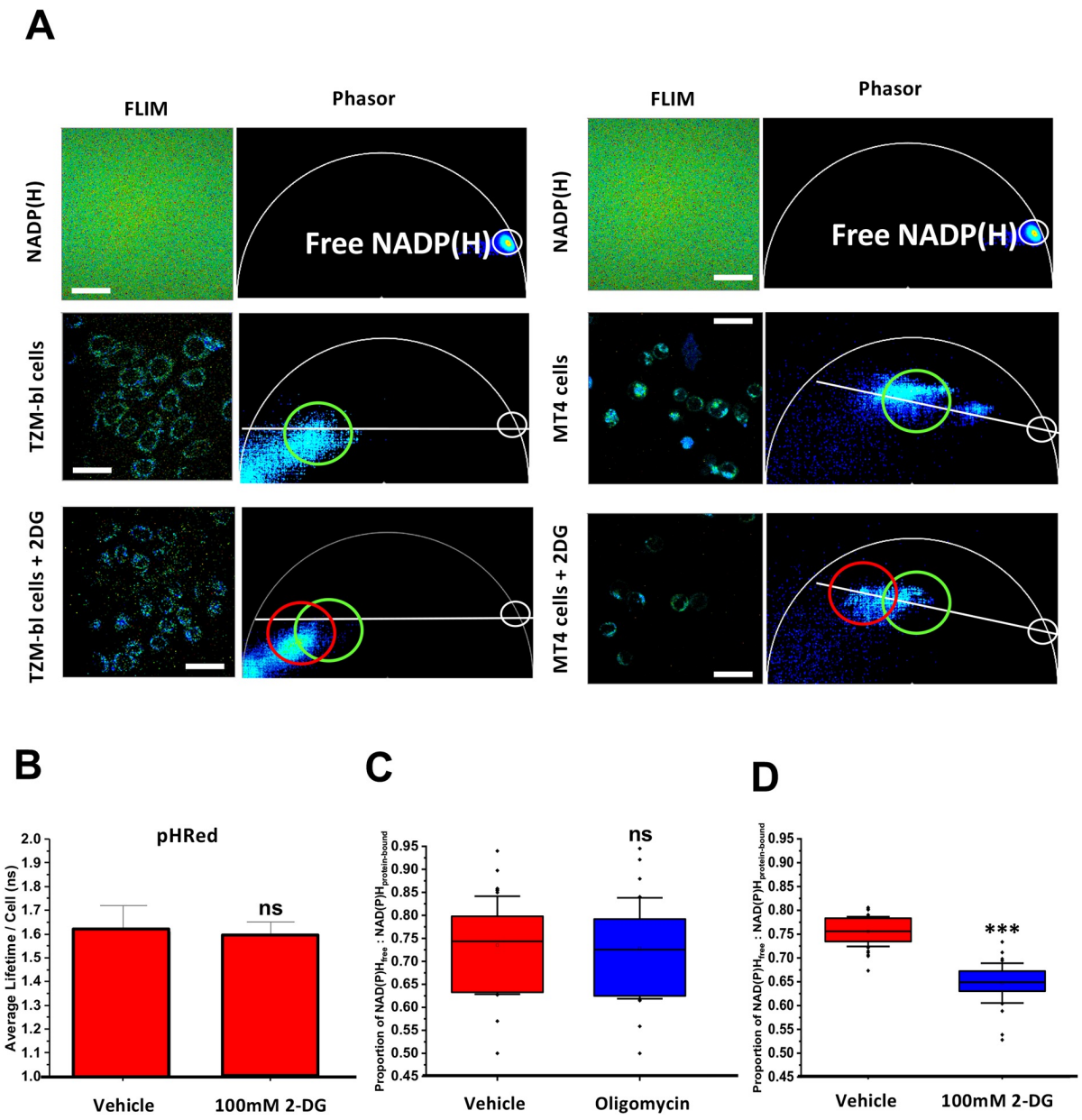

Figure 2.3.3. Acute treatment with 2-DG inhibits glycolytic flux in a pH-independent manner in cell lines. (A) (Top row) Representative images (left) and phasor plots (right) of lifetime distributions of NAD(P)H in solution. NB, the images used in the right and left top row are the same image. The middle row depicts representative images and phasor plots of NAD(P)H lifetime distributions of vehicle-treated TZM-bl (left) and MT4 (right) cells. (Bottom row) Same as middle row, but the indicated cells were pre-treated with 100mM 2-DG; scale bar 5 μm. Phasor FLIM plots illustrate each pixel converted via Fourier Transform to the phase domain. The phasor plots illustrate longer lifetimes (i.e. enzyme-bound NAD(P)H, lower glycolytic flux) to the left and shorter lifetimes (free NAD(P)H, higher glycolytic flux) to the right. (**B**) TZM-bl cells were transiently transfected with intracellular pH biosensor pHRed and pre-treated with the indicated conditions before lifetime imaging. Bar charts depict lifetimes extracted from single TZM-bl cells expressing intracellular pH biosensor pHRed. Error bar indicates standard deviation. At least 30 cells per condition acquired from three independent experiments (**D**) Box diagrams representing $NAD(P)H_{free}$ vs. $NAD(P)H_{protein-bound}$ ratios of MT4 cells pre-treated with either (**C**) oligomycin or (**D**) 2-DG. For both (**C**) and (**D**), single MT4 cells were selected as regions of interest and two-exponential fluorescence decay from all pixels this region was constructed to extract the ratio of protonated and non-protonated NAD(P)H. Box plots represent data acquired from at least 30 cells per condition acquired from three independent experiments. Error bar indicates standard deviation. *** $p<0.001$ as determined by one-way student's T-test.

2.3.2 Basal metabolic state is a determinant of HIV-1 fusion in reporter cells

To pinpoint at which step in HIV-1_{JR-FL} infection is influenced by glycolytic activity in TZM-bl cells, we took advantage of our imaging approach above and assessed HIV-1_{JR-FL} fusion with the β-lactamase assay as previously described [229]. We chose this approach as it allows separation based on pre- or post-fusion determinants. Furthermore, as both HIV-1-based pseudoviruses used to challenge MT4 cells were sensitive to 2-DG treatment, infection arrest in glycolytically inactive cells may be, in part, attributable to the virus entry step. Therefore, we multiplexed our FLIM-based reporter system in cells and used HIV-1_{JR-FL} harbouring the β-lactamase-Vpr fusion protein (BlaM-Vpr) as previously described [229] (Figure 2.3.4A and Figure 2.3.4B). Importantly, the BlaM fluorescence profile is not skewed by the Perceval or Laconic biosensors owing to their non-overlapping excitation profiles.

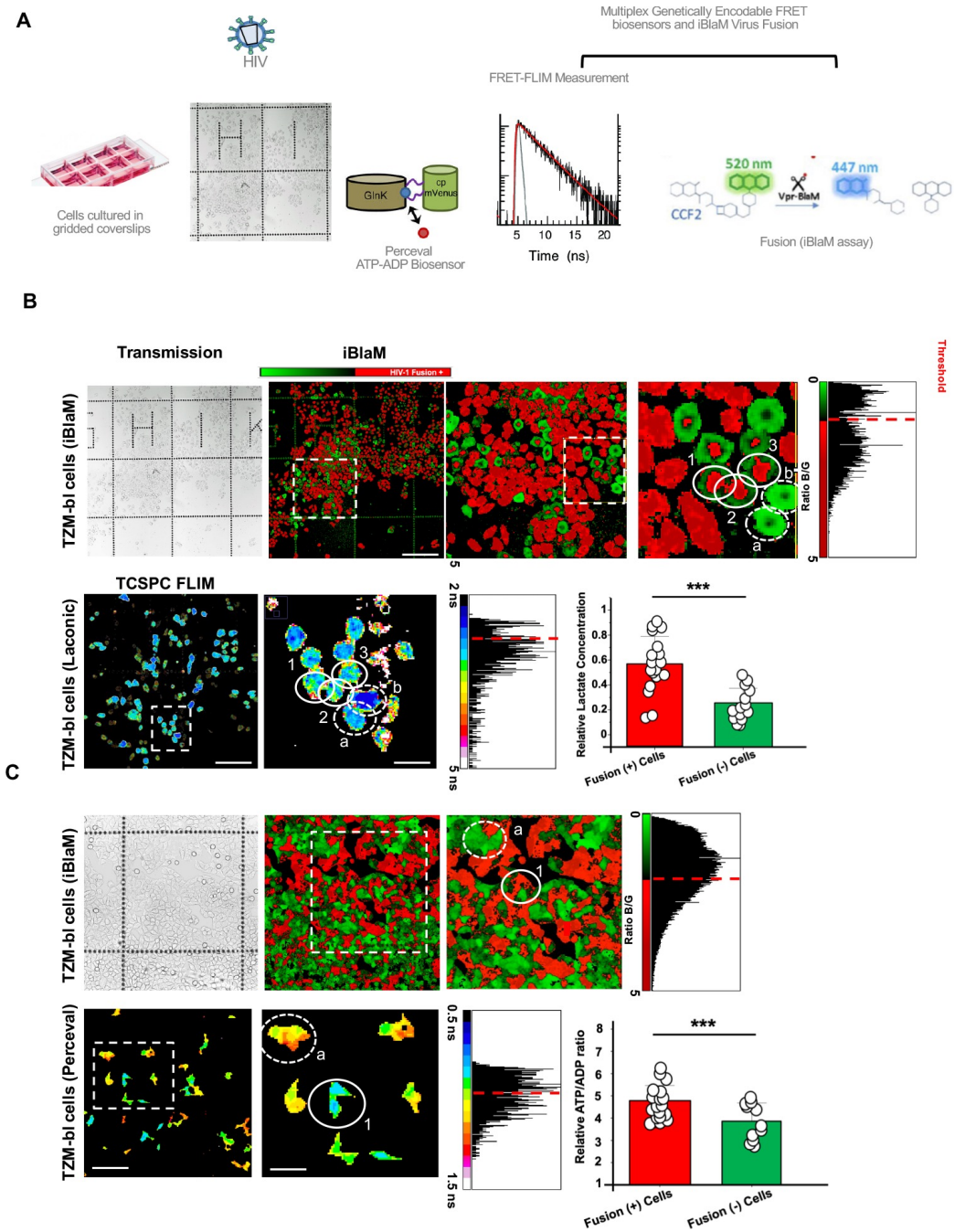

Figure 2.3.4. Relative lactate and ATP/ADP concentrations in single cells correlate with HIV-1 fusion. (**A**) Cartoon diagram describing our approach to record glycolytic flux and HIV-$1_{JR\text{-}FL}$ fusion in TZM-bl cells concomitantly. TZM-bl cells were seeded onto an Ibidi 8-well gridded dish and transiently transfected with Laconic or Perceval. FLIM images of biosensor-positive cells were recorded along with their location on the grid. These cells were then challenged with HIV-$1_{JR\text{-}FL}$. After 90 minutes, pseudoviruses were washed away and a β-lactamase assay was performed on the same cells as a readout of HIV-$1_{JR\text{-}FL}$ fusion. (**B**) (Top row) Representative brightfield (left) and ratiometric fluorescent intensity images (right) calculated from the blue/green channel ratio of CCF2-loaded cells recorded 90 minutes after HIV-$1_{JR\text{-}FL}$ challenge. Solid white circles denote red cells supporting HIV-$1_{JR\text{-}FL}$ fusion whereas dotted white circles denote green cells which did not support HIV-$1_{JR\text{-}FL}$ fusion. (Bottom row) basal FLIM images of Laconic-expressing TZM-bl cells before HIV-$1_{JR\text{-}FL}$ treatment illustrating cells with higher intracellular lactate concentrations (warm colours, solid white circles) were more likely to support HIV-$1_{JR\text{-}FL}$ fusion; scale bar, in order of appearance: 200 µm, 100 µm, 50 µm. (**C**) (Top row) Representative brightfield (left) and ratiometric fluorescent intensity images (right) calculated from the blue/green channel ratio of CCF2-loaded cells recorded 90 minutes after HIV-$1_{JR\text{-}FL}$ challenge. Solid white circles denote red cells supporting HIV-$1_{JR\text{-}FL}$ fusion whereas dotted white circles denote green cells which did not support HIV-$1_{JR\text{-}FL}$ fusion. (Bottom row) basal FLIM images of Perceval-expressing TZM-bl cells before HIV-$1_{JR\text{-}FL}$ treatment illustrating cells with higher ATP:ADP ratios (cool colours, solid white circles) were more likely to support HIV-$1_{JR\text{-}FL}$ fusion; scale bar, in order of appearance 100µm, 50µm. For (**B**) and (**C**), bar charts depicting the relative intracellular lactate concentration (**B**) or ATP:ADP ratios (**C**) are a mean of three experiments with at least 30 analysed cells per condition. Error bars indicate standard error *** $p<0.001$ as determined by Student T test of three independent experiments.

As shown in Figure 2.3.4B and Figure 2.3.4C, in a similar pattern to HIV-1_{JR-FL} infection, single TZM-bl cells with relatively higher intracellular lactate concentrations or ATP:ADP ratios were more likely to be fusion positive as determined by the β-lactamase assay. These results suggest that cells harbouring higher glycolytic flux are more likely to support HIV-1_{JR-FL} fusion, and consequently HIV-1_{JR-FL} infection.

2.3.3. Inhibition of glycolysis blocks HIV-1 fusion at hemifusion

Our FLIM-reporter based system in TZM-bl cells suggested that HIV-1 entry may be dependent on host cell glycolytic flux. Therefore, we assessed whether acute glycolytic arrest would abrogate HIV-1 fusion via the β-lactamase assay. Acute treatment of TZM-bl cells with increasing concentrations of 2-DG resulted in a stepwise reduction in both ATP:ADP ratio and intracellular lactate levels in biosensor-expressing cells with minimal loss in cell viability (Figure 2.3.1B-3.3.1D, and Figure 2.3.7A). Importantly, this treatment also resulted in a similar stepwise reduction in HIV-1_{JR-FL} fusion (Figure 2.3.6A). Notably, pulse-treatment with 100 mM 2-DG blocked HIV-1_{JR-FL} fusion by nearly 80%. This reduction in HIV-1 pseudovirus fusion was not attributable to alterations in cell-surface expression of CD4 or CCR5 co-receptors in TZM-bl cells (Figure 2.3.7C). Furthermore, we observed similar results when assessing HIV-1_{HXB2} fusion in primary CD4+ T cells pre-treated with 2-DG (Figure 2.3.5A and Figure 2.3.5B). Moreover, we observed that glucose deprivation, in the place of 2-DG treatment, resulted in diminished HIV_{JR-FL} fusion events (Figure 2.3.7B). Interestingly, pre-treatment of TZM-bl cells with 2-DG also

disrupted HIV_{VSV-G} fusion, although to a lesser degree (Figure 2.3.6B). These results suggest that glycolytic activity of the host may regulate of HIV-1 fusion in human target cells to some degree.

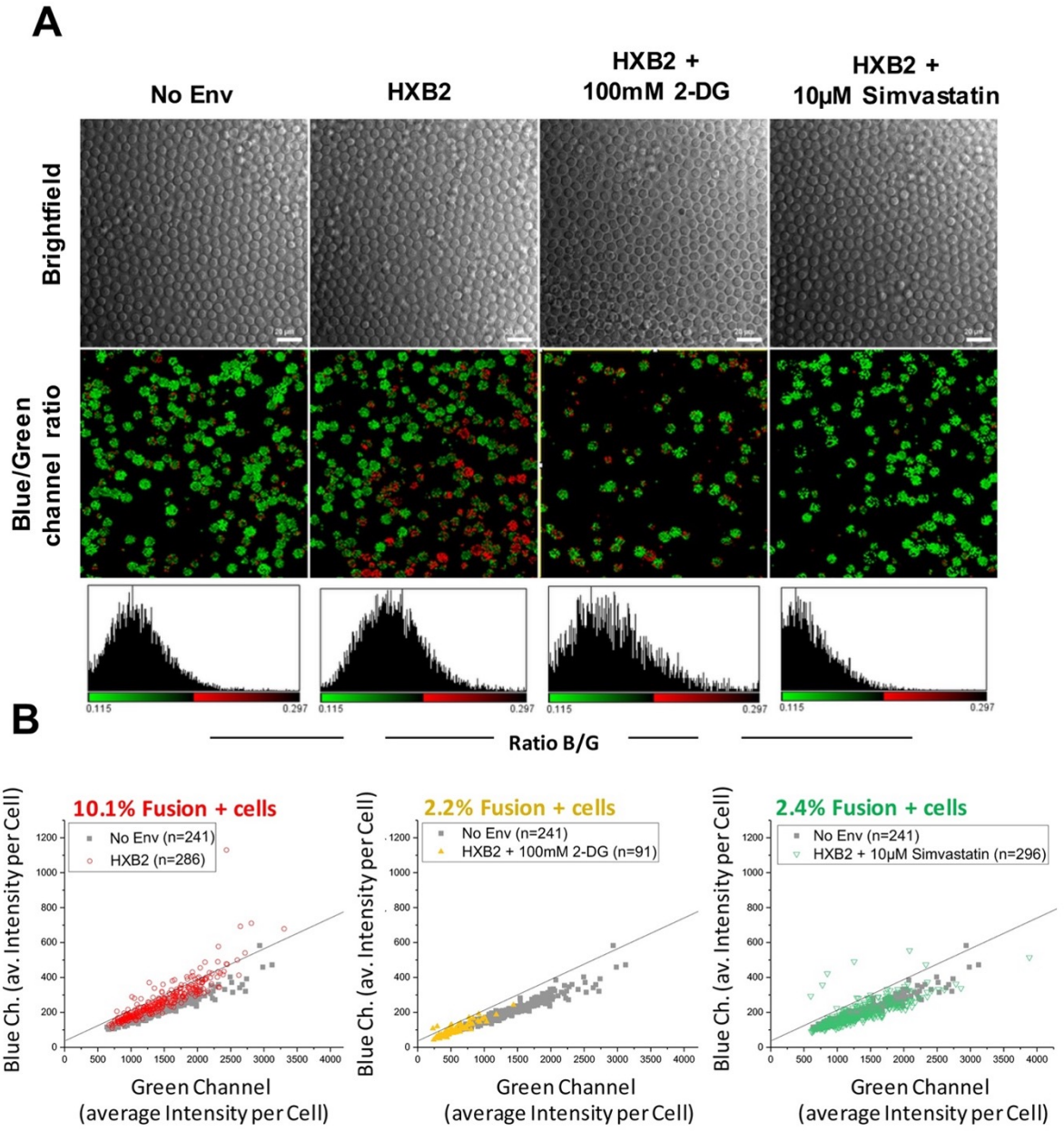

Figure 2.3.5. Acute treatment with 2-DG or simvastatin abrogates HIV-1_{HXB2} fusion in primary CD4+ T cells. (**A**) Primary CD4+ T cells were seeded on Ibidi 8-well gridded dishes and challenged with either naked (i.e. No Env) HIV-1 or HIV-1_{HXB2} virions. In the indicated conditions, primary CD4+ T cells were pre-treated with a mock vehicle, 100 mM 2-DG or 10μM Simvastatin before virus challenge. (Top Row) Brightfield images show that in all cases the integrity of the cells was maintained. (Bottom Row) The ratio of fluorescent intensity images in blue and green channels were used to construct BlaM assay images for HIV fusion for each condition. Red indicate fusion-positive cells whereas green indicate fusion-negative cells. Below each fluorescence BlaM ratio image are pixel-by-pixel histograms. (**B**) Best-fit threshold graphs utilized to determine the blue/green ratio in order to indicate fusion-positive cells. Naked HIV_{HXB2} particles (grey dots from which the grey line of best fit was constructed) was used as a threshold for fusion. At least 100 cells were analysed in each condition and each symbol represents an individual cell. Colour symbols indicate individual cells for each treatment condition (red, vehicle; yellow, 2-DG; green, simvastatin). n, indicates number of cells analysed in each treatment condition.

As our results suggested that acute inhibition of glycolysis may block HIV-1 fusion in TZM-bl cells, we utilised single virus tracking (SVT) to pinpoint which step of fusion was inhibited [230]. Therefore, we co-labelled particles with DiD (identifying the viral membrane) and HIV-1 Gag fused to eGFP (identifying the viral core) and tracked these labelled virus particles upon exposure to TZM-bl cells [231]. During image acquisition, loss of DiD signal with eGFP-Gag maintenance indicates lipid mixing between viral and cell membranes. However, owing to differences in surface area between the plasma and endosomal membranes, the DiD dye will dilute according to two different behaviours. Lipid mixing within endosomal membranes will, at most, minimally diminish DiD fluorescence, whereas lipid mixing within the plasma membrane will result in loss of fluorescent signal (Figure 2.3.6C). Irrespective of the lipid mixing site, loss of eGFP-Gag signal indicates viral core disassembly has occurred.

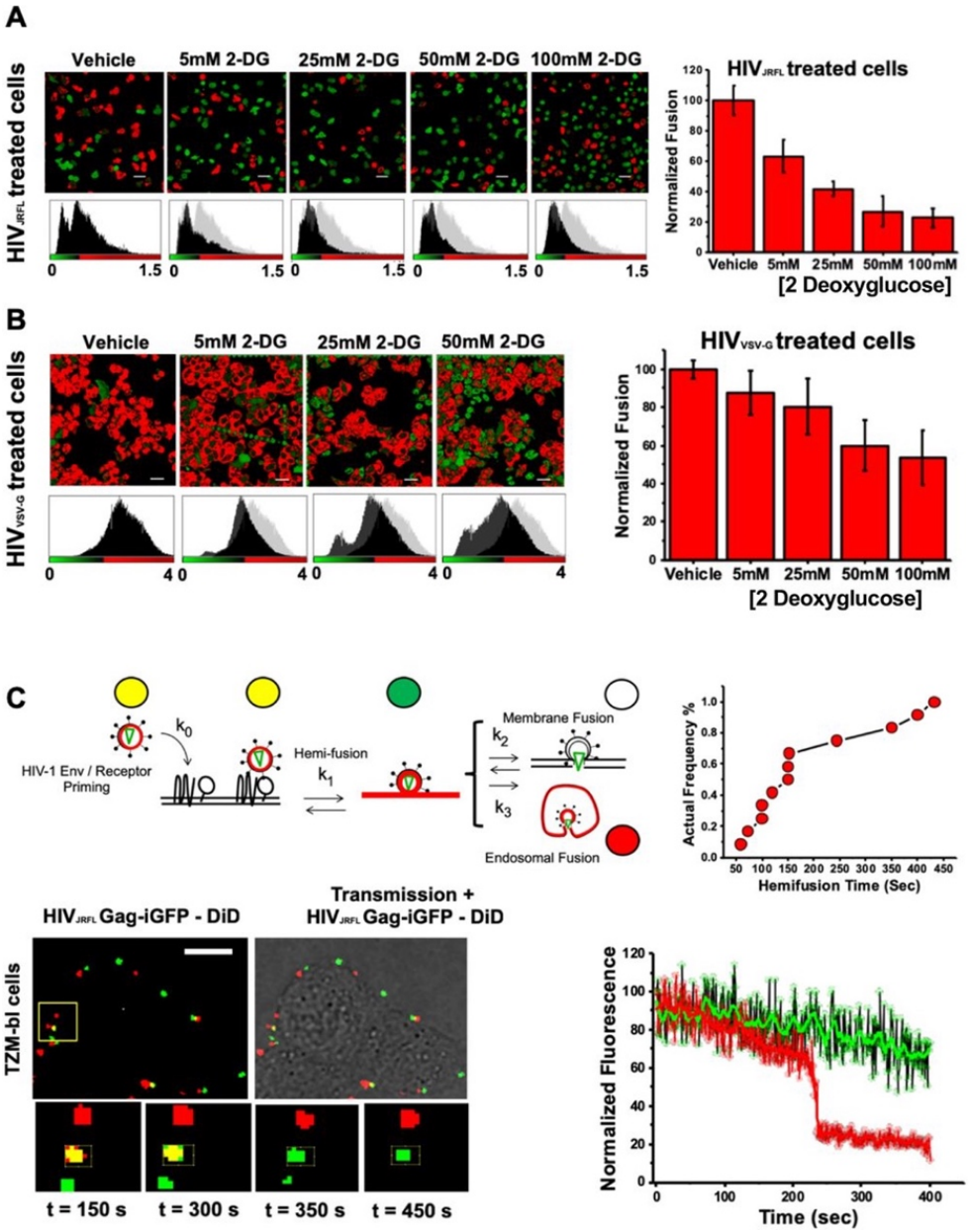

Figure 2.3.6. 2-DG pre-treatment in TZM-bl cells arrests HIV-1 fusion at the hemifusion stage. (**A**) TZM-bl cells were seeded onto an Ibidi 8-well gridded dish and were then challenged with the indicated pseudovirions or bald HIV-1 virions. After 90 minutes, pseudoviruses were washed away and a β-lactamase assay was performed on the same cells as a readout of pseudovirion fusion. TZM-bl cells were treated with the indicated concentrations of 2-DG for 2 hours prior to pseudovirion addition. (Left) Representative and ratiometric fluorescent intensity images calculated from the blue/green channel ratio of CCF2-loaded cells recorded 90 minutes after HIV-$1_{JR\text{-}FL}$ challenge. Below each fluorescence BlaM ratio image are the associated pixel-by-pixel histograms. (Right) Corresponding bar graphs depicting the ratio of cells supporting HIV-$1_{JR\text{-}FL}$ fusion to those free of HIV-$1_{JR\text{-}FL}$ fusion from three independent experiments normalized to vehicle. Error bars indicate standard deviation. (**B**) (Left) Representative and ratiometric fluorescent intensity images calculated from the blue/green channel ratio of CCF2-loaded cells recorded 90 minutes after HIV-1_{VSVG} challenge. Below each fluorescence BlaM ratio image are the associated pixel-by-pixel histograms. (Right) Corresponding bar graphs depicting the ratio of cells supporting HIV-1_{VSVG} fusion to those free of HIV-1_{VSVG} fusion from three independent experiments normalized to vehicle. Error bars indicate standard deviation. (**C**) (Top row, left) Cartoon diagram illustrating single virus tracking with HIV-1 pseudovirions double-labelled with DiD and eGFP-gag. Briefly, double-labelled virions entering via endosomal fusion lose their eGFP-gag signal whilst DiD signal is retained in the mobile endosome. Virions entering via plasma membrane fusion will have their DiD signal infinitely diluted in this compartment whereas the eGFP-gag signal is retained and mobile. Hemifusion is denoted when DiD signal infinitely diluted in the plasma membrane whereas the eGFP-gag signal is retained and immobile. (Top row, right) Kinetics of individual hemifusion events plotted as cumulative distributions as a function of time. (Bottom row, left) Representative panel of images illustrating doubled-labelled HIV-1_{JRFL} particles losing DiD signal (red) and maintaining immobile eGFP signal (green) when attempting fusion in 2-DG treated TZM-bl cells, suggesting arrest at hemifusion. (Bottom row, right) Line graphs representing the corresponding eGFP (green) and DiD (red) intensities from the SVT acquisition shown to the right. Total number events tracked in control conditions: 217. Total number of events tracked in 2-DG-treated conditions: 236.

We visualized co-localized eGFP and DiD signals corresponding to co-labelled HIV-1_{JR-FL} pseudovirus particles during infection of TZM-bl cells. This co-labelled signal subsequently turned red (mean $t_{1/2}$ = 10.25 minutes) (Figure 2.3.7D), suggesting loss of Gag-eGFP while DiD was retained in an intracellular membrane. This observation is in line with previous reports indicating that HIV-1_{JR-FL} pseudoparticles utilise endocytosis to infect TZM-bl cells [229,231]. In contrast, in TZM-bl cells pre-treated with 2-DG, we observed co-localized (e.g. yellow) particles turn green during acquisition ($t_{1/2}$ = 2.53 minutes) (Figure 2.3.6C). This observation indicates dilution of DiD signal within the plasma membrane in the absence of viral content release, suggestive of hemifusion and likely incomplete fusion pore formation or dilation [230–232]. Importantly, our observed DiD-labelled lipid mixing kinetics reflect previously reported hemifusion events [230]. Our analysis of several alleged hemifusion events uncovered two distinct types of DiD dilution events. The first population (7% of events) illustrated a near-asymptotic loss of DiD signal (Figure 2.3.6C), whereas the second population demonstrated a much slower, gradual decay of DiD signal lasting 10 minutes or longer (93% of events) (Figure 2.3.7E), which is similar to previous reports [230]. Collectively, our SVT data suggests that TZM-bl cells acutely treated with inhibitors of glycolysis display reduced levels of pseudovirion fusion owing to a potential arrest at hemifusion.

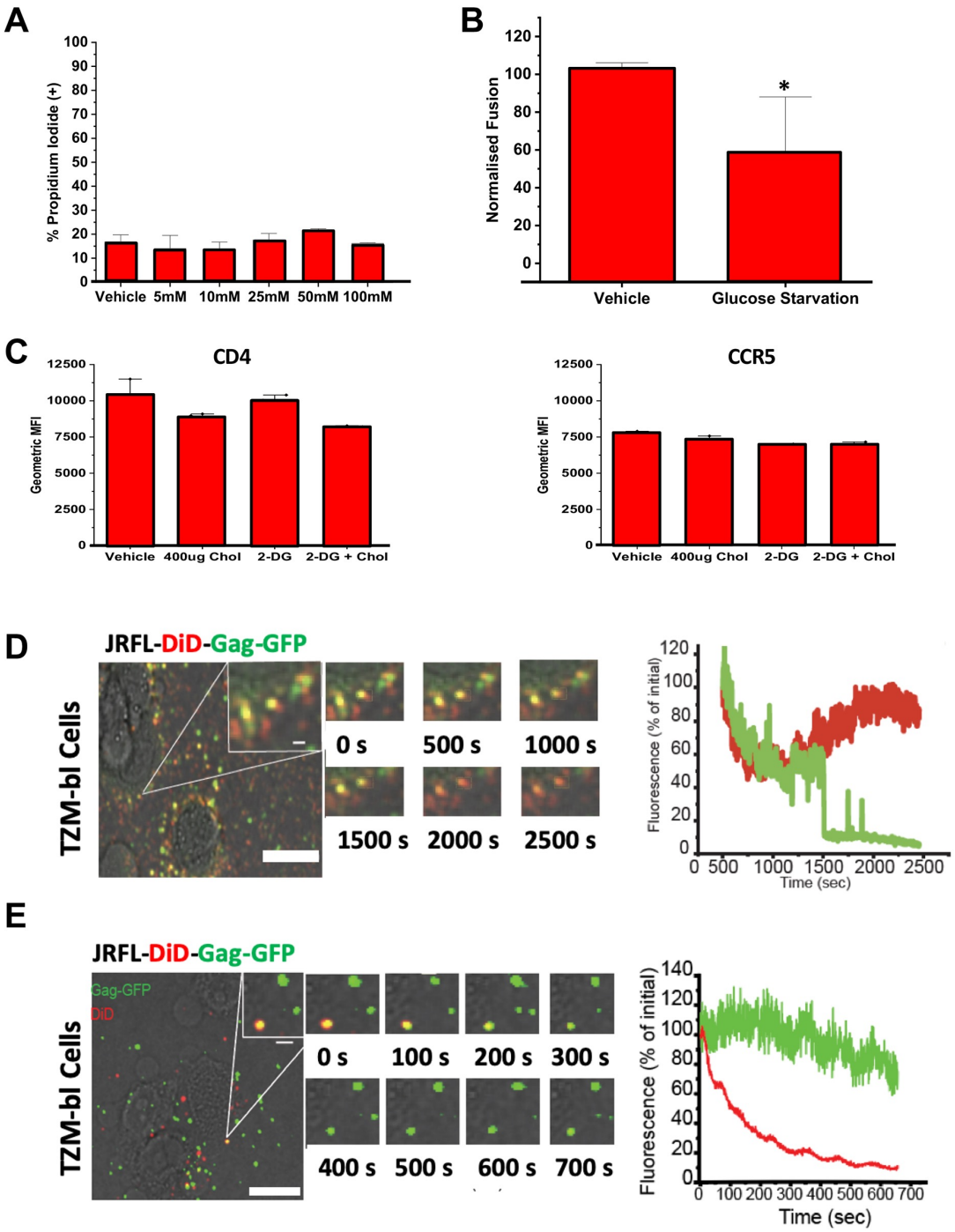

Figure 2.3.7. Acute treatment with 2-DG does not alter cell viability or cell-surface receptor expression, and single virus tracking of HIV-1_{JR-FL} in vehicle or 2-DG-treated conditions. (**A**) TZM-bl cells were seeded in Ibidi 35 mm dishes and treated with indicated concentrations of 2-DG for 2 hours prior to quantification by propidium iodide to evaluate cell viability. Error bars indicate standard deviation. (**B**) TZM-bl cells were seeded in Ibidi 35 mm dishes and treated with glucose-free medium for 2 hours prior challenge by HIV-1_{JR-FL}. 90 minutes post virus addition, virions were washed away and TZM-bl cells were evaluated for HIV-1_{JR-FL} fusion by the β-lactamase assay. Bar graphs indicate percent fusion positive cells normalized to vehicle. Error bars indicate standard deviation. *$p<0.5$, **$p<0.01$ *** $p<0.001$ as determined by student's T-test. (**C**) TZM-bl cells were seeded in Ibidi 35 mm dishes and treated with the indicated conditions for 2 hours prior to fixation and quantification of CD4 (left) or CCR5 (right) surface staining by flow cytometry; representative of a mean of three independent experiments. (**D**) Representative fluorescence series of images (left) and single virus tracking traces (right) of Gag-eGFP (green) and DiD (red) dual-label HIV-1_{JR-FL} pseudovirions attempting fusion in vehicle-treated TZM-bl cells. (**E**) Representative fluorescence series of images (left) and single virus tracking traces (right) of Gag-eGFP (green) and DiD (red) dual-label HIV-1_{JR-FL} pseudovirions attempting fusion in TZM-bl cells pre-treated with 2-DG. MFI, mean fluorescence intensity.

Although able to increase the efficiency of infection, spinoculation may bias HIV-1 entry sites in cell lines [138,233,234]. In line with these reports, we also observed spinoculated TZM-bl cells incubated with HIV-1_{JR-FL} favoured endosomal fusion events (Figure 2.3.8). In contrast, non-spinoculated TZM-bl cells incubated with HIV-1_{JR-FL} supported virus entry events both at plasma membrane and in endosomes (Figure 2.3.8). Owing to this potential bias, we did not utilise spinoculation, allowing us to visualise fusion events at both the host plasma membrane and endosomes. Furthermore, these results suggest that the HIV-1_{JR-FL} hemifusion arrest we observed in TZM-bl cells pre-treated with 2-DG may occur at the plasma membrane.

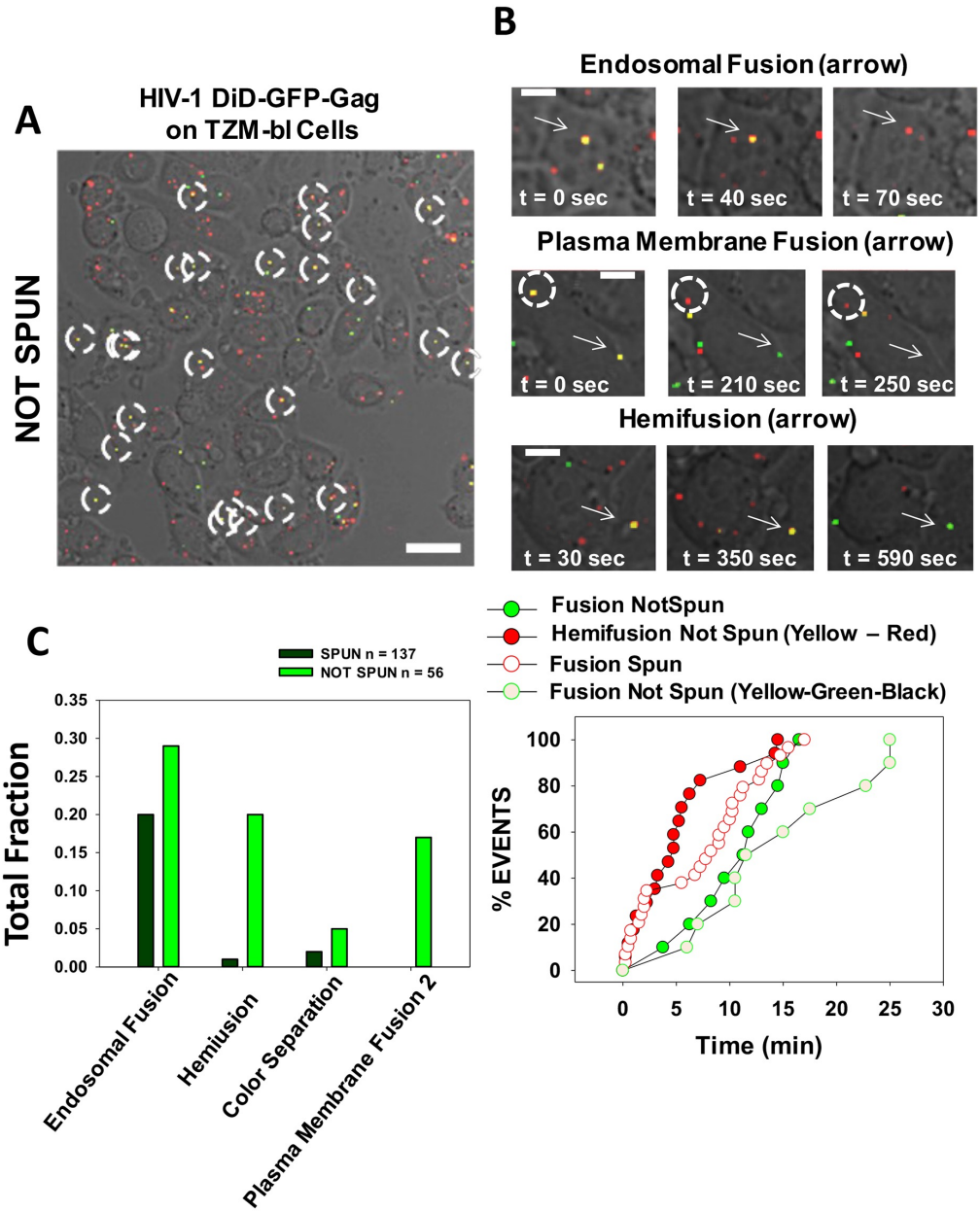

Figure 2.3.8. Single virus tracking of HIV-1$_{JR-FL}$ viruses comparing spinoculated vs. non-spinoculated TZM-bl cells. (**A**) HIV$_{JR-FL}$ pseudoviruses co-labelled with DiD and Gag-GFP were exposed on TZM-bl at 4°C for 30 min. Following this incubation, TZM-bl cells were placed under the microscope at 37°C to start the entry process. White dashed circles indicate the HIV-1 particles co-labelled with both fluorescent probes (red for DiD and green for Gag-GFP). A subset of these particles are only labelled with either Gag-GFP (green dots) or DiD (red dots). These particles were ignored. Scale Bar = 10 µm (**B**) (Top row) endosomal fusion depicted by a double-labelled particle (arrow) turning red, signifying DiD redistribution within the endosomal compartment and Gag-GFP release. (Middle row) plasma membrane (PM) fusion depicted by a double-labelled particle (arrow) first changing from yellow to green indicating hemifusion (i.e. DiD dilution on the PM) and then Gag-GFP disappearance. A white circle also indicates a particle undergoing endosomal fusion, which indicates that both fusion event types can occur in non-spinoculated cells simultaneously. (Bottom row) hemifusion depicted by a double-labelled particle unable to progress toward full fusion as the GFP-Gag remains through time. Scale bar for each image, 1 µm. (**C**) (Left) Bar charts indicating the proportion (0 to 1) of each fusion event type for spun (dark green) or non-spun (light green) cells. Total events for spinoculated and non-spinoculated TZM-bl cells are n = 137 and n = 56, respectively. A small fraction of events for both spun and not-spun conditions showed colour separation; colour separation is defined as double-labelled (yellow viruses) internalized within endosomes (labeled with DiD and Gag-GFP) undergoing fusion. However, right at the moment of fusion, DiD redistributes around the endosomal membrane and partially uncleaved Gag-GFP is released into the cytosol. (Right) Cumulative distribution kinetics for HIV-1 particles undergoing: i) fusion for spinoculated cells (solid green dots); ii) hemifusion for non-spinoculated cells (solid red dots), iii) full endosomal fusion for spinoculated cells (open red dots) and iv) plasma membrane fusion non-spinoculated cells (open green dots).

2.3.4. Single-cell glycolytic state is linked to global cell membrane cholesterol content

Both intracellular and plasma membrane lipid content are linked to several metabolic pathways in host cells [177,235–237]. Of these lipids, plasma membrane and endosomal cholesterol content is critical for virus entry [212,213,217,218]. As we observed a disruption in HIV-1_{JR-FL} fusion upon 2-DG treatment in TZM-bl cells, we were curious if treatment of either reporter TZM-bl, MT4, or primary CD4+ T cells with 2-DG altered cell-surface cholesterol content as determined by filipin staining. In both TZM-bl and MT4 T cells, we discovered that acute treatment with 2-DG led to reductions in cell surface cholesterol content by 20% and 50%, respectively, compared to a mock-treated control (Figure 2.3.9A and Figure 2.3.9B). We confirmed these results by immunofluorescence imaging of filipin-stained TZM-bl and MT4 cells (Figure 2.39A). Notably, treatment with oligomycin did not significantly alter plasma membrane cholesterol content (Figure 2.3.10B). Additionally, treatment with 1mM methyl-β-cyclodextrin (MBCD), a well-described cholesterol depletion reagent [238], reproduced reductions in filipin fluorescence similar to those of 2-DG treatment (Figure 2.3.10A). We also determined by immunofluorescence microscopy that in TZM-bl cells, 2-DG treatment did not exclusively deplete cholesterol content from the plasma membrane, but endosomes as well (Figure 2.3.10C and Figure 2.3.10D). Importantly, treatment of primary CD4+ T cells with 2-DG similarly decreased cell-surface cholesterol content when compared to TZM-bl cells (Figure 2.3.10E). Collectively, these results suggest that acute glycolytic arrest in cells may rapidly diminish cholesterol content in both cell lines and primary cells.

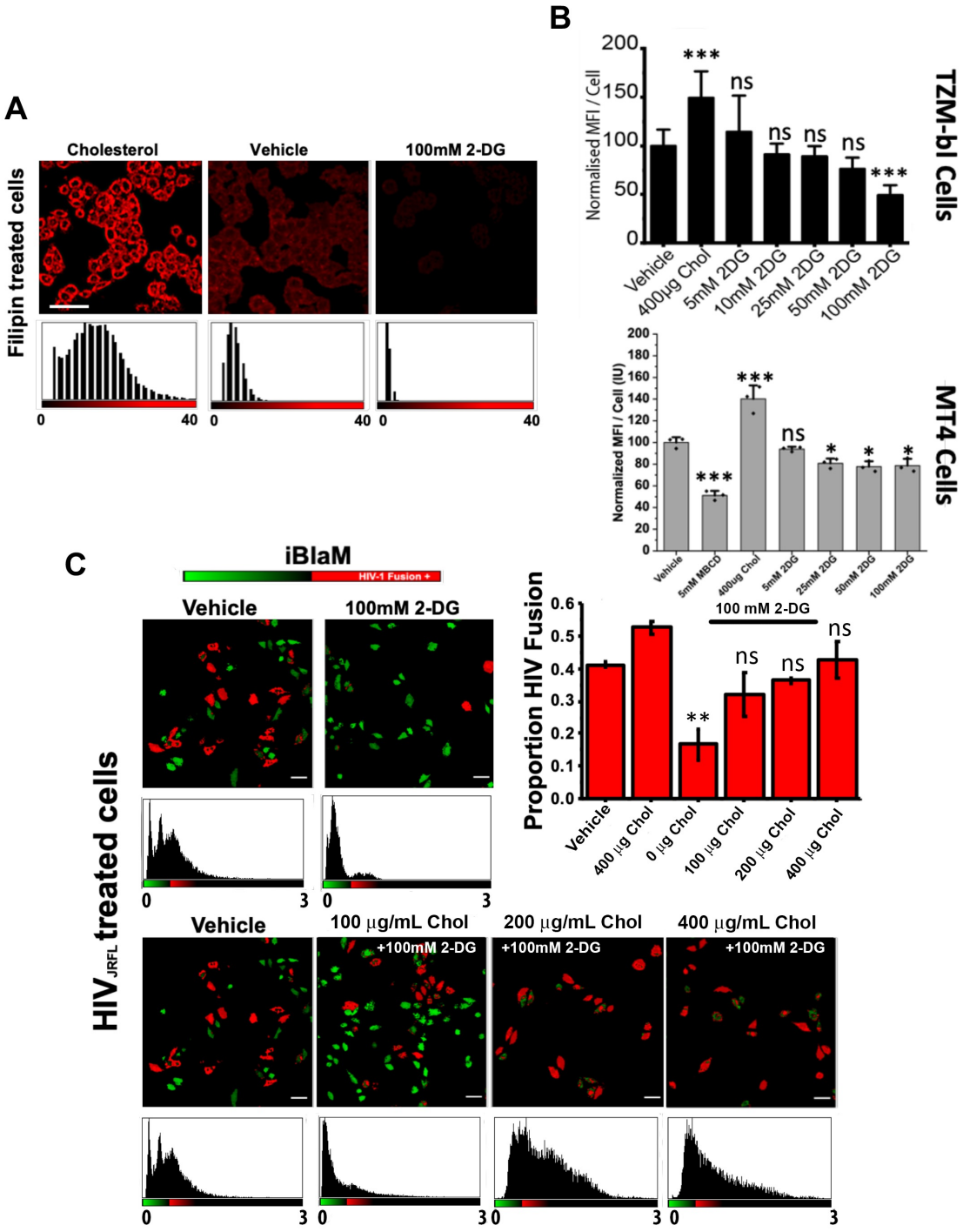

Figure 2.3.9. Addition of 2-DG sequesters cholesterol from the cell membrane. (**A**) TZM-bl cells were seeded onto Ibidi 35mm dishes and stained with filipin for cholesterol quantification as described in the material and methods. As indicated, cells were treated with 400 µg cholesterol, a vehicle control, or 100 mM 2-DG for 2 hours prior to staining and imaging. Representative images of filipin-stained TZM-bl cells; scale bar 50 µm. (**B**) Bar charts depicting MFI values extracted from each cell at least three independent experiments; each condition is normalised to vehicle. TZM-bl cells (top) and MT4 cells (bottom) were treated as in (**A**). Error bars indicate standard deviation (**C**) TZM-bl cells were seeded onto Ibidi 8 well grided dishes and challenged with HIV-1_{JR-FL} for 90 minutes prior to CCF2 loading and imaging to calculate the blue/green ratio to identify cells supporting HIV-1_{JR-FL} fusion. (Left) Representative ratiometric images calculated from the blue/green channel ratio of TZM-bl cells in each treatment condition; scale bar, 50 µm. Below each image is its corresponding pixel-by-pixel histogram. NB, the vehicle images in the top and bottom rows are the same image. (Right) Bar charts collating the percent fusion positive TZM-bl cells (normalized to vehicle as 100) in each treatment condition from three independent experiments. Error bars indicate standard error. *p<0.5, **p<0.01 *** p<0.001 as determined by one-way ANOVA. ns, not significant.

As our results indicated that inhibition of glycolysis led to a reduction in both HIV-1 pseudovirus fusion and host cell cholesterol content, we supplemented our 2-DG-treated reporter cells with increasing concentrations of cholesterol to determine if HIV-1_{JR-FL} fusion was restored. Interestingly, we observed a near-complete rescue of HIV-1_{JR-FL} fusion when glycolytically-inactivated TZM-bl cells were supplemented with 100μg/mL cholesterol (Figure 2.3.9C). We confirmed these results via confocal microscopy of β-lactamase-stained cells (Figure 2.3.9C). Collectively, these results suggest that cholesterol depletion during glycolysis inhibition diminishes HIV-1_{JR-FL} fusion potential in TZM-bl cells. To determine if cholesterol depletion would reproduce a similar reduction in HIV-1 infection in primary CD4+ T cells, we treated these cells with simvastatin, an HMG-CoA-reductase inhibitor which lowers cholesterol. Importantly, simvastatin-treated CD4+ T cells only poorly supported HIV-1 fusion (Figure 2.35A and Figure 2.3.5B).

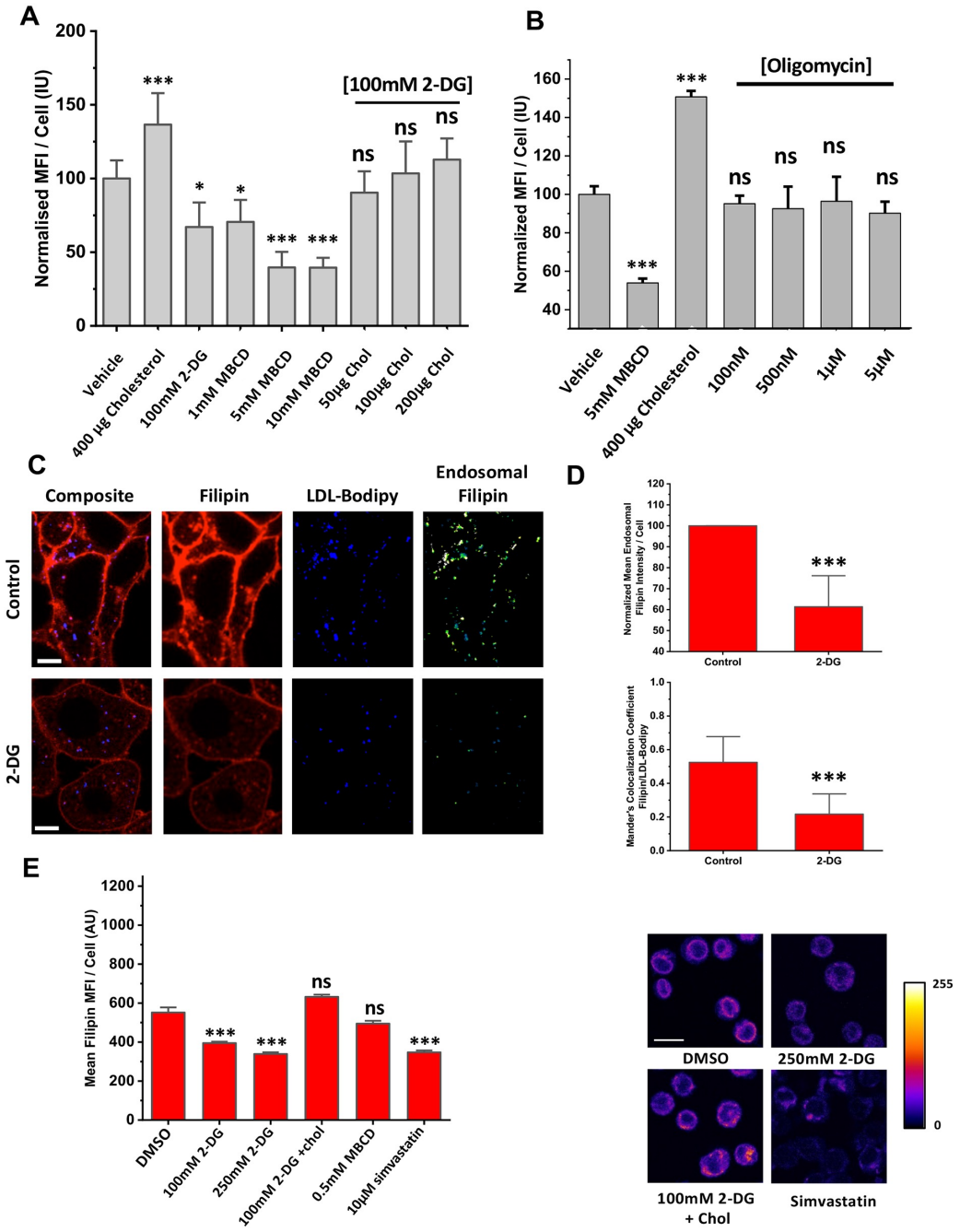

Figure 2.3.10. Acute treatment with 2-DG leads to cell surface cholesterol reduction in cell lines and primary cells in addition to the endosomal compartment. (**A**) TZM-bl cells were seeded in Ibidi 35 mm dishes and then subjected to the indicated treatment conditions for 2 hours prior to filipin staining as described in the material and methods. Error bars indicate standard deviation and treatment conditions were normalized to vehicle. *p<0.5, **p<0.01 *** p<0.001 as determined by either one-way ANOVA. (**B**) MT4 cells were seeded in Ibidi 35 mm dishes and then subjected to the indicated concentration of oligomycin for 2 hours prior to filipin staining as described in the material and methods. Error bars indicate standard deviation and treatment conditions were normalized to vehicle. *p<0.5, **p<0.01 *** p<0.001 as determined by either one-way ANOVA. (**C**) TZM-bl cells seeded in Ibidi 35 mm dishes and subsequently grown in vehicle (top) or 2-DG-treated (bottom) conditions for two hours after being loaded with LDL-Bodipy staining to label endosomal compartments. TZM-bl cells were then fixed, permeabilized, and filipin staining was performed as described in the material and methods. Filipin signal (red) labelled cholesterol at both the cell surface and LDL-Bodipy labelled endosomal compartments (blue). In the far-right image, green signal labels LDL-Bodipy associated cholesterol; scale bar 10µm. (**D**) (Top) Bar charts illustrating normalized filipin mean fluorescence intensity in LDL-Bodipy labelled endosomal compartments as in (**C**) in vehicle and 2-DG-treated conditions. (Bottom) Colocalization coefficients of LDL-Bodipy with filipin quantified in z-stacks of 5 medial slices as in (**C**). *p<0.5, **p<0.01 *** p<0.001 as determined by student's T test. (**E**) (Left) Bar charts depicting raw filipin mean fluorescence intensity values in individual primary CD4+ T cells. In the indicated conditions, cells were pre-treated for 2 hours with the indicated regimen before filipin staining as described in the material and methods. (Right) Representative images of primary CD4+ T cells (from left) stained with filipin after treatment conditions listed. Mean values were calculated from at least 50 cells per condition from three independent experiments. *p<0.5, **p<0.01 *** p<0.001 as determined by one-way ANOVA. MFI, mean fluorescence intensity. ns, not significant.

2.3.5 Single-cell glycolytic activity regulates host cell membrane order and tension

Membrane order (i.e. membrane rigidity) has been previously shown to influence fusion reactions in live cells, including those which support virus-cell fusion [105,212,239]. To determine if glycolytic activity is correlated with membrane order in single cells, we used FliptR, a planarizable, photostable push-pull probe previously established to report membrane rigidity in live cells via FLIM [240–242]. Importantly, this probe segregates into different membrane phases equally and maintains the intrinsic membrane order of cells (Figure 2.3.11A). In all treatment conditions, we recorded a homogenous distribution of FliptR lifetimes when constructing TCSPC lifetime images of FliptR stained cells, indicating that liquid-ordered and disordered phases are mixed, as previously reported [240,243]. Additionally, cells subjected to hypo-osmotic shock did not report a significant change in FliptR lifetimes, indicating that this reporter could reliably report changes in membrane rigidity independent of changes to membrane tension (Figure 2.3.11B).

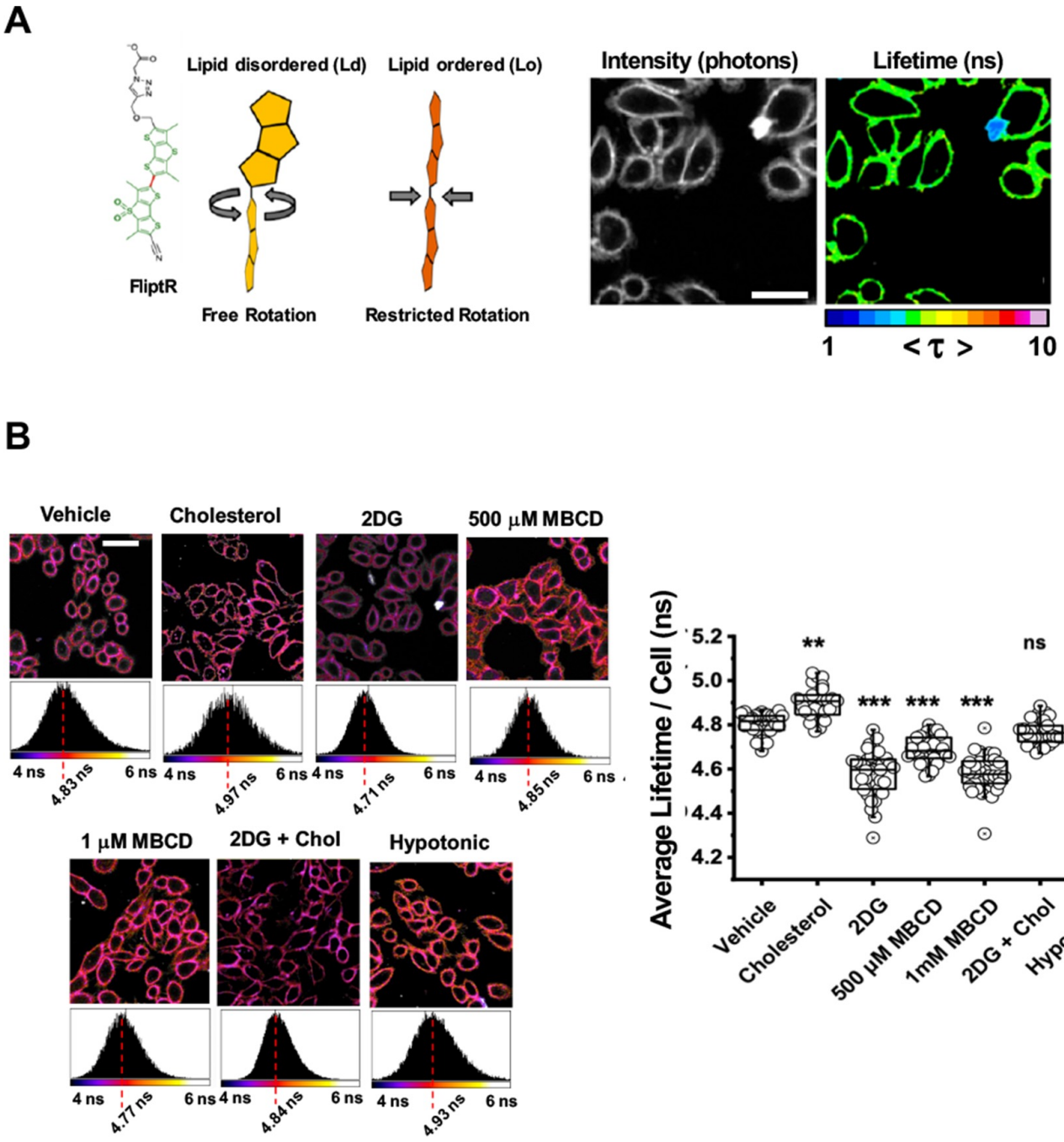

Figure 2.3.11. Addition of 2-DG decreases cellular plasma membrane order. (**A**) (Left) Cartoon diagram depicting the planarizable, push-pull membrane order probe FliptR in either a Ld or Lo environments. (Right) TZM-bl cells were seeded onto Ibidi gridded 8-well dishes and stained with 1 μM FliptR for 15 min and imaged by FLIM. The whole-cell mean fluorescence lifetime components from a two-exponential decay fit (τ) was calculated using Symphotime for a minimum of 40 cells per condition. Representative image of fluorescence intensity (left) and FliptR lifetime (right) images captured from FliptR-stained cells in vehicle-treated conditions; scale bar 25μm. (**B**) (Left) TZM-bl cells were seeded onto Ibidi gridded 8-well dishes and stained with 1 μM FliptR for 5 min and imaged by FLIM. In the conditions indicated, TZM-bl cells were either treated with 100 mM 2-DG, the indicated amount of MBCD, 400 μg of cholesterol, a combination of 2-DG and cholesterol, or a hypotonic solution for 2 hours washed away prior to staining with FliptR and imaging. Representative images of FliptR-stained cells in these treatment conditions depict the extracted τ_m; scale bar 25μm. (Right) The whole-cell mean fluorescence lifetime components from a two-exponential decay fit (τ) was calculated using Symphotime and the long lifetime component (τ_1) from three independent experiments are shown here in box plots (n = at least 30 per condition, collected during the course of three independent experiments). * $p<0.05$ ** $p<0.01$ *** $p<0.001$ as determined by one-way ANOVA. Dots correspond to individual cells. Error bars indicate standard deviation. ns, not significant.

Importantly, live, FliptR-stained TZM-bl cells pre-treated with 2-DG reported reductions in FliptR lifetimes (~200 ps), similar to MBCD-treated cells, indicating a decrease in membrane rigidity (Figure 2.3.11B). These results suggest that inhibition of glycolysis depletes the plasma membrane of high-ordered domains. Notably, supplementation of 2-DG-treated cells with cholesterol restored FliptR lifetimes back to mock-treated control cells (Figure 2.3.11B). These results indicate that inhibition of glycolysis may lead to reductions in membrane order.

Another critical membrane biophysical property known to influence the course of virus-cell fusion is membrane tension [166,182,183,202]. Indeed, large levels of membrane tension are known to drive fusion pore expansion [92]. However, little is known about the role of membrane tension in regulating the hemifusion to fusion transition. To monitor changes in membrane tension in single cells during acute glycolytic arrest, we transiently transfected TZM-bl cells with a previously characterized FRET-based reporter of membrane tension, MSS [244] prior to 2-DG treatment. MSS is an eCFP-YPet-based FRET reporter an elastic tension-sensing module linking both fluorophores which are anchored in raft and non-raft associated regions of the plasma membrane (Figure 2.3.12A) [244]. TZM-bl cells transiently expressing the MSS reporter were subjected to the same treatment conditions utilised when evaluating membrane order as above. Interestingly, acute cholesterol depletion with MBCD increased the eCFP donor lifetime by more than 100ps (Figure 2.3.12B). This result suggests that cholesterol content may regulate membrane tension in cells, which has been demonstrated previously [202]. Additionally, treatment of TZM-bl cells with 2-DG resulted in a larger increase in recorded eCFP donor lifetime (i.e. $\Delta\tau$ = 165ps), suggesting increased membrane tension in these cells (Figure 2.2.12). Moreover, supplemental cholesterol addition to 2-DG-treated cells restored membrane tension values comparable to those

of a mock-treated control (Figure 2.3.12B). Importantly, no treatment altered the lifetime value of the control KMSS probe which lacks the Lyn domain required for tension sensing (Figure 2.3.12B). Collectively, these results indicate that abrupt glycolysis inhibition may increase membrane tension in TZM-bl cells.

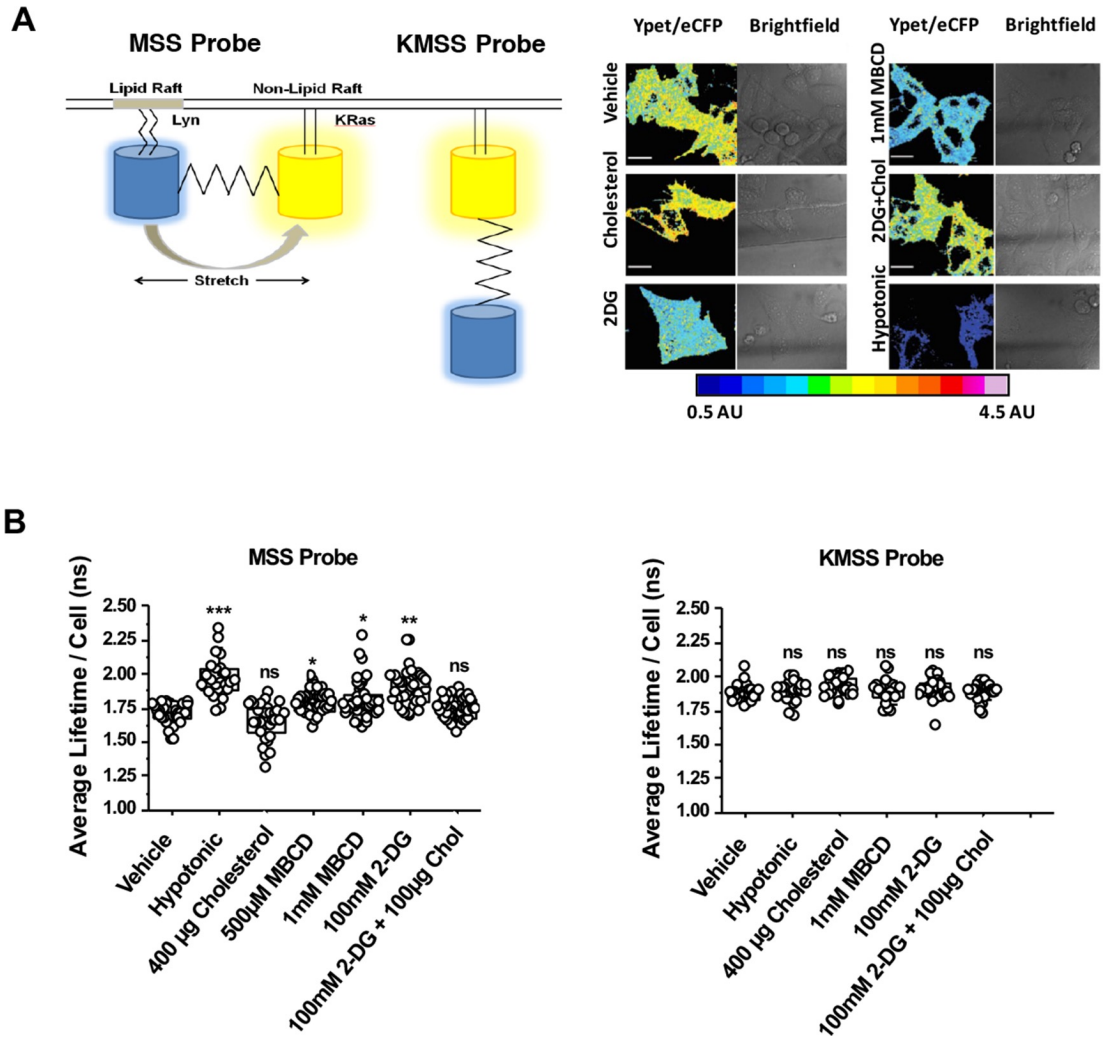

Figure 2.3.12. Acute treatment of TZM-bl cells with 2-DG increases plasma membrane tension. (**A**) (Left) Cartoon model depicting membrane tension FRET probe MSS and its control KMSS. The donor (eCFP) and acceptor (YPet) are anchored to different components of the plasma membrane by Lyn and KRas domains, respectively. The donor and acceptor fluorophores are connected by an elastic tension-sensing module. In contrast, the KMSS probe lacks the Lyn domain. (Right) TZM-bl cells were seeded onto Ibidi gridded 8 well dishes and transiently transfected with MSS. 48 hours post-transfection, TZM-bl cells were imaged by both FRET and FLIM. In the conditions indicated, TZM-bl cells were either treated with 100 mM 2-DG, 1 mM MBCD, 400 µg of cholesterol, a combination of 2-DG and cholesterol, or a hypotonic solution for 2 hours and then imaged Representative pseudocoloured FRET efficiency and brightfield images constructed in ImageJ for each condition are shown; scale bar 10µm. (**B**) (Left) Box plots depicting donor CFP lifetimes of TZM-bl cells transiently-transfected with the MSS probe. Donor lifetime values were extracted from at least 20 single cells, as described in the materials and methods, in each treatment condition over the course of three independent experiments; *p<0.5, **p<0.01 *** p<0.001 as determined by either one-way ANOVA. (Right) Box plots depicting donor CFP lifetimes of TZM-bl cells transiently-transfected with the KMSS probe. Donor lifetime values were extracted from at least 30 single cells, as described in the materials and methods, in each treatment condition over the course of three independent experiments; ns, not significant; determined by either one-way ANOVA. Dots represent single cells. ns, not significant.

2.3.6 Single-cell glycolytic activity influences HIV-1 fusion by regulating membrane order and tension

Together, our results have revealed a possible priorly unappreciated connection between the glycolytic state of the host and biophysical properties of membranes which regulate HIV-1 fusion. To better probe this possible relationship, we assessed the impact of membrane tension on the fusion process between HIV_{JR-FL} pseudoparticles TZM-bl cells. Therefore, we analysed single TZM-bl cells transiently expressing the MSS tension probe upon exposure to mCherry-Gag-labelled HIV-1_{JR-FL} by combining fast FLIM and single particle tracking (Figure 2.3.13A and Figure 2.3.13B). Additionally, we concomitantly recorded the mean lifetime fluctuations of all pixels for TZM-bl cells transiently expressing the MSS biosensor in the presence or absence of mCherry-Gag-labelled HIV-1_{JR-FL} under different treatment conditions. Consequently, we could record fast mean lifetime fluctuations to assess local and global plasma membrane tension during fusion of labelled HIV-1_{JR-FL} particles at the plasma membrane. Virus fusion was reported by the rapid loss of mCherry signal. Importantly, the mCherry-Gag-labelled HIV-1_{JR-FL} spectrally complements the MSS FRET probe such that minimal excitation and emission overlap could be achieved. The disappearance of mCherry-Gag signal for labelled HIV-1_{JR-FL} for viruses surfing the MSS-labelled plasma membrane was a marker for plasma membrane fusion (Figure 2.3.13B).

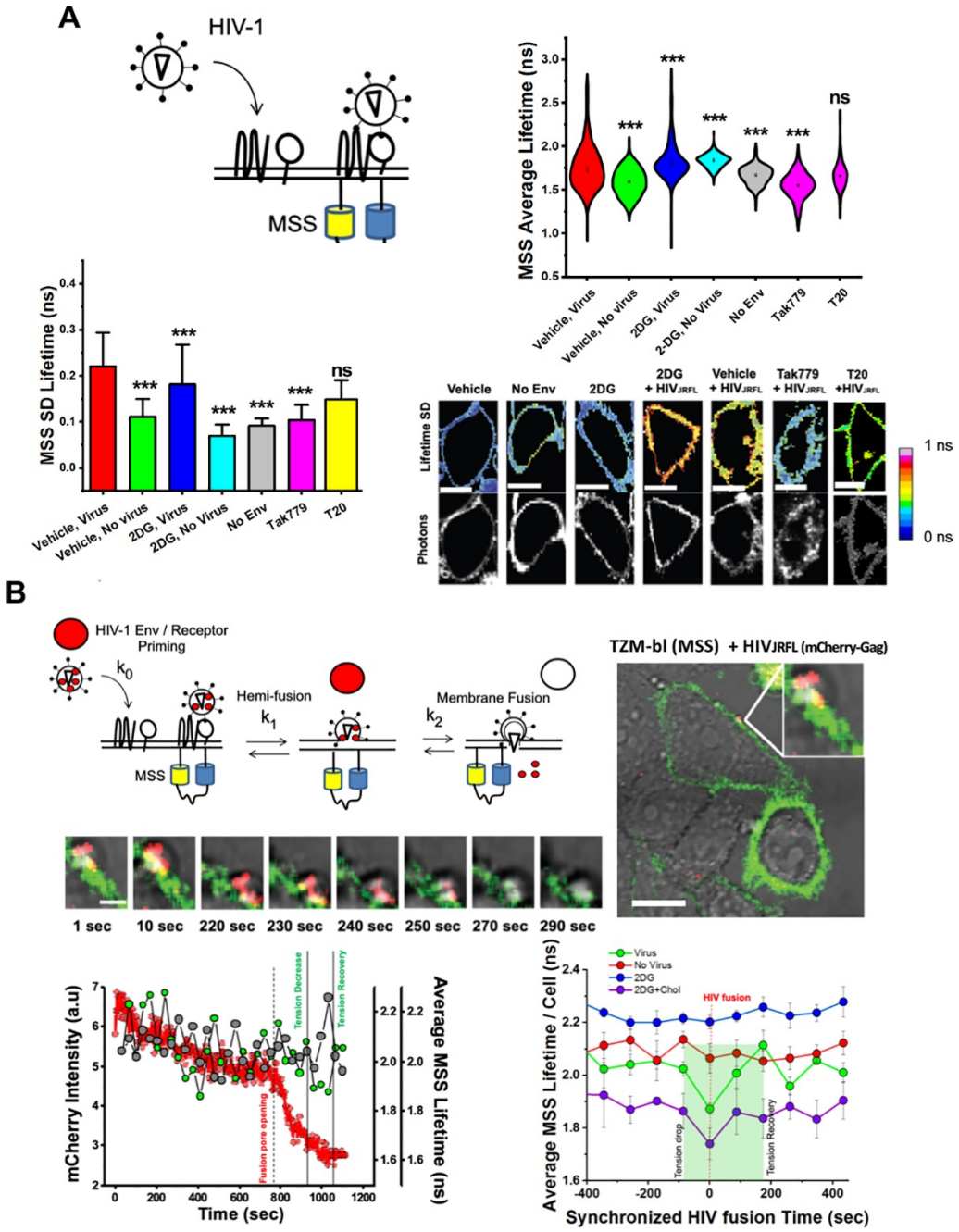

Figure 2.3.13. Multiplexed FLIM with SVT reveals a drop in local tension during single HIV-1 fusion in live cells. (**A**) (Top Left) Cartoon diagram depicting approach to quantify plasma membrane tension fluctuations during virus entry. TZM-bl cells were seeded in Ibidi 35 mm dishes and transiently transfected with MSS. 48 hours later, cells were challenged with HIV-$1_{JR\text{-}FL}$ and subjected to FLIM imaging 90 minutes after virus addition. (Top Right) Violin plots of mean MSS lifetimes acquired per cell per frame during FLIM acquisition during viral entry in transiently-transfected TZM-bl cells. Dots in each plot represent the mean of each condition, which was the calculated from at least 50 frames for at least 20 cells per condition during three independent experiments. * $p<0.05$ ** $p<0.01$ *** $p<0.001$ as determined by one-way ANOVA. (Bottom Left) Standard deviation of MSS lifetimes per cell per frame from FLIM acquisition during viral entry in TZM-bl cells as in the top row, which was calculated from at least 50 frames for at least 20 cells per condition during three independent experiments. * $p<0.05$ ** $p<0.01$ *** $p<0.001$ as determined by one-way ANOVA. (Bottom Right) Representative images depicting the standard deviation of MSS lifetimes per cell for each condition as described in the top row; scale bar 2μm. (**B**) (Top) Approach combining single virus tracking and MSS lifetime imaging to analyse local membrane tension fluctuations during HIV-$1_{JR\text{-}FL}$ entry. Briefly, TZM-bl cells were seeded in Ibidi 35 mm dishes and transiently transfected with MSS. 48 hours later, cells were challenged with mCherry-Gag labelled HIV-$1_{JR\text{-}FL}$ pseudovirions and subjected to FLIM imaging. Representative images of a single -mCherry-Gag JR-FL pseudotyped VLP entering transient MSS-expressing TZM-bl cells are shown; scale bar is 20μm and 2μm for the large and smaller insets, respectively. (Bottom Left) Representative line-graphs depicting local lifetimes in overlapping mCherry-Gag regions (green) and non-overlapping regions (grey) for a single virus particle during entry (loss of mCherry signal, red) in TZM-bl cells. (Bottom Right) Compiled local MSS lifetimes during multiple viral fusion events (green) and respective virus-free regions within the same cell (red) compared to regions of 2-DG treated cells where viruses were incapable of fusion (blue) or rescued events due to cholesterol treatment (purple) in TZM-bl cells. Each point represents a mean timepoint calculated from at least 20 cells obtained from three separate experiments. ns, not significant.

We initially recorded global changes in target TZM-bl cell plasma membrane tension during HIV-1_{JR-FL} entry [245]. Interestingly, TZM-bl cells supporting HIV-1_{JR-FL} fusion reported larger mean eCFP lifetime fluctuations regardless of 2-DG treatment (Figure 2.3.13A). These results indicate that cells exposed to HIV-1_{JR-FL} support global alterations in host membrane tension. Importantly, we noticed that these fluctuations in host plasma membrane tension were Env-dependent, as MSS-expressing TZM-bl cells exposed to bald HIV-1 particles failed to reproduce these fluctuations during acquisition (Figure 2.3.13A). To determine which step in the HIV-1 entry process triggers these observed plasma membrane tension fluctuations, we pre-treated our transiently MSS-expressing TZM-bl cells with Tak779, a CCR5 co-receptor antagonist or T20, an HIV-1 fusion inhibitor which competitively binds to gp41 to block the fusion reaction. Interestingly, TZM-bl cells treated with Tak779 were unable to reproduce robust fluctuations in CFP donor lifetime, similar to bald HIV-1 virions (Figure 2.3.13A). In contrast, CFP donor lifetime fluctuations were restored in TZM-bl cells treated with T20, suggesting that target TZM-bl plasma membrane tension fluctuations during HIV-1_{JR-FL} entry are, at least in part, CCR5-dependent. We confirmed these results by assessing the standard deviations of MSS-containing pixels of whole cells during HIV-1_{JR-FL} entry (Figure 2.3.13A).

In addition, we also analysed local changes in plasma membrane tension limited to sites of HIV-1_{JR-FL} entry signalled by the loss of mCherry-Gag signal (Figure 2.3.13B). Therefore, we recorded MSS eCFP donor lifetimes in 3 x 3 pixel regions at the plasma membrane overlapping with pixels containing mCherry-Gag labelled HIV-1_{JR-FL}. In mock-treated TZM-bl cells exposed to mCherry-Gag-labelled HIV-1_{JR-FL}, we noticed a sharp decrease in MSS donor lifetimes in plasma membrane regions coinciding with the disappearance of proximal mCherry-Gag signal

(Figure 2.3.13B). These sharp decreases in CFP lifetime values during mCherry-Gag signal disappearance was not observed when analysing whole cell CFP lifetimes (Figure 2.3.14A), suggesting that this decrease is limited to sites of HIV-1_{JR-FL} entry. Importantly, this observed drop in local MSS donor lifetime was significant when compared to other 3 x 3 MSS-containing pixel regions free of mCherry-Gag signal in the same cell (Figure 2.3.14B). In some cases, we noticed that the drop in CFP lifetimes occurred with a delay after mCherry-Gag release, although the lifetime recovered before the full release of mCherry-Gag, likely at the moment of fusion pore formation. Furthermore, we noticed that this local drop in MSS donor lifetime was transient (Figure 2.3.13B). In particular, we observed a rapid restoration of the MSS donor lifetime immediately following the loss of the mCherry-Gag signal in all events analysed (Figure 2.3.13B and Figure 2.3.14D). Collectively, these results demonstrate that during HIV-1_{JR-FL} plasma membrane fusion in TZM-bl cells, there is a local sharp, transient reduction in plasma membrane tension that is restored following virus fusion.

To determine if these observed precipitous drops in MSS donor lifetimes during mCherry-Gag signal loss was due to baseline differences in CFP donor lifetime values, we compared 3 x 3 pixel MSS-labelled regions containing or devoid of mCherry-Gag signal (Figure 2.3.14C). We observed no statistically significant difference in CFP donor lifetimes at these time points. These results indicate that the rapid drop in MSS donor lifetimes during mCherry-Gag signal loss was not due to differences in baseline CFP donor lifetime values.

We also analysed MSS donor lifetimes in similar plasma membrane regions of TZM-bl cells containing mCherry-Gag signal in the context of 2-DG pre-treatment. Interestingly, we

noticed that mCherry-Gag-labelled virions which were unable to enter cells overlapped with regions of the plasma membrane with significantly elevated CFP donor lifetimes (i.e. high membrane tension values) when compared to mock-treated conditions (Figure 2.3.13B). As before, higher CFP donor lifetime values were also recorded when assessing the MSS-labelled regions of the whole cell (Figure 2.3.13B). Notably, in 2-DG-treated TZM-bl cells, we failed to recover rapid decreases in MSS lifetimes in local PM regions overlapping with mCherry-Gag signal in all events recorded (Figure 2.3.13B). These results suggest that the drop in local plasma membrane tension required during mCherry-Gag-labelled HIV-1_{JR-FL} entry may be hindered by elevated plasma membrane tension values resulting from 2-DG treatment.

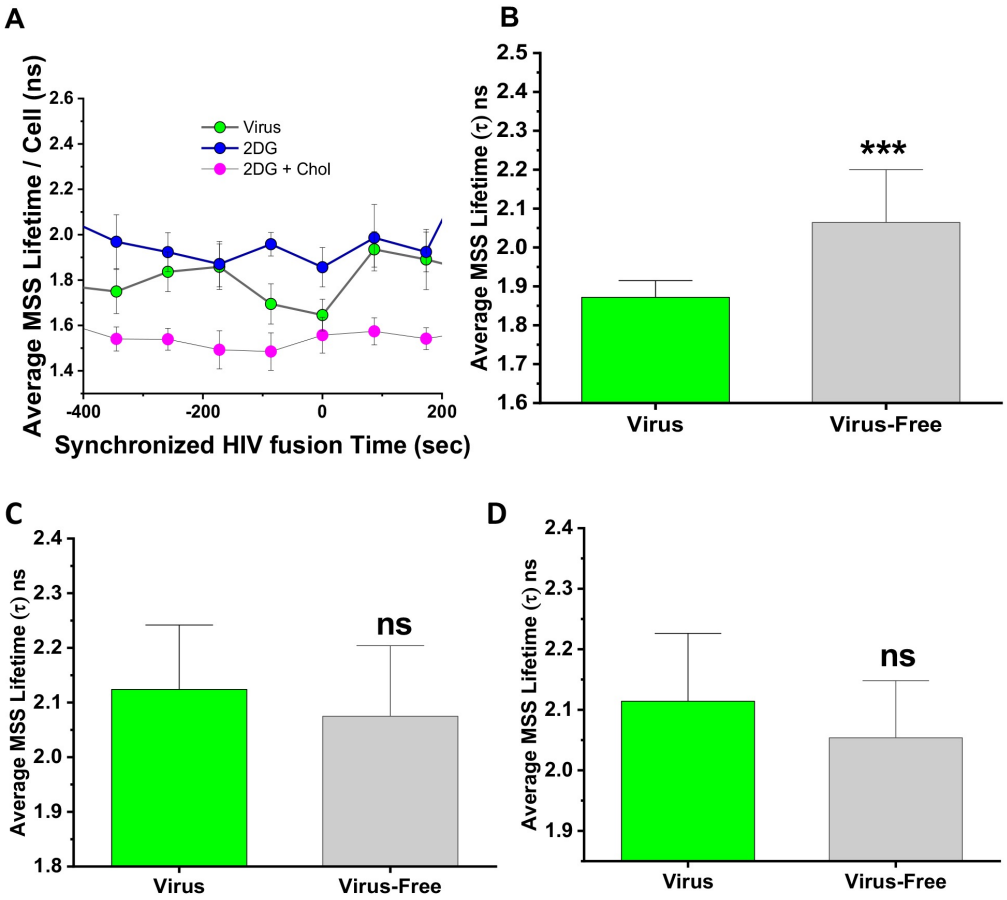

Figure 2.3.14. Multiplexed FLIM with SVT reveals no drop in local tension during single HIV-1 fusion in live cells treated with 2-DG. (**A**) Acquisitions were obtained as described in Figure 2.3.13B. Compiled MSS lifetimes extracted from whole TZM-bl cells during challenge with mCherry-labelled HIV-1_{JR-FL} in either vehicle (green), 2-DG pre-treated cells (blue), or treated with 2-DG and cholesterol (purple). Each dot represents mean whole-cell MSS lifetimes at each time point calculated from at least 20 cells obtained during three separate experiments. (**B**) Bar charts comparing MSS lifetimes of TZM-bl local cell surface regions overlapping with mCherry-labelled HIV-1_{JR-FL} during mCherry signal loss (i.e. virus fusion) with virus-free control areas in the same cell at the same timepoint. Each condition represents a mean of at least 20 cells obtained during three separate experiments. *** $p<0.001$ as determined by one-way student's T-test. (**C**) Bar charts comparing MSS lifetimes of TZM-bl local cell surface regions overlapping with mCherry-labelled HIV-1_{JR-FL} and virus-free control areas in the same cell immediately before fusion. Each condition represents a mean of at least 20 cells obtained during three separate experiments. (**D**) Bar charts comparing MSS lifetimes of TZM-bl local cell surface regions overlapping with mCherry-labelled HIV-1_{JR-FL} and virus-free control areas in the same cell immediately after fusion. Each condition represents a mean of at least 20 cells obtained during three separate experiments. Each condition represents a mean of at least 20 cells obtained during three separate experiments. ns, not significant.

As we and others have demonstrated that cholesterol-treatment may relax plasma membrane tension values [202] and restore HIV-1_{JR-FL} fusion during glycolytic arrest [191], we were curious if supplementing 2-DG treated TZM-bl cells transiently expressing MSS with exogenous cholesterol would support mCherry-Gag-labelled HIV-1_{JR-FL} entry. Additionally, we were curious if exogenous cholesterol treatment would restore the pattern of MSS donor lifetime

decrease and recovery concomitant with mCherry-Gag signal loss. Remarkably, we recovered MSS lifetime traces similar to mock-treated cells when 2-DG-treated TZM-bl cells were supplemented with exogenous cholesterol (Figure 2.3.13B). Collectively, these results suggest that the glycolytic activity of the target cells may regulate plasma membrane tension values which determines the success of HIV-1 fusion. Ultimately, our report may indicate that the glycolytic activity of the TZM-bl reporter cells may regulate cell-surface cholesterol availability which buffers plasma membrane tension values required for supporting HIV-1 fusion at the plasma membrane.

2.4 Discussion

Previous investigations have suggested host metabolism and HIV-1 infection are interlinked [197,198,207]. More recently, the metabolic activity of increasingly differentiated T cell subsets was correlated with HIV-1 infection susceptibility [207]. Indeed, inhibition of glycolysis diminishes HIV-1 infection in culture and in primary CD4+ T cells. However, our study here has uncovered a possible connection linking diminished HIV-1 fusion with altered host cell membrane composition as a result of abrogated glycolytic activity. Here, we show that HIV-1 pseudoparticles are less capable of infecting primary T cells, MT4, and TZM-bl reporter cells subjected to 2-DG treatment, corroborating prior investigations. Additionally, we combined a FLIM-based reporter system of glycolytic activity with virus fusion and infection assays to reveal that the metabolic landscape predetermines the propensity for HIV-1 fusion and infection in TZM-bl reporter cells. Furthermore, we showed that acute glycolytic inhibition in T cells and TZM-bl cells specifically sequesters cholesterol from the plasma membrane, which perturbs membrane order and tension at this HIV-1 fusion site. Moreover, SVT combined with membrane tension measurements via FLIM indicated that glycolytic activity regulates plasma membrane tension levels and can determine success of the HIV-1_{JR-FL} fusion reaction. Collectively, these results suggest that the metabolic landscape may correlate with target cell susceptibility for HIV-1 fusion by modulating biophysical properties at virus fusion sites.

Multiple virus envelope glycoproteins were used to pseudotype HIV-1 in this study: VSV-G, HXB2, NL4.3, and JR-FL. VSV-G pseudotyped HIV-1 has previously been shown to enter host cells via endocytosis [246]. However, the precise site of HIV-1 entry is still heavily debated and

is likely dependent on the target cell [247]. Both R5- and X4-tropic HIV-1 have been shown to enter T cells at the plasma membrane [248,249]. However, in TZM-bl cells, previous studies have reported productive HIV-1 infection via entry through endocytosis [230]. Notably, this latter study utilized spinoculation in their virus-cell fusion assays, and we have shown here that spinoculation may bias HIV-1 entry through endocytosis. Consequently, endocytosis may be dispensable for HIV-1 entry in other cell types [248,249]. By avoiding spinoculation in our imaging assays, we focused our analysis on events which occur at the plasma membrane. Focusing our study at this site, we showed that glycolytic activity may regulate plasma membrane cholesterol content and subsequently fusion of HIV-$1_{JR\text{-}FL}$ pseudoparticles at this site. Importantly, our results could be reproduced in bulk HIV-1 fusion assays in T cell lines and primary T cells exposed to HIV-$1_{NL4.3}$ and HIV-1_{HXB2}, respectively. Interestingly, HIV-$1_{VSV\text{-}G}$ infection was also linked to target TZM-bl glycolytic activity, albeit to a lesser extent. These results may suggest that glycolytic activity broadly regulates fusion of enveloped viruses at the plasma membrane and possibly in endosomes. Nevertheless, factors regulating fusion at these separate sites may be different.

Additionally, we utilised fluorescent probes of membrane order (i.e. FliptR) and tension (i.e. MSS) to study these plasma membrane biophysical parameters. Therefore, conclusions drawn from these experiments should be carefully interpreted and may not be directly applicable for virus entry in endosomes. Nevertheless, filipin-stained TZM-bl cells co-labelled with endosomal marker LDL-Bodipy reported reduced cholesterol content in this compartment in addition to the plasma membrane. Consequently, it is plausible that reductions in plasma membrane cholesterol content are reflected in endosomes as well [177,250]. Further investigations will probe membrane order

and tension values in endosomes during 2-DG treatment in HIV-1 target cells and examine how alterations in these membrane properties regulate HIV fusion at this site.

Importantly, we reported that host cell glycolytic activity regulates the availability of ordered lipids in the plasma membrane of HIV-1 target cells. This result is significant owing to the fact that cell membranes are organised into laterally segregated lipid domains (i.e. Lo and Ld domains) [251,252]. Lo domains contain saturated lipids and sterols and are surrounded by Ld domains comprised of unsaturated phospholipids. Importantly, the boundaries between these microdomains facilitate the fusion reaction for a range of viruses, including HIV-1. These sites enhance the HIV-1 fusion reaction due to the ability for these boundaries to drive membrane bending required for fusion pore formation, consequently diminishing the energy barrier necessary to perform virus-cell fusion reaction [211]. Membrane curvature is likely generated owing to the line tension which arises due to mismatch in lipid length at these boundaries [184]. In line with our data reported here, it is possible that the reductions in plasma membrane cholesterol during 2-DG treatment in TZM-bl, MT4 or primary CD4+ T cells disrupt the integrity or size of Lo domains, reducing the size of Lo/Ld domain boundaries (Figure 2.3.15). Therefore, both line tension and the ability to drive membrane bending necessary for virus-cell fusion may be diminished.

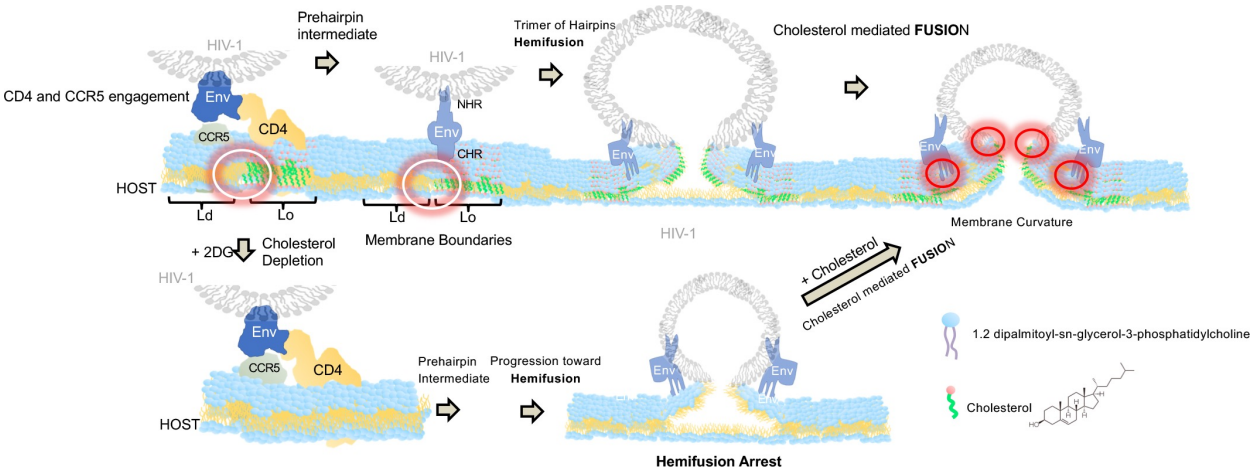

Figure 2.3.15. Cholesterol availability regulates the transition between HIV-1 hemifusion and fusion. (Top Row) HIV-1 Env sequentially interacts with CD4 and CCR5 at the boundaries of ordered lipid domains to bring host and viral membrane leaflets into close proximity to generate a hemifusion intermediate, which is not cholesterol dependent. Following this, the line tension and membrane curvature offered at the boundary of cholesterol-laden Lo and cholesterol-depleted Ld domains enable the progression to fusion pore formation and expansion. (Bottom row) Viruses exposed to cells pre-treated with 2-DG are arrested at hemifusion owing to depletion of cholesterol at Lo and Ld domain boundaries. Hemifusion intermediates are also likely to collapse under high membrane tension values. The addition of cholesterol buffers high membrane tension values in glycolytically inactive target cells, restores Lo domains, and rescues full fusion. White circles represent lipid boundaries where HIV-1 Env priming and fusion may occur. Red circles represent a potential role for cholesterol inducing membrane curvature and buffering membrane tension during fusion pore formation.

As we recorded increases in membrane tension via FLIM of MSS-expressing TZM-bl cells, it is tempting to speculate that these increases in local plasma membrane tension values may negate the ability for Lo/Ld boundaries to drive membrane bending required for the fusion reaction or collapse hemifusion intermediates (Figure 2.3.15) [184,185]. Indeed, membrane tension and membrane order influence each other, and these biophysical parameters of the host cell membrane contribute to virus fusion [93,208]. Future studies investigating how membrane tension regulate bending rigidities in artificial membranes will be the first step in answering these key questions important for the virus-cell fusion process in live target cells.

We hypothesise that glycolysis either directly or indirectly regulates cholesterol in cell membranes as 2-DG treatment diminished host cholesterol quantity without affecting CD4 or co-receptor levels. Further investigations are necessary to elucidate the mechanism of cholesterol

reduction in glycolytically inactivated cells. As described above, the loss of membrane cholesterol likely disrupts the hydrophobic mismatch between Lo and Ld domains, rendering HIV-1 fusion less favourable. Furthermore, with elevated plasma membrane tension, the energy required for the fusion peptide to complete the fusion reaction during hemifusion is likely incompatible (Figure 2.3.15). Our data suggests this mechanism is plausible because cells treated with 2-DG and supplemented with cholesterol enabled full HIV-1 fusion to be completed. Additionally, these data indicate that cholesterol may be an essential factor facilitating the transition between HIV-1 hemifusion and fusion.

The glycolytic activity of the host cell may also regulate plasma membrane phospholipid availability essential for not only HIV-1 entry, but the entry of other enveloped viruses. Phospholipid biosynthesis is tightly linked to glycolysis intermediates, such as dihydroxyacetone phosphate. Several phospholipids enhance HIV-1 entry [253], however, these mediators are thought to promote the restructuring of viral glycoproteins to mediate the fusion reaction [253]. Nevertheless, it is plausible that specific phospholipids may alter other biophysical properties of the membrane, such as membrane order [115,179,240]. Further investigations which assess the role of glycolysis on phospholipid availability at virus entry sites and its consequences are therefore warranted.

Collectively, our results provide evidence that glycolytic flux is necessary to maintain high lipid order and relatively low membrane tension in HIV-1 target cells which promote HIV-1 fusion. Additionally, we show in both reporter cells, MT4, and primary CD4+ T cells that target cell glycolytic flux regulates membrane cholesterol availability and HIV-1 entry. Importantly, we

show for the first time with high spatiotemporal resolution that HIV-1 entry at the cell surface in target TZM-bl cells requires local membrane tension which transiently, yet sharply decreases during virus fusion, and these biophysical alterations are dependent on plasma membrane cholesterol content. Ultimately, our results suggest that acute inhibition of glycolysis creates a biophysical environment which abrogates HIV-1 fusion at the cell surface, suggesting a novel link between host cell metabolic and membrane biophysical landscapes.

2.5 Acknowledgements

Irene Carlon-Andres and Ewoud Compeer performed experiments with primary cells. Sergi Padilla-Parra performed single-virus tracking experiments analysing the effects of spinoculation on HIV-1_{JR-FL} entry in TZM-bl cells. This work was originally published in *PLoS Pathogens*.

Coomer CA, Carlon-Andres I, Iliopoulou M, Dustin ML, Compeer EB, Compton AA, et al. (2020) Single-cell glycolytic activity regulates membrane tension and HIV-1 fusion. PLoS Pathog 16(2): e1008359. https://doi.org/10.1371/journal.ppat.1008359

Chapter 3: Homology-guided identification of a conserved motif linking the antiviral functions of IFITM3 to its oligomeric state

3.1. Introduction

Human cells are equipped with an arsenal of constitutively expressed or inducible antiviral proteins, culminating a critical arm of the cell-intrinsic immune system. These proteins are upregulated by cytokines, particularly interferon, creating an "antiviral state" via the expression of hundreds of antiviral genes. The protein products of these genes converge on multiple steps of the virus lifecycle to potently block infection and halt virus spread [10,254]. Additionally, there are constitutively-expressed "front-line" antiviral proteins which create a persistent barrier to virus infection, may be further upregulated by interferons, and are expressed in multiple tissues.

The interferon-inducible transmembrane (IFITM) proteins are part of these front-line defences and are the earliest acting restriction factors identified [17,94]. These proteins inhibit the replication of an expanding list of viruses, including orthomyxoviruses, flaviviruses, coronaviruses, and retroviruses, including human immunodeficiency virus (HIV-1) [17]. There are three interferon-responsive IFITM protein family members (IFITM1, IFITM2, and IFITM3) with the most well-characterised member being IFITM3, owing to its critical role in protecting humans from severe influenza virus infection [31,32] and rapid progression of HIV-1 infection [37]. While the precise mechanism by which IFITM3 reduces virus-cell fusion remains incompletely characterised, it is suspected to restrict virus-cell membrane fusion by altering the properties of lipid membranes such that fusion pore formation is prevented [86,87,103,255,256].

Two models have been offered to describe how IFITM3 inhibits virus-cell fusion. One model posits that IFITM3 indirectly inhibits virus-cell fusion by associating with VAMP-associated protein A (VAPA) to disrupt intracellular cholesterol homeostasis and subsequently load endosomes with excess cholesterol accumulation [87]. Consequently, it is thought that increased endosomal cholesterol content may block fusion of the virus-containing vesicle with the limiting membrane of the late endosome. Indeed, although disruption of endosomal cholesterol trafficking has been shown to deter virus entry [257], this proposed mechanism of IFITM3 has been challenged by multiple subsequent investigations [79,86,103,256], whilst being supported by very few [255].

Contrastingly, an alternative model suggests that IFITM3 directly inhibits fusion of inbound viruses by locally rigidifying membranes and disrupting membrane curvature [51,103]. Membrane order and curvature regulate a wide range of fusion processes [258] and several investigations have presented evidence which is consistent with this hypothesis. For example, a juxtamembrane amphipathic helix has been shown to be critical for IFITM3 antiviral activity [56], and amphipathic helices of various prokaryotic and eukaryotic proteins are known to bind and bend membranes [99]. Furthermore, enveloped viruses containing IFITM3 within their membranes also have impaired ability to fuse with target cells, suggesting that IFITM3 may deform the membranes in which it resides [73,74,96,102]. Nevertheless, a full understanding of IFITM3's mechanism of action would be benefited by studies analysing the impact of IFITM3 on membranes which utilise mutants lacking antiviral function.

Another key property thought to contribute to the antiviral function of IFITM3 is its ability to form oligomers. Previous reports have demonstrated IFITM3's ability to form higher-order oligomers is critical for restriction of IAV [104]. Furthermore, recent investigations utilising nanoscopy approaches illustrated that IFITM3 forms clusters on virus-containing vesicles [91]. However, the ability of IFITM3 to oligomerise was originally mapped to two phenylalanine residues at position 75 and 78 within its CD225 domain [104], and recently, these residues have been shown to be unnecessary for IFITM3 oligomerisation in living cells [118]. Consequently, IFITM3 oligomerisation is influenced by currently unknown determinants and its relevance to antiviral function is poorly understood.

In this chapter, we performed an investigation which took advantage of a homology-guided approach to identify loss-of-function mutations in IFITM3 to better describe IFITM3's antiviral function. As described in chapter one, the *IFITM* genes are members of a much larger group of genes named the Dispanins/CD225 family owing to their shared CD225 domain [11,12]. Curiously, proline-rich transmembrane protein 2 (PRRT2), another member of this family, has been extensively characterised owing to its underlying role in convulsive neurological disorders typified by involuntary movements, benign familial infantile seizures, and episodic ataxia [107,108]. In line with these clinical observations, PRRT2 is expressed in neurons and localises to pre-synaptic terminals to block synaptic vesicle fusion [259–261]. Several non-synonymous, disease-associated mutations identified within the CD225 domain of PRRT2 (e.g. G305W/R) have been shown to diminish the ability of PRRT2 to check neurotransmitter release [109,262–265]. Importantly, missense mutations (i.e. G95W/R) of the homologous residue in human IFITM3 also result in partial loss of restriction against IAV infection [104]. Nevertheless, the mechanism by

which this homologous residue facilitates the biological function of these CD225 proteins was unknown.

We discovered that the G95 residue of human IFITM3 is located within a highly conserved ^{91}GxxxG^{95} motif among vertebrate orthologs and is homologous to the G305 site within PRRT2. Mutation of either glycine residue within this motif in IFITM3 potently decreased restriction against IAV (in target cells) and HIV-1 (in virus-producing cells). Furthermore, fluorescence lifetime imaging microscopy (FLIM) and Förster resonance energy transfer (FRET) studies of fluorophore-tagged IFITM3 expressed in living cells indicated that an intact ^{91}GxxxG^{95} motif is necessary for IFITM3 oligomerisation.

Because mutations targeting the ^{91}GxxxG^{95} motif not only resulted in loss of IFITM3 antiviral function, but also reduced oligomerisation efficiency, we predicted that these two phenotypes were functionally related. Consequently, we used these oligomerisation-defective IFITM3 mutants to reveal other mechanistic correlates of IFITM3 antiviral function. Using a fluorescent-based reporters of membrane order and these oligomerisation-defective mutants, we discovered that IFITM3 oligomerisation is required to increase the rigidity of resident membranes. We confirmed our results by demonstrating that Amphotericin B decreases the rigidity of IFITM3-containing membrane and thwarts IFITM3-mediated restriction against IAV. Finally, we showed that homologous mutations in fluorophore-tagged PRRT2 rendered it incapable of oligomerisation via FLIM. Together, these results reveal a mechanism by which IFITM3 inhibits the fusion of a broad range of pathogenic enveloped viruses and suggest that oligomerisation is a shared

requirement for distinct anti-fusion functions performed by the CD225 homologs IFITM3 and PRRT2.

3.2 Material and Methods

3.2.1 Sequence alignments and phylogenetic analysis

UniProt (www.uniprot.org) was used to gather protein sequences for all CD225 proteins analysed (i.e. TUSC5, PRRT2, and IFITM proteins) and ClustalX (www.ebi.ac.uk/tools/msa/muscle/) was utilised to perform multi-sequence alignments.

3.2.2 Cell lines and plasmids

HEK293T (ATCC: CRL-3216) and TZM-bl (NIH AIDS Reagent Resource: 8129) were cultured in DMEM (Gibco) supplemented with 10% foetal bovine serum (Hyclone) and 1% penicillin-streptomycin (Gibco) and cultivated at 37°C and 5% CO_2. Cell passaging was performed regularly with the aid of Trypsin-EDTA 0.05% (Gibco). Retroviral pQCXIP vectors encoding IFITM3 with amino-terminal FLAG tags were previously described and were used to create subsequent derivatives of this plasmid [14]. In particular, IFITM3 fused with amino-terminal myc was produced by appending the myc tag to the open reading frame of IFITM3 with PCR and cloning into BamH1/EcoR1 sites in the pQCXIP vector. Additionally, site-directed mutagenesis (QuikChange Lightning) or ligation-independent cloning was utilized to introduce IFITM3 mutations G91L, G95L, and G95W. HEK293T cell lines which stably express pQCXIP plasmids were generated by transfecting 250,000 cells in a 12-well plate with 0.8μg of DNA using Lipofectamine 2000 (Invitrogen) with subsequent 10 μg/mL puromycin selection performed for

two weeks. Wildtype PRRT2 fused to carboxy-terminal YFP or mCherry was produced by Integrated DNA Technologies.

3.2.3 Virus productions, infections and virus-cell fusion assay

Influenza A Virus [A/PR/8/34 (PR8), H1N1] was purchased from Charles River Laboratories as clarified allantoic fluid. Infectious virus titres were calculated using a flow cytometry-based method in HEK293T cells as previously described [266]. To perform infections, a total of 50,000 HEK293T cells per well either stably expressing or transiently transfected with 1.5 μg of pQCXIP, WT IFITM3, or the indicated mutant, were seeded in 24-well plates and allowed to grow overnight. The following day, the indicated amount of viruses diluted in 225 μL of DMEM was added to the wells and allowed to incubate for approximately 18 hours. Following this, cells were washed with 1X PBS, dissociated with Trypsin-EDTA, and subsequently fixed and permeabilized with Cytofix/Cytoperm (BD). To detect IAV infection, cells were immunostained with anti-IAV NP (AA5H; Abcam) and analysed on a LSRFortessa flow cytometer (BD).

To produce replication-incompetent HIV-1 pseudotyped with IAV WSN HA and NA, Lenti-X-HEK293T cells were transfected with: 2 μg pR8ΔEnv, 1 μg pcRev (NIH AIDS Reagent Resource: 11415), 3 μg Gag-GFP, 1.5 μg of hemagglutinin, and 1.5 μg of neuraminidase from IAV WSN strain, H1N1 (gifts from G. Melikyan) using GeneJuice (Novagen) according to the manufacturer's protocol. 12 hours post-transfection, the medium was removed from the cells, the cells were washed gently with 1X PBS, and then supplemented with complete DMEM F12 (Gibco) devoid of phenol-red. These cells were then allowed to incubate for a further. 48 hours post

transfection, the supernatant containing produced virus particles were harvested, filtered with a 0.45 μm syringe filter (Sartorius Stedim Biotech) and stored at -80 °C.

To produce replication-competent HIV-1, HEK293T cells were transfected with 15 μg pNL4-3 and 5 μg empty pQCXIP, pQCXIP encoding IFITM3 WT, or the indicated mutant fused with amino-terminal FLAG using the calcium-phosphate method. For virus-cell fusion assays, replication-incompetent HIV-1 pseudotyped with VSV-G was produced by transfecting HEK293T via the calcium-phosphate method with 15 μg pNL4-3ΔEnv, 5 μg pCMV4-BlaM-Vpr, and 5 μg pMD2.G (VSV-G). The calcium-phosphate method of transfection was performed as follows: 6 million HEK293T cells were seeded in a T75 flask and the associated plasmid DNA was mixed with H_2O, $CaCl_2$, and Tris-EDTA buffer. This plasmid DNA-containing mixture was combined with Hepes-buffered saline and mixed. Subsequently, the transfection mixture was added to the flask drop-wise and the cells were incubated for 48 hours. Supernatants were purified by centrifugation and filtration through a 0.45-μm filter, and ultimately were concentrated via ultracentrifugation at 25000 x g for 1 hour at 4°C through a 20% sucrose cushion. Titration of lentiviruses was performed via an HIV-1 p24 ELISA kit (XpressBio). Infectivity of lentiviruses was measured by adding equivalent volumes containing 50 ng p24 to TZM-bl cells. 48 hours post-infection, these cells were fixed and permeabilised as above and infection was detected by immunostaining with anti-Gag KC57-FITC (BD), and analysed by flow cytometry. Virus-cell fusion was quantified by adding 100-300 ng p24 equivalent HIV-1-VSV-G containing the BlaM-Vpr construct to HEK293T cells stably expressing WT IFITM3 or the indicated mutant for 2.5 hours at 37°C. Following incubation, cells were washed with CO_2-independent DMEM (Gibco) and stained with CCF2/AM containing probenecid for 1 hour at room temperature, protected from

light. After staining, cells were washed with cold 1X PBS, fixed/permeabilised with Cytofix/Cytoperm (BD), and analysed on a LSRII flow cytometer.

3.2.4 Confocal immunofluorescence microscopy

A total of 30,000 HEK293T cells per well were seeded in µ-slide 8 well chambers and allowed to grow overnight. The following day, these cells were transfected with either 0.2 µg empty pQCXIP, pQCXIP-FLAG-WT IFITM3 or the indicated amino-terminal FLAG-tagged mutant via Lipofectamine2000 (Invitrogen). Following 48 hours post-transfection, cells were fixed and permeabilised with Cytofix/Cytoperm and subsequently immunostained with anti-IFITM3 antibody (EPR5242; Abcam) and anti-CD63 antibody (MX-49, sc-5275; Santa Cruz Biotechnology). After immunostaining, cells were imaged for immunofluorescence using a Leica TCS SP8 confocal microscope. Cells were selected under a 63X oil-immersion objective. All image analysis was performed in Fiji (ImageJ).

3.2.5 Immunoprecipitation, SDS-PAGE, and Western blot analysis

A total of 250,000 HEK293T cells per well were seeded in 12 well plates and allowed to grow overnight in DMEM media (Gibco) supplemented with 10% FBS. The following day, HEK293T cells were transfected with 1.5 µg empty pQCXIP or a combination of 0.75 µg pQCXIP-FLAG-IFITM3 and 0.75 µg pQCXIP-myc-IFITM3 (encoding either WT or G95L). Cells were allowed to subsequently grow for 48 hours, upon which time they were lysed in a buffer composed 0.5% IGEPAL (Sigma), 50 mM Tris (pH 7.4), 150 mM NaCl, and 1 mM EDTA, which was supplemented with a 1% Halt Protease Inhibitor mixture, EDTA-free (ThermoFisher). Lysates were subsequently immunoprecipitated using anti-FLAG M2 magnetic beads (Sigma) for of 3 hours with rotation at 4°C. Following immunoprecipitation, magnetic beads were captured with a

DynaMag-2 magnet (Thermo Fisher) and washed with a buffer composed of 50 mM Tris (pH 7.4) and 150 mM NaCl prior to the addition of 1X NuPAGE LDS sample buffer and 1X NuPAGE Sample Reducing Reagent (Invitrogen). Both the whole cell lysates and immunoprecipitated pull-down fractions were denatured by heating 90°C for 15 minutes. Following denaturation, 12 µL and 5 µL of whole cell lysates and immunoprecipitated pull-down fractions, respectively, were loaded into Criterion XT 12% Bis-Tris polyacrylamide gels (Bio-Rad) for SDS-PAGE using NuPAGE MES SDS Running Buffer (Invitrogen). Separated protein fractions were transferred to Amersham Protran Premium Nitrocellulose Membranes, pore size 0.20 µm (GE Healthcare) and were blocked overnight with Odyssey blocking buffer in PBS (Li-COR). The following day, membranes were incubated with anti-FLAG M2 (F1804; Sigma) and anti-c-Myc (C3956; Sigma) diluted in Intercept T20 antibody diluent (Li-COR) for two hours. Following washing with 0.01% Tween-PBS solution three times, secondary antibodies conjugated to DyLight 800 or 680 (Li-COR) diluted in Intercept T20 antibody diluent (Li-COR) and stained membranes for one hour. A Li-COR Odyssey imaging system were used to reveal specific protein detection and resulting images were analysed and generated using ImageStudioLite (Li-COR).

Comparison of steady-state expression levels of WT IFITM3 and mutants was accomplished by transiently transfecting HEK293T cells with 1.5 µg of empty pQCXIP or pQCXIP-FLAG-IFITM3 (encoding WT or the indicated mutants) using Lipofectamine 2000 (Sigma). Expression was measured by staining for FLAG with anti-FLAG M2 (F1804; Sigma) and detected via flow cytometry or western blot analysis. For analysis by flow cytometry, at 48 hours post-transfection cells were fixed and permeabilised with Cytofix/Cytoperm (BD) followed by immunostaining with anti-FLAG M2 (F1804; Sigma) and analysed on a LSRFortessa (BD). Western blots were performed by lysing cells and separation via SDS-PAGE as indicated above

with immunoblotting performed with anti-FLAG M2 (F1804; Sigma) and anti-actin (C4, sc-47778; Santa Cruz Biotechnology).

HIV-1 proteins were analysed by western blotting of cell lysates and concentrated virus supernatants. Lysis of the cells or virions was accomplished with radioimmunoprecipitation (RIPA) buffer (ThermoFisher) complemented with Halt Protease Inhibitor mixture EDTA-free (Thermo Fisher) or 0.01% Triton-X (Sigma), respectively. Cell and virion lysates were then heat denatured at 90°C for 15 minutes after treatment with 1X NuPAGE LDS sample buffer and 1X NuPAGE Sample Reducing Reagent (Invitrogen). Migration and transfer of protein samples were performed as indicated above. Immunoblotting was performed with the following antibodies: anti-gp120b (NIH AIDS Reagent Resource: 288), anti-gp41 2F5 (NIH AIDS Reagent Resource: 1475), anti-p24 CA (NIH AIDS Reagent Resource: 3537), anti-FLAG M2 (F1804; Sigma), and anti-actin (C4, sc-47778; Santa Cruz Biotechnology).

3.2.6 Blue native PAGE

A total of 750,000 HEK293T cells per well were seeded in 6-well plates and allowed to grow overnight. The following day, these cells were transfected with either 1 μg of empty pQXCIP, pQXCIP-FLAG-IFITM3 WT or pQXCIP-FLAG-IFITM3 G95L. 48 hours post-transfection, cell lysates were generated via treatment with 1X NativePAGE Sample Buffer (Invitrogen) supplemented with 1% digitonin. Lysates were subsequently prepared by mixing with 5% Coomassie G-250 at a 20:1 volume-to-volume ratio. For each condition, 20 μg of prepared protein sample was loaded onto a NativePAGE Novex 4-16% Bis-Tris polyacrylamide gel (Invitrogen) according to manufacturer's protocol with NativeMark Unstained Protein Standard (Invitrogen) loaded as a reference standard ladder. Following protein separation, proteins were transferred to

an Immobile FL PVDF membrane (EMD Millipore). Anti-FLAG (F1804; Sigma) was used to immunoblot for FLAG-tagged proteins and a secondary antibody conjugated to either DyLight 680 or 800 (Li-COR) was used for signal detection, which was accomplished by a Li-COR Odyssey imaging system. All images were analysed and generated via ImageStudioLite (Li-COR).

3.2.7 FRET and FLIM for oligomerization studies

A total of 50,000 HEK293T cells per well were seeded in μ-slide 8 well chambers (Ibidi) and allowed to grow overnight in complete Fluorobrite DMEM (Gibco). The following day, these cells were transiently transfected with 0.25 μg IFITM3-YFP and 0.25 μg mCherry, or 0.25 μg IFITM3-YFP and 0.25 μg IFITM3-mCherry using TransIT-293 (Mirus) with the fluorophore fused to the amino-terminus. For experiments analysing oligomerisation of PRRT2, pairs of plasmids encoding PRRT2-YFP and PRRT2-mCherry were co-transfected instead, and the fluorophore was fused to the protein's carboxy-terminus. Imaging of these live cells in Fluorobrite DMEM (Gibco) was performed with a Zeiss LSM 780 confocal microscope and cells were selected with a 63X oil-immersion objective. To perform FRET experiments, following excitation with a 514 nm laser, donor YFP fluorescence was captured with a gallium arsenide phosphide photomultiplier tube (GaAsP PMT) with a 520-550 nm emission window. Following excitation by a 561 nm laser, acceptor mCherry fluorescence was captured with a GaAsP PMT detector set with an emission window at 570-615 nm. The FRET channel was collected with a GaAsP PMT detector set to a 570-615 nm emission window after excitation with a laser tuned to 514 nm. For each condition, at least 50 cells were examined in each experiment. Using the FRET and co-localisation analyser plugin(https://imagej.nih.gov/ij/plugins/fret-analyzer/fret-analyzer.htm) in Fiji (ImageJ), FRET indices were calculated for each cell. Evaluation of the donor lifetime was performed

concomitantly with the FRET experiments via excitation with a 950 nm two-photon pulsed laser (Coherent) tuned to 80 MHz with single photon counting electronics (Becker Hickl) and signal detection with an HPM-100-40 module GaAsP hybrid PMT (Becker Hickl). To exclude the effects of photobleaching or low-signal-to-noise, analysis of cells was limited those which contained 250-1000 photons per pixel. The corresponding fluorescence decay curves of each pixel in FlipTR-stained cells were acquired and analysed by Symphotime 64 software (Picoquant). Fluorescence decays of each pixel were acquired and analysed in SPCImage NG software (Becker Hickl), and each decay was deconvoluted with the instrument response function and fitted to a Marquandt nonlinear least-square algorithm with a two-exponential model. Mean fluorescence lifetimes were calculated as performed previously [267] in SPCImage NG and at least 30 cells per condition were analysed in each experiment.

3.2.8 Number and Brightness analysis

A total of 50,000 HEK293T cells transiently expressing either mCherry-tagged pQCXIP-WT IFITM3, IFITM3-G95L, or unfused mCherry were seeded in each well of μ-slide 8 well chamber slides (Ibidi) and allowed to grow overnight in complete Fluorobrite DMEM (Gibco). The following day, live cells in Flurobrite DMEM (Gibco) imaging media were selected with a Zeiss LSM 780 confocal microscope using a 63X oil-immersion objective. To perform the fluorescence fluctuation acquisition, areas of interest were limited to regions of cells which were 1.) immobile and 2.) confined to the plasma membrane to excluded intracellular signal from vascular membranes which would confound labelled particle mobility. Additionally, the axial position of the chamber slides was stabilized using the Adaptive Focus Control module. mCherry fluorescence was detected with a 570-615 nm emission window after excitation with a 561 nm laser. For every cell selected, 100 frames were acquired at a rate of 0.385 frames per second with

a 9.75 µs pixel dwell time and pixel size of 151.38 nm. In order for the pixel size to remain 3-4 times smaller than the point-spread function, images were acquired in a 256 x 256 pixel format. A detrending algorithm was used in order to correct for confounding effects caused by photobleaching of fluorescent proteins during acquisition [149]. Pixel-by-pixel brightness values were calculated in Fiji (ImageJ) and at least twenty cellular regions were examined per condition.

3.2.9 FLIM for study of membrane order with FliptR

A total of 50,000 HEK293T cells transiently transfected with or stably expressing either empty pQXCIP, pQCXIP-WT IFITM3, or the indicated mutant were seeded in individual wells of a µ-slide 8 well chamber (Ibidi) and allowed to grow overnight in complete Fluorobrite DMEM (Gibco). The following day, these cells were and stained with 1 µM FliptR (Spirochrome) for 5 mins according to the manufacturer's protocol. Cells were visualised with a 63X oil-immersion objective on a SP8-X-SMD confocal microscope (Leica). When drug treatment is indicated, cells transiently transfected with or stably expressing either empty pQXCIP were treated with either 5 mM methyl-cyclo-beta-dextrin (MßCD) (C4555, Sigma) to deplete cholesterol, 400 µg/mL soluble cholesterol (C4951, Sigma) to supplement cholesterol, or 1 µM Amphotericin B (A2942, Sigma) for one hour prior to washing with PBS, staining with FliptR, and imaging. Following excitation by a pulsed laser tuned to 488 nm and 20 MHz, fluorescence was detected by external hybrid detectors set in photon-counting mode with single photon counting electronics (PicoHarp 300). To exclude the effects of photobleaching or low-signal-to-noise, analysis of cells was limited those which contained 250-1000 photons per pixel. The corresponding fluorescence decay curves of each pixel in FlipTR-stained cells were acquired and analysed by Symphotime 64 software (Picoquant). Before analysis, the fluorescence decay was deconvoluted with the instrument

response function and fitted to a Marquandt nonlinear least-square algorithm with two exponential models. As previously described, individual component lifetimes (long and short lifetimes, τ_1 and τ_2), as well as the mean fluorescence lifetime (τ) were calculated and extracted using Symphotime, yet only the long lifetime, τ_1, was reported [240]. At least 30 cells per condition were analysed in each experiment.

3.2.10 Laurdan Labelling

The membrane probe Laurdan (6-dodecanoyl-2-dimethylamino naphthalene, Invitrogen) was dissolved in DMSO to make a stock solution of 9.19 mM. A total of 250,000 HEK293T cells stably expressing an empty vector (pQCXIP) IFITM3 WT, or IFITM3 G95L were seeded per well in a 12 well plate and were allowed to grow overnight. The following day, these cells were incubated with 1.8 µM Laurdan for 1 hour at 37°C. To add or deplete membrane-associated cholesterol, cells were incubated with either 400 µg/mL water-soluble cholesterol or 10 mM MβCD for 1 h at 37°C before washing with PBS and staining with Laurdan. All cells were rinsed with PBS once before imaging.

3.2.11 Laurdan Imaging

Generalised polarization (GP) is a ratiometric method which quantitatively measures membrane order in live cells [268]. The GP value is calculated via the expression:

$$Generalised\ polarization = \frac{I_{blue} - I_{green}}{I_{blue} + I_{green}}$$

where I_{blue} and I_{green} are the intensities centred at 440nm and 490nm, respectively. Conventionally, 440 nm and 490 nm are the emission maximums for ordered lipid and disordered lipid bilayers,

respectively. GP data was acquired with a Zeiss LSM780 laser scanning microscope using a 63X oil immersion objective, coupled to a 2-photon Ti:Sapphire laser (Coherent) tuned to 780 nm and 80 MHz. A SP 760 nm dichroic filter was used to separate the laser light from the fluorescence signal. The fluorescence signal was captured from 416 nm to 474 nm for the blue channel and from 475 nm to 532 nm for the green channel using the GaAsP PMT detectors of the LSM 780. ImageJ was utilised to process the GP data as previously described [269]. GP values were calculated for each cell of interest and the numeric difference in GP values for the entire cell are presented normalised to the empty vector control.

3.3. Results

3.3.1. Identification of a putative oligomerisation motif within CD225 domain containing proteins

Recent investigations have suggested both IFITM3 and PRRT2 adopt a type II transmembrane topology [54,57,270]. This topology consists of a cytoplasmic N-terminus, a CD225 domain consisting of 1.) a hydrophobic intramembrane (IM) domain 2.) a cytoplasmic intracellular loop (CIL) and 3.) a hydrophobic transmembrane (TM) domain, followed by a short C-terminus facing the extracellular space or the intracellular lumen [54,57,270]. To visualise this topology of IFITM3 (Figure 3.3.1A) and PRRT2 (Figure 3.3.1B), we utilized Protter, a tool which highlights annotated and predicted protein features onto the topological maps of transmembrane proteins [271]. Notably, although both PRRT2 and IFITM3 exhibited similar topology, the N-terminus of PRRT2 was considerably longer. We also aligned protein sequences of these CD225 proteins and searched for previously uncharacterised shared motifs among them. Interestingly, we noticed the presence of a GxxxG motif in the CIL of both IFITM3 and PRRT2 as well as other interferon-responsive IFITM proteins and CD225 proteins (Figure 3.3.1C). GxxxG motifs, also known as glycine zippers, have been previously associated with facilitating membrane protein-protein interactions [272,273]. Furthermore, this motif has also been shown to mediate protein oligomerisation of hydrophobic TM helices between proteins within a bilayer via their cytoplasmic loops [274]. To determine if this motif was conserved in IFITM3, we aligned *IFITM3* protein sequences from of diverse range of vertebrate species and determined that the GxxxG motif is conserved in *IFITM3* of vertebrates (Figure 3.3.1D). These results indicate that the GxxxG motif may play a conserved role in IFITM3 function, and perhaps the function of other CD225 proteins.

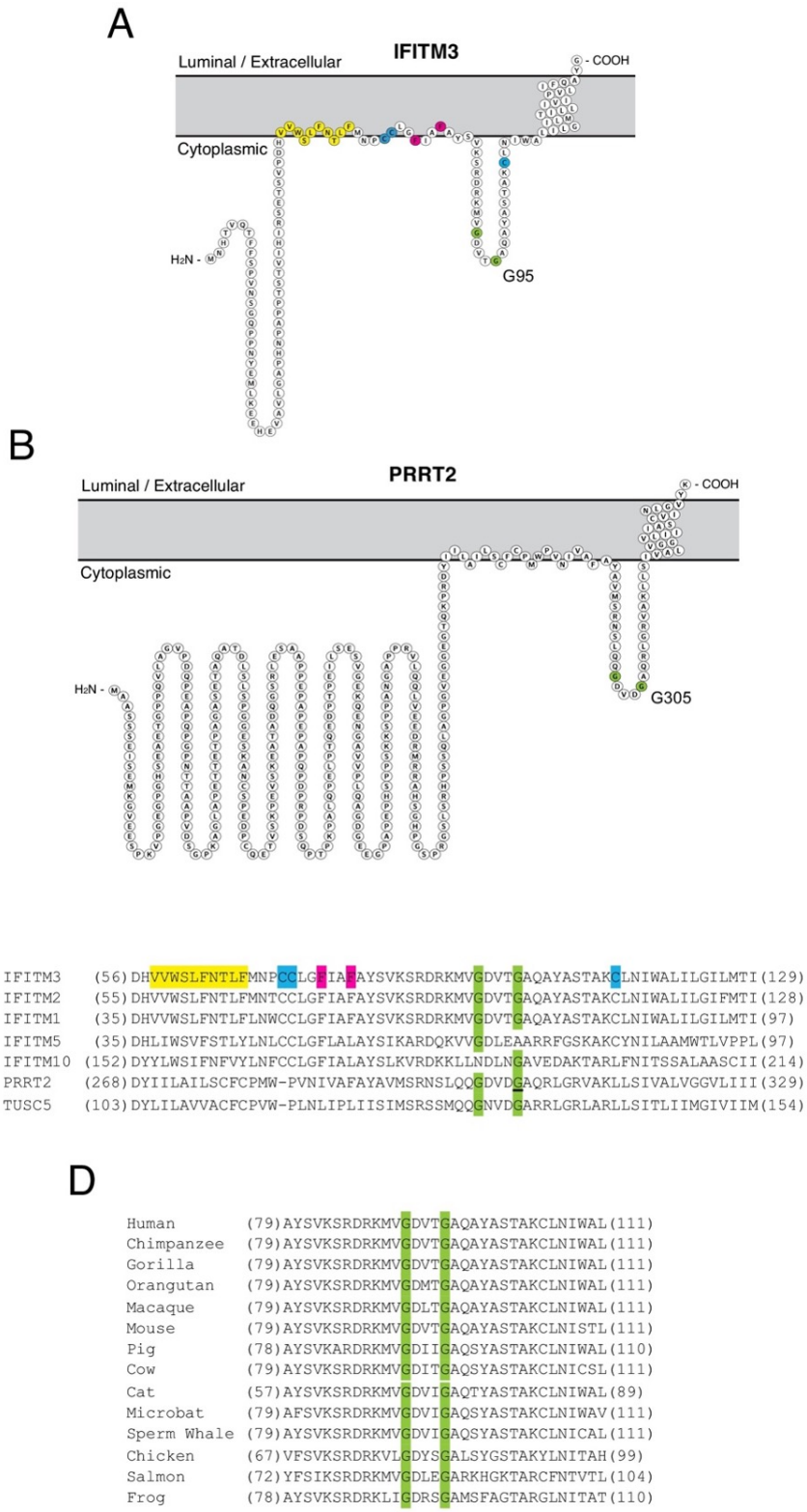

Figure 3.3.1. Homology-guided identification of a putative oligomerization motif within CD225 domains. (**A**) Illustrative schematic of the membrane topology of IFITM3 generated by Protter. (**B**) Illustrative schematic of the membrane topology of IFITM3 generated by Protter. Residues corresponding to the glycines of the GxxxG motif (green) are indicated. (**C**) A partial amino acid alignment of CD225 domains from IFITM proteins, PRRT2, and TUSC5 constructed with ClustalX. The position of the glycine in PRRT2 associated with neurological disease (i.e. G305W) is underlined. (**D**) A partial amino acid alignment of IFITM3 orthologs in vertebrates constructed with ClustalX. For **A-D**, palmitoylated cysteines are blue, phenylalanines associated with oligomerization are red, residues corresponding to the amphipathic helix are yellow, and the glycines contained within the GxxxG motif are in green.

3.3.2. ^{91}GxxxG^{95} is critical for IFITM3 antiviral function

We next created FLAG-tagged IFITM3 constructs in which glycine-91 and glycine-95 were mutated to leucine (i.e. G91L and G95L), following a report elucidating the role of GxxxG motif mediated oligomerisation of the human folate transporter [275]. In addition, owing to the previously reported identification of SNP rs779445843 which results in IFITM3 G95W/R [276,277] and its homologous loss-of-function, disease-associated SNP in PRRT2 (i.e. G305W) [109], we generated an IFITM3 G95W mutant. Furthermore, we produced HEK293T cell lines stably expressing FLAG-tagged wildtype (WT) or mutant IFITM3 constructs to assess their antiviral function.

Transient transfection of the IFITM3 mutants resulted in similar protein levels as wildtype, as determined by flow cytometry (Figure 3.3.2A-3.3.2B). However, analysis of these FLAG-tagged constructs by western blotting illustrated diminished expression for the G91L mutant (Figure 3.3.2C). In contrast, the stably transfected cells exhibited similar expression of WT or mutant IFITM3 constructs with the exception of IFITM3 G95W (Figure 3.3.4A-3.3.4B). These results suggest that mutations in IFITM3 glycine-91 or glycine-95 minimally affect steady-state protein expression in a transient expression system, and that mutation of glycine-91 may generate an IFITM3 mutant that is differentially soluble during lysis, resulting in apparent reduced expression by western blotting. Furthermore, these results may explain why previous investigations were unable to express IFITM3 mutants containing adjacent alanine mutations spanning residues 90 to 95 [104,256].

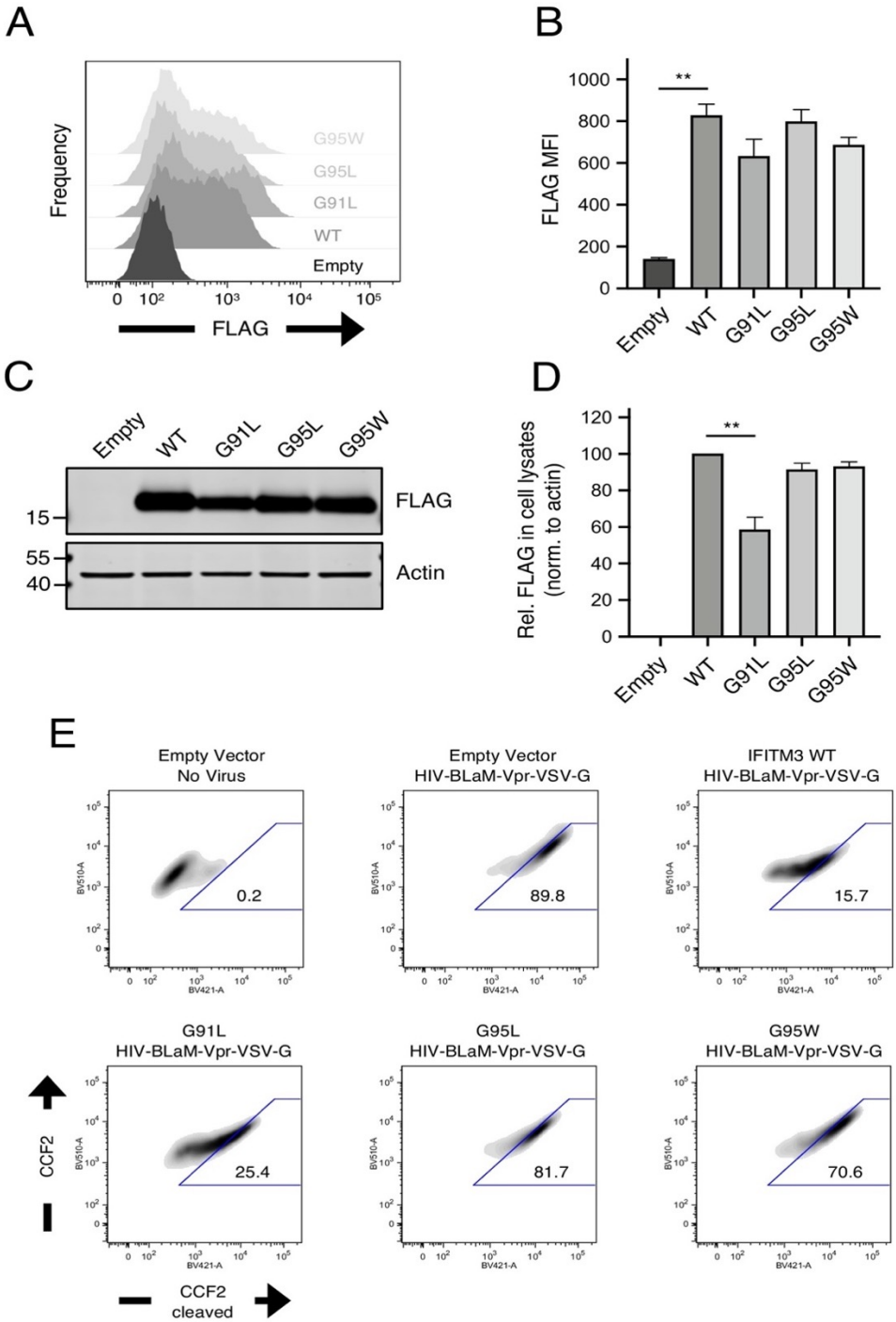

Figure 3.3.2. Quantitative measurement of IFITM3 construct expression following transient transfection and flow cytometric analysis of virus-cell fusion. (**A**) We transiently transfected HEK293T cells with 1.5 µg of the following constructs: empty pQCXIP, IFITM3 WT-FLAG, or the indicated mutants. 48 hours later, cells were fixed, permeabilized, and stained with anti-FLAG and construct expression was by flow cytometry. (**B**) Bar graph depicting mean fluorescence intensity (MFI) measurements of FLAG staining for conditions in (**A**) from three independent experiments. (**C**) Western blot of whole cell lysates produced from HEK293T transiently transfected with conditions in (**A**) and lysed 48 hours after transfection. Construct expression was detected with anti-FLAG and actin served as a loading control. (**D**) FLAG signal from western blots described in (C) were measured by capturing DyLight-conjugated secondary antibody fluorescence and was normalized actin signal in three independent experiments. FLAG signal was normalized to that of IFITM3 WT (set to 100). (**E**) Representative flow cytometry plots from a single experiment of data summarized in Figure 4.3.4E. Error bars in (**B**) and (**D**) indicate standard error. Statistical analysis was performed using one-way ANOVA. *, $p<0.05$; **, $p<0.001$. Rel., relative. Norm., normalized.

To determine if alteration of the GxxxG motif of IFITM3 disrupts its subcellular localisation, we used confocal immunofluorescence microscopy in both transient and stably expressing systems. In particular, we assessed the extent to which WT IFITM3 or its mutant constructs colocalises with the early and late endosomal markers EEA1-GFP or CD63, respectively, as previously described (Figure 3.3.3) [68,88,94]. In stably or transiently transfected 293T cells, the G91L, G95L, and G95W mutations did not lead to obvious mis-localisation from early endosomes or CD63+ late endosomes relative to WT IFITM3. Therefore, these results suggest that mutations in the GxxxG motif likely do not impact the subcellular localisation of IFITM3.

We then challenged HEK293T cell lines which stably expressed WT IFITM3 or mutants to assess antiviral function. Although IFITM3 WT strongly prevented IAV infection, the G95L and G95W mutations resulted in significant attenuation of virus restriction (Figure 3.3.4C and 3.3.4D). Notably, the G91L mutation did not result in a similar loss of antiviral activity against IAV (Figure 3.3.4C and 3.3.4D). Similarly, the G95L and G95W mutations also diminished the restriction of HIV-1 pseudotyped with VSV glycoprotein as assessed by virus-cell fusion via the β-lactamase assay (Figure 3.3.2E and Figure 3.3.4E). Collectively, these results illustrate that a homology-guided approach identified glycine-95 within IFITM3 as an essential residue for the restriction of virus entry and that glycine-91 plays a modest role in this activity. We did not pursue further characterisation of the G95W mutant IFITM3 construct further given the G95L and G95W mutations appeared functionally redundant.

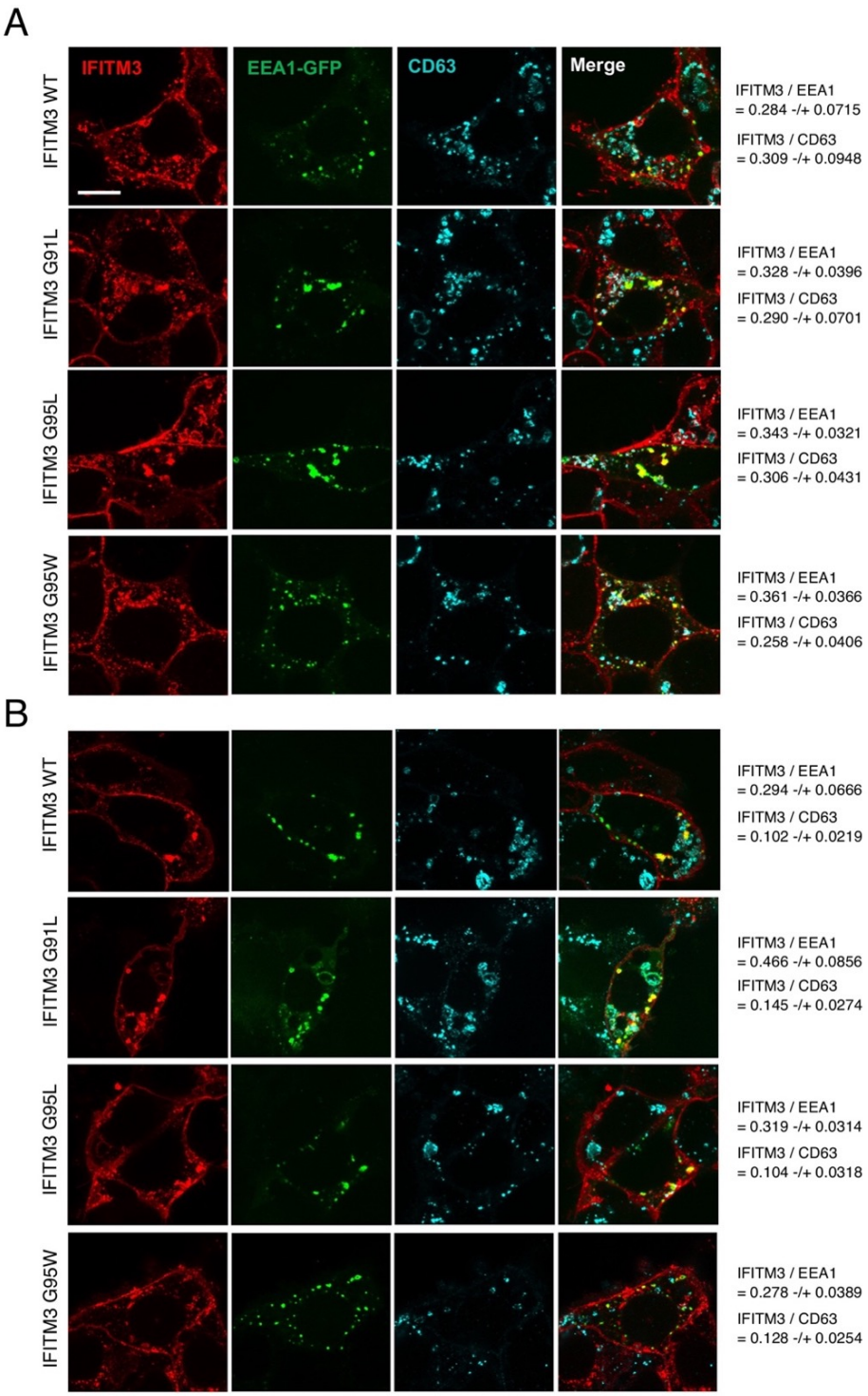

Figure 3.3.3. The subcellular localisation of IFITM3 WT and mutants determined by confocal immunofluorescence microscopy. (**A**) HEK293T cells stably expressing pQCXIP-IFITM3 WT-FLAG or the indicated mutant were transfected with 0.2 µg of EEA1-GFP. 48 hours post-transfection, these cells were fixed, permeabilized, and stained with anti-CD63 and anti-IFITM3. These cells were subsequently analyzed by immunofluorescence confocal microscopy. Scale bars, 10 µm. (**B**) HEK293T cells were transiently co-transfected with 0.2 µg of pQCXIP-IFITM3 WT-FLAG or the indicated mutant along with 0.2 µg of EEA1-GFP. 48 hours post-transfection, cells were fixed, permeabilized, and immunostained with anti-IFITM3 and anti-CD63. Subsequently, these cells were analyzed by immunofluorescence confocal microscopy. All images are representative of mean intensity averages (Z-stacks) from five consecutive medial sections. Scale bars, 10 µm. These Z-stacks were used to compute the colocalization between IFITM3 and EEA1-GFP and IFITM3 and CD63 via Imaris software. The mean Pearson's correlation coefficient values and standard deviations (noted the right of each condition) were calculated from at least 10 cells containing detectable EEA1-GFP signal.

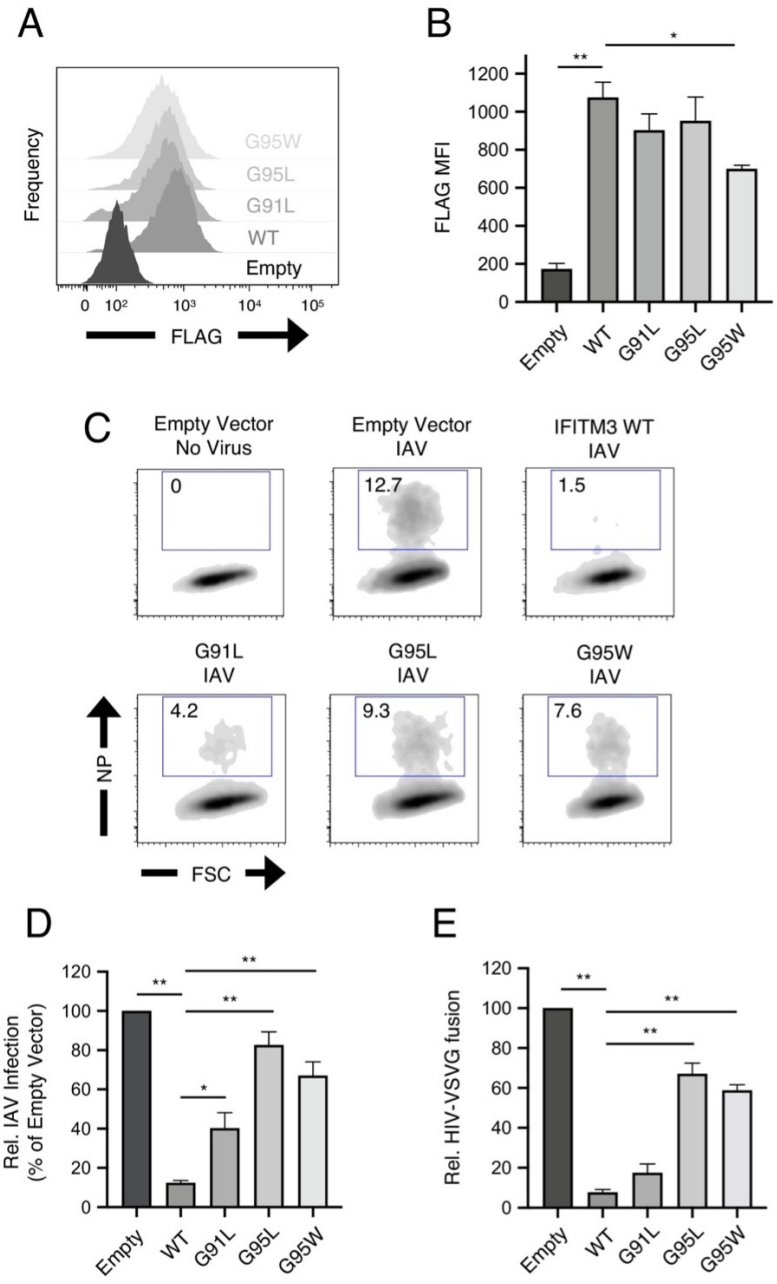

Figure 3.3.4. ^{91}GxxxG^{95} is crucial for IFITM3-mediated restriction of virus entry. A) HEK293T cells stably transfected with empty pQCXIP, IFITM3 WT-FLAG, or the indicated mutants were fixed, permeabilized, and stained with anti-FLAG antibody and assessed by flow cytometry to quantify FLAG expression levels (depicted as histograms). (**B**) Bar graph depicting the mean fluorescence intensity (MFI) of FLAG staining in (**A**) for three independent experiments. (**C**) HEK293T cells stably transfected with empty pQCXIP, IFITM3 WT-FLAG, or the indicated mutants were challenged with IAV PR8 strain (MOI of 0.1) and were subsequently fixed and permeabilized 18 hours post-infection. These cells were then stained with an anti-nucleoprotein antibody and assessed by flow cytometry. Representative results for each condition are pictured as dot plots. (**D**) Bar graph depicting infection results from 5–8 independent experiments as in (**C**) normalized to empty vector (set to 100%). (**E**) HEK293T cells stably transfected with empty pQCXIP, IFITM3 WT-FLAG, or the indicated mutants were challenged with replication-incompetent HIV-1 pseudotyped with VSV glycoprotein and incorporating BlaM-Vpr. 2.5 hours post-virus addition, virus-cell fusion was quantified using the beta lactamase assay via flow cytometry. A bar graph incorporating results from three independent experiments is pictured here, and the results are normalized to empty vector (set to 100%). Error bars indicate standard error. Statistical analysis was performed using one-way ANOVA. *, $p<0.05$; **, $p<0.001$. Rel., relative

3.3.3. ^{91}GxxxG^{95} is critical for the restriction of HIV-1 virion infectivity by IFITM3

Numerous investigations have reported that IFITM3 is critical in restricting virus entry in both naïve target cells as well as virus-producing cells. In particular, IFITM3 has been reported to incorporate into nascent virions and reduce viral glycoprotein abundance and function, thereby diminishing their fusogenic potential [74,95,97,102,278]. Accordingly, we determined whether mutation of glycine-91 or glycine-95 disrupted restriction of HIV-1 virion infectivity. Consistent with prior investigations, ectopic expression of WT IFITM3 in HIV-1 producing cells reduced HIV-1 infection of target TZM-bl cells (Figure 3.3.5A and Figure 3.3.5B). In contrast, mutation of glycine-91 or glycine-95 substantially decreased activity against HIV-1 infectivity of target cells (Figure 3.3.5A and Figure 3.3.5B). Additionally, WT IFITM3 decreased both the abundance of and incorporation of HIV-1 Env in cell lysates and nascent virions (Figure 3.3.5C and Figure 3.3.5D). Furthermore, WT IFITM3 expression diminished the processing of the HIV-1 Env gp160 precursor (as determined by gp120/gp160 ratio), in line with previous reports (Figure 3.3.5D) [96,98,102]. Strikingly, both IFITM3 G91L and IFITM3 G95L exhibited diminished activity against HIV-1 Env processing and incorporation (Figure 3.3.5C and 3.3.5D). This effect was recorded in triplicate immunoblotting experiments (Figure 3.3.5E-3.3.5G). Interestingly, both IFITM3 G9lL and G95L were incorporated into virions less efficiently than WT IFITM3 (Figure 3.3.4D), suggesting that the IFITM3 content in virions correlates with HIV-1 infectivity reduction. Importantly, as the G91L and G95L mutations resulted in differential HIV-1 restriction, it is likely other mechanisms are critical for restriction other than Env quantity. Together, these results indicate that both antiviral functions enacted by IFITM3 (i.e. early-stage and late-stage inhibition of virus entry and infection, respectively) are regulated by both the G91 and G95 residues.

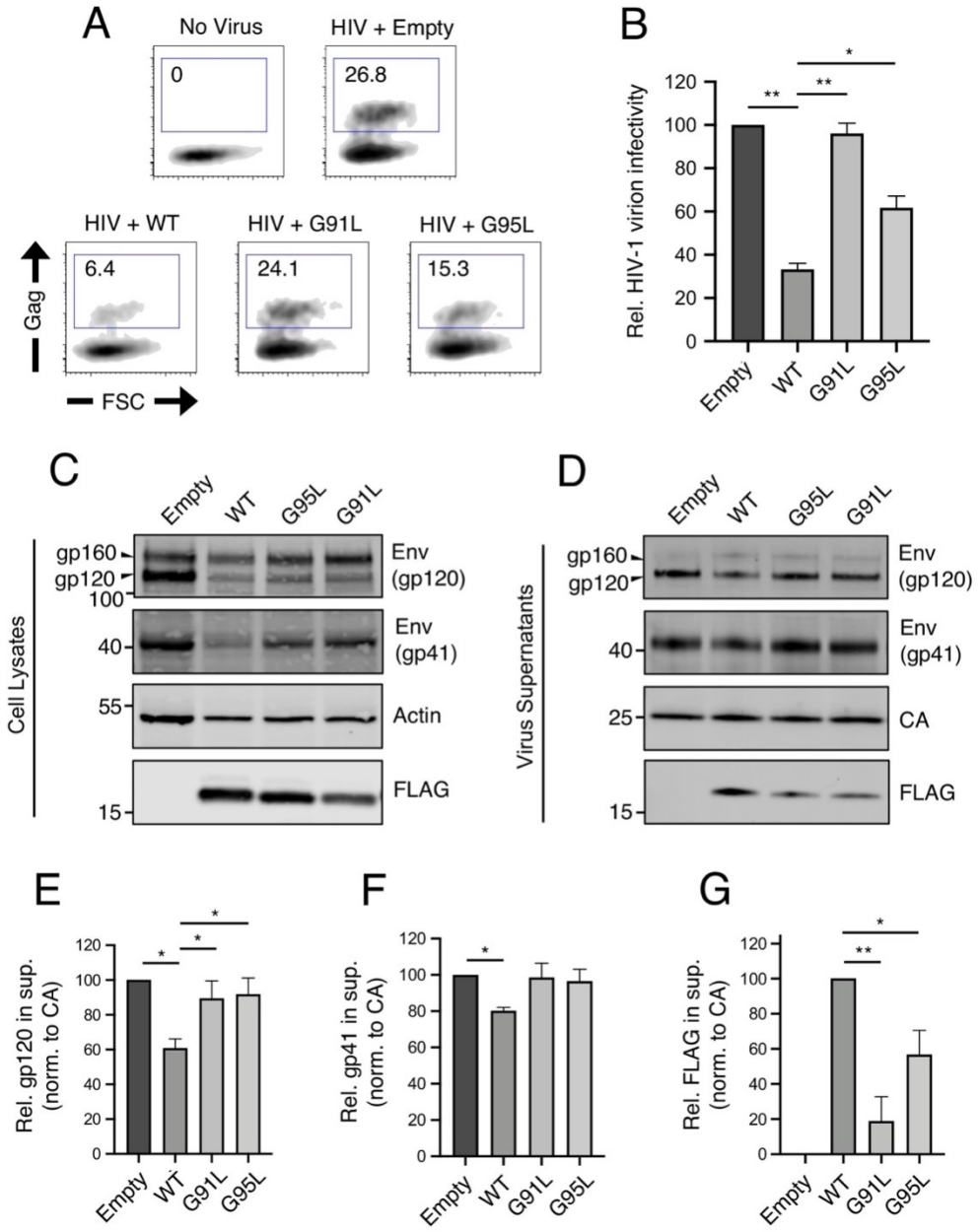

Figure 3.3.5. ^{91}GxxxG^{95} is important for restriction of HIV-1 virion infectivity by IFITM3. (**A**) HEK293T were co-transfected with HIV-1 molecular clone pNL4.3 and empty pQCXIP, IFITM3 WT-FLAG, or the indicated mutant. 48 hours post-transfection, the virus-containing supernatants were harvested and processed via ultracentrifugation over 20% sucrose pellets. Virion content was quantified by p24 CA ELISA. To measure virus infectivity, 50 ng p24 equivalent was added to TZM.bl cells. 48 hours post-infection, TZM-bl cells were fixed, permeabilized, stained with anti-CA antibody, and processed by flow cytometry to quantify infection. (**B**) Bar graphs depicting mean infection results of TZM.bl using virus derived from three independent experiments as in (**A**) and normalized to empty vector (set to 100%). (**C**) Whole cell lysates and (**D**) virus-containing supernatants were collected from HEK293T co-transfected as in (**A**). Whole cell lysates and virus-containing supernatants were collected at 48 hours post-transfection. Virus-containing supernatants were processed by ultracentrifugation through 20% sucrose cushions. Both lysates and 50 ng p24 equivalent of concentrated, purified virus-containing supernatants were subjected to SDS-PAGE and western blot analysis. Immunoblotting was performed with anti-gp120, anti-gp41, anti-CA, anti-actin, and anti-FLAG. (**E**) Bar graphs depicting virion-associated levels of gp120 Env in three independent experiments as determined by DyLight-conjugated secondary antibody fluorescence and were normalized to levels of CA. (**F**) Bar graphs depicting virion-associated levels of gp41 Env and (**G**) IFITM3-FLAG were quantified similarly. For anti-Env immunoblotting, the amount of gp120 or gp41 in virions was presented relative to empty vector (set to 100%). For anti-FLAG immunoblotting, the amount of IFITM3 WT in virions was set to 100%. Error bars indicate standard error. Statistical analysis was performed using one-way ANOVA. *, $p<0.05$; **, $p<0.001$. Rel., relative. Norm., normalized.

3.3.4. The ^{91}GxxxG^{95} motif within IFITM3 mediates homo-oligomerisation in living cells

Owing to the fact that glycine-95 is positioned within a conserved GxxxG motif, and that GxxxG motifs are thought to mediate homotypic protein-protein interactions, we utilised FRET microscopy to determine the role of glycine-91 and glycine-95 residues in mediating self-oligomerisation of IFITM3. To create FRET pairs, we created constructs expressing IFITM3 fused with yellow fluorescent protein (YFP) or mCherry at their N-terminus (Appendix Figure 5.1.2A). In this context, excitation of YFP (e.g. the FRET donor) results in energy transfer to mCherry (e.g. the FRET acceptor) if the FRET pair is in close proximity (i.e. interacting). Co-transfection of mCherry and IFITM3-YFP enabled the detection of background FRET signal. Interestingly, co-transfection of WT IFITM3-YFP and WT-IFITM3-mCherry resulted in high calculated FRET index values (Figure 3.3.6A and Figure 3.3.6B). In contrast, co-transfection of YFP- or mCherry-tagged IFITM3 containing either the G91L or G95L mutation produced FRET index values which were substantially reduced compared to WT, albeit to a lesser extent in G91L (Figure 3.3.6A and Figure 3.3.6B). These results indicate that residues glycine-95, and to a lesser extent glycine-91, are key determinants of IFITM3 oligomerisation. Additionally, co-transfection of heterologous pairs of tagged constructs (e.g. G95L-YFP and WT IFITM3-mCherry, and vice versa) resulted in intermediate levels of FRET, indicating intermediate levels of oligomerisation (Figure 3.3.6B).

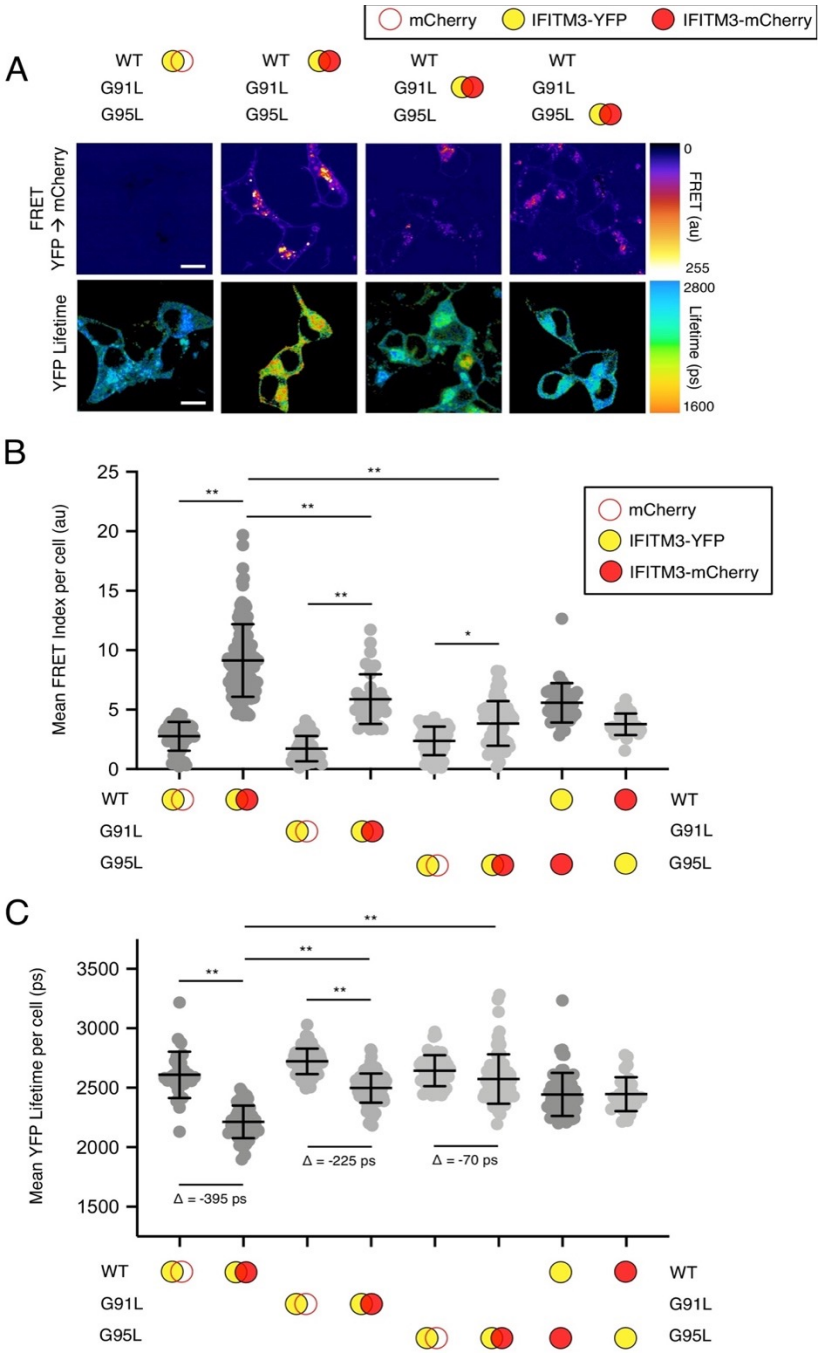

Figure 3.3.6. ^{91}GxxxG^{95} regulates oligomerisation of IFITM3 in living cells. (**A**) HEK293T were transiently co-transfected with IFITM3-YFP and mCherry or IFITM3-YFP and IFITM3-mCherry. Fluorescently tagged IFITM3 constructs encoded WT IFITM3 or the indicated mutant. FRET or FLIM images were created and representative images of FRET signal and YFP lifetimes of 12–20 captured images per condition are shown. (**B**) Scatter plot depicting whole-cell FRET measurements from a minimum of 50 cells per condition; the results of three independent experiments were pooled. Dots correspond to individual cells. (**C**) Scatter plot depicting whole-cell YFP donor lifetime measurements from a minimum of 50 cells per condition; the results of three independent experiments were pooled. Dots correspond to individual cells. A mean delta (Δ) value is provided to indicate the drop in donor YFP lifetime resulting from the pairing of IFITM3-YFP and mCherry versus the pairing of IFITM3-YFP and IFITM3-mCherry. Filled yellow circles are used to depict IFITM3-YFP (either WT, G91L, or G95L), filled red circles are used to depict IFITM3-mCherry (either WT, G91L, or G95L), and empty red circles are used to depict mCherry. Error bars indicate standard deviation. Statistical analysis was performed using one-way ANOVA. *, $p<0.05$; **, $p<0.001$. Scale bars, 10 μm. Ps, picoseconds. Au, arbitrary units.

Our FRET results were complemented by quantifying the fluorescence lifetimes of the FRET donor (YFP), which allows for measurements independent of fluorophore expression level or light-path [279]. In line with our FRET data, co-transfection of WT IFITM3-YFP and WT IFITM3-mCherry resulted in significant decreases in donor lifetimes, whereas co-transfection of either G95L-YFP and G95L-mCherry failed to do so (Figure 3.3.6C). Interestingly, co-transfection of G91L-YFP and G91L-mCherry resulted in significant reductions in donor lifetime, although not as marked as WT (Figure 3.3.6C). In line with our FRET data, co-transfection of heterologous pairs of tagged constructs resulted in modest decreases in donor lifetime, indicating intermediate levels of oligomerisation (Figure 3.3.6C). These results are consistent with the notion that the glycine-95 residue, and to a lesser extent glycine-91, is required for IFITM3-IFITM3 interactions.

To confirm that conclusions obtained from our FRET/FLIM approach are relevant to IFITM3-mediated restriction of virus infection, we determined if the fluorescently-tagged versions of IFITM3 above were capable of inhibiting IAV relative to previously examined FLAG-tagged constructs. The results show that both WT IFITM3-YFP and WT IFITM3-mCherry lost approximately 20% of their restriction activity against IAV (Figure 3.3.7A and Figure 3.3.7B). Importantly, similarly to Figure 3.3.4D, fluorescently-tagged G95L exhibited substantially diminished antiviral activity against IAV than their fluorescently-tagged WT counterparts (Figure 3.3.7A and Figure 3.3.7B).

Recently, Suddala et al. created an internally-positioned (i.e. after residue 40), fluorescently-tagged version of IFITM3 (Appendix Figure 5.1.2B) which maintained near-complete antiviral activity [84]. To confirm our results above, we produced additional IFITM3

constructs using this novel fluorescent-labelling strategy to label IFITM3 with YFP or mCherry. Using the same FRET and FLIM-based approach, we discovered that co-transfection of WT IFITM3-(i)YFP and WT IFITM3-(i)mCherry resulted in high calculated FRET index values, whereas co-transfection of IFITM3-(i)YFP and WT IFITM3-(i)mCherry containing the G95L mutation produced FRET index values which were substantially reduced (Figure 3.3.7C). Similarly, co-transfection of internally-tagged WT IFITM3-YFP and WT IFITM-mCherry resulted in significant decreases in donor lifetimes, whereas co-transfection of internally-tagged G95L-YFP and G95L-mCherry failed to reproduce this reduction in donor lifetime (Figure 3.3.7C). Interestingly, we discovered that this internal fluorophore-labelling approach for IFITM3 did not result in superior restriction activity against IAV infection when compared to the previously utilized IFITM3 tagged at the N-terminus with either YFP or mCherry. In fact, our results show that the internally-tagged IFITM3 constructs lost more than 40% of their restriction activity against IAV, compared to the 20% loss with the N-terminally tagged constructs (Figure 3.3.7A and 3.3.7B). Ultimately, these results are consistent with the notion that the glycine-95 residue is required for IFITM3-IFITM3 interactions regardless of position of the fluorophore at the N terminus or starting at the 40^{th} residue of IFITM3. However, placement of YFP or mCherry at the N-terminus of IFITM3 better preserves antiviral function.

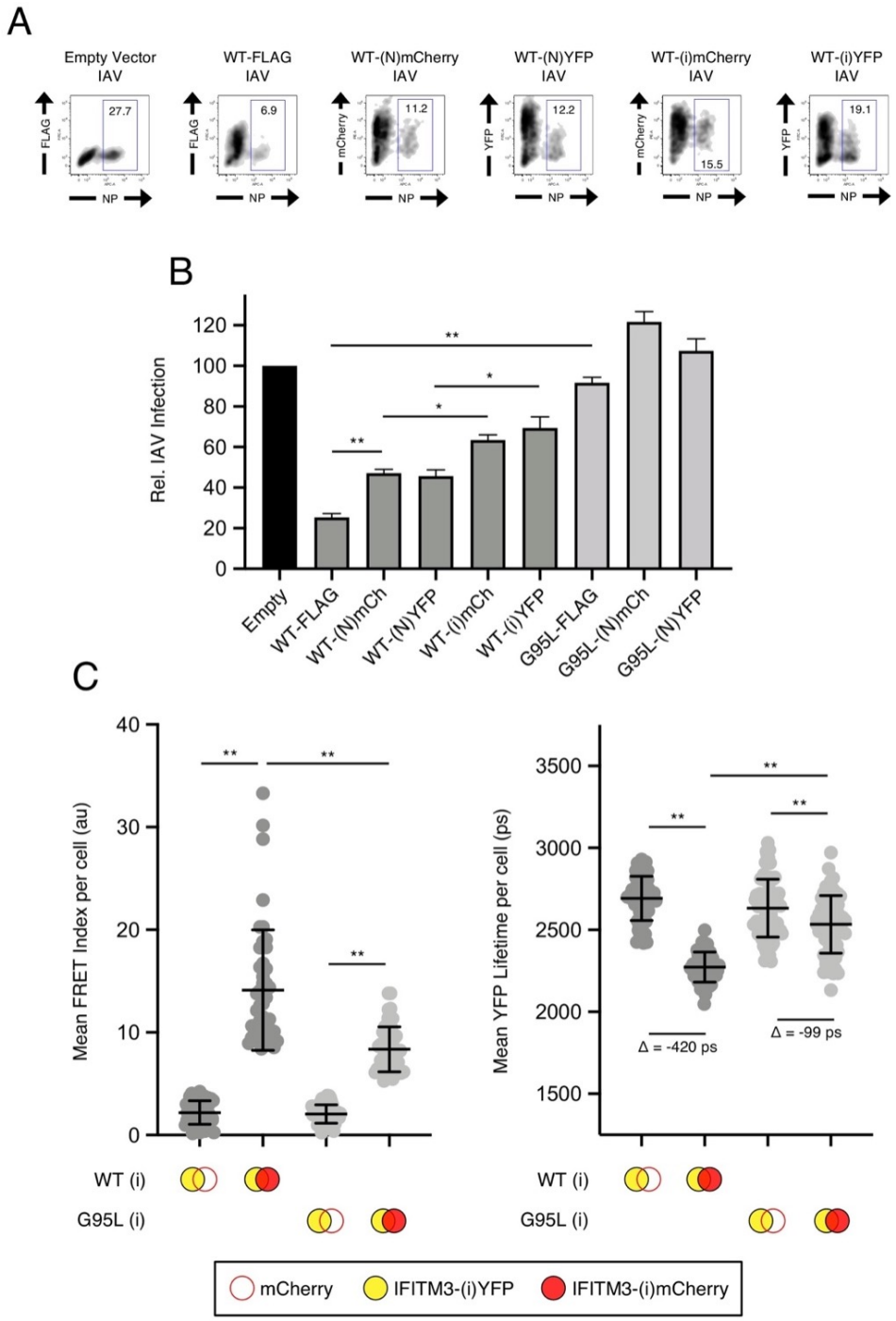

Figure 3.3.7. Assessing the functional impact of fluorescent protein position within IFITM3 fusion protein constructs. (**A**) HEK293T were transiently transfected with 1.5 µg of empty pQCXIP or pQCXIP encoding IFITM3-FLAG (N-terminal FLAG), IFITM3-(N)YFP (N-terminal YFP), IFITM3-(N)mCherry (N-terminal mCherry), IFITM3-(i)YFP (internal YFP), IFITM3-(i)mCherry (internal mCherry) or the indicated constructs encoding G95L. 48 hours post-transfection, cells were challenged with IAV PR8 strain (MOI of 0.2). 18 hours post-infection, were fixed permeabilized, and stained with anti-nucleoprotein antibody and infection was quantified via flow cytometry. (**B**) Bar charts depicting mean infection results from five independent experiments normalized to empty pQCXIP vector (set to 100%). Error bars indicate standard error. (**C**) HEK293T were transiently co-transfected with IFITM3-(i)YFP and mCherry or IFITM3-(i)YFP and IFITM3-(i)mCherry. Constructs encoded IFITM3 WT or IFITM3 G95L. Scatter plots depict whole-cell FRET (left) and whole-cell YFP lifetimes (right) which were collected from at least 50 cells per condition; the results of three independent experiments were pooled. Dots correspond to individual cells. A mean delta (Δ) value is provided to represent the drop in YFP lifetime resulting from the pairing of IFITM3-YFP and mCherry versus the pairing of IFITM3-YFP and IFITM3-mCherry. Filled yellow circles are used to depict IFITM3-YFP (either WT, G91L, or G95L), filled red circles are used to depict IFITM3-mCherry (either WT, G91L, or G95L), and empty red circles are used to depict mCherry. Error bars indicate standard deviation. Statistical analysis was performed using one-way ANOVA. *, $p<0.05$; **, $p<0.001$. Scale bars, 10 µm. Ps, picoseconds. Au, arbitrary units. Rel., relative.

Oligomerisation has been regarded as a key determinant of IFITM3 antiviral activity [91,104]. Previously investigations have purported that IFITM3 residues F75 and F78 are key determinants for IFITM3 oligomerisation [104]. However, a recent report employing a FRET-based analysis indicated that these residues are not involved in IFITM3-IFITM3 interactions [118]. To confirm that IFITM3 F75 and F78 do not play a role in IFITM3 oligomerisation, we utilised our FRET and lifetime imaging assay described above with N-terminally tagged IFITM3 with either YFP or mCherry containing the F75 and F78 mutations. Our results indicate that IFITM3 harbouring dual F75A and F78A mutations reported both FRET values and reductions in donor lifetimes similar to that of IFITM3 WT (Figure 3.3.8).

Additionally, an amphipathic helix proximal to the IM domain of IFITM3 has been shown to be critical for its antiviral function [56,101]. As amphipathic helices have been previously shown to modulate biophysical properties of membranes, we were curious to determine whether mutations in the amphipathic helix of IFITM3 would modulate its ability to form homotypic oligomeric interactions. Our results indicate that IFITM3 harbouring a triple mutation (i.e. S61A, N64A, T65A) reported both high FRET index values and reductions in donor lifetimes similar to that of WT IFITM3 (Figure 3.3.8). Therefore, these results indicate that IFITM3 proteins harbouring mutations in F75/F78 and the amphipathic helix are still able to create IFITM3-IFITM3 interactions, and that IFITM3-IFITM3 oligomerisation may be a separate, but necessary requirement for antiviral function in membranes.

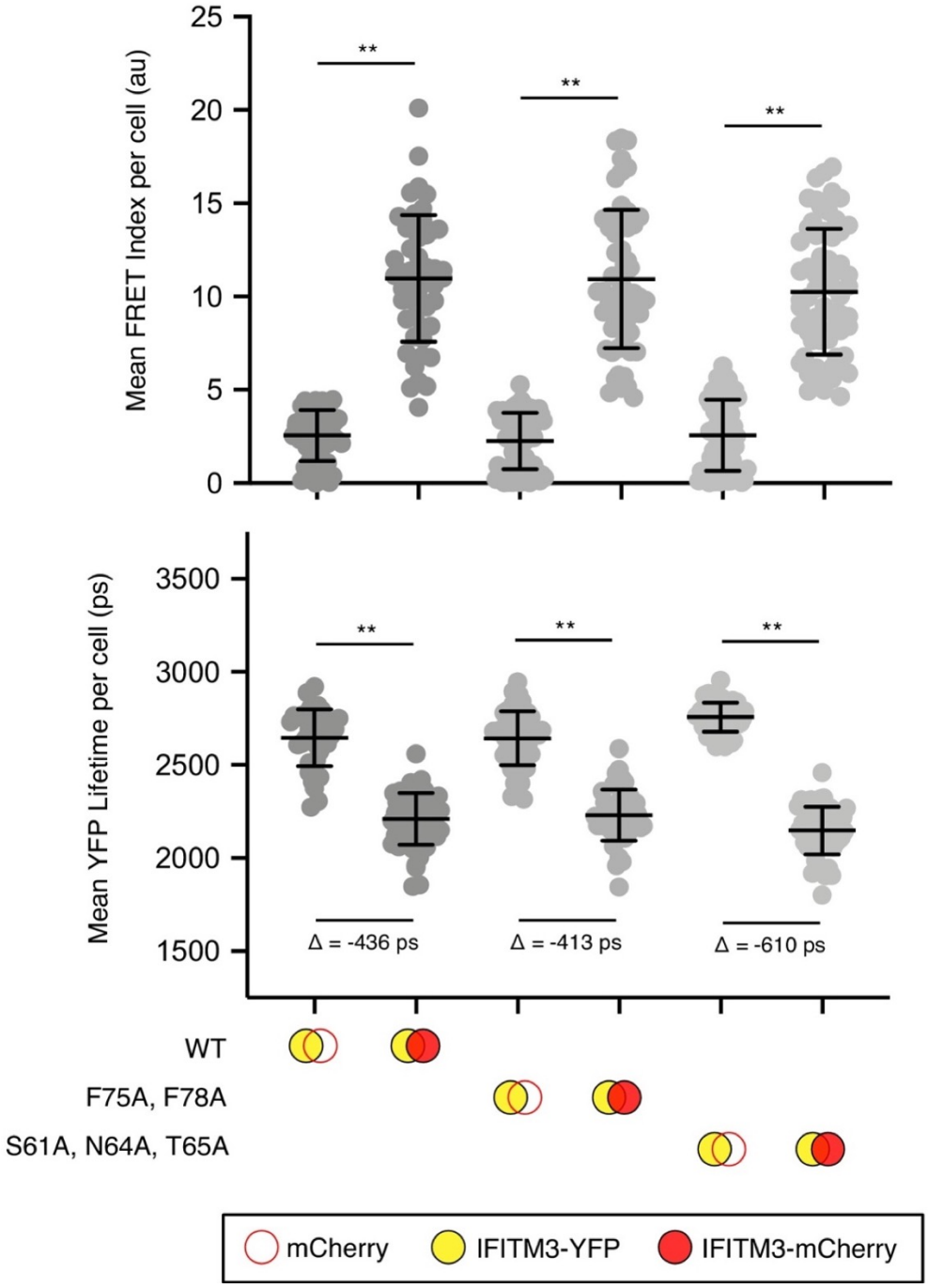

Figure 3.3.8. Assessment of amphipathic helix or phenylalanine IFITM3 mutations on oligomerization as measured by FRET-FLIM. HEK293T were transiently co-transfected with IFITM3-YFP and mCherry or IFITM3-YFP and IFITM3-mCherry (fluorescent proteins were positioned at the N-terminus). Constructs encoded either IFITM3 WT, IFITM3 F75A/F78A, or IFITM3 S61A/N64A/T65A. FRET and FLIM images were created and images were used to calculate (Top) whole-cell FRET index values or (bottom) whole-cell YFP lifetimes for a minimum of 50 cells per condition; the results of three independent experiments were pooled. Dots correspond to individual cells. A mean delta (Δ) value is provided to represent the drop in YFP lifetime resulting from the pairing of IFITM3-YFP and mCherry versus the pairing of IFITM3-YFP and IFITM3-mCherry. Filled yellow circles are used to depict IFITM3-YFP (either WT, G91L, or G95L), filled red circles are used to depict IFITM3-mCherry (either WT, G91L, or G95L), and empty red circles are used to depict mCherry. Error bars indicate standard deviation. Statistical analysis was performed using one-way ANOVA. *, $p<0.05$; **, $p<0.001$. Scale bars, 10 μm. Ps, picoseconds. Au, arbitrary units.

Several studies have indicated that IFITM3 performs its function by disrupting cholesterol homeostasis [87,255]. Additionally, a recent report has indicated the ability of IFITM3 to alter membrane curvature is dependent on the presence of cholesterol in artificial membranes [101]. Furthermore, Kuhnl and colleagues indicated that late endosome/lysosomal cholesterol loading inhibits IAV infection and this phenomenon is promoted by IFITM3 [255]. Collectively, these studies indicate that the ability of IFITM3 to restrict fusion between virus and host membranes may be dependent on the lipid environment, particularly the cholesterol content, in which this restriction factor resides. To determine if host cell cholesterol content is linked to the restrictive properties of IFITM3, we treated HEK293T cells stably overexpressing IFITM3 with increasing concentrations of MBCD, a cholesterol sequestering reagent, before addition of HIV-H1N1 pseudotyped virions. Modest amounts of MBCD treatment did not diminish reduction in infection of HIV particles pseudotyped with H1N1 compared with mock-treated cells (Figure 3.3.9B). However, treatment of IFITM3 stably expressing cells with high amounts of MBCD (i.e. 10mM) led to increases in infection (Figure 3.3.9B). Notably, cells treated with this concentration of MBCD were round and easily detached. To determine if host cell cholesterol depletion disrupts IFITM3 multimerization, we treated HEK293T cells transiently co-transfected with WT IFITM3-mCherry and WT IFITM3-YFP with increasing concentrations of MBCD prior measuring FRET and donor lifetimes by FLIM. As shown in Figure 3.3.9A, high values of FRET and low donor lifetimes were still recorded for cells treated with high concentrations of MBCD (i.e. 10mM). Therefore, host cell cholesterol content likely minimally affects the ability of IFITM3 to perform its antiviral function via oligomerisation.

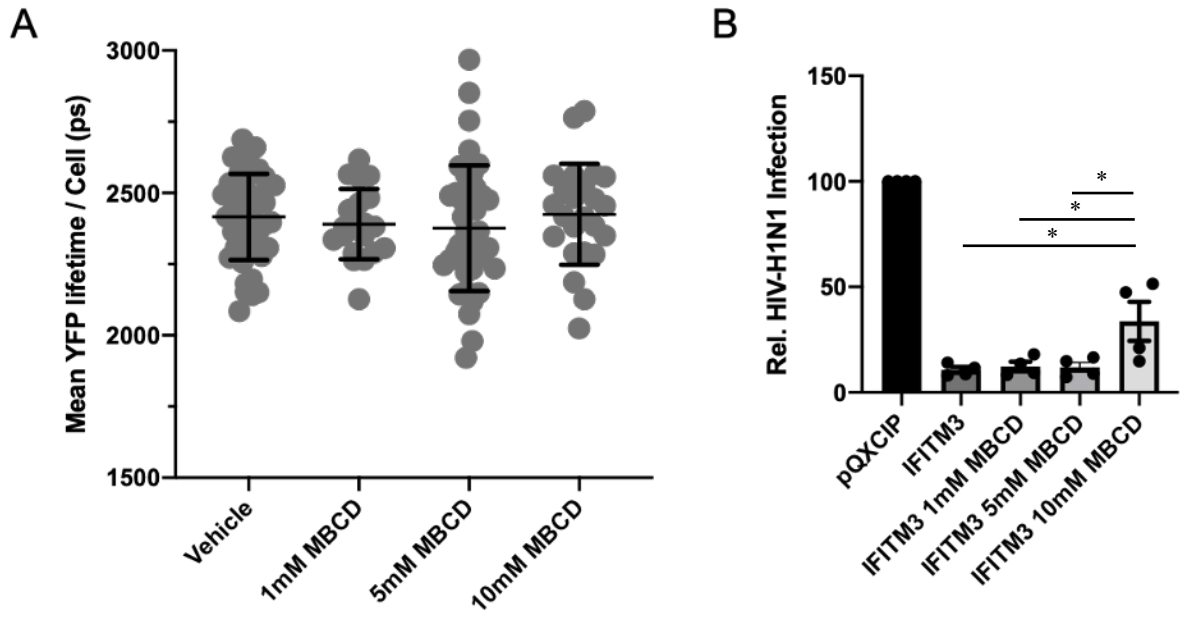

Figure 3.3.9. IFITM3 oligomerisation and restriction activity against influenza hemagglutinin is independent of host cell cholesterol content. HEK293T were transiently co-transfected with IFITM3-YFP and mCherry or IFITM3-YFP and IFITM3-mCherry (fluorescent proteins were tagged at the amino-terminus). 48 hours post-tranfection, cells were treated for one hour with the indicated concentration of methyl-beta-cyclodextrin prior to lifetime imaging (**A**) FLIM measurements were made and 8-12 images were used to extract whole-cell YFP lifetimes; the results of three independent experiments were pooled. Dots correspond to individual cells. Error bars represent standard deviation. (**B**) HEK293T cells stably transfected with empty pQCXIP or IFITM3 WT-FLAG were challenged with HIV pseudotyped with hemagglutinin (HA) from IAV WSN strain at a MOI of 1. In the condition indicated, increasing concentrations of methyl-beta-cyclodextrin cells were added to these cells for 1 hr prior to virus addition. Cells were fixed at 48 hr post-infection and infection was scored by GFP expression using flow cytometry. Error bars represent standard error.

3.3.5. Glycine-95 regulates oligomerisation of IFITM3 in denaturing and native conditions

Thus far, these data together for the first time suggest that glycine-91 and glycine-95 are key residues within IFITM3 that mediate self-oligomerisation. In order to resolve the relative stoichiometry of IFITM3 oligomers under these conditions, we performed Number and Brightness (N&B) analysis, a fluorescence fluctuation spectroscopy technique routinely utilised to measure the concentration of labelled proteins [144,149]. Analysis was restricted to cells transfected with IFITM3-mCherry and within pixels excluding mobile vesicular structures which would confound calculated brightness values. Interestingly, on average, we found that WT IFITM3-mCherry

produced brightness values more than two-fold greater than mCherry monomers (Figure 3.3.10E) [280]. Contrastingly, G95L-mCherry brightness was not appreciably different than mCherry monomers (Figure 3.3.10E). Additionally, although both WT IFITM3-mCherry and G95L-mCherry formed high-order assemblies that could be up to five-fold brighter relative to mCherry, G95L-mCherry was less-capable of forming these higher order oligomers relative to WT IFITM3-mCherry (Figure 3.3.10E). One important caveat to this analysis is that mCherry monomers are cytosolic and do not target membranes [281]. Nevertheless, these results indicate that fluorescently-tagged IFITM3 is not only primarily capable of forming dimers, but also higher-order oligomeric structures in the plasma membrane of live cells in a glycine-95 dependent fashion.

To corroborate our studies of IFITM3 oligomerisation in living cells, we additionally analysed the ability of IFITM3 pairs tagged with either FLAG or myc to co-immunoprecipitate from whole cell lysates when co-transfected in HEK293T cells. Cell lysates were prepared from HEK293T cells co-transfected with IFITM3-FLAG and IFITM3-myc, followed by FLAG immunoprecipitation and SDS-PAGE (Figure 3.3.10A and Figure 3.3.10B). Interestingly, these results revealed that G95L-myc pulled down with G95L-FLAG approximately 50% less-efficiently than WT IFITM3-myc and WT IFITM3-FLAG pairs (Figure 3.3.10A and Figure 3.3.10B). Furthermore, immunoblot of heterologous pairs (i.e. WT IFITM-myc and G95L-FLAG) revealed an intermediate level of co-immunoprecipitation relative to solely WT constructs (Figure 3.3.11A and Figure 3.3.11B). Therefore, membrane-extracted IFITM3 is capable of efficiently forming oligomers in a glycine-95 dependent manner. Importantly, mutation of the glycine-95 residue reduces the ability of IFITM3 to oligomerise. As our co-immunoprecipitation studies required denaturation of proteins within cell lysates, we complemented these results by performing

blue native PAGE and immunoblotting to analyse the oligomeric state of IFITM3 under non-denaturing conditions. Interestingly, this approach revealed two populations of IFITM3 oligomers, exhibiting sizes of approximately 300 and 480 kilodaltons, yet these oligomers were observed to a substantially lesser extent for IFITM3 G95L (Figure 3.3.10C and Figure 3.3.10D). We did not observe dimers that we quantified in the N&B analysis previously described, above which may be attributable to the conditions in which the blue native PAGE was performed. The uncropped native PAGE image is shown in Figure 3.3.11C. Nevertheless, the reduced ability of IFITM3 G95L to form higher-order oligomers here is consistent with our FRET, FLIM, N&B and co-immunoprecipitation studies. Therefore, our results indicate that glycine-95 is vital for efficient IFITM3 oligomerisation and that oligomerisation is necessary for its antiviral function.

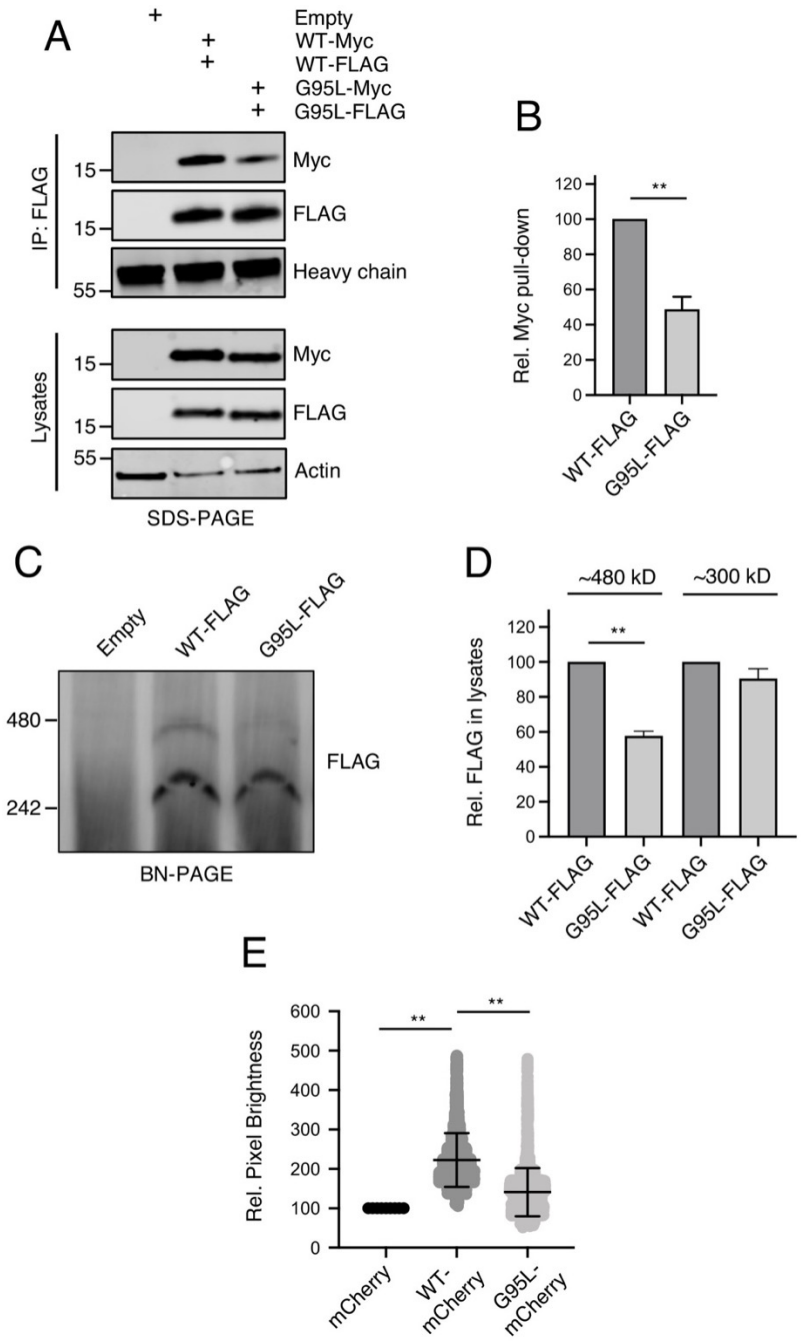

Figure 3.3.10. Glycine-95 regulates oligomerisation of IFITM3 in denaturing and non-denaturing conditions. (**A**) HEK293T were transiently transfected with a total of 1.5 µg of empty pQCXIP or the following pairs: IFITM3 WT-FLAG and IFITM3 WT-myc or G95L-FLAG and G95L-myc. Whole cell lysates were generated with mildly denaturing conditions and immunoprecipitation (IP) using anti-FLAG beads was performed for three hours at 4C with rotation. Both IP fractions and whole cell lysates were analyzed by SDS-PAGE and Western blot analysis. Immunoblotting was performed with anti-FLAG and anti-myc. Heavy chain IgG served as the loading control in the IP fraction and actin served as the loading control in the lysates fraction. Number and tick marks indicate size (kilodaltons) and position of protein standards in ladder. (**B**) Bar graph depicting the levels of IFITM3-myc (either WT or G95L) co-immunoprecipitated by anti-FLAG IP as in (**A**) from three independent experiments. Error bars indicate standard error. (**C**) HEK293T were transiently transfected with a total of 1.5 µg of empty pQCXIP, IFITM3 WT-FLAG or G95L-FLAG. Cell lysates were produced with 1% digitonin. Subsequently, blue native PAGE and immunoblotting with anti-FLAG was performed. Number and tick marks indicate size (kilodaltons) and position of protein standards in ladder. (**D**) Bar graph depicting the levels of IFITM3-FLAG (either WT or G95L) located at approximately 480 kd and 300 kD quantified in (**C**) from three independent experiments. Error bars indicate standard error. (**E**) Number and Brightness analysis was performed on monomeric mCherry and IFITM3-mCherry (either WT or G95L) as described in the materials and methods. Statistical analysis was performed using student's T test. *, $p<0.05$; **, $p<0.001$. Rel., relative.

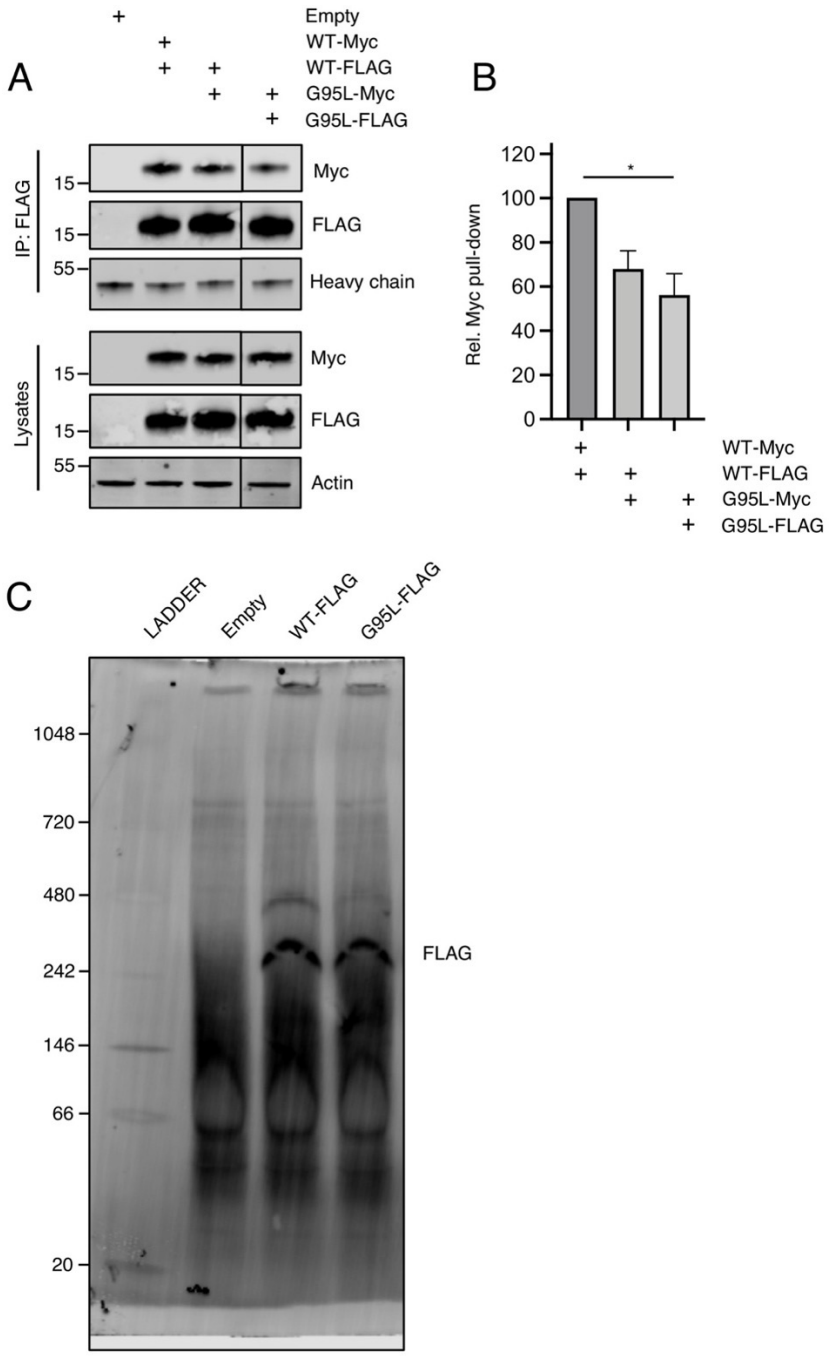

Figure 3.3.11. Blue native PAGE of IFITM3 and assessment of heteromultimerization between IFITM3 WT-FLAG and G95L-myc. (**A**) HEK293T were transiently transfected with a total of 1.5 µg of empty pQCXIP or the following pairs: IFITM3 WT-FLAG and IFITM3 WT-myc, IFITM3 WT-FLAG and G95L-myc, or G95L-FLAG and G95L-myc. Whole cell lysates were generated with mildly denaturing conditions and immunoprecipitation (IP) using anti-FLAG beads was performed for three hours at 4C with rotation. Both IP fractions and whole cell lysates were analyzed by SDS-PAGE and Western blot analysis. Immunoblotting was performed with anti-FLAG and anti-myc. Heavy chain IgG served as the loading control in the IP fraction and actin served as the loading control in the lysates fraction. Number and tick marks indicate size (kilodaltons) and position of protein standards in ladder. (**B**) Bar graphs depicting the levels of IFITM3-myc (either WT or G95L) co-immunoprecipitated by anti-FLAG IP from three independent experiments. Error bars indicate standard error. Statistical analysis was performed using one-way ANOVA. *, $p<0.05$; **, $p<0.001$. (**C**) A full scan of the membrane depicted in Figure 4.3.10C is shown. Immunoblotting was performed with anti-FLAG. Number and tick marks indicate size (kilodaltons) and position of protein standards in ladder. Rel., relative.

3.3.6. IFITM3 oligomerisation increases membrane order which is a correlate of antiviral function

Previous investigations have indicated that overexpression of IFITM3 increases membrane order in host cells, such that the fluidity of membranes where virus entry occurs is reduced [51,103,104]. However, studies which have correlated IFITM3's antiviral activity with its ability to rigidify membranes have not been conducted. As we have identified a loss-of-function IFITM3 mutant (G95L) devoid of antiviral activity and a reduced ability to oligomerise, we also utilised this mutant to assess whether restriction by IFITM3 is functionally associated with its ability to decrease membrane fluidity. Here, we took advantage of two fluorescent probes—fluorescent lipid tension reporter (FliptR) and Laurdan—in order to assess membrane order in cells either transiently expressing or stably expressing IFITM3 or its mutant version G95L. Previous reports documenting IFITM family members' ability to enhance membrane rigidity have utilised Laurdan, a hydrophobic fluorescent probe that is exquisitely sensitive to lipid phases. To confirm our results using an analysis that is independent of fluorescence intensity, we additionally stained these cells in parallel experiments with FliptR, a planarizable push-pull probe which efficiently incorporates into living cell membranes [240]. The fluorescence lifetime of FliptR is sensitive to local changes in lipid packing (i.e. membrane order), such that increases in membrane order in both plasma membranes reports longer FliptR fluorescence lifetimes as detected by FLIM [240,242].

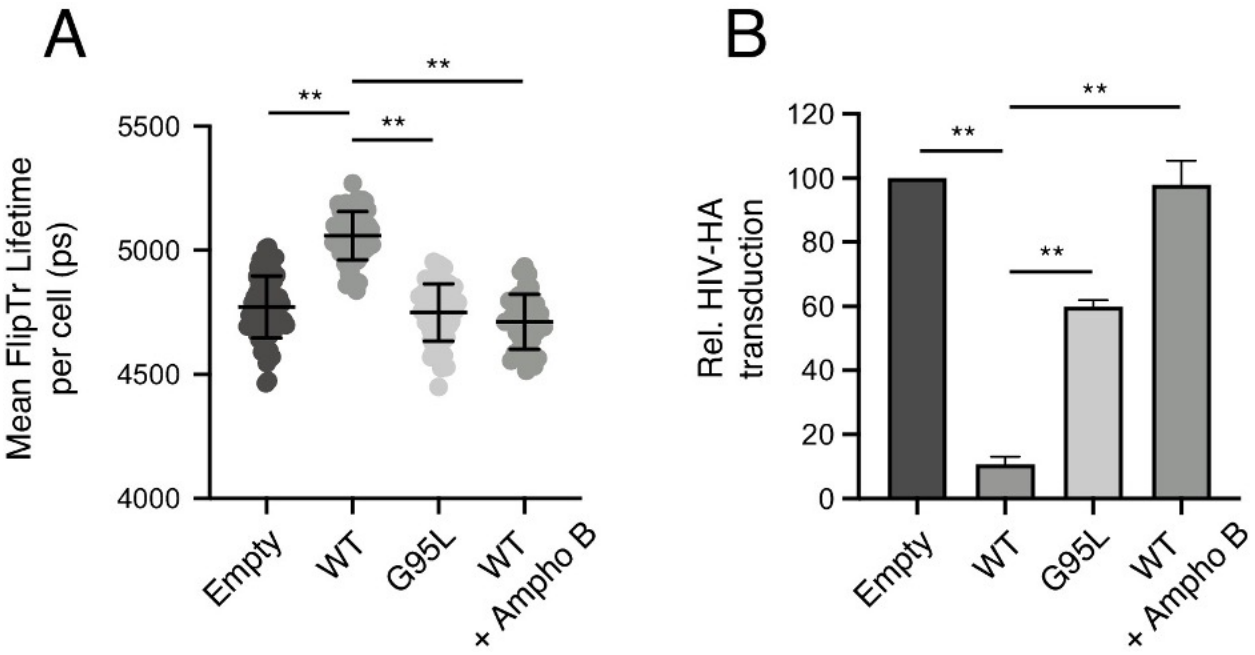

Figure 3.3.12. IFITM3 oligomers increase membrane order in an Ampho B-sensitive manner. (**A**) HEK293T cells stably transfected with empty pQCXIP, IFITM3 WT-FLAG, or G95L-FLAG were stained with 1 μM FliptR for 15 min and imaged by FLIM. In conditions treated with Amphotericin B, 1 μM Amphotericin B was added to cells for 1 hr and washed away prior to staining with FliptR and imaging. The whole-cell mean fluorescence lifetime components from a two-exponential decay fit (τ) was calculated using Symphotime for a minimum of 40 cells per condition and the long lifetime component (τ_1) from three independent experiments are shown here. Dots correspond to individual cells. Error bars indicate standard deviation. (**B**) HEK293T cells stably transfected with empty pQCXIP, IFITM3 WT-FLAG, or G95L-FLAG were challenged with HIV pseudovirions harboring the hemagglutinin (HA) from IAV WSN strain (MOI of 1). In conditions treated with Amphotericin B, 1 μM Amphotericin B was added to cells for 1 hr prior to virus addition. Cells were fixed at 48 hr post-infection, and infection was scored by GFP expression using flow cytometry. Statistical analysis was performed using one-way ANOVA. *, $p<0.05$; **, $p<0.001$. Ps, picoseconds. Rel., relative.

Leveraging this imaging platform, we discovered that FliptR-stained HEK293T cells stably expressing WT FLAG-IFITM3 reported significantly increased fluorescence lifetimes (Figure 3.3.12A). These results indicate that WT IFITM3 expression substantially increases membrane rigidity, consistent with previous reports [51]. In fact, the IFITM3-induced enhancement of membrane rigidity as recorded by FliptR was remarkably similar to those of cells treated with excess soluble cholesterol (Figure 3.3.13A and Figure 3.3.13B). Treatment of HEK293T cells with cholesterol-depleting methyl-beta-cyclodextrin resulted in significant decreases in membrane order, as expected (Figure 3.3.13A and Figure 3.3.13B). Strikingly, FliptR-stained HEK293T cells stably expressing FLAG-IFITM3 G95L did not demonstrate an increase in membrane order

(Figure 3.3.12A). These data suggest that increases in membrane order are achieved by WT IFITM3, but not with its mutant G95L form, and may be linked to IFITM3's ability to oligomerise.

To validate our results, we calculated general polarizability values of live, Laurdan-stained HEK293T cells stably expressing WT IFITM3 or IFITM3 G95L. As previously reported, cells expressing WT IFITM3 demonstrated increases in general polarizability values relative to cells stably expressing an empty vector (Figure 3.3.13C and Figure 3.3.13D). Similar to measurements obtained with FliptR-stained cells, Laurdan-stained cells stably expressing WT FLAG-IFITM3 reported general polarizability values similar to that of cells treated with soluble cholesterol. In contrast, cells overexpressing IFITM3 G95L were unable to reproduce similar increases in general polarizability. Collectively, these results suggest that functional IFITM3 increases the rigidity of membranes and that IFITM3's antiviral role may correlate with this phenotype.

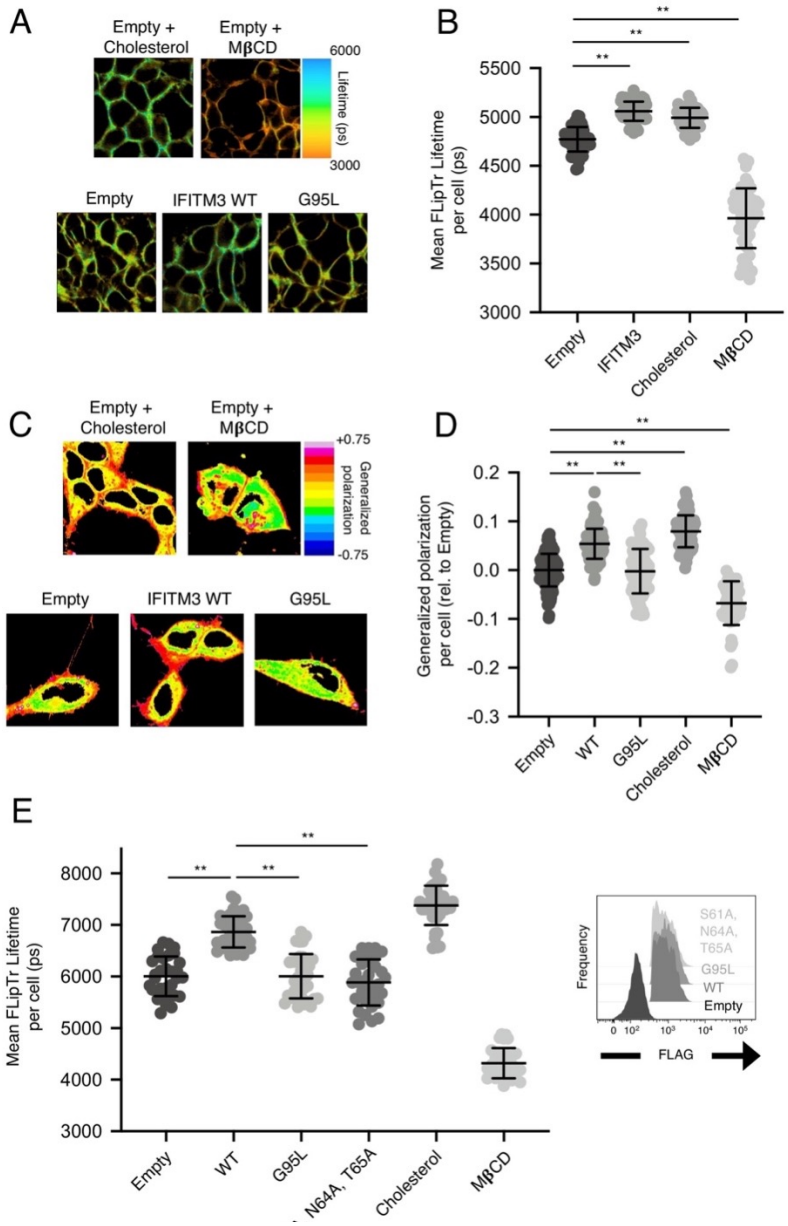

Figure 3.3.13. Assessment of cholesterol addition and cholesterol depletion on membrane order by FliptR and Laurdan. (**A**) Representative fluorescent lifetime images of FliptR-stained cells from conditions plotted in Figure 4.3.12. In addition, soluble cholesterol (100 µg/mL) or methyl-beta-cyclo-dextrin (5 mM) were added to untransfected HEK293T cells for 1 hr and washed away prior to addition FliptR staining and FLIM imaging as described in Figure 4.3.12A. (**B**) HEK293T cells stably transfected with empty pQCXIP or IFITM3 WT-FLAG were compared to cholesterol-treated and MBCD-treated cells. The long lifetime component (τ_l) extracted from FliptR-stained cells was recorded for a minimum of 40 cells per condition and the results three independent experiments are shown as scatter plots. Dots correspond to individual cells. Error bars indicate standard deviation. (**C**) HEK293T cells stably transfected with empty pQCXIP, IFITM3 WT-FLAG, or G95L-FLAG were incubated with 1.8 µM Laurdan for 1 hr, rinsed with PBS, and imaged. Where indicated, soluble cholesterol (100 µg/mL) or methyl-beta-cyclo-dextrin (5 mM) were added to untransfected HEK293T cells for 1 hr and washed away prior to addition of Laurdan. Representative images depicting generalized polarization values are shown. (**D**) Scatter plot depicting whole-cell generalized polarization values calculated for at least 40 cells per condition from three independent experiments. Dots correspond to individual cells. Error bars indicate standard deviation. (**E**) (Left) HEK293T were transiently transfected with 1.5 µg of either empty pQCXIP, IFITM3 WT-FLAG, G95L-FLAG, or S61A/N64A/T65A-FLAG and stained with FliptR and imaged as described in Figure 4.3.12A. In the conditions indicated, soluble cholesterol (100 µg/mL) or methyl-beta-cyclo-dextrin (5 mM) were added to untransfected HEK293T cells for 1 hr and washed away prior to addition of FliptR. The long lifetime component (τ_l) extracted from FliptR-stained cells was recorded for a minimum of 40 cells per condition and the results three independent experiments are shown a scatter plots. Dots correspond to individual cells. Error bars indicate standard deviation. (Right) Representative flow cytometry histograms indicate the expression of IFITM3 WT-FLAG, G95L-FLAG, or S61A/N64A/T65A-FLAG following transient transfection and immunostaining with anti-FLAG. Statistical analysis was performed using one-way ANOVA. *, $p<0.05$; **, $p<0.001$. Ps, picoseconds. Rel., relative.

To further characterise the functional importance of membrane order in IFITM3's ability to restrict virus fusion, we quantified membrane order in FliptR-stained cells in the presence of Amphotericin B (Ampho B). Ampho B is an antimycotic polyene which has been previously shown to counteract the antiviral activity of IFITM3 [103]. Nevertheless, how Ampho B counteracts this cell-intrinsic barrier in cells was not known. Strikingly, FliptR-stained HEK293T cells stably expressing WT IFITM3 which were treated with Ampho B were unable to reproduce increased membrane rigidity (Figure 3.3.12A). Moreover, in parallel experiments, we showed that these Ampho B-treated, WT IFITM3 stably expressing were unable to restrict HA-mediated virus entry (Figure 3.3.12B). Together, these data indicate for the first time that Ampho B negates the antiviral mechanism of IFITM3 by enhancing membrane fluidity. Consequently, these data collectively suggest that IFITM3-mediated virus restriction is mediated by oligomerisation-dependent enhancement of local membrane rigidity.

Finally, we endeavoured to assess the impact of mutations disrupting the amphipathic helix of IFITM3 on its ability to rigidify host cell membranes using FliptR. Previous reports have indicated that IFITM3 requires an intact amphipathic helix to perform its antiviral function. Furthermore, amphipathic helices have been shown to bind and modulate key biophysical properties of membranes, such as membrane order and curvature. Additionally, the amphipathic helix of IFITM3 was recently reported to be necessary and sufficient to increase membrane order in artificial membranes composed of phosphatidylethanolamine and cholesterol [101]. Our results indicate that cells stably expressing IFITM3 containing the triple mutation S61A, N63A, T64A were also unable to rigidify membranes to a similar extent as IFITM3 G95L (Figure 3.3.13E).

These results highlight that IFITM3 requires both the amphipathic helix and its ability to form oligomers to increase membrane rigidity.

3.3.7. Disease-associated G305W impairs oligomerisation of PRRT2

Previous reports have shown that mutations within the GxxxG motif in PRRT2 (i.e. glycine-305) significantly correlates with neurological disease in humans [109]. As we discovered the GxxxG motif is shared between CD225 family members IFITM3 and PRRT2, we additionally evaluated the ability of WT and mutant PRRT2 to oligomerise by leveraging the FRET and FLIM platform described previously. As before, we generated PRRT2 constructs fused with either YFP or mCherry to create FRET pairs. Co-transfection of WT PRRT2-YFP and PRRT2-mCherry in HEK293T cells resulted substantial increases in FRET (Figure 3.3.14A). In contrast, FRET indices were not appreciably enhanced when HEK293T cells were co-transfected with G305W-YFP and G305W-mCherry. Furthermore, HEK293T cells co-transfected with G305W-YFP and G305W-mCherry did not demonstrate significant losses in YFP lifetimes relative to their WT counterparts (Figure 3.3.14B). Collectively, these data indicate that glycine-305 in PRRT2 is important for PRRT2 oligomerisation. Therefore, despite divergent functions played by these CD225 proteins, homologues IFITM3 and PRRT2 regulate diverse fusion processes via a common determinant for oligomerisation, a GxxxG motif.

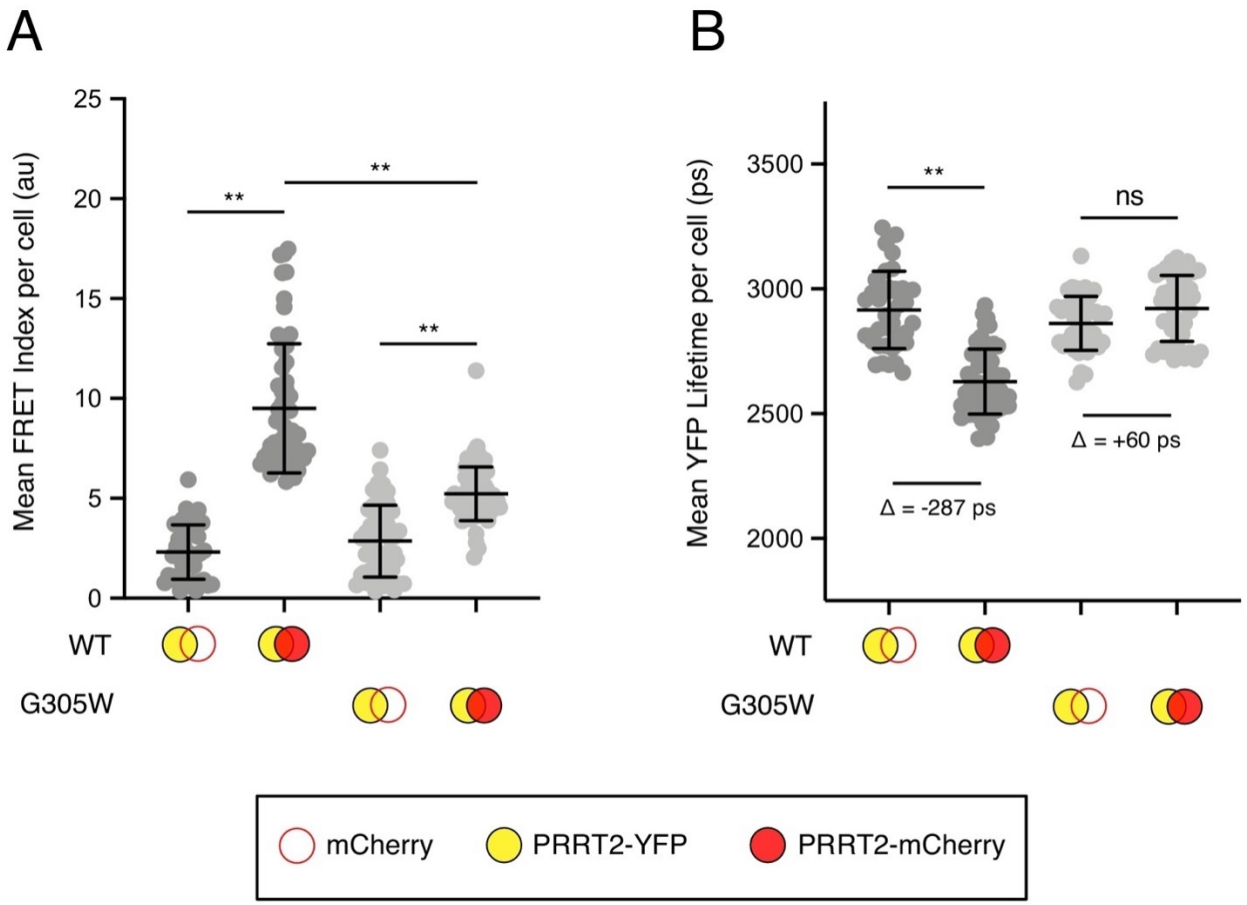

Figure 3.3.14. Disease-associated G305W disrupts the oligomerization of PRRT2 in living cells. (**A**) HEK293T were transiently co-transfected with either PRRT2-YFP and mCherry or PRRT2-YFP and PRRT2-mCherry. Constructs encoding PRRT2 were either WT or contained the G305W mutation. Whole-cell FRET index values (**A)** or YFP donor lifetimes (**B**) were extracted from at least 50 cells per condition and the results of three independent experiments were pooled. Dots correspond to individual cells. In (**B**) mean delta (Δ) values are provided to indicate the drop in YFP lifetime resulting from the pairing of PRRT2-YFP and mCherry versus the pairing of PRRT2-YFP and PRRT2-mCherry. Filled red circles are used to depict PRRT2-mCherry (either WT or G305W), filled yellow circles are used to depict PRRT2-YFP (either WT or G305W), and empty red circles are used to depict mCherry. Error bars indicate standard deviation. Statistical analysis was performed using one-way ANOVA. *, $p<0.05$; **, $p<0.001$. Au, arbitrary units. Ps, picoseconds.

3.4. Discussion

Although investigations continually broaden the range of virus infections controlled by IFITM3 *in vitro* and *in vivo* [282,283], its mechanism of restriction is incompletely understood. Several investigations have indicated IFITM3 may remodel membranes by altering membrane order and/or curvature. However, functional proof of this restriction model was lacking. Two recent reports have provided significant insight in elucidating the mechanism of IFITM3. The first indicated that IFITM3 utilises its amphipathic helix within its intramembrane domain to restrict virus fusion [56]. This result supports the notion that IFITM3 may bend or stiffen membranes in which it resides. The second illustrated that inbound, IFITM3-sensitive virions are intercepted in IFITM3-containing vesicles, whereas IFITM3-insensitive viruses evade this encounter [82,84]. Together, these results suggest a proximity-based model of restriction by local modifying membrane biophysical properties via IFITM3's amphipathic helix to prevent virus fusion pore formation (Figure 3.3.15). Notably, this model may also underpin the antiviral effect of IFITM3-laden virions [73,74,97,102].

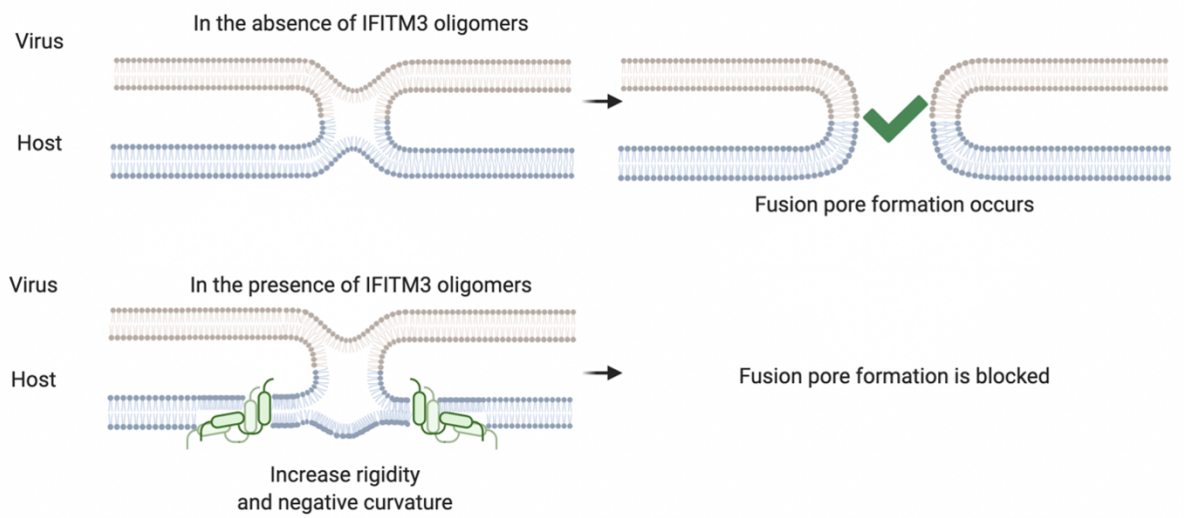

Figure 3.3.15. Oligomerisation of IFITM3 rigidifies and bends host membranes to prevent virus infection. (Top row) During virus-cell fusion, the viral (brown) and host (blue) membranes initially pass through a hemifusion intermediate (left) before proceeding to the formation of a fusion pore (right) enabling virus content release into the cytoplasm. (Bottom row) In the presence of IFITM3 oligomers (green) in the host cell membrane (e.g. the plasma membrane or endosomes), this restriction factor bends alters the curvature and increases the rigidity (bolded lipids) locally at sites of virus-cell fusion. Consequently, although hemifusion intermediates (left) are allowed to form, fusion pore formation and expansion (right) is disallowed. Created with BioRender.

This report demonstrates an additional requirement for IFITM3 to enact its antiviral mechanism: self-oligomerisation. Previous investigations identified two phenylalanine residues (F75 and F78) as primary determinants for IFITM3 oligomerisation *in vitro* [104]. Owing to its alanine scanning mutagenesis approach, this previous study did not report a role for glycine-91 or glycine-95 in IFITM3 oligomerisation, as this mutant protein was undetectable by western blot [104,256]. Although it was confirmed later that F75A and F78A mutations diminish IFITM3's antiviral activity [78,84], recent FRET-based measurements in living cells indicated that these mutations failed to disrupt IFITM3 oligomerisation [118]. Here, we similarly report that F75A and F78A mutations do not prevent IFITM3 oligomerisation. However, we show for the first time that the GxxxG motif facilitates IFITM3 oligomerisation in live cells and *in vitro*. In particular, we show that the G91L mutation partially disrupts IFITM3 oligomerisation, whereas the G95L mutation almost completely obliterates IFITM3's ability to oligomerise. In support of the notion

that oligomerisation is a requirement for IFITM3 antiviral activity, we show that the G95L mutant potently disrupts both the antiviral potential of IFITM3 and its ability to rigidify membranes. We additionally demonstrate that Ampho B blocks increases in membrane rigidity in IFITM3 overexpressing cells. These results indicate that the ability for IFITM3 to increase the order of membranes is tightly linked with its antiviral function in cells. Further investigations are needed to reveal if this membrane stiffening function of IFITM3 is a correlate of restriction within virions as well.

To begin answering this question, we discovered that IFITM3's glycine-91 and glycine-95 are also critical for restricting HIV-1 virion infectivity. Interestingly, the G91L mutation abrogated IFITM3 antiviral activity in virus-producing cells to a greater extent than the G95L mutation. This result may suggest that IFITM3 oligomerisation may not be critical for restricting HIV-1 virion infectivity as opposed to restriction of inbound virions in target cells. IFITM3 incorporates into virions in virus-producing cells at HIV-1 assembly sites (i.e. at the plasma membrane) [14]. In our live-cell imaging approach, we detected that the majority of FRET signal in cells co-expressing IFITM3-YFP and IFITM3-mCherry was located in intracellular vesicles, whereas low FRET signal was detected at the cell surface. Consequently, it is plausible that the oligomerisation-mediated antiviral effect of IFITM3 is more efficacious in endosomes than the plasma membrane. This hypothesis is consistent with our results indicating that viruses entering cells via endosomal fusion (i.e. IAV) are potently restricted by IFITM3 oligomers. Nevertheless, further experiments assessing how virion associated IFITM3 impacts the rigidity of the virion membrane will be critical in determining whether its restriction mechanism is similar at this site.

Although our data clearly indicates that oligomerisation of IFITM3 is required to rigidify membranes, further investigation is necessary to assess how IFITM3 oligomerisation may or may not alter membrane curvature in cells. IFITM3 overexpression in cells has been previously documented to induce positive membrane curvature in cells [51], in contrast to a recent investigation demonstrating that IFITM3 incorporation into unilamellar vesicles induces negative membrane curvature and the formation of intraluminal vesicles [101]. As highlighted by the latter report, amphipathic helices, including that of IFITM3, are able to interact with and bend membranes [284–286]. Furthermore, it is known that some transmembrane proteins require self-oligomerisation in order to bend host membranes [287]. Additionally, disruption of membrane rigidity is usually accompanied by changes in membrane curvature [100]. Here, we illustrate that the amphipathic helix of IFITM3 is vital to enhance membrane order in cells. Importantly, as we demonstrate that membrane order enhancement requires the GxxxG motif, we propose that oligomerisation of IFITM3 may "prime" the membrane deformation activity of its amphipathic helix, and therefore, its restriction activity. Thus, IFITM3 oligomerisation may provide a means to insert multiple amphipathic helices into membrane regions where viruses enter cells to disfavour virus-cell fusion.

Several reports have indicated that the GxxxG motifs within transmembrane proteins may also facilitate interactions between different proteins (i.e. hetero-multimerization) [281,288]. Therefore, in addition to mediating IFITM3 oligomer formation, this motif may also promote IFITM3 interactions with other transmembrane proteins. It is known that IFITM3 associates with IFITM1 and IFITM2 [104]. Additionally, as IFITM1 and IFITM2 contain the GxxxG motif, it is possible that this motif enhances the ability of IFITM3 to form heteromultimers with these family

members in membranes to restrict virus entry. Importantly, IFITM3 has been previously reported to interact with host proteins other than IFITM family members [87,289]. In particular, cholesterol trafficking regulator VAPA and ZMPSTE24 have been described as cofactors necessary for IFITM3 antiviral activity [87,289]. Therefore, it is possible that mutations in this motif within IFITM3 may also disrupt associations with cofactors necessary for restrictive function. Future experiments utilising the loss-of-function mutant IFITM3 G95L may help clarify the role of ZMPSTE24, VAPA, and cholesterol as key regulators of IFITM3 antiviral function.

Finally, we illustrate that the homologous site in CD225 family member PRRT2, glycine-305, is important for its own oligomerisation as well. Patients harbouring the naturally-occurring G305W/R mutation suffer from convulsive neurological dysfunction owing to loss of PRRT2's regulatory role in neurotransmitter release. Consequently, our results may propose how this loss-of-function mutation in PRRT2 disrupts its function in deterring neurotransmitter release. Furthermore, the presence of a shared GxxxG motif in these proteins, as well as other CD225 family members, may suggest that an ancestral CD225 protein performed an unknown function that required oligomerisation. Interestingly, human IFITM5 and IFITM10 lack a GxxxG motif. Therefore, it is possible that the loss of the GxxxG motif is one reason why these IFITM proteins have not been typically associated with possessing antiviral activity. It is tempting to speculate that multiple CD225 proteins regulate membrane fusion processes in cells. Similarly, it is likely that CD225 protein oligomerisation may alter protein architecture to facilitate protein-protein interactions, broadening their functional repertoire.

3.5. Acknowledgements

Stable cell lines, sequence alignments, and blue native PAGE gel experiments were performed by Kazi Rahman. Immunofluorescence, virus-cell fusion assays, and virion-content studies were performed by Saliha Majdoul. This work was originally published in *eLife*.

K. Rahman*, C. Coomer*, S. Majdoul, S. Ding, S. Padilla-Parra, A. Compton (2020). A conserved motif functionally links the antiviral activity of IFITM3 with its oligomeric state in membranes. eLife. 9:e58537 DOI: 10.7554/eLife.58537.

Chapter 4: Restoration of a GxxxG motif in human IFITM5 potentiates its oligomerisation capacity and antiviral activity

4.1 Introduction

Chapters 1 and 3 indicated that the *IFITM* gene family underwent accordion-like evolution over time, such that different vertebrate species harbour a diverse portfolio of *IFITM* genes and pseudogenes, in both sequence and copy number. Although this gene expansion and diversification is consistent with adaptive evolution, *IFITM5* and *IFITM10* are not typically considered to hold antiviral function. Indeed, currently *IFITM10* has no known function and IFITM5 plays a cryptic role in bone development. Nevertheless, recent literature has suggested that orthologous IFITM10 in chickens may restrict VSV-G infection [290]. Additionally, ectopic expression of human IFITM5 inhibits IAV infection, albeit less efficiently compared to IFITM3 [68].

In Chapter 3, we revealed that a ^{91}GxxxG^{95} motif the intracellular loop of IFITM3 potentiates its antiviral activity by facilitating self-oligomerisation and that oligomerisation facilitated the rigidification of host membranes [105]. Interestingly, human IFITM5 and IFITM10 lack this oligomerisation motif (Figure 3.3.1C). Furthermore, investigations probing the oligomerisation capacity of several human IFITM proteins revealed that fluorophore-labelled IFITM5 was less capable of self-association in a FRET-based flow cytometry assay [118]. Therefore, it is tempting to suggest that the loss of the GxxxG motif is one reason why IFITM5 or IFITM10 have not been typically associated with antiviral function.

Although IFITM5 has yet to be formally associated with antiviral immunity, this CD225 protein has been associated with human disease. In particular, several reports have suggested that IFITM5 facilitates bone formation and mineralisation *in vitro* and *in vivo*, although this role remains incompletely understood [15,116]. In cultured osteoblasts, bone mineralisation has been shown to be promoted when IFITM5 is overexpressed, whereas when *IFITM5* is knocked down, this process is suppressed [116]. To confirm these results and contextualise their physiological importance, *Ifitm5* knockout mice were generated and studies investigating bone formation and structure were conducted [15,291]. Nevertheless, these investigations did not demonstrate any abnormalities in bone formation or morphology in this *in vivo* model [15,291]. Therefore, although IFITM5 seems to play a substantial role in bone mineralisation *in vitro*, these results suggest that IFITM5 is not critical for bone formation *in vivo*.

Complicating these results are multiple clinical reports indicating patients diagnosed with osteogenesis imperfecta (OI) type V are heterozygous for a point mutation (c.-14C > T) in the 5' untranslated region of *IFITM5* [117,292–294]. OI is a genetic disease which causes fragile bones, typified by hyperplastic callous formation, dislocation of the radius, interosseous membrane calcifications and high fracture risk, although symptoms vary tremendously [295]. Nevertheless, this polymorphism which is associated with OI in humans results in an upstream shift in the *IFITM5* start codon, such that five amino acids (MALEP) are added to the N-terminus.

Research aimed at characterising the stunted antiviral properties of IFITM5 may assist in better describing IFITM evolution, in addition to uncovering IFITM5's cryptic role in bone formation. For example, it is tempting to speculate whether the role of IFITM5 in bone

mineralisation is tied to its ability to regulate an unidentified fusion process. Therefore, identifying the residues necessary to perform or enhance its antiviral function may inform its role in bone development. Alternatively, IFITM5 may have separate roles in human physiology altogether. Interestingly, it was reported that IFITM5 directly associates with FKBP11 to disrupt its interaction with the CD81-[FPRP/CD9] complex in osteoblasts, increasing expression of several interferon-inducible genes. These genes included BST2, IRGM, IFIT3, and MHC class I [296]. Therefore, these results suggest that IFITM5 may not only be involved in bone formation, but also immune activation.

To determine whether the homologous ^{70}GxxxA^{74} residues in IFITM5 impact its capacity to oligomerise, we generated pairs of fluorescently-tagged IFITM5 to measure FRET with fluorescence lifetime imaging in living cells. Co-expression of wildtype IFITM5-YFP and wildtype IFITM5-mCherry resulted in little change in YFP lifetimes, indicative of low levels of FRET via IFITM5 oligomerisation. However, A74G IFITM5-YFP and A74G IFITM5-mCherry co-expression resulted in greater levels of FRET and a potent decrease in YFP lifetimes, indicating increased propensity for oligomerisation. While IFITM5 exhibits some antiviral activity, restoration of the GxxxG motif via the A74G mutation increased restriction activity against Vesicular Stomatitis and Influenza A viruses when transiently overexpressed in HEK293T cells. In contrast, neither IFITM5 nor IFITM5 A74G inhibited Sendai virus infection, which is insensitive to the antiviral effects of IFITM proteins. Together, these results suggest that IFITM5 has a reduced capacity to oligomerise, which may partially explain its less potent antiviral potential relative to other IFITM family members. Our findings provide an understanding of how IFITM5

diverged over evolutionary time to take on a non-antiviral role in cells which do not require oligomerisation.

4.2 Material and Methods

4.2.1 Sequence alignments and phylogenetic analysis

UniProt (www.uniprot.org) was used to gather protein sequences for all CD225 proteins analysed and ClustalX (www.ebi.ac.uk/tools/msa/muscle/) was utilized to perform multi-sequence alignments.

4.2.2 Cell lines and plasmids

HEK293T (ATCC: CRL-3216) were cultured in DMEM (Gibco) supplemented with 10% foetal bovine serum (Hyclone) and 1% penicillin-streptomycin (Gibco) and cultivated at 37°C and 5% CO_2. SaO2 cells (ATCC: HTB-85) were cultured in McCoy's 5A medium (ATCC) and supplemented with 10% foetal bovine serum (Hyclone) and 1% penicillin-streptomycin (Gibco) and cultivated at 37°C and 5% CO_2. Cell passaging was performed regularly with the aid of Trypsin-EDTA 0.05% (Gibco). Additionally, site-directed mutagenesis (QuikChange Lightning) was utilized to introduce IFITM5 mutations A74G and A74L. Wildtype IFITM fused to carboxy-terminal YFP or mCherry was produced by Integrated DNA Technologies. Site-directed mutagenesis (QuikChange Lightning) was utilized to introduce IFITM5 mutations A74G and A74L into these fluorophore-tagged constructs.

4.2.3 Pseudotyped virus production and infections

To produce VSV pseudotyped with either HA or VSV-G, 293T cells were seeded onto six-well plates pre-coated with poly--lysine (Sigma-Aldrich). The following day, these cells were transfected with 1200ng of p18-VSVG or pCAGGS-HA (WSN strain) (from Stephan Pohlmann). After 24 hours, transfected cells were infected with VSVΔG/GFP particles pseudotyped with VSVG as previously described [297]. Approximately 1 hr of incubation at 37 °C, cells were washed with PBS three times and incubated with DMEM supplemented with L-glutamine, 2% FBS and penicillin-streptomycin for 48 hrs. Following this, cell supernatants were collected, cleared from cell debris by centrifugation at 500g for 10 minutes, aliquoted and stored at −80 °C.

To perform infections, a total of 50,000 HEK293T cells transiently transfected with 1.5 μg of pQCXIP, FLAG-tagged WT IFITM5, or the indicated FLAG-tagged mutant were seeded in 24-well plates and allowed to grow overnight. The following day, the indicated amount of virus diluted in 250 μL of DMEM was added to the wells and allowed to incubate for approximately 18 hours. Following this, cells were washed with 1X PBS, dissociated with Trypsin-EDTA, and subsequently fixed and permeabilized with Cytofix/Cytoperm (BD). FLAG+ cells were detected with a rabbit anti-FLAG antibody (Sigma) and a goat anti-rabbit secondary antibody conjugated to AlexaFluor647 (Invitrogen). To detect VSV-VSVG or VSV-HA infection, cells were scored on a LSRFortessa flow cytometer (BD) for eGFP positivity. Sendai virus (Cantell strain) supplied as clarified allantoic fluid was purchased from Charles River Laboratories. Infections were performed as above an MOI of 0.1. Approximately 18 hours after virus exposure, cells were fixed/permeabilized and stained with polyclonal anti-SeV antibodies and analysed on a LSRFortessa flow cytometer (BD). FLAG+ cells were detected with a rabbit anti-FLAG antibody

(Sigma) and a goat anti-rabbit secondary antibody conjugated to AlexaFluor647 (Invitrogen). Infection was scored in FLAG+ cells.

4.2.4 FRET and FLIM for oligomerisation studies

A total of 50,000 HEK293T cells per well were seeded in µ-slide 8 well chambers (Ibidi) and allowed to grow overnight in complete Fluorobrite DMEM (Gibco). The following day, these cells were transiently transfected with 0.25 µg IFITM5-YFP and 0.25 µg mCherry, or 0.25 µg IFITM5-YFP and 0.25 µg IFITM5-mCherry using TransIT-293 (Mirus) with the fluorophore fused to the amino-terminus. Imaging of these live cells in Fluorobrite DMEM (Gibco) was performed with a Zeiss LSM 780 confocal microscope and cells were selected with a 63X oil-immersion objective. To perform FRET experiments, following excitation with a 514 nm laser, donor YFP fluorescence was captured with a gallium arsenide phosphide photomultiplier tube (GaAsP PMT) with a 520-550 nm emission window. Following excitation by a 561 nm laser, acceptor mCherry fluorescence was captured with a GaAsP PMT detector set with an emission window at 570-615 nm. The FRET channel was collected with a GaAsP PMT detector set to a 570-615 nm emission window after excitation with a laser tuned to 514 nm. For each condition, at least 50 cells were examined in each experiment. Using the FRET and co-localisation analyser plugin (https://imagej.nih.gov/ij/plugins/fret-analyzer/fret-analyzer.htm) in Fiji (ImageJ), FRET indices were calculated for each cell.

Evaluation of the donor lifetime was performed concomitantly with the FRET experiments via excitation with a 950 nm two-photon pulsed laser (Coherent) tuned to 80 MHz with single

photon counting electronics (Becker Hickl) and signal detection with an HPM-100-40 module GaAsP hybrid PMT (Becker Hickl). To exclude the effects of photobleaching or low-signal-to-noise, analysis of cells was limited those which contained 250-1000 photons per pixel. Fluorescence decays of each pixel were acquired and analysed in SPCImage NG software (Becker Hickl), and each decay was deconvoluted with the instrument response function and fitted to a Marquandt nonlinear least-square algorithm with a two-exponential model. Mean fluorescence lifetimes were calculated as performed previously [267] in SPCImage NG and at least 30 cells per condition were analysed in each experiment.

4.2.5. Structural predictions for IFITM5

IFITM5 amino acid sequences were obtained via Uniprot (www.uniprot.org). Structural predictions for human IFITM5 were performed using the Iterative Threading Assembly Refinement (I-TASSER) bioinformatic method without additional restraints or templates (zhanglab.ccmb.med.umich.edu/I-TASSER) [298,299]. Helical wheel projection plots used to visualise IFITM5 residues 38-47 (IWSVFSTLYL) was created using HELIQUEST software (https://heliquest.ipmc.cnrs.fr/) [300]. Notably, the arrows represent the magnitude and orientation of the mean hydrophobic moment value were calculated by HELIQUEST software. Additional analyses were performed using PSIPRED (http://bioinf.cs.ucl.ac.uk/psipred/) [301,302], NetSurfP version 2.0 (www.cbs.dtu.dk/services/NetSurfP) [303], PredictProtein (www.predictprotein.org) [304,305], and POLYVIEW-2D (polyview.cchmc.org) [306], each with default settings. *De novo* structural predictions of the IFITM5 peptide of residues 38-47 (IWSVFSTLYL) were performed using PEP-FOLD 3.1 (bioserv.rpbs.univ-paris-diderot.fr/services/PEP-FOLD) [307].

4.3 Results

4.3.1. Human IFITM5 does not contain a GxxxG motif

Chapter 1 and 3 indicated that CD225 proteins adopt a type II transmembrane topology consisting of a cytoplasmic N-terminus, a CD225 domain (Figure 1.1.4), and a short extracellular or luminal C-terminus [54,57,270]. Phylogenetic analysis of CD225 domains found in the *IFITM* family (consisting of *IFITM1, IFITM2, IFITM3, IFITM5,* and *IFITM10* in humans) and other CD225 proteins (human *PRRT2* and *TUSC5*) support this notion of common ancestry (Figure 4.3.1A). As in Chapter 3, we visualised this topology of IFITM5, which also has been suggested to adopt a similar orientation in host cell membranes [16] using Protter, as previously described (Figure 4.3.1B) [105,271]. Notably, although IFITM5 adopted a similar topology compared to that of IFITM3 and PRRT2 (Figure 3.3.1A and Figure 3.3.1B), IFITM5's N-terminus was shorter than that relative to both IFITM3 and PRRT2.

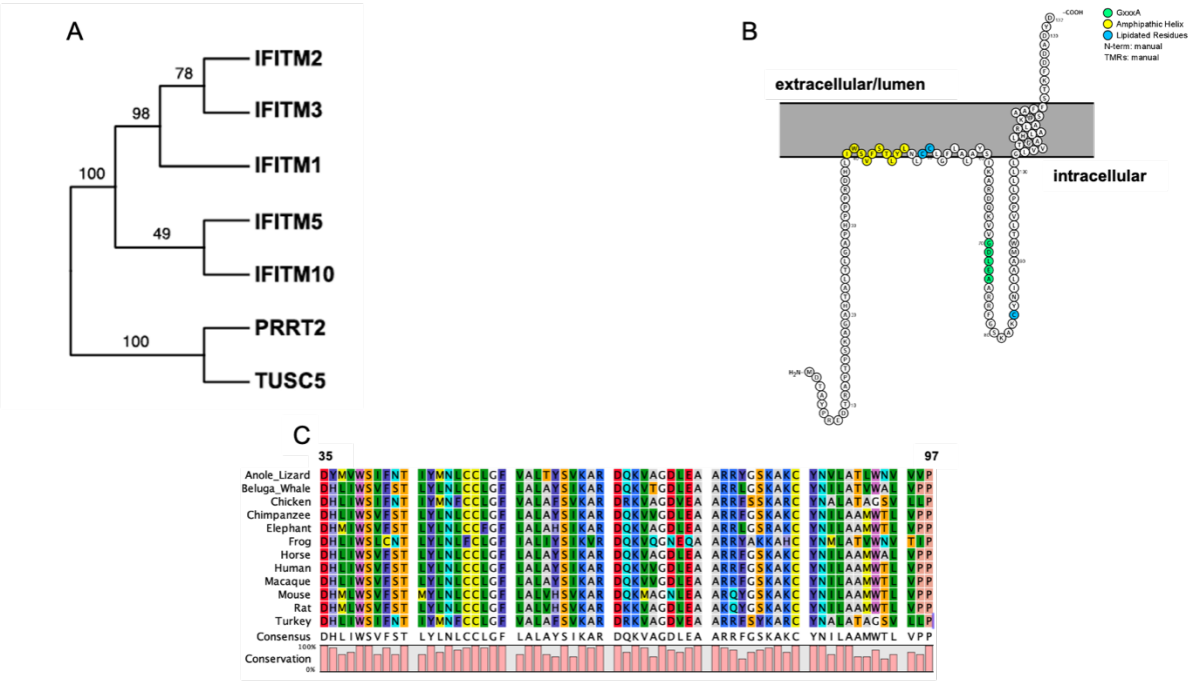

Figure 4.3.1. IFITM5 does not harbour an intact GxxxG motif in its CD225 domain. (A) A phylogenetic tree of CD225 amino acid sequences from human IFITM and human CD225 proteins was reconstructed by maximum likelihood and presented as a cladogram. Reliability of internal branch topology was assessed by bootstrapping (100 replicates). (B) Schematic representation of the membrane topology of IFITM5 made with Protter. Residues corresponding to the amphipathic helix (yellow), palmitoylated cysteines (blue), and the non-intact GxxxG motif (green) are indicated. (C) A partial amino acid alignment of the CD225 domain from IFITM5 orthologs in vertebrates and amphibians. A plot denoting the consensus sequence and percent conservation is listed below the alignment.

As we previously reported that IFITM3 and PRRT2 harbour the GxxxG motif to facilitate membrane protein-protein interactions [272,273] and IFITM5 has been shown to oligomerise less efficiently than the antiviral IFITMs [118], we sought to determine whether this motif was conserved in IFITM5. Accordingly, we aligned *IFITM5* protein sequences from a diverse range of vertebrate species and determined that the GxxxG motif is not conserved in *IFITM5* of vertebrates (Figure 4.3.1C). Instead, although IFITM5 contains a glycine at position 70, which is homologous to IFITM3 glycine-91, IFITM5 contains an alanine residue at position 74, which is homologous to IFITM3 glycine-95. These results indicate that the GxxxG motif is not conserved in human *IFITM5*.

4.3.2. Restoration of GxxxG in human IFITM5 enhances its oligomerisation

Human *IFITM5* is not typically associated with antiviral function. Nevertheless, ectopic expression of human IFITM5 inhibits IAV infection, albeit less efficiently compared to IFITM3 [68]. As described in Chapter 3, we discovered IFITM3 antiviral activity is dependent on an intact GxxxG motif located within its CD225 domain. Human IFITM5, along with other vertebrate orthologs, lack an intact GxxxG motif, harbouring GxxxA instead. Although GxxxA motifs have been shown to facilitate oligomerisation of TM domains of type II transmembrane proteins, GxxxG motifs have been found to be the most frequently associated with transmembrane protein interactions [272], and disruption of GxxxA motifs have been found to minimally impact protein oligomerisation in prior investigations [308,309]. Although likely dependent on sequence context [272], the added steric hindrance of an alanine side-chain could make the GxxxA of human IFITM5 less prone to support oligomerisation to the same capacity of human IFITM3 [272]. These results are supported by studies describing substantial loss in protein-interaction capability when glycines within GxxxG motifs are mutated to alanine [310].

As IFITM5's alanine-74 is homologous to the latter glycine within IFITM3's conserved GxxxG motif, and that IFITM3's glycine-95 is the more influential determinant in formation of higher-order oligomers relative to glycine-91 (Chapter 3), we utilized FRET microscopy to determine if substituting glycine at IFITM5's alanine-74 residue facilitates self-oligomerisation of IFITM5. To create FRET pairs, we created constructs expressing IFITM5 fused with yellow fluorescent protein (YFP) or mCherry at its N-terminus as before. In this context, excitation of YFP (e.g. the FRET donor) results in energy transfer to mCherry (e.g. the FRET acceptor) if the

FRET pair is in close proximity (i.e. interacting). Co-transfection of mCherry and IFITM5-YFP enabled the detection of background FRET signal.

Interestingly, co-transfection of WT IFITM5-YFP and WT-IFITM5-mCherry resulted in low levels of FRET (Figure 4.3.2A and Figure 4.3.2B), indicating a low ability to oligomerise in live cells, which has been previously reported [118]. However, co-transfection of YFP- and mCherry-tagged IFITM5 harbouring the A74G mutation produced FRET index values which were substantially higher compared to WT IFITM5 (Figure 4.3.2A and Figure 4.3.2B). Furthermore, the majority of detected FRET signal occurred in intracellular vesicular structures (Figure 4.3.2B). These results suggest that restoration of the GxxxG motif in IFITM5 enhances its ability to oligomerise in live cells, particularly in intracellular compartments.

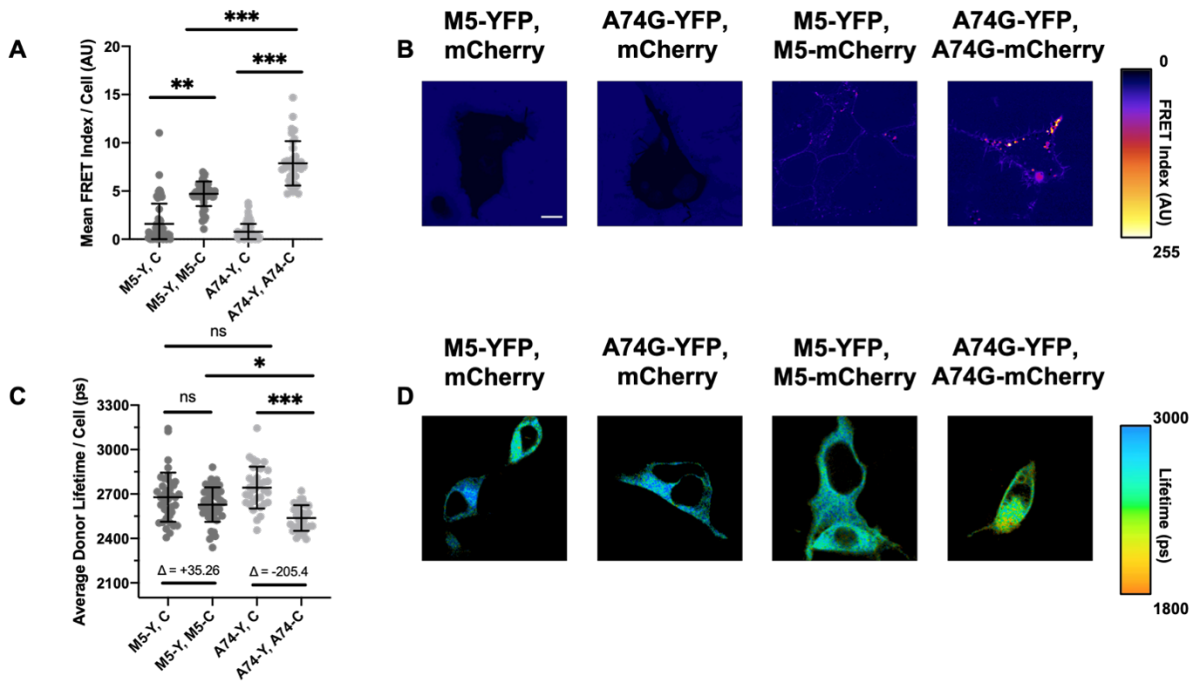

Figure 4.3.2. Restoration of a GxxxG motif in IFITM5 enhances its oligomerisation in living cells. HEK293T were transiently co-transfected with IFITM5-YFP and mCherry or IFITM5-YFP and IFITM5-mCherry. Fluorescently tagged IFITM3 constructs encoded WT IFITM5 or the indicated mutant. (**A**) Scatter plot depicting whole-cell FRET measurements from a minimum of 50 cells per condition; the results of three independent experiments were pooled. Dots correspond to individual cells. (**B**) FRET images were created and representative images of FRET signal of 12–20 captured images per condition are shown. (**C**) Scatter plot depicting whole-cell YFP donor lifetime measurements from a minimum of 30 cells per condition; the results of three independent experiments were pooled. Dots correspond to individual cells. A mean delta (Δ) value is provided to indicate the drop in donor YFP lifetime resulting from the pairing of IFITM5-YFP and mCherry versus the pairing of IFITM5-YFP and IFITM5-mCherry. (**D**) FLIM images were created and representative images of the YFP donor lifetime of 12–20 captured images per condition are shown. Error bars indicate standard deviation. Statistical analysis was performed using one-way ANOVA. ***, p<0.0, ****, p<0.001. Scale bars, 10 μm. Ps, picoseconds. Au, arbitrary units.

To corroborate our FRET results, we performed fluorescence lifetime imaging of the FRET donor (YFP), which allows for measurements independent of fluorophore expression level or light-path [279]. In line with our FRET data, co-transfection of WT IFITM5-YFP and WT IFITM5-mCherry resulted in minimal decreases in donor lifetimes (Figure 4.3.2C and Figure 4.3.2D). In contrast, co-transfection of either IFITM5 A74G-YFP and IFITM5 A74G-mCherry enhanced the reductions in donor lifetimes. Collectively, these results suggest that the alanine-74 residue is a regulator of IFITM5-IFITM5 interactions, and that loss of the GxxxG motif in IFITM5 diminishes its capacity to oligomerise in live cells.

4.3.3. The GxxxG motif of IFITM5 imposes broad-spectrum anti-viral activity

Our FRET and FLIM results suggested that restoration of the GxxxG motif within IFITM5 enhanced its ability to oligomerise in live cells. Furthermore, we previously determined that disruption of this motif in human IFITM3 deterred its antiviral activity against IAV and VSV infection [105]. To determine if restoration of the GxxxG motif in human IFITM5 restored its antiviral activity, we challenged HEK293T cell lines which ectopically expressed WT IFITM5 or IFITM5 with a restored GxxxG motif to assess antiviral function by flow cytometry (Figure 4.3.3). As our IFITM5 constructs were not highly expressed in HEK293T cells, we limited our analysis to cells ectopically expressing IFITM5, as determined by anti-FLAG staining (Figure 4.3.3A; for gating strategy, refer to Appendix Figure 5.1.3). Importantly, WT IFITM5 and mutants were expressed at similar levels in FLAG-positive cells (Figure 4.3.3A and 4.3.3B). Interestingly, although ectopic expression of WT IFITM5 in HEK293T cells modestly restricted both VSV pseudovirus particles decorated with VSVG (Figure 4.3.3C) and influenza hemagglutinin (Figure 4.3.3D), cells ectopically overexpressing A74G IFITM5 demonstrated enhanced restriction of both of these pseudoviruses (Figure 4.3.3C and Figure 4.3.3D). As these pseudoviruses differed only by the envelope glycoprotein, these results suggest that IFITM5 may restrict virus infection at the entry step, similar to IFITM3. Importantly, HEK293T cells overexpressing WT IFITM5 and its mutants were able to support infection of Sendai virus (Figure 4.3.6E), which is known to be resistant to IFITM-mediated restriction [21], supporting the notion that IFITM5 restriction of VSV-VSVG and VSV-HA infection is likely due to the activity of IFITM5 restricting the virus entry step.

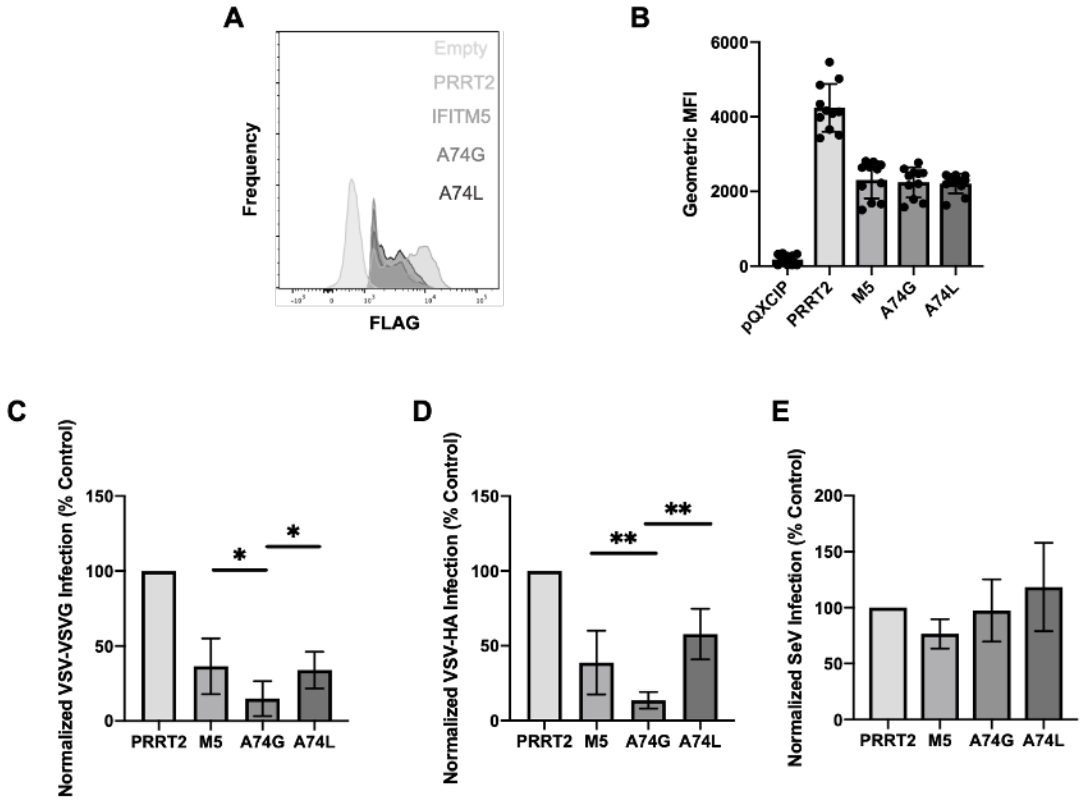

Figure 4.3.3. ^{70}GxxxG^{74} is crucial for potent IFITM5-mediated restriction of pseudovirus infection. **A**) HEK293T cells stably transfected with empty pQCXIP, IFITM5 WT-FLAG, or the indicated mutants were fixed, permeabilized, and stained with anti-FLAG antibody and assessed by flow cytometry to quantify FLAG expression levels (depicted as histograms). (**B**) Bar graph depicting the mean fluorescence intensity (MFI) of FLAG staining in (**A**) for three independent experiments. Both (**A**) and (**B**) focus solely on the FLAG+ cells in the analysed population due to low transfection efficiency of IFITM5 (**C-D)** HEK293T ectopically expressing non-antiviral PRRT2, IFITM5 WT-FLAG, or the indicated mutants were challenged with VSV pseudotyped with VSVG (**C**) or IAV hemagglutinin (**D**) (MOI of ~0.1) and were subsequently fixed and permeabilized 18 hours post-infection. These cells were then stained with an anti-FLAG+ antibody and assessed by flow cytometry and scored for infection by the presence of GFP. (**D**) Bar graph depicting infection results from 3-5 independent experiments normalized to cells ectopically expressing non-antiviral FLAG-PRRT2 (set to 100%) for VSV pseudvirions decorated with VSVG. (**E**) Bar graph depicting infection results from 3-5 independent experiments normalized to cells ectopically expressing non-antiviral FLAG-PRRT2 (set to 100%) for VSV pseudvirions decorated with influenza hemagglutinin. (**F**) Bar graph depicting infection results from 3-5 independent experiments normalized to cells ectopically expressing non-antiviral FLAG-PRRT2 (set to 100%) for Sendai virus. Error bars indicate standard deviation. Statistical analysis was performed using one-way ANOVA. *, $p<0.05$; **, $p<0.001$. MFI, mean fluorescence intensity.

Owing to bulky side-chain residues interfering with the oligomerisation of TM proteins dependent on a (small)xxx(small) motif, as exemplified by our results previously in Chapter 3 [105], we challenged HEK293T cell lines ectopically overexpressing A74L IFITM5 with VSV

pseudovirus particles decorated with VSVG (Figure 4.3.3C) and influenza hemagglutinin (Figure 4.3.3D). Interestingly, although mutation of alanine-74 to leucine resulted in similar levels of VSV-VSVG restriction relative to WT (Figure 4.3.3C), this mutation partially reduced the antiviral activity of IFITM5 passed WT levels when challenged with VSV-HA, albeit not to a statistically significant extent (Figure 4.3.3D). Collectively, these results illustrate that an intact GxxxG motif is necessary for IFITM5 to potently restrict VSV pseudovirion infection in HEK293T cells and suggests that one reason for loss of IFITM5 antiviral activity may be due to the loss of its GxxxG motif.

4.3.4. IFITM5 contains an amphipathic helix

We and others recently reported that the amphipathic helix of IFITM3 is vital for its ability to increase membrane order in living cells, alter membrane curvature in artificial membranes, and to perform antiviral function [56,101,105]. As IFITM5 originated from *IFITM* gene expansion in humans [12,13], is a membrane-localised CD225 protein, and has previously been reported to contain some level of antiviral function [68], we were curious if IFITM5 may contain an amphipathic helix which may support its partial antiviral activity. Therefore, we performed structural prediction analyses for human IFITM5 using PSIPRED, a PSI-blast based secondary structure prediction method, as previously described [301,302]. Similar to IFITM3, (Figure 4.3.4D shows the first of three alpha helical structures), PSIPRED identified three alpha helical structures within IFITM5 with high confidence (Appendix Figure 5.1.4). These putative alpha helices were allocated between two hydrophobic domains (HD), similar to IFITM3 (Appendix Figure 5.1.4) [56]. In particular, the first two helices of IFITM5 were located within HD1, whereas a much

longer alpha helix was predicted within HD2 (Appendix Figure 5.1.4). Importantly, we obtained similar results when analysing the secondary structure of IFITM5 using NetSurfP (Figure 4.3.4A) [303], PredictProtein (Figure 4.3.4B) [304,305] and POLYVIEW-2D (Figure 4.3.4C) [306]. Collectively, these structural predictions define the location and boundaries of three alpha helices within IFITM5.

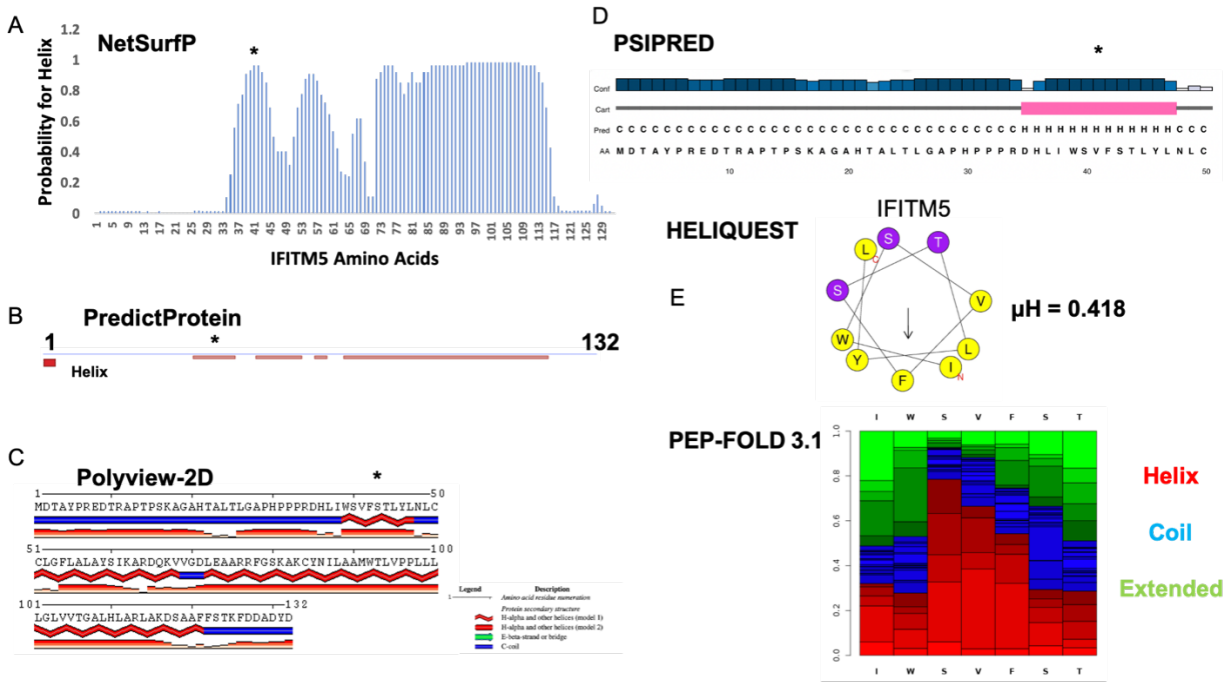

Figure 4.3.4. The first alpha helix within IFITM5 is predicted to be amphipathic. Secondary structure predictions for the human IFITM5 amino acid sequence using (**A**) NetSurfP, (**B**) PredictProtein, (**C**) POLYVIEW-2D, and (**D**) PSIPRED online programs. *denotes the predicted amphipathic helix region of interest examined in this study. Note 'C' and 'H' indicates predicted coiled or helical structures, respectively. (**E**) (Top) Visualization of IFITM5 residues IWSVFSTLYL on a helical wheel projection plot constructed via HELIQUEST software. Hydrophobic residues are displayed as yellow, while hydrophilic residues are displayed as purple. The arrow represents the magnitude and orientation of the mean hydrophobic moment, which is calculated by HELIQUEST software and displayed to the right. (Bottom) Structural probability prediction of IFITM5 residues IWSVFSTLYL via PEP-FOLD 3.1.

As IFITM3 has been previously shown to contain an amphipathic helix within its first HD, we analysed the first alpha helix (residues IWSVFSTLYL) located in IFITM5 using PEP-FOLD software, as similarly described [307]. Similar to above, the PEP-FOLD algorithm predicted an

alpha helical structure for these residues (Figure 4.3.4E and Appendix Figure 5.1.5). Importantly, this algorithm noted separation of hydrophobic and hydrophilic amino acids on opposing sides of the alpha helix, suggesting it is amphipathic (Appendix Figure 5.1.5). In support of this notion is a strong, albeit slightly decreased hydrophobic moment relative to IFITM3, was recorded for this alpha helix within IFITM5, using HELIQUEST software (Figure 4.3.4E). In line with putative structural predictions for IFITM3, we hypothesised that this amphipathic helix may be remnant of ancient antiviral activity and thus supports a similar membrane topology for IFITM5 (Figure 4.3.1). Collectively, these results suggest a model where IFITM5 may use its amphipathic helix for its modest antiviral activity, which is enhanced upon oligomerisation via restoration of its GxxxG motif.

4.4 Discussion

Although the mechanism of IFITM3 is steadily becoming solidified, understanding the loss of restriction activity of the non-antiviral human IFITM family members will help better inform their 1.) physiological role *in vivo* and 2.) which specific residues in these family members render them unable to perform virus restriction. These results will assist investigations aimed at better understanding the broad antiviral action of IFITM1, IFITM2 and IFITM3.

We reported in Chapter 3 that IFITM3 rigidifies membranes to restrict virus infection by leveraging a mutant (i.e. G95L), which was limited in its ability oligomerise and increase membrane order, providing functional proof for this model [105]. Interestingly, this glycine residue was embedded within a GxxxG motif, which is known to mediate oligomerisation of transmembrane proteins [272]. As the human *IFITM* locus expanded over evolutionary time, giving rise to several paralogs, the genes of this locus were allowed the opportunity to diversify (Figure 4.3.1A) [11]. Consequently, some members, notably *IFITM5* and *IFITM10*, may have developed physiological roles outside of antiviral immunity during this diversification process. Although *IFITM10* currently has no known physiological role, *IFITM5* likely plays an incompletely understood role in bone development [116,291]. Importantly, these members notably lack a GxxxG motif, where human IFITM5 contains a conserved ^{70}GxxxA^{74} (Figure 4.3.1C) and human IFITM10 contains a ^{187}NxxxG^{191} (Figure 3.3.1).

Owing to the fact that IFITM5 contains a disrupted GxxxG motif, and that IFITM5 has been shown to inefficiently oligomerise previously by a FRET-based flow cytometry assay [118],

we thought to restore this motif in human IFITM5 to determine if its loss contributed to diminished antiviral activity [68,105]. Due to aberrant ectopic expression of IFITM10 in HEK293T cells, this approach for this protein was not pursued further.

Using a FRET-based approach with fluorophores attached to the IFITM5 N-terminus, we confirmed that WT human IFITM5 poorly oligomerises, as exemplified by minimally elevated FRET indices and partially reduced donor lifetime values relative to background levels (Figure 4.3.2). These results are in line with Winkler and colleagues [118]. However, it is plausible that attachment of fluorophores to the N-terminus of IFITM5 may disrupt proper localisation of this protein, diminishing recorded FRET levels or reductions in donor lifetimes. Furthermore, fluorophores appended to the N-terminus of IFITM5 may have improper orientation of their dipoles, thus rendering accurate quantification of their capacity to form oligomers by FRET or FLIM less likely [134,279]. Importantly, we were able to detect an increase in calculated whole-cell FRET indices and decreases in calculated whole-cell donor lifetime values for A74G-IFITM5, suggesting that this motif does mediate, to some degree, an increased capacity to self-associate in live cells (Figure 4.3.2).

Supporting our notion that the loss of the GxxxG motif in human IFITM5 has led to its diminished antiviral activity, we observed that HEK293T cells ectopically expressing human IFITM5 containing the A74G mutation were offered significantly more protection against pseudovirus infection compared to cells ectopically expressing wildtype human IFITM5. These results not only suggest that the GxxxG motif is broadly integral to the antiviral activity of the human IFITMs, but also solidifies and contextualises the importance of IFITM oligomerisation in

restricting infection of target cells. Although our analysis was limited to single-cycle pseudovirus infections, future investigations analysing the antiviral activity of human IFITM5 with a restored GxxxG motif against replication competent viruses will confirm the physiological relevance of these results.

Although overexpression of human IFITM5 has typically not been associated with antiviral immunity, it has been reported that overexpression of IFITM5 may lead to disruption of the FKBP11 and CD81-[FPRP/CD9] complex and subsequently upregulate several interferon-inducible genes [119,296]. Although the canonical antiviral human IFITMs were not probed for in this analysis, it is tempting to speculate that if upregulated by this complex dissociation, these IFITMs could utilise their GxxxG motif to oligomerise with IFITM5 and restrict viral infection. Furthermore, given that several interferon-inducible genes are upregulated, future investigations must separate any purported antiviral action of IFITM5 with the activity of these genes.

An important caveat of this report is that the amino acid context in which the GxxxG motif is located within human IFITM5 was not investigated. Several residues within or adjacent to GxxxG motifs may enhance or inhibit the interaction between transmembrane proteins [272,311]. Accordingly, the ability for A74G to enhance IFITM5 oligomerisation, as measured by our FRET-FLIM analysis, was diminished compared to human IFITM3. These results may suggest that other uncharacterised residues, whether within, adjacent to, or elsewhere relative to the GxxxG motif, play critical roles in mediating IFITM-IFITM interactions. Future investigations targeted at elucidating the role of these neighbouring residues which may facilitate transmembrane protein interactions via GxxxG motifs will benefit from comparing closely related paralogs. Not only will

these studies further reveal why IFITM5 has lost much of its antiviral activity, but also may uncover a role for IFITM5 oligomerisation in its cryptic association with bone development. As GxxxG motifs mediate interactions between transmembrane proteins, and IFITM5 has been shown to associate with various protein complexes *in vitro* [15,119,296], it is tempting to speculate that loss of this GxxxG motif may enable interactions with other membrane proteins to perform a critical role in bone mineralisation, which may or may not involve fusion. Emerging as a shared feature of CD225 proteins, such as SynDIG1 [120], we demonstrated in Chapter 3 that the GxxxG motif in PRRT2 was necessary for its ability to oligomerise, and this property may track with its ability to bind SNARE proteins to regulate neurotransmitter release [105,109].

Although this investigation purports that the GxxxG motif is able to partially restore the antiviral activity of human IFITM5, it is likely orthologous *IFITM5* genes of other vertebrates have similarly lost their antiviral activity due to disruption of the GxxxG motif. In this vein, we are currently assessing the antiviral activity and oligomerisation capacity of non-human IFITM5 orthologs which do not contain an intact GxxxG motif and evaluating if restoration of this motif enhances their potential antiviral function. Ultimately, our report here emphasises the role of the GxxxG motif in the broader evolution of the human *IFITM* locus.

Chapter 5: Conclusions and Future Directions

Utilising fluorescent imaging techniques which quantify membrane biophysical properties is a powerful approach to characterise determinants of virus-cell fusion. Although this dissertation involves three distinct projects, the focus of each centralises on identifying and describing regulators within the cell which construct a biophysical landscape to influence the fusion of pathogenic viruses with host membranes. Collectively, these projects have contributed to our understanding and knowledge of virus-cell fusion and its restriction in several ways.

The first project (Chapter 2) utilises several imaging assays to uncover a novel, indirect regulator of HIV-1 fusion with target cells: host cell metabolism. In particular, we discovered that diminished or acute arrest of glycolytic activity (Figure 2.3.4), in both target cell lines and primary CD4+ cells, disrupts fusion of several HIV-1 pseudoviruses at the point of hemifusion (Figures 2.3.5-2.3.7). Furthermore, this investigation supports prior studies that host cell metabolism is buffered by plasma membrane lipid content [177], where acute depletion of glycolysis leads to the catabolism of cholesterol [177,200]. Accordingly, we observed decreases in host cell cholesterol from both the plasma membrane and in endosomes in cell lines and primary CD4+ T cells during treatment with 2-DG (Figure 2.3.9A, Figure 2.3.9B, Figure 2.3.10) and supplementation of cholesterol in 2-DG-treated cells restored HIV-1 pseudovirus fusion (Figure 2.3.9C). This concomitant loss of cholesterol correlated with perturbations in target cell membrane order and tension (Figure 2.3.11 and Figure 2.3.12), such that glycolytically-inactivated cells harboured decreases in membrane order and higher levels of membrane tension, ultimately disfavouring the HIV-1 fusion reaction (Figure 2.3.13). Importantly, this work implemented a novel FLIM assay

measuring membrane tension concomitantly with single particle tracking, paving the way for future work to determine host membrane biophysical requirements necessary for other pathogenic viruses. Moreover, future work may extend this platform to evaluate local changes in membrane tension during overexpression of potent restriction factors of virus entry, such as IFITM3, to better characterise their mechanism of action. Modifications of this membrane tension reporter which enable its localisation to other sites of viral entry, such as endolysosomal compartments, will assist these future investigations as well.

Although our investigation determined that decreases in HIV-1 pseudovirus infection and fusion were not dependent on target TZM-bl cell viability or host cell receptor or co-receptor surface expression (Figure 2.3.7A and 2.3.7C), several supporting investigations should be conducted to determine the physiological significance of our results. For example, although prior investigations have utilised similar concentrations of 2-DG to block glycolysis in primary CD4+ T cells [207], these cells were treated for several days, instead of hours, and consequently reported higher levels of cytotoxicity and death. Additionally, 2-DG may alter levels of actin polymerisation owing to acute cellular ATP depletion. In particular, ATP depletion in several cell lines has been reported to increase levels of polymerised (F) actin, which although may increase plasma membrane tension [178], is thought to be required for HIV-1 fusion in reporter and primary CD4+ T cells [312]. It is likely that our observation in global changes in membrane tension during HIV-1 entry in TZM-bl cells (Figure 2.3.13) may be, in part, due to HIV-1-induced changes in actin polymerisation during the entry process [313]. Future investigations aimed at dissecting the role of metabolism on HIV-1 fusion in target cells would benefit from experiments which independently evaluate the role of actin polymerisation, membrane tension and glycolysis to

separate the contribution of these potentially confounding factors, which all likely influence the HIV-1 fusion reaction.

Using a FLIM-based reporter system of glycolytic flux concomitant with assays of fusion and infection, we detected that heterogenous differences in host cell metabolism may lead to downstream differences in HIV-1 infection and fusion (Figure 2.3.2 and Figure 2.3.4) in reporter cells. To extend our results to more physiologically relevant target cells, we attempted to apply our FLIM-based reporter system to primary CD4+ T cells. Unfortunately, neither DNA nor RNA transfection led to expression of FLIM-based reporters in these cells. Therefore, future investigations solving these barriers in primary cells are required in order to determine if our findings are applicable to these more physiologically relevant targets of HIV-1.

Nevertheless, it is tempting to speculate that our results described here may be extended to HIV-1 target cells residing in tissues, such as lymph nodes or the gastrointestinal tract, which contain an array of metabolic microenvironments [197,198,200]. Therefore, our work here paves the way for future investigations to determine the role of metabolism in HIV-1 target cell susceptibility in tissues. Studies which employ multi-photon microscopy-based platforms which enable deep tissue penetration, such as two-photon FLIM, would allow the spatial resolution required to visualise the metabolic state of several HIV-1 target cells in discrete tissue microenvironments which may increase or decrease susceptibility to productive HIV-1 infection. Additionally, although our investigation described here applies specifically to acute HIV-1 entry and infection, it is likely that the tools developed here would reveal metabolic differences in target cells which are latently infected with HIV-1 versus those which are acutely infected. Recently, one

such study has illustrated the establishment of HIV-1 latency correlates with potent decreases in glycolytic flux and an increased reliance of the host cell on antioxidants for cell survival [314]. Importantly, owing to this increased antioxidant dependency, latently-infected cells which are pharmacologically-prevented from replenishing this antioxidant pool favours HIV-1 reactivation [314]. Therefore, it is possible that understanding the role of host cell metabolism is not only relevant to understand events leading to HIV-1 entry, but the establishment and potential disruption of HIV-1 latency.

Although our results implicate that acute 2-DG treatment sequesters cholesterol from multiple membrane compartments in reporter and primary CD4+ T cells, further work is necessary to characterise this pathway. Additionally, it is critical to determine if other membrane lipids (e.g. sphingomyelin) and phospholipids (e.g. phosphatidylserine) are regulated similarly to cholesterol during glycolytic arrest, as they too have been shown to facilitate the HIV-1 fusion reaction [253,315]. Furthermore, as we determined that both membrane order and cholesterol content are decreased in 2-DG-treated cells, it is possible that target cell CD4 and co-receptor mobility necessary for HIV-1 infection is also altered [155,315]. Therefore, future investigations using fluorescence fluctuation spectroscopy-based methods to track HIV-1 receptor and co-receptor mobility will determine if diminished membrane order or lipid content would disrupt receptor mobility required for HIV-1 entry. Finally, as our results reinforce previous findings that host membrane cholesterol is necessary for HIV-1 fusion, it is tempting to speculate that treatment with cholesterol-lowering reagents, such as simvastatin (Figure 2.3.5) may lead to decreased HIV-1 trans-infection *in vivo*. These results, in part, may explain previous clinical studies showing that

HIV-1 target cells from long-term non-progressors have substantially lower plasma membrane cholesterol content [217,218].

The second project, discussed in Chapter 3, draws upon the tools utilised in Chapter 2 to dissect the mechanism of restriction of virus-cell fusion by the potent restriction factor IFITM3. In particular, we provide functional proof for the first time that IFITM3 remodels membranes (i.e. increases membrane rigidity) in a manner that is dependent on its amphipathic helix and its ability to oligomerise to inhibit virus-cell fusion [105]. Consequently, these results complement recent investigations positing how and when IFITM3 inhibits virus-cell membrane fusion: the amphipathic helices of IFITM3 oligomers may locally stiffen and/or bend membranes [56,101] in endosomal vesicles carrying virions to block escape into the cytoplasm [82,84,91]. Furthermore, given that human IFITM1 and IFITM2 also harbour the GxxxG motif (Figure 3.3.1C), it is likely these antiviral proteins self-oligomerise as well in order to perform their antiviral function. Moreover, as GxxxG motifs also enable hetero-multimerization [272], it is likely that this motif enhances the formation of IFITM hetero-oligomers as well [77,104]. Importantly, as IFITM3 is critical in controlling several viral infections *in vivo* [31,32,283], including that of pandemic SARS-CoV2 [316], understanding its mechanism of action may not only help design novel therapeutics which target the fusion process, but also explain how other pathogenic viruses escape its antiviral activity.

Interestingly, our model of IFITM3 restriction of virus-cell fusion also supports the antiviral function of IFITM3 in viral membranes [74,95,97,102,278]. In particular, we observed that transient expression of WT IFITM3 in HIV-1 producing cells substantially diminished HIV-

1 virion infectivity (Figure 3.3.5A and Figure 3.3.5B). Furthermore, although we showed that mutation of IFITM3 glycine-91 or glycine-95 substantially decreased anti-viral activity against HIV-1 (Figure 3.3.5A and Figure 3.3.5B), restored the levels of HIV-1 Env in cells and nascent virions (Figure 3.3.5C and Figure 3.3.5D), and rescued HIV-1 Env processing (Figure 3.3.5D), these mutations resulted in differential HIV-1 restriction. Consequently, it is likely other mechanisms are necessary for restriction other than Env quantity, and that IFITM3 oligomerisation may not be critical for restricting HIV-1 virion infectivity as opposed to blocking virus-cell fusion.

Moreover, IFITM3 harbouring the G91L or G95L mutation incorporated in virions less efficiently relative to wildtype (Figure 3.3.5D and Figure 3.3.5G), and it is likely their varying levels of incorporation correlates to the differential impact on antiviral activity (Figure 3.3.5A, Figure 3.3.5B, Figure 3.3.5D and Figure 3.3.5G). Although we did not detect any obvious alterations in cell surface staining of FLAG-WT-IFITM3 or its corresponding mutants (Figure 3.3.3), higher levels of FRET were visible at the cell surface in 293T cells co-expressing N-terminal-tagged WT-IFITM3-YFP or WT-IFITM3-mCherry compared to constructs containing the G91L or G95L mutation (Figure 3.3.6). Therefore, although it is likely that the quantity of WT-IFITM3 oligomers is higher at the cell surface than the glycine-91 or glycine-95 mutants, further work is needed to dissect the impact of IFITM3 oligomers on its own and Env's incorporation during HIV-1 assembly. Finally, it is likely that IFITM3-laden virions may have altered membrane order which may impact Env quality, such that their ability to fuse with target cells becomes drastically diminished, although further work is needed to confirm this hypothesis.

Encouragingly, several future studies can be envisioned to answer these questions. In particular, the capacity for IFITM3 to form oligomers in membranes may differ between cell membranes and virions [156,317]. To determine the oligomeric state of IFITM3 in producer cells and in virions, cells may be transfected to express fluorescently-tagged IFITM3 and fluorescently-tagged HIV-1, where labelled virions harbouring fluorophore-tagged IFITM3 and can be harvested from supernatants and purified through a sucrose cushion, fixed on imaging grids, and stained with nanobodies [155] to resolve IFITM3 oligomers and quantify their stoichiometry via STORM imaging. Recent investigations have already begun to utilise this platform to measure the stoichiometry of other HIV-1 restriction factors, such as serine incorporator protein 5 (SERINC5) in 2D and 3D space within virus particles [318].

To visualise the oligomeric state of IFITM3 at sites of viral assembly and egress, Gag-labelled HIV-1 may be produced in 293T cells and the plasma membrane may be concomitantly labelled. As Gag traffics to the plasma membrane to initiate the virus assembly process, it may act as a marker for assembly sites [319]. Pools of IFITM3 and Gag localised to the plasma membrane may then subsequently be imaged with STORM and colocalization thus can be assessed, as well as the quantification of IFITM3 oligomers at these sites. In parallel, an anti-p17 Matrix antibody can be used to identify processed (i.e. mature) Gag generated during the budding of infectious virions. If these experiments include the oligomerisation defective IFITM3 mutant (i.e. G91L and G95L), such investigations will be able to assess how oligomerisation impacts IFITM3 localisation to virus assembly sites and incorporation into virions.

Although STORM has been previously used to resolve the oligomeric state of proteins in cellular membranes and in membranes of enveloped viruses [155,320], these studies are performed under fixed conditions and do not measure protein dynamics through time. Furthermore, fixatives applied to samples for STORM imaging may disrupt the morphology of cells and viruses to be imaged [321]. Moreover, many fixatives cross-link proteins and thus could disrupt their propensity to oligomerise [321]. Stimulated emission depletion-fluorescent correlation spectroscopy (STED-FCS) is one imaging platform that can overcome these limitations [156]. Briefly, STED-FCS enables the non-invasive and sensitive measurement of complex dynamic processes (e.g. diffusion and kinetics of proteins) with nanoscale resolution. Therefore, future investigations which track the evolution of the oligomeric state of labelled IFITM proteins in real-time during HIV-1 biogenesis will be benefitted via a STED-FCS approach [156,163]. We have illustrated that IFITM3 labelled with STED-adapted fluorophores retain antiviral function against IAV (Figure 3.3.7A). Therefore, initial experiments to apply this method to IFITM3 restriction must also determine fluorescently-tagged IFITM3 is active against HIV-1 when expressed in virus-producing cells. Following this, STED-FCS microscopy may be applied to measure IFITM3 diffusion coefficients (i.e. mobility) at virus assembly sites, within virions and to calculate IFITM3 stoichiometry at these sites.

Although the proposed experiments above enable the elucidation of IFITM3's oligomeric state, they do not reveal the impact of IFITM3 oligomers on virion membrane order. IFITM3 is suspected to restrict virus-cell fusion by altering membrane order and curvature in host cells [51,86] and we showed that IFITM3 increases membrane order in host cells (Figure 3.3.12 and Figure 3.3.13) [117]. It is tempting to speculate that IFITM3 residing in HIV-1 virions increases

the order of viral membranes as well. Membrane stiffening has been shown to hinder HIV-1 fusion [322] and prior reports have demonstrated that multiple regions of HIV-1 Env interact with ordered lipids [323]. Therefore, increases in viral lipid order may explain how virion-associated IFITM3 disrupts HIV-1 fusion. To determine this, we will use FLIM imaging of mature HIV-1 virions that contain or do not contain IFITM3 to quantify viral lipid order using the probes Laurdan and FliptR, two probes which report membrane stiffness [105,137,156,240]. Moreover, as our G95L mutant was defective in increasing membrane order in cells, we will use this mutant to determine if IFITM3 oligomerisation in virions is required to increase viral lipid order. Ultimately, results from these investigations will reveal, for the first time, the oligomeric state of IFITM3 in viral membranes important to the HIV lifecycle as well as its impact on membrane order at these sites.

IFITM3 has also been shown to disrupt cholesterol homeostasis, such that the endolysosmal pathway is laden with excess cholesterol to prevent lipid mixing and virus escape [87,255]. Furthermore, IFITM3 has been shown to bind preferentially to specific membrane phospholipids [115], although the ability of IFITM3 to bind sterols directly has not been tested. Future investigations are needed to untangle the role of IFITM3 and cholesterol homeostasis. In particular, as we have revealed that the GxxxG motif enables IFITM3 homotypic interactions, it is tempting to infer that this motif facilitates oligomerisation with other proteins as well, such as VAPA, or an unidentified protein, such that cholesterol homeostasis may be altered. Mass spectrometry studies will assist in identifying differences in binding partners between wildtype IFITM3 and IFITM3 mutants harbouring the G91L or G95L mutation. Additionally, this approach may also be used to determine if any observed alteration in HIV-1 lipid order observed in virions is due to differential lipid composition between virions containing IFITM3 versus virions devoid

of IFITM3. At present, studies analysing IFITM3-induced changes in viral lipid composition have failed to separate virus particles from exosomes [256]. Moreover, studies analysing virion lipid content in the context of IFITM3 have restricted their analyses to cholesterol and cholesterol esters via kits [256]. To overcome this challenge, gradient centrifugation may be used to reliably generate exosome-free virus preps. These results will identify if IFITM3 alters the lipid composition of HIV-1 virions, in addition to its impact on lipid order in host cells.

Although these proposed studies have mapped a path to observe IFITM3 oligomerisation in virions and link this phenomenon to virion membrane order and HIV-1 infectivity, they may also be used to assess how IFITM3 impacts Env quality in virions. Env mobility is necessary to form the entry "claw" required for infectivity [324], and membrane protein mobility is heavily influenced by membrane rigidity [325]. Previous work has illustrated that single HIV-1 virions can be labelled concomitantly with immunolabeled Env and avoid antibody-induced clustering [162]. Furthermore, nanoscopy platforms are becoming increasingly adapted to track Env mobility with heightened spatiotemporal resolution [155,156,159,163,318,324]. Therefore, STED-FCS microscopy may be applied to assess whether IFITM3 affects the clustering and diffusion of labelled Env that is necessary for entry into target cells. Immature virions, produced by mutations in Gag which prevent its proteolytic maturation, may serve as a negative control, as Env mobility in these virions is potently reduced [324]. Additionally, armed with the oligomerisation-defective mutant of IFITM3 (G95L), one could investigate how IFITM3 oligomers impact this process. We anticipate that IFITM3 oligomers may decrease the mobility of HIV-1 Env, and consequently, its ability to form infectious clusters on the virion surface. One caveat to this approach, however, is that STED-FCS suffers requires high laser power, and therefore risks photobleaching and

damaging of the sample, thus confounding the auto-correlation curve, which may distort the measurements of HIV-1 Env or IFITM3 mobility [326].

Finally, prior studies have demonstrated that IFITM3's activity against HIV-1 transmitted-founder (TF) viruses is decreased [98]. Furthermore, this resistance has been mapped to multiple regions of HIV-1 Env [323]. Therefore, application of the approaches described above to HIV-1 virions harbouring T/F Env may help elucidate how these viruses escape restriction. Ultimately, these investigations will reveal with sub-diffraction resolution, how IFITM3 restricts HIV-1 virion infectivity.

In Chapter 4, we further investigated the role of the GxxxG motif in IFITM protein function by determining if loss of this oligomerisation motif over the course of *IFITM* evolution contributed to the absence of antiviral activity in human IFITM5. We discovered that multiple vertebrate orthologs of IFITM5 harboured ^{70}GxxxA^{74} instead of GxxxG. Interestingly, several (small)xxxx(small) motifs have been shown to facilitate transmembrane protein oligomerisation [272,273,308,309]. Nevertheless, previous investigations dissecting the role of these motifs in mediating protein self-association have shown that mutation of glycine to a larger hydrophobic residue may increase steric hindrance which could diminish oligomerisation propensity [308,311]. Our results suggest that the homologous GxxxG motif in the *IFITM* locus is exquisitely sensitive to such mutations, as changing glycine-95 to leucine in IFITM3 and the presence of alanine-74 in IFITM5 resulted in diminished or minimally detectable oligomerisation as reported by our live cell FRET and FLIM assays. Furthermore, restoration of the GxxxG motif in IFITM5 enhanced its detected FRET signal and restriction activity against VSV-HA and VSV-VSVG, suggesting this

motif was lost during the course of IFITM5 evolution, which likely contributed to its diminished antiviral activity. These results collectively indicate that the GxxxG motif is required for oligomerisation of both antiviral and non-antiviral IFITMs.

Further work is required to solidify our results presented in Chapter 4. For example, although human IFITM5 is typically not associated with antiviral immunity, it has been reported that overexpression of IFITM5 may lead to disruption of the plasma membrane protein complexes, resulting in the upregulation of several interferon-inducible genes downstream [119,296]. These results suggest that IFITM5 could create hetero-oligomeric interactions with other protein binding partners which may have multiple physiological consequences, which could account for some of its previously noted low antiviral activity [68]. In turn, it is just as likely that restoration of the GxxxG motif in IFITM5 may disrupt several protein complexes or promote the formation of others in the plasma membrane or elsewhere. For example, it is possible that the IFITM5 A74G may be capable of forming hetero-oligomeric complexes with antiviral IFITM3. Consequently, we cannot rule out that overexpression of IFITM5 or its mutants could lead to upregulation of antiviral genes or formation of complexes which deter virus infection. Nevertheless, the fact that IFITM5 partakes in hetero-oligomeric interactions and associate with different complexes in the plasma membrane may be relevant to uncovering IFITM5's cryptic role in bone mineralisation if investigated further.

Although this investigation purports that the GxxxG motif is able to partially restore the antiviral activity of human IFITM5, it is likely orthologous *IFITM5* of other vertebrates have also lost their antiviral activity due to disruption of the GxxxG motif. Therefore, it is prudent to assess the oligomerisation capacity of non-human IFITM5 orthologs which lack an intact GxxxG motif,

and if restoration of this motif enhances their antiviral function and oligomerisation propensity. Finally, even though we predict the first alpha helix of IFITM5 is amphipathic, which may explain its partial antiviral activity, functional assays must confirm these predictions. For example, alanine mutagenesis of the polar residues or substitution of large polar amino acids on the hydrophobic face of this helix would disrupt its amphipathicity. Consequently, if these mutated versions of IFITM5 lost their ability to restrict infection, it is likely that its mechanism of restriction is similar to IFITM3. Nevertheless, our report here emphasises the role of the GxxxG motif in the broader evolution of the *IFITM* locus.

Together, this dissertation has utilised a combination of biochemical and microscopy strategies to uncover novel determinants of host membrane order and tension and link their influence to target cell susceptibility to viral infection and the course of the virus-cell fusion reaction. Furthermore, these findings support the proposed metabolic hierarchy of T cell susceptibility to HIV-1 infection, offer a more complete model of how IFITM3 broadly restricts virus infection, and suggest further avenues of study to dissect how non-antiviral IFITMs have lost their restrictive function. Importantly, the research described here create frameworks to explore these biophysical properties in human physiology outside the context virus-cell fusion. Indeed, given the conserved, membrane-altering features shared within the CD225 protein superfamily, it is tempting to speculate several poorly characterised members alter membrane order, tension or curvature to regulate fusion processes which remains to be realised. For example, poorly-understood CD225 proteins SynDIG1 and SynDIG4 are known regulators of excitatory synapse development and must localise to membranes to perform this role, which is known to be dependent on membrane fluidity [120,327,328]. Additionally, research connecting disrupted plasma

membrane tension and membrane order with pathologic intracellular signalling is now appearing, particularly in mechano-transduction, cell growth and haematological cancers, where IFITM proteins have recently been shown to be centrally involved [115,179]. Utilising live-cell imaging approaches to quantify these biophysical parameters, it is inevitable that additional, uncharacterised fusion events underpinning several physiological processes will be uncovered. Undoubtedly, the probing and manipulation of the membrane biophysical landscape in live cells will continue to uncover new and exciting fusion processes in human disease.

Appendices

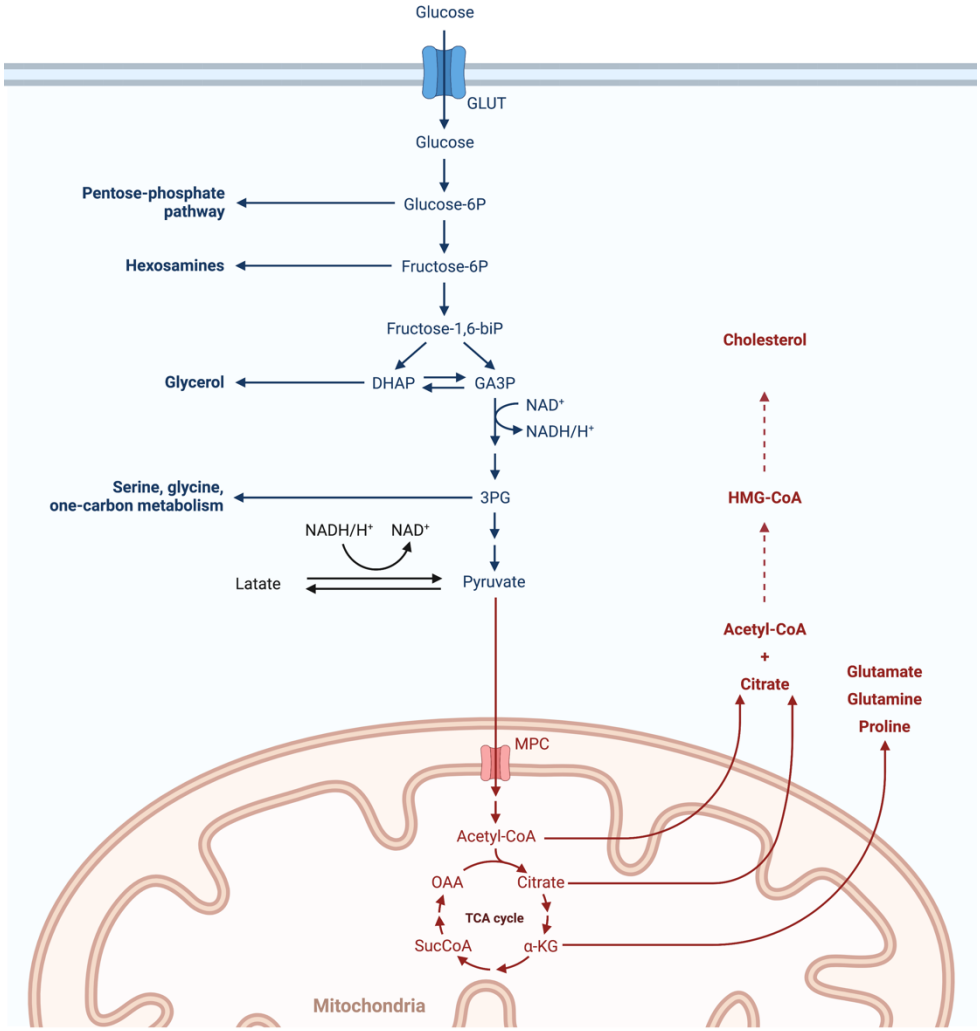

Figure 5.1.1. Aerobic glycolysis end-products drive cytosolic lipogenesis. Glycolysis derived pyruvate enters the mitochondrion via mitochondrial pyruvate carriers (MPC) to fuel the tricarboxylic acid (TCA) cycle to drive oxidative phosphorylation (not shown). In addition, cancer cells or activated immune cells may export citrate to the cytosol, where it is converted back to acetyl coenzyme A (acetyl-CoA) by ATP citrate lyase. A surplus of cytosolic acetyl-CoA enables fatty acid synthesis and cholesterol synthesis. Cholesterol synthesis begins when citrate is converted to acetyl-CoA, and three molecules of acetyl-CoA are consumed to create HMG-CoA, the precursor of cholesterol and is consumed by HMG-CoA reductase to initiate the committed step of cholesterol biogenesis. Created with Biorender.

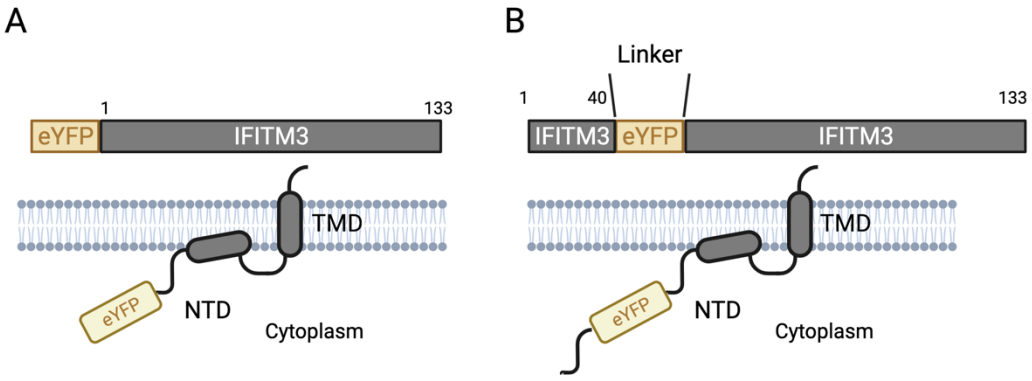

Figure 5.1.2. Construction of IFITM3 tagged with fluorescent proteins. (**A**) Cartoon and schematic representation of the N-terminally tagged IFITM3 fusion protein. The fluorescent protein may represent either eYFP (pictured) or mCherry and was fused to the N-terminus of IFITM3. (**B**) Cartoon and schematic representation of the internally tagged IFITM3-eYFP fusion protein. eYFP was flanked with flexible linkers (GGGSGG) and inserted after residue 40 of IFITM3. The fluorescent protein may represent either eYFP (pictured) or mCherry. NTD, N-terminal domain. TMD, transmembrane domain. The N-terminally-tagged IFITM3 constructs were used in the FRET, FLIM and Number and Brightness studies in Chapter 3. The internally-tagged IFITM3 constructs were used in confirmatory FRET and FLIM experiments.

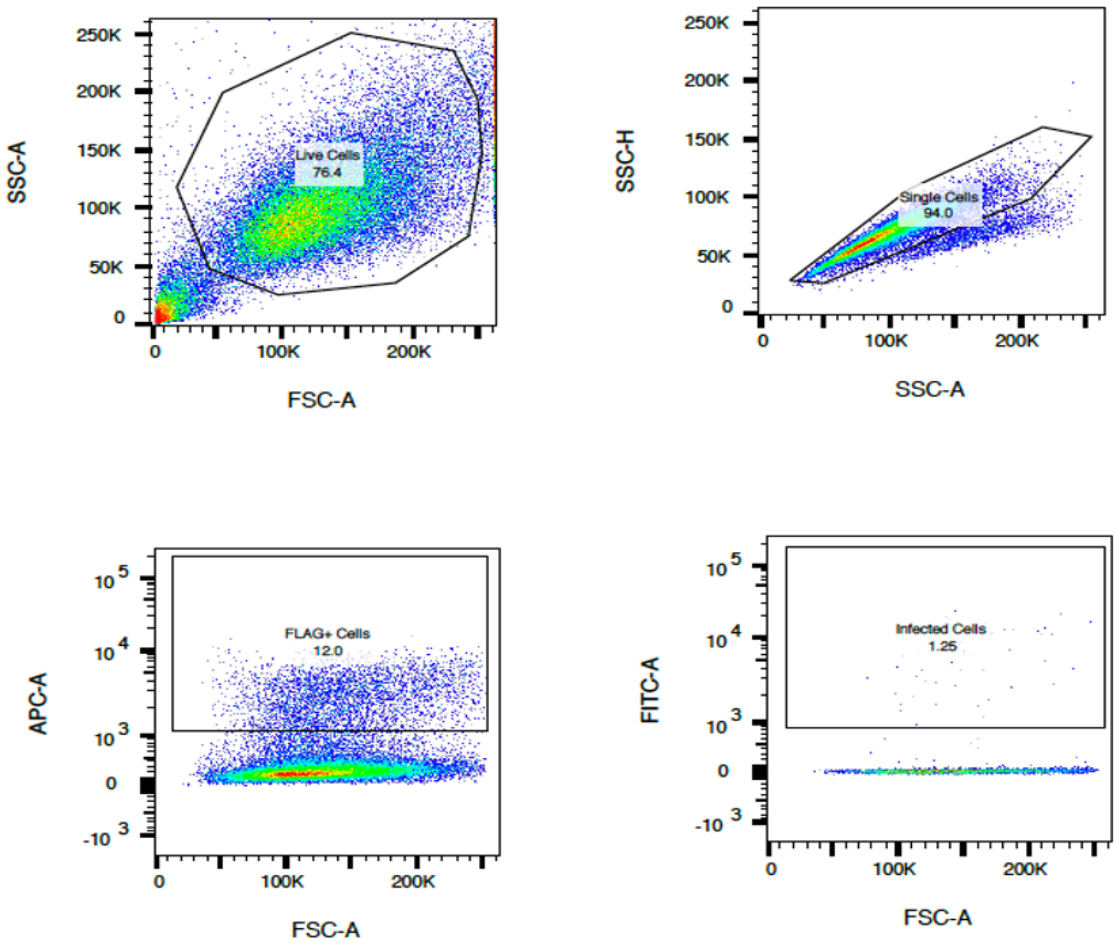

Figure 5.1.3. Gating strategy to identify IFITM5-expressing, virus infected cells. Live, single cells were broadly selected for using a forward and side scatter gating strategy (Top Row). From this point, FLAG+ cells were gated on, and the proportion of GFP+ positive cells were recorded for infection.

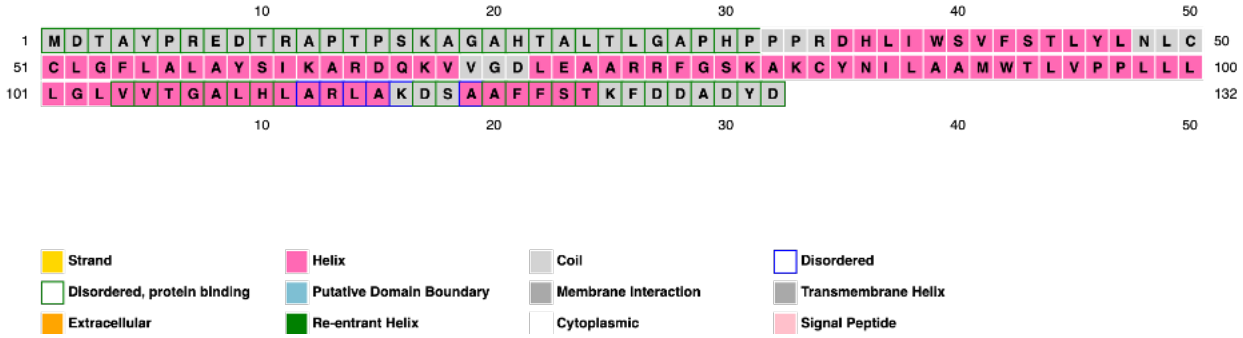

Figure 5.1.4. PSIPRED structural prediction program suggests multiple helical domains in IFITM5. Secondary structure prediction for human IFITM5 primary amino acid sequence using PSIPRED.

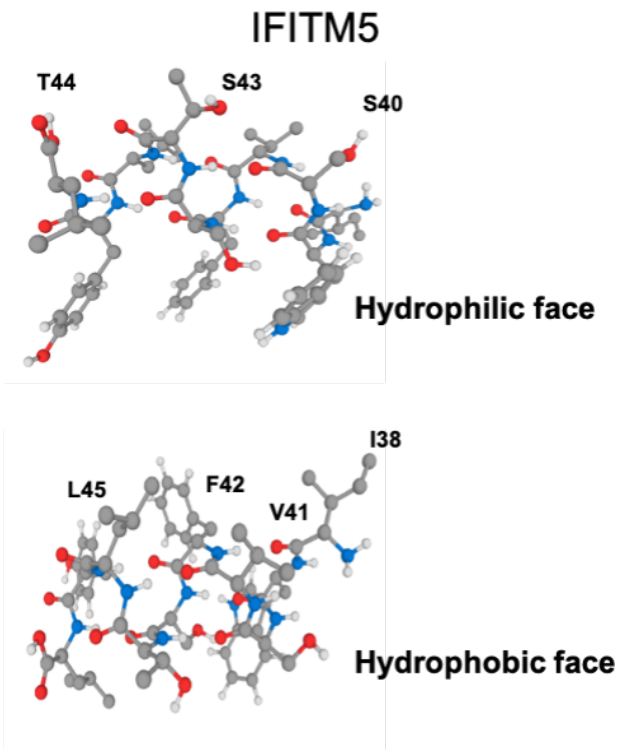

Figure 5.1.5. Secondary structure prediction via PEP-FOLD supports identification of an amphipathic helix within IFITM5. Different views of the helix predicted for amino acid residues IWSVFSTLYL produced using the PEP-FOLD prediction program displaying both a hydrophilic (Top) and hydrophobic (Bottom) face.

References:

[1] S. Koyama, K.J. Ishii, C. Coban, S. Akira, Innate immune response to viral infection, Cytokine. 43 (2008) 336–341. https://doi.org/10.1016/j.cyto.2008.07.009.

[2] M.R. Thompson, J.J. Kaminski, E.A. Kurt-Jones, K.A. Fitzgerald, Pattern recognition receptors and the innate immune response to viral infection, Viruses. 3 (2011) 920–940. https://doi.org/10.3390/v3060920.

[3] S.R. Talemi, T. Höfer, Antiviral interferon response at single-cell resolution, Immunol. Rev. 285 (2018) 72–80. https://doi.org/10.1111/imr.12699.

[4] S. Akira, S. Uematsu, O. Takeuchi, Pathogen recognition and innate immunity, Cell. 124 (2006) 783–801. https://doi.org/10.1016/j.cell.2006.02.015.

[5] R. Medzhitov, Recognition of microorganisms and activation of the immune response, Nature. 449 (2007) 819–826. https://doi.org/10.1038/nature06246.

[6] W.M. Schneider, M.D. Chevillotte, C.M. Rice, Interferon-Stimulated Genes: A Complex Web of Host Defenses, Annu. Rev. Immunol. 32 (2014) 513–545. https://doi.org/10.1146/annurev-immunol-032713-120231.

[7] C.J. Secombes, J. Zou, Evolution of interferons and interferon receptors, Front. Immunol. 8 (2017) 2–11. https://doi.org/10.3389/fimmu.2017.00209.

[8] J.W. Schoggins, C.M. Rice, Interferon-stimulated genes and their antiviral effector functions, Curr. Opin. Virol. 1 (2011) 519–525. https://doi.org/10.1016/j.coviro.2011.10.008.

[9] M. Colomer-Lluch, A. Ruiz, A. Moris, J.G. Prado, Restriction Factors: From Intrinsic Viral Restriction to Shaping Cellular Immunity Against HIV-1, Front. Immunol. 9 (2018) 2876. https://doi.org/10.3389/fimmu.2018.02876.

[10] P.D. Bieniasz, Intrinsic immunity: A front-line defense against viral attack, Nat. Immunol. 5 (2004) 1109–1115. https://doi.org/10.1038/ni1125.

[11] Z. Zhang, J. Liu, M. Li, H. Yang, C. Zhang, Evolutionary Dynamics of the Interferon-Induced Transmembrane Gene Family in Vertebrates, PLoS One. 7 (2012) 1–13. https://doi.org/10.1371/journal.pone.0049265.

[12] M. Sällman Almén, N. Bringeland, R. Fredriksson, H.B. Schiöth, The Dispanins: A novel gene family of ancient origin that contains 14 human members, PLoS One. 7 (2012). https://doi.org/10.1371/journal.pone.0031961.

[13] D. Hickford, S. Frankenberg, G. Shaw, M.B. Renfree, Evolution of vertebrate interferon inducible transmembrane proteins, BMC Genomics. 13 (2012). https://doi.org/10.1186/1471-2164-13-155.

[14] A.A. Compton, N. Roy, F. Porrot, A. Billet, N. Casartelli, J.S. Yount, C. Liang, O. Schwartz, Natural mutations in IFITM 3 modulate post-translational regulation and toggle antiviral specificity , EMBO Rep. 17 (2016) 1657–1671. https://doi.org/10.15252/embr.201642771.

[15] J. Hanagata, X. Li, H. Morita, T. Takemura, J. LI, T. Minowa, Characterization of the osteoblast-specific transmembrane protein IFITM5 and analysis of IFITM5-deficient mice, J. Bone Miner. Metab. 29 (2011) 279–290.

[16] A. Patoine, M.H. Gaumond, P.K. Jaiswal, F. Fassier, F. Rauch, P. Moffatt, Topological mapping of BRIL reveals a type II orientation and effects of osteogenesis imperfecta mutations on its cellular destination, J. Bone Miner. Res. 29 (2014) 2004–2016. https://doi.org/10.1002/jbmr.2243.

[17] C.C. Bailey, G. Zhong, I. Huang, M. Farzan, IFITM-Family Proteins : The Cell ' s First

Line of Antiviral Defense, (2014). https://doi.org/10.1146/annurev-virology-031413-085537.

[18] X. Zhao, J. Li, C.A. Winkler, P. An, J.T. Guo, IFITM genes, variants, and their roles in the control and pathogenesis of viral infections, Front. Microbiol. 10 (2019) 1–12. https://doi.org/10.3389/fmicb.2018.03228.

[19] X. Wu, V.L. Dao Thi, Y. Huang, E. Billerbeck, D. Saha, H.H. Hoffmann, Y. Wang, L.A.V. Silva, S. Sarbanes, T. Sun, L. Andrus, Y. Yu, C. Quirk, M. Li, M.R. MacDonald, W.M. Schneider, X. An, B.R. Rosenberg, C.M. Rice, Intrinsic Immunity Shapes Viral Resistance of Stem Cells, Cell. 172 (2018) 423-438.e25. https://doi.org/10.1016/j.cell.2017.11.018.

[20] C.X. Wang, B.D. Sather, X. Wang, J. Adair, I. Khan, S. Singh, A. Adams, G. Curinga, H. Kiem, C.H. Miao, D.J. Rawlings, B.E. Torbett, C.X. Wang, B.D. Sather, X. Wang, J. Adair, I. Khan, S. Singh, S. Lang, A. Adams, G. Curinga, H. Kiem, C.H. Miao, D.J. Rawlings, B.E. Torbett, Rapamycin relieves lentiviral vector transduction resistance in human and mouse hematopoietic stem cells, 124 (2014) 913–923. https://doi.org/10.1182/blood-2013-12-546218.

[21] G. Shi, S. Ozog, B.E. Torbett, A.A. Compton, mTOR inhibitors lower an intrinsic barrier to virus infection mediated by IFITM3, 115 (2018) 10069–10078. https://doi.org/10.1073/pnas.1811892115.

[22] E. Knight, D. Fahey, D. Blomstrom, Interferon-beta Enhances the Synthesis of a 20,000-dalton Membrane Protein: A Correlation With the Cessation of Cell Growth, J Interf. Res. 5 (1985) 305–313.

[23] G.A. Deblandre, O.P. Marinx, S.S. Evans, S. Majjaj, O. Leo, D. Caput, G.A. Huez, M.G.

Wathelet, Expression cloning of an interferon-inducible 17-kDa membrane protein implicated in the control of cell growth, J. Biol. Chem. 270 (1995) 23860–23866. https://doi.org/10.1074/jbc.270.40.23860.

[24] D. Alber, P. Staeheli, Partial Inhibition of Vesicular Stomatitis Virus by the Interferon-Induced Human 9-27 Protein, J Interf. Cytokine Res. 16 (1996) 375–380.

[25] H. Zhu, C. Liu, Interleukin-1 Inhibits Hepatitis C Virus Subgenomic RNA Replication by Activation of Extracellular Regulated Kinase Pathway, J. Virol. 77 (2003) 5493–5498. https://doi.org/10.1128/jvi.77.9.5493-5498.2003.

[26] M. Saitou, A molecular programme for the germ line specification in mice, Seikagaku. 75 (2003) 42–46.

[27] S. Tanaka, Y. Matsuia, Developmentally regulated expression of mil-1 and mil-2, mouse interferon-induced transmembrane protein like genes, during formation and differentiation of primordial germ cells, Gene Expr. Patterns. 2 (2003) 297–303. https://doi.org/10.1016/S0.

[28] U.C. Lange, D.J. Adams, C. Lee, S. Barton, R. Schneider, A. Bradley, M.A. Surani, Normal Germ Line Establishment in Mice Carrying a Deletion of the Ifitm/Fragilis Gene Family Cluster, Mol. Cell. Biol. 28 (2008) 4688–4696. https://doi.org/10.1128/mcb.00272-08.

[29] Y.S. Wee, J.J. Weis, L.C. Gahring, S.W. Rogers, J.H. Weis, Age-related onset of obesity corresponds with metabolic dysregulation and altered microglia morphology in mice deficient for Ifitm proteins, PLoS One. 10 (2015) 1–16. https://doi.org/10.1371/journal.pone.0123218.

[30] A.L. Brass, I.C. Huang, Y. Benita, S.P. John, M.N. Krishnan, E.M. Feeley, B.J. Ryan, J.L.

Weyer, L. van der Weyden, E. Fikrig, D.J. Adams, R.J. Xavier, M. Farzan, S.J. Elledge, The IFITM Proteins Mediate Cellular Resistance to Influenza A H1N1 Virus, West Nile Virus, and Dengue Virus, Cell. 139 (2009) 1243–1254. https://doi.org/10.1016/j.cell.2009.12.017.

[31] A.R. Everitt, S. Clare, T. Pertel, S.P. John, R.S. Wash, S.E. Smith, C.R. Chin, E.M. Feeley, J.S. Sims, D.J. Adams, H.M. Wise, L. Kane, D. Goulding, P. Digard, V. Anttila, J.K. Baillie, T.S. Walsh, D.A. Hume, A. Palotie, Y. Xue, V. Colonna, C. Tyler-Smith, J. Dunning, S.B. Gordon, R.L. Smyth, P.J. Openshaw, G. Dougan, A.L. Brass, P. Kellam, K. Everingham, H. Dawson, D. Hope, P. Ramsay, A. Campbell, S. Kerr, D. Harrison, K. Rowan, J. Addison, N. Donald, S. Galt, D. Noble, J. Taylor, N. Webster, I. Taylor, J. Aldridge, R. Dornan, C. Richard, D. Gilmour, R. Simmons, R. White, C. Jardine, D. Williams, M. Booth, T. Quasim, V. Watson, P. Henry, F. Munro, L. Bell, J. Ruddy, S. Cole, J. Southward, P. Allcoat, S. Gray, M. McDougall, J. Matheson, J. Whiteside, D. Alcorn, K. Rooney, R. Sundaram, G. Imrie, J. Bruce, K. McGuigan, S. Moultrie, C. Cairns, J. Grant, M. Hughes, C. Murdoch, A. Davidson, G. Harris, R. Paterson, C. Wallis, S. Binning, M. Pollock, J. Antonelli, A. Duncan, J. Gibson, C. McCulloch, L. Murphy, C. Haley, G. Faulkner, T. Freeman, D. Chaussabel, W.E. Adamson, W.F. Carman, C. Thompson, M.C. Zambon, P. Aylin, D. Ashby, W.S. Barclay, S.J. Brett, W.O. Cookson, L.N. Drumright, R.A. Elderfield, L. Garcia-Alvarez, B.G. Gazzard, M.J. Griffiths, M.S. Habibi, T.T. Hansel, J.A. Herberg, A.H. Holmes, T. Hussell, S.L. Johnston, O.M. Kon, M. Levin, M.F. Moffatt, S. Nadel, J.O. Warner, S.J. Aston, A. Hay, J. McCauley, A. O'Garra, J. Banchereau, A. Hayward, P. Kellam, P. Simmonds, P.S. McNamara, M.G. Semple, J.S. Nguyen-Van-Tam, L.P. Ho, A.J. McMichael, IFITM3 restricts the morbidity and

mortality associated with influenza, Nature. 484 (2012) 519–523. https://doi.org/10.1038/nature10921.

[32] C.C. Bailey, I.C. Huang, C. Kam, M. Farzan, Ifitm3 Limits the Severity of Acute Influenza in Mice, PLoS Pathog. 8 (2012). https://doi.org/10.1371/journal.ppat.1002909.

[33] A. Antonopoulou, F. Baziaka, T. Tsaganos, M. Raftogiannis, P. Koutoukas, A. Spyridaki, M. Mouktaroudi, A. Kotsaki, A. Savva, M. Georgitsi, E.J. Giamarellos-Bourboulis, Role of tumor necrosis factor gene single nucleotide polymorphisms in the natural course of 2009 influenza A H1N1 virus infection, Int. J. Infect. Dis. 16 (2012) e205–e209. https://doi.org/10.1016/j.ijid.2011.11.012.

[34] J. Zhou, K.K.W. To, H. Dong, Z.S. Cheng, C.C.Y. Lau, V.K.M. Poon, Y.H. Fan, Y.Q. Song, H. Tse, K.H. Chan, B.J. Zheng, G.P. Zhao, K.Y. Yuen, A functional variation in CD55 increases the severity of 2009 pandemic H1N1 influenza a virus infection, J. Infect. Dis. 206 (2012) 495–503. https://doi.org/10.1093/infdis/jis378.

[35] M.J. Ciancanelli, S.X.L. Huang, P. Luthra, H. Garner, Y. Itan, S. Volpi, F.G. Lafaille, C. Trouillet, M. Schmolke, R.A. Albrecht, E. Israelsson, H.K. Lim, M. Casadio, T. Hermesh, L. Lorenzo, L.W. Leung, V. Pedergnana, B. Boisson, S. Okada, C. Picard, B. Ringuier, F. Troussier, D. Chaussabel, L. Abel, I. Pellier, L.D. Notarangelo, A. García-Sastre, C.F. Basler, F. Geissmann, S.Y. Zhang, H.W. Snoeck, J.L. Casanova, Life-threatening influenza and impaired interferon amplification in human IRF7 deficiency, Science (80-.). 348 (2015) 448–453. https://doi.org/10.1126/science.aaa1578.

[36] Y.H. Zhang, Y. Zhao, N. Li, Y.C. Peng, E. Giannoulatou, R.H. Jin, H.P. Yan, H. Wu, J.H. Liu, N. Liu, D.Y. Wang, Y.L. Shu, L.P. Ho, P. Kellam, A. McMichael, T. Dong, Interferon-induced transmembrane protein-3 genetic variant rs12252-C is associated with

severe influenza in Chinese individuals, Nat. Commun. 4 (2013) 2–7. https://doi.org/10.1038/ncomms2433.

[37] Y. Zhang, S. Makvandi-Nejad, L. Qin, Y. Zhao, T. Zhang, L. Wang, E. Repapi, S. Taylor, A. McMichael, N. Li, T. Dong, H. Wu, Interferon-induced transmembrane protein-3 rs12252-C is associated with rapid progression of acute HIV-1 infection in Chinese MSM cohort, AIDS. 29 (2015) 889–894. https://doi.org/10.1097/QAD.0000000000000632.

[38] R. Jia, Q. Pan, S. Ding, L. Rong, S.-L. Liu, Y. Geng, W. Qiao, C. Liang, The N-Terminal Region of IFITM3 Modulates Its Antiviral Activity by Regulating IFITM3 Cellular Localization, J. Virol. 86 (2012) 13697–13707. https://doi.org/10.1128/jvi.01828-12.

[39] T.L. Foster, H. Wilson, S.S. Iyer, K. Coss, K. Doores, S. Smith, P. Kellam, A. Finzi, P. Borrow, B.H. Hahn, S.J.D. Neil, Resistance of Transmitted Founder HIV-1 to IFITM-Mediated Restriction, Cell Host Microbe. 20 (2016) 429–442. https://doi.org/10.1016/j.chom.2016.08.006.

[40] A.G. Randolph, W.K. Yip, E.K. Allen, C.M. Rosenberger, A.A. Agan, S.A. Ash, Y. Zhang, T.R. Bhangale, D. Finkelstein, N.Z. Cvijanovich, P.M. Mourani, M.W. Hall, H.C. Su, P.G. Thomas, Evaluation of IFITM3 rs12252 Association with Severe Pediatric Influenza Infection, J. Infect. Dis. 216 (2017) 14–21. https://doi.org/10.1093/infdis/jix242.

[41] T.C. Mills, A. Rautanen, K.S. Elliott, T. Parks, V. Naranbhai, M.M. Ieven, C.C. Butler, P. Little, T. Verheij, C.S. Garrard, C. Hinds, H. Goossens, S. Chapman, A.V.S. Hill, IFITM3 and susceptibility to respiratory viral infections in the community, J. Infect. Dis. 209 (2014) 1028–1031. https://doi.org/10.1093/infdis/jit468.

[42] M. López-Rodríguez, E. Herrera-Ramos, J. Solé-Violán, J.J. Ruíz-Hernández, L. Borderías, J.P. Horcajada, E. Lerma-Chippirraz, O. Rajas, M. Briones, M.C. Pérez-

González, M.A. García-Bello, E. López-Granados, F. Rodriguez de Castro, C. Rodríguez-Gallego, IFITM3 and severe influenza virus infection. No evidence of genetic association, Eur. J. Clin. Microbiol. Infect. Dis. 35 (2016) 1811–1817. https://doi.org/10.1007/s10096-016-2732-7.

[43] S.S. Prabhu, T.T. Chakraborty, N. Kumar, I. Banerjee, Association between IFITM3 rs12252 polymorphism and influenza susceptibility and severity: A meta-analysis, Gene. 674 (2018) 70–79. https://doi.org/10.1016/j.gene.2018.06.070.

[44] E.K. Allen, A.G. Randolph, T. Bhangale, P. Dogra, M. Ohlson, C.M. Oshansky, A.E. Zamora, J.P. Shannon, D. Finkelstein, A. Dressen, J. DeVincenzo, M. Caniza, B. Youngblood, C.M. Rosenberger, P.G. Thomas, SNP-mediated disruption of CTCF binding at the IFITM3 promoter is associated with risk of severe influenza in humans, Nat. Med. 23 (2017) 975–983. https://doi.org/10.1038/nm.4370.

[45] Y.C. Kim, M.J. Jeong, B.H. Jeong, Strong association of regulatory single nucleotide polymorphisms (SNPs) of the IFITM3 gene with influenza H1N1 2009 pandemic virus infection, Cell. Mol. Immunol. (2019) 3–5. https://doi.org/10.1038/s41423-019-0322-1.

[46] R.A. Smith, J. Young, J.J. Weis, J.H. Weis, Expression of the mouse fragilis gene products in immune cells and association with receptor signaling complexes, Genes Immun. 7 (2006) 113–121. https://doi.org/10.1038/sj.gene.6364278.

[47] Y. Chen, K. Welte, D. Gebhard, R. Evans, Induction of T cell aggregation by antibody to a 16kd human leukocyte surface antigen, J. Immunol. 133 (1984) 2496–2501.

[48] S. Takahashi, C. Doss, S. Levy, R. Levy, TAPA-1, the target of an antiproliferative antibody, is associated on the cell surface with the Leu-13 antigen., J. Immunol. 145 (1990) 2207–2213.

[49] A.L. Brass, D.M. Dykxhoorn, Y. Benita, N. Yan, A. Engelman, R.J. Xavier, J. Lieberman, S.J. Elledge, Identification of host proteins required for HIV infection through a functional genomic screen, Science (80-.). 319 (2008) 921–926. https://doi.org/10.1126/science.1152725.

[50] J.M. Weidner, D. Jiang, X.-B. Pan, J. Chang, T.M. Block, J.-T. Guo, Interferon-Induced Cell Membrane Proteins, IFITM3 and Tetherin, Inhibit Vesicular Stomatitis Virus Infection via Distinct Mechanisms, J. Virol. 84 (2010) 12646–12657. https://doi.org/10.1128/jvi.01328-10.

[51] K. Li, R.M. Markosyan, Y. Zheng, O. Golfetto, B. Bungart, M. Li, S. Ding, Y. He, C. Liang, J.C. Lee, E. Gratton, F.S. Cohen, S. Liu, IFITM Proteins Restrict Viral Membrane Hemifusion, PLoS Pathog. 9 (2013). https://doi.org/10.1371/journal.ppat.1003124.

[52] J.S. Yount, B. Moltedo, Y.Y. Yang, G. Charron, T.M. Moran, C.B. López, H.C. Hang, Palmitoylome profiling reveals S-palmitoylation-dependent antiviral activity of IFITM3, Nat. Chem. Biol. 6 (2010) 610–614. https://doi.org/10.1038/nchembio.405.

[53] J.S. Yount, R.A. Karssemeijer, H.C. Hang, S-palmitoylation and ubiquitination differentially regulate interferon-induced transmembrane protein 3 (IFITM3)-mediated resistance to influenza virus, J. Biol. Chem. 287 (2012) 19631–19641. https://doi.org/10.1074/jbc.M112.362095.

[54] C.C. Bailey, H.R. Kondur, I.C. Huang, M. Farzan, Interferon-induced transmembrane protein 3 is a type II transmembrane protein, J. Biol. Chem. 288 (2013) 32184–32193. https://doi.org/10.1074/jbc.M113.514356.

[55] Bor Luen Tang, Siew Heng Wong, Seng Hui Low, W. Hong, Retention of a type II surface membrane protein in the endoplasmic reticulum by the Lys-Asp-Glu-Leu

sequence, J. Biol. Chem. 267 (1992) 7072–7076.

[56] N.M. Chesarino, A.A. Compton, T.M. McMichael, A.D. Kenney, L. Zhang, V. Soewarna, M. Davis, O. Schwartz, J.S. Yount, IFITM 3 requires an amphipathic helix for antiviral activity , EMBO Rep. 18 (2017) 1740–1751. https://doi.org/10.15252/embr.201744100.

[57] S. Ling, C. Zhang, W. Wang, X. Cai, L. Yu, F. Wu, L. Zhang, C. Tian, Combined approaches of EPR and NMR illustrate only one transmembrane helix in the human IFITM3, Sci. Rep. 6 (2016) 1–8. https://doi.org/10.1038/srep24029.

[58] S. Blaskovic, M. Blanc, F.G. Van Der Goot, What does S-palmitoylation do to membrane proteins?, FEBS J. 280 (2013) 2766–2774. https://doi.org/10.1111/febs.12263.

[59] T.M. McMichael, L. Zhang, M. Chemudupati, J.C. Hach, A.D. Kenney, H.C. Hang, J.S. Yount, The palmitoyltransferase ZDHHC20 enhances interferon-induced transmembrane protein 3 (IFITM3) palmitoylation and antiviral activity, J. Biol. Chem. 292 (2017) 21517–21526. https://doi.org/10.1074/jbc.M117.800482.

[60] E. Garst, H. Lee, T. Das, S. Bhattacharya, A. Percher, R. Wiewiora, I.P. Witte, Y. Li, M. Goger, T. Peng, W. Im, H.C. Hang, Site-specific lipidation enhances IFITM3 membrane interactions and antiviral activity, BioRxiv. (2020) 1–32.

[61] R. Jia, F. Xu, J. Qian, Y. Yao, C. Miao, Y.M. Zheng, S.L. Liu, F. Guo, Y. Geng, W. Qiao, C. Liang, Identification of an endocytic signal essential for the antiviral action of IFITM3, Cell. Microbiol. 16 (2014) 1080–1093. https://doi.org/10.1111/cmi.12262.

[62] N.M. Chesarino, T.M. McMichael, J.C. Hach, J.S. Yount, Phosphorylation of the Antiviral Protein Interferon-inducible Transmembrane Protein 3 (IFITM3) Dually Regulates Its Endocytosis and Ubiquitination, J. Biol. Chem. 289 (2014) 11986–11992. https://doi.org/10.1074/jbc.M114.557694.

[63] K.N. Pandey, Small peptide recognition sequence for intracellular sorting, Curr. Opin. Biotechnol. 21 (2010) 611–620. https://doi.org/10.1016/j.copbio.2010.08.007.

[64] D. Rotin, S. Kumar, Physiological functions of the HECT family of ubiquitin ligases, Nat. Rev. Mol. Cell Biol. 10 (2009) 398–409. https://doi.org/10.1038/nrm2690.

[65] N.M. Chesarino, T.M. McMichael, J.S. Yount, E3 Ubiquitin Ligase NEDD4 Promotes Influenza Virus Infection by Decreasing Levels of the Antiviral Protein IFITM3, PLoS Pathog. 11 (2015) 1–18. https://doi.org/10.1371/journal.ppat.1005095.

[66] S.A. Wagner, P. Beli, B.T. Weinert, M.L. Nielsen, J. Cox, M. Mann, C. Choudhary, A Proteome-wide, Quantitative Survey of In Vivo Ubiquitylation Sites Reveals Widespread Regulatory Roles, Mol. Cell. Proteomics. 10 (2011) M111.013284. https://doi.org/10.1074/mcp.m111.013284.

[67] S.A. Wagner, P. Beli, B.T. Weinert, C. Schölz, C.D. Kelstrup, C. Young, M.L. Nielsen, J. V. Olsen, C. Brakebusch, C. Choudhary, Proteomic analyses reveal divergent ubiquitylation site patterns in murine tissues, Mol. Cell. Proteomics. 11 (2012) 1578–1585. https://doi.org/10.1074/mcp.M112.017905.

[68] I.C. Huang, C.C. Bailey, J.L. Weyer, S.R. Radoshitzky, M.M. Becker, J.J. Chiang, A.L. Brass, A.A. Ahmed, X. Chi, L. Dong, L.E. Longobardi, D. Boltz, J.H. Kuhn, S.J. Elledge, S. Bavari, M.R. Denison, H. Choe, M. Farzan, Distinct patterns of IFITM-mediated restriction of filoviruses, SARS coronavirus, and influenza A virus, PLoS Pathog. 7 (2011). https://doi.org/10.1371/journal.ppat.1001258.

[69] R. Mudhasani, J.P. Tran, C. Retterer, S.R. Radoshitzky, K.P. Kota, L.A. Altamura, J.M. Smith, B.Z. Packard, J.H. Kuhn, J. Costantino, A.R. Garrison, C.S. Schmaljohn, I.-C. Huang, M. Farzan, S. Bavari, IFITM-2 and IFITM-3 but Not IFITM-1 Restrict Rift Valley

Fever Virus, J. Virol. 87 (2013) 8451–8464. https://doi.org/10.1128/jvi.03382-12.

[70] T.M. McMichael, Y. Zhang, A.D. Kenney, L. Zhang, A. Zani, M. Lu, M. Chemudupati, J. Li, J.S. Yount, IFITM3 Restricts Human Metapneumovirus Infection, J. Infect. Dis. 218 (2018) 1582–1591. https://doi.org/10.1093/infdis/jiy361.

[71] J.W. Schoggins, S.J. Wilson, M. Panis, M.Y. Murphy, C.T. Jones, P. Bieniasz, C.M. Rice, A diverse range of gene products are effectors of the type i interferon antiviral response, Nature. 472 (2011) 481–485. https://doi.org/10.1038/nature09907.

[72] J. Lu, Q. Pan, L. Rong, S. Liu, C. Liang, The IFITM Proteins Inhibit HIV-1 Infection, J. Virol. 85 (2011) 2126–2137. https://doi.org/10.1128/JVI.01531-10.

[73] A.A. Compton, T. Bruel, F. Porrot, A. Mallet, M. Sachse, M. Euvrard, C. Liang, N. Casartelli, O. Schwartz, IFITM proteins incorporated into HIV-1 virions impair viral fusion and spread, Cell Host Microbe. 16 (2014) 736–747. https://doi.org/10.1016/j.chom.2014.11.001.

[74] K. Tartour, R. Appourchaux, J. Gaillard, X.N. Nguyen, S. Durand, J. Turpin, E. Beaumont, E. Roch, G. Berger, R. Mahieux, D. Brand, P. Roingeard, A. Cimarelli, IFITM proteins are incorporated onto HIV-1 virion particles and negatively imprint their infectivity, Retrovirology. 11 (2014) 1–14. https://doi.org/10.1186/s12977-014-0103-y.

[75] A.R. Everitt, S. Clare, J.U. McDonald, L. Kane, K. Harcourt, M. Ahras, A. Lall, C. Hale, A. Rodgers, D.B. Young, A. Haque, O. Billker, J.S. Tregoning, G. Dougan, P. Kellam, Defining the range of pathogens susceptible to ifitm3 restriction using a knockout mouse model, PLoS One. 8 (2013) 1–12. https://doi.org/10.1371/journal.pone.0080723.

[76] S.E. Smith, M.S. Gibson, R.S. Wash, F. Ferrara, E. Wright, N. Temperton, P. Kellam, M. Fife, Chicken Interferon-Inducible Transmembrane Protein 3 Restricts Influenza Viruses

and Lyssaviruses In Vitro , J. Virol. 87 (2013) 12957–12966. https://doi.org/10.1128/jvi.01443-13.

[77] X. Zhao, F. Guo, F. Liu, A. Cuconati, J. Chang, T.M. Block, J.T. Guo, Interferon induction of IFITM proteins promotes infection by human coronavirus OC43, Proc. Natl. Acad. Sci. U. S. A. 111 (2014) 6756–6761. https://doi.org/10.1073/pnas.1320856111.

[78] X. Zhao, M. Sehgal, Z. Hou, J. Cheng, S. Shu, S. Wu, F. Guo, S.J. Le Marchand, H. Lin, J. Chang, J.-T. Guo, Identification of Residues Controlling Restriction versus Enhancing Activities of IFITM Proteins on Entry of Human Coronaviruses, J. Virol. 92 (2017) 1–17. https://doi.org/10.1128/jvi.01535-17.

[79] F. Wrensch, M. Winkler, S. Pöhlmann, IFITM Proteins Inhibit Entry Driven by the MERS-Coronavirus Spike Protein: Evidence for Cholesterol-Independent Mechanisms, Viruses. 6: (2014) 3683–3698. https://doi.org/10.3390/v6093683.

[80] G. Shi, A.D. Kenney, E. Kudryashova, L. Zhang, L. Hall-Stoodley, R.T. Robinson, D.S. Kudryashov, A.A. Compton, J.S. Yount, Opposing activities of IFITM proteins in SARS-CoV-2 infection., BioRxiv Prepr. Serv. Biol. (2020) 1–12. https://doi.org/10.1101/2020.08.11.246678.

[81] A.A. Anafu, C.H. Bowen, C.R. Chin, A.L. Brass, G.H. Holm, Interferon-inducible transmembrane protein 3 (IFITM3) restricts reovirus cell entry, J. Biol. Chem. 288 (2013) 17261–17271. https://doi.org/10.1074/jbc.M112.438515.

[82] J.S. Spence, R. He, H. Hoffmann, T. Das, E. Thinon, C.M. Rice, T. Peng, K. Chandran, H.C. Hang, IFITM3 directly engages and shuttles incoming virus particles to lysosomes, Nat. Chem. Biol. 15 (2019). https://doi.org/10.1038/s41589-018-0213-2.

[83] C. Li, S. Du, M. Tian, Y. Wang, J. Bai, P. Tan, W. Liu, R. Yin, M. Wang, Y. Jiang, Y. Li,

N. Zhu, Y. Zhu, T. Li, S. Wu, N. Jin, F. He, The host restriction factor interferon-inducible transmembrane protein 3 inhibits vaccinia virus infection, Front. Immunol. 9 (2018) 1–14. https://doi.org/10.3389/fimmu.2018.00228.

[84] K.C. Suddala, C.C. Lee, P. Meraner, M. Marin, R.M. Markosyan, T.M. Desai, F.S. Cohen, A.L. Brass, G.B. Melikyan, Interferon-induced transmembrane protein 3 blocks fusion of sensitive but not resistant viruses by partitioning into virus-carrying endosomes, 2019. https://doi.org/10.1371/journal.ppat.1007532.

[85] S. Ranjbar, V. Haridas, L.D. Jasenosky, J. V. Falvo, A.E. Goldfeld, A Role for IFITM Proteins in Restriction of Mycobacterium tuberculosis Infection, Cell Rep. 13 (2015) 874–883. https://doi.org/10.1016/j.celrep.2015.09.048.

[86] T. Desai, M. Marin, C. Chin, G. Savidis, A. Brass, E. Al, IFITM3 Restricts Influenza A Virus Entry by Blocking the Formation of Fusion Pores following Virus-Endosome Hemifusion, PLoS Pathog. 10 (2014) e1004048.

[87] S. Amini-Bavil-Olyaee, Y.J. Choi, J.H. Lee, M. Shi, I. Huang, M. Farzan, The Antiviral Effector IFITM3 Disrupts Intracellular Cholesterol Homeostasis to Block Viral Entry, Cell Host Microbe. 13 (2013) 452–464. https://doi.org/10.1016/j.chom.2013.03.006.

[88] E.M. Feeley, J.S. Sims, S.P. John, C.R. Chin, T. Pertel, L.M. Chen, G.D. Gaiha, B.J. Ryan, R.O. Donis, S.J. Elledge, A.L. Brass, IFITM3 inhibits influenza a virus infection by preventing cytosolic entry, PLoS Pathog. 7 (2011). https://doi.org/10.1371/journal.ppat.1002337.

[89] T. Gerlach, L. Hensen, T. Matrosovich, J. Bergmann, M. Winkler, C. Peteranderl, H. Klenk, F. Weber, S. Herold, S. Pöhlmann, M. Matrosovich, Membrane Fusion Determines Sensitivity of Influenza A Viruses to the Interferon- Induced Antiviral State and IFITMs,

J. Virol. 91 (2017) 1–16.

[90] H.K. Johannsdottir, R. Mancini, J. Kartenbeck, L. Amato, A. Helenius, Host Cell Factors and Functions Involved in Vesicular Stomatitis Virus Entry, J. Virol. 83 (2009) 440–453. https://doi.org/10.1128/jvi.01864-08.

[91] S. Kummer, O. Avinoam, H.G. Kräusslich, IFITM3 clusters on virus containing endosomes and lysosomes early in the influenza a infection of human airway epithelial cells, Viruses. 11 (2019). https://doi.org/10.3390/v11060548.

[92] L. V. Chernomordik, M.M. Kozlov, Mechanics of membrane fusion, Nat. Struct. Mol. Biol. 15 (2008) 675–683. https://doi.org/10.1038/nsmb.1455.

[93] M.M. Kozlov, L. V Chernomordik, Membrane tension and membrane fusion, Curr. Opin. Struct. Biol. 33 (2015) 61–67. https://doi.org/10.1016/j.sbi.2015.07.010.

[94] G. Shi, O. Schwartz, A.A. Compton, More than meets the I : the diverse antiviral and cellular functions of interferon - induced transmembrane proteins, Retrovirology. (2017) 1–11. https://doi.org/10.1186/s12977-017-0377-y.

[95] A.A. Compton, T. Bruel, F. Porrot, A. Mallet, M. Sachse, M. Euvrard, C. Liang, N. Casartelli, O. Schwartz, IFITM proteins incorporated into HIV-1 virions impair viral fusion and spread, Cell Host Microbe. 16 (2014) 736–747. https://doi.org/10.1016/j.chom.2014.11.001.

[96] J. Yu, M. Li, J. Wilkins, S. Ding, T.H. Swartz, A.M. Esposito, Y.M. Zheng, E.O. Freed, C. Liang, B.K. Chen, S.L. Liu, IFITM Proteins Restrict HIV-1 Infection by Antagonizing the Envelope Glycoprotein, Cell Rep. 13 (2015) 145–156. https://doi.org/10.1016/j.celrep.2015.08.055.

[97] K. Tartour, X.N. Nguyen, R. Appourchaux, S. Assil, V. Barateau, L.M. Bloyet, J. Burlaud

Gaillard, M.P. Confort, B. Escudero-Perez, H. Gruffat, S.S. Hong, M. Moroso, O. Reynard, S. Reynard, E. Decembre, N. Ftaich, A. Rossi, N. Wu, F. Arnaud, S. Baize, M. Dreux, D. Gerlier, G. Paranhos-Baccala, V. Volchkov, P. Roingeard, A. Cimarelli, Interference with the production of infectious viral particles and bimodal inhibition of replication are broadly conserved antiviral properties of IFITMs, PLoS Pathog. 13 (2017) 1–30. https://doi.org/10.1371/journal.ppat.1006610.

[98] Y. Wang, Q. Pan, S. Ding, Z. Wang, J. Yu, A. Finzi, S.-L. Liu, C. Liang, The V3 Loop of HIV-1 Env Determines Viral Susceptibility to IFITM3 Impairment of Viral Infectivity, J. Virol. 91 (2017). https://doi.org/10.1128/jvi.02441-16.

[99] G. Drin, B. Antonny, Amphipathic helices and membrane curvature, FEBS Lett. 584 (2010) 1840–1847. https://doi.org/10.1016/j.febslet.2009.10.022.

[100] M. Giménez-Andrés, A. Čopič, B. Antonny, The many faces of amphipathic helices, Biomolecules. 8 (2018) 1–14. https://doi.org/10.3390/biom8030045.

[101] X. Guo, J. Steinkühler, M. Marin, X. Li, W. Lu, R. Dimova, G.B. Melikyan, Interferon-Induced Transmembrane Protein 3 Blocks Fusion of Diverse Enveloped Viruses by Locally Altering Mechanical Properties of Cell Membranes, BioRxiv. (2020) 2020.06.25.171280. https://doi.org/10.1101/2020.06.25.171280.

[102] Y.S. Ahi, D. Yimer, G. Shi, S. Majdoul, K. Rahman, A. Rein, A.A. Compton, IFITM3 reduces retroviral envelope abundance and function and is counteracted by glycogag, MBio. 11 (2020) 1–15. https://doi.org/10.1128/mBio.03088-19.

[103] T. Lin, C.R. Chin, A.R. Everitt, S. Clare, J.M. Perreira, G. Savidis, A.M. Aker, S.P. John, D. Sarlah, E.M. Carreira, S.J. Elledge, P. Kellam, A.L. Brass, Amphotericin B Increases Influenza A Virus Infection by Preventing IFITM3-Mediated Restriction, Cell Rep. 5

(2013) 895–908. https://doi.org/10.1016/j.celrep.2013.10.033.

[104] S.P. John, C.R. Chin, J.M. Perreira, E.M. Feeley, A.M. Aker, G. Savidis, S.E. Smith, A.E.H. Elia, A.R. Everitt, M. Vora, T. Pertel, S.J. Elledge, P. Kellam, A.L. Brass, The CD225 Domain of IFITM3 Is Required for both IFITM Protein Association and Inhibition of Influenza A Virus and Dengue Virus Replication, J. Virol. 87 (2013) 7837–7852. https://doi.org/10.1128/jvi.00481-13.

[105] K. Rahman, C.A. Coomer, S. Majdoul, S. Ding, S. Padilla-Parra, A.A. Compton, Homology-guided identification of a conserved motif linking the antiviral functions of IFITM3 to its oligomeric state, Elife. 9 (2020) e58537. https://doi.org/10.1101/2020.05.14.096891.

[106] C.A. Coomer, K. Rahman, A.A. Compton, CD225 Proteins: A Family Portrait of Fusion Regulators, Trends Genet. (2021) 2–5. https://doi.org/10.1016/j.tig.2021.01.004.

[107] A.R. Gardiner, F. Jaffer, R.C. Dale, R. Labrum, R. Erro, E. Meyer, G. Xiromerisiou, M. Stamelou, M. Walker, D. Kullmann, T. Warner, P. Jarman, M. Hanna, M.A. Kurian, K.P. Bhatia, H. Houlden, The clinical and genetic heterogeneity of paroxysmal dyskinesias, Brain. 138 (2015) 3567–3580. https://doi.org/10.1093/brain/awv310.

[108] F. Valtorta, F. Benfenati, F. Zara, J. Meldolesi, PRRT2: from Paroxysmal Disorders to Regulation of Synaptic Function, Trends Neurosci. 39 (2016) 668–679. https://doi.org/10.1016/j.tins.2016.08.005.

[109] J. Coleman, O. Jouannot, S.K. Ramakrishnan, H. Houlden, J.E. Rothman, S.S. Krishnakumar, Modulating SNARE Complex Assembly Article PRRT2 Regulates Synaptic Fusion by Directly Modulating SNARE Complex Assembly, Cell Rep. 22 (2018) 820–831. https://doi.org/10.1016/j.celrep.2017.12.056.

[110] A. Méneret, C. Gaudebout, F. Riant, M. Vidailhet, C. Depienne, E. Roze, PRRT2 mutations and paroxysmal disorders, Eur J Neurol. 20 (2013) 872–8.

[111] I.T. Alves, D. Cano, R. Böttcher, H. van der Korput, W. Dinjens, G. Jenster, J. Trapman, A mononucleotide repeat in PRRT2 is an important, frequent target of mismatch repair deficiency in cancer, Oncotarget. 8 (2017) 6043–6056. https://doi.org/10.18632/oncotarget.13464.

[112] N. Beaton, C. Rudigier, H. Moest, S. Müller, N. Mrosek, E. Röder, G. Rudofsky, T. Rülicke, J. Ukropec, B. Ukropcova, R. Augustin, H. Neubauer, C. Wolfrum, TUSC5 regulates insulin-mediated adipose tissue glucose uptake by modulation of GLUT4 recycling, Mol. Metab. 4 (2015) 795–810. https://doi.org/10.1016/j.molmet.2015.08.003.

[113] L. Xu, R. Zhou, L. Yuan, S. Wang, X. Li, H. Ma, M. Zhou, C. Pan, J. Zhang, N. Huang, M. Shi, J. Bin, Y. Liao, W. Liao, IGF1/IGF1R/STAT3 signaling-inducible IFITM2 promotes gastric cancer growth and metastasis, Cancer Lett. 393 (2017) 76–85. https://doi.org/10.1016/j.canlet.2017.02.014.

[114] J. Hu, S. Wang, Y. Zhao, Q. Guo, D. Zhang, J. Chen, J. Li, Q. Fei, Y. Sun, Mechanism and biological significance of the overexpression of IFITM3 in gastric cancer, Oncol. Rep. 32 (2014) 2648–2656. https://doi.org/10.3892/or.2014.3522.

[115] G. Xiao, T. Sadras, G. Deb, J. Winchester, K.N. Cosgun, H. Geng, L.N. Chan, K. Kume, T.P. Miettinen, Y. Zhang, M.A. Nix, A. Thomas-tikhonenko, M. Farzan, J.U. Jung, D.M. Weinstock, IFITM3 functions as a PIP3 scaffold to amplify PI3K signalling in B cells, Nature. (2020). https://doi.org/10.1038/s41586-020-2884-6.

[116] P. Moffatt, M.H. Gaumond, P. Salois, K. Sellin, M.C. Bessette, É. Godin, P.T. De Oliveira, G.J. Atkins, A. Nanci, G. Thomas, Bril: A novel bone-specific modulator of

mineralization, J. Bone Miner. Res. 23 (2008) 1497–1508. https://doi.org/10.1359/jbmr.080412.

[117] T.J. Cho, K.E. Lee, S.K. Lee, S.J. Song, K.J. Kim, D. Jeon, G. Lee, H.N. Kim, H.R. Lee, H.H. Eom, Z.H. Lee, O.H. Kim, W.Y. Park, S.S. Park, S. Ikegawa, W.J. Yoo, I.H. Choi, J.W. Kim, A single recurrent mutation in the 5′-UTR of IFITM5 causes osteogenesis imperfecta type v, Am. J. Hum. Genet. 91 (2012) 343–348. https://doi.org/10.1016/j.ajhg.2012.06.005.

[118] M. Winkler, F. Wrensch, P. Bosch, M. Knoth, M. Schindler, S. Gärtner, S. Pöhlmann, Analysis of IFITM-IFITM interactions by a flow cytometry-based FRET assay, Int. J. Mol. Sci. 20 (2019). https://doi.org/10.3390/ijms20163859.

[119] T. Tsukamoto, X. Li, H. Morita, T. Minowa, T. Aizawa, N. Hanagata, M. Demura, Role of S-Palmitoylation on IFITM5 for the Interaction with FKBP11 in Osteoblast Cells, PLoS One. 8 (2013) 1–13. https://doi.org/10.1371/journal.pone.0075831.

[120] E. Kalashnikova, R.A. Lorca, I. Kaur, G.A. Barisone, B. Li, T. Ishimaru, J.S. Trimmer, D.P. Mohapatra, E. Díaz, SynDIG1: An Activity-Regulated, AMPA- Receptor-Interacting Transmembrane Protein that Regulates Excitatory Synapse Development, Neuron. 65 (2010) 80–93. https://doi.org/10.1016/j.neuron.2009.12.021.

[121] V.S. Rao, K. Srinivas, G.N. Sujini, G.N.S. Kumar, Protein-Protein Interaction Detection: Methods and Analysis, Int. J. Proteomics. 2014 (2014) 147648. https://doi.org/10.1155/2014/147648.

[122] T. Forster, Zwischenmolekulare Energiewanderung und Fluoreszenz, Ann. Phys. 437 (1948) 55–75.

[123] R.Y. Tsien, the Green Fluorescent Protein, Annu. Rev. Biochem. 67 (1998) 509–544.

https://doi.org/10.1146/annurev.biochem.67.1.509.

[124] B. Giepmans, S. Adams, M. Ellisman, R. Tsien, The Fluorescent Toolbox for Assessing, Science (80-.). (2006) 217–225.

[125] W.R. Algar, N. Hildebrandt, S.S. Vogel, I.L. Medintz, FRET as a biomolecular research tool — understanding its potential while avoiding pitfalls, Nat. Methods. 16 (2019) 815–829. https://doi.org/10.1038/s41592-019-0530-8.

[126] B.T. Bajar, E.S. Wang, S. Zhang, M.Z. Lin, J. Chu, A guide to fluorescent protein FRET pairs, Sensors (Switzerland). 16 (2016) 1–24. https://doi.org/10.3390/s16091488.

[127] M. Cavrois, C. de Noronha, W.C. Greene, A sensitive and specific enzyme-based assay detecting HIV-1 virion fusion in primary T lymphocytes, Nat. Biotechnol. 20 (2002) 1151–1154. https://doi.org/10.1038/nbt745.

[128] I. Carlon-Andres, S. Padilla-Parra, Quantitative FRET-FLIM-BLAM to assess the extent of HIV-1 fusion in live cells, Viruses. 12 (2020). https://doi.org/10.3390/v12020206.

[129] G.B. Cole, S.E. Reichheld, S. Sharpe, FRET Analysis of the Promiscuous yet Specific Interactions of the HIV-1 Vpu Transmembrane Domain, Biophys. J. 113 (2017) 1992–2003. https://doi.org/10.1016/j.bpj.2017.09.010.

[130] J.R. Lakowicz, K.W. Berndt, Fluorescence Lifetime Imaging, Anal. Biochem. 330 (1992) 316–330.

[131] S. Padilla-Parra, N. Audugé, M. Tramier, M. Coppey-Moisan, Time-domain fluorescence lifetime imaging microscopy: A quantitative method to follow transient protein–protein interactions in living cells, Cold Spring Harb. Protoc. 2015 (2015) 508–521. https://doi.org/10.1101/pdb.top086249.

[132] H. Szmacinski, J.R. Lakowicz, Fluorescence lifetime-based sensing and imaging, Sensors

and Actuators. 29 (1995) 16–24.

[133] A. Leray, S. Padilla-Parra, J. Roul, L. Héliot, M. Tramier, Spatio-Temporal Quantification of FRET in Living Cells by Fast Time-Domain FLIM: A Comparative Study of Non-Fitting Methods, PLoS One. 8 (2013). https://doi.org/10.1371/journal.pone.0069335.

[134] R. Datta, T.M. Heaster, J.T. Sharick, A.A. Gillette, M.C. Skala, Fluorescence lifetime imaging microscopy: fundamentals and advances in instrumentation, analysis, and applications, J. Biomed. Opt. 25 (2020) 1. https://doi.org/10.1117/1.jbo.25.7.071203.

[135] T.S. Blacker, T. Berecz, M.R. Duchen, G. Szabadkai, Assessment of Cellular Redox State Using NAD(P)H Fluorescence Intensity and Lifetime., Bio-Protocol. 7 (2017) 1–20. https://doi.org/10.21769/BioProtoc.2105.

[136] M. Raspe, K.M. Kedziora, B. Van Den Broek, Q. Zhao, S. De Jong, J. Herz, M. Mastop, J. Goedhart, T.W.J. Gadella, I.T. Young, K. Jalink, SiFLIM: Single-image frequency-domain FLIM provides fast and photon-efficient lifetime data, Nat. Methods. 13 (2016) 501–504. https://doi.org/10.1038/nmeth.3836.

[137] C.A. Coomer, I. Carlon-Andres, M. Iliopoulou, M.L. Dustin, E.B. Compeer, A.A. Compton, S. Padilla-Parra, Single-cell glycolytic activity regulates membrane tension and HIV-1 fusion, 2020. https://doi.org/10.1371/journal.ppat.1008359.

[138] D.M. Jones, L.A. Alvarez, R. Nolan, H. Novak-kotzer, M.L. Dustin, S. Padilla-parra, Dynamin-2 Stabilizes the HIV-1 Fusion Pore with a Article Dynamin-2 Stabilizes the HIV-1 Fusion Pore with a Low Oligomeric State, Cell Rep. 18 (2017) 443–453. https://doi.org/10.1016/j.celrep.2016.12.032.

[139] N. Bag, T. Wohland, Imaging Fluorescence Fluctuation Spectroscopy: New Tools for Quantitative Bioimaging, Annu. Rev. Phys. Chem. 65 (2014) 225–248.

https://doi.org/10.1146/annurev-physchem-040513-103641.

[140] A.G. York, S.H. Parekh, D.D. Nogare, R.S. Fischer, K. Temprine, M. Mione, A.B. Chitnis, C.A. Combs, H. Shroff, Resolution doubling in live, multicellular organisms via multifocal structured illumination microscopy, Nat. Methods. 9 (2012) 749–754. https://doi.org/10.1038/nmeth.2025.

[141] D. MacDonald, Noise and Fluctuations: An Introduction., New York, NY, 1962.

[142] D. Magde, E. Elson, W. Webb, Thermodynamic Fluctuations in a Reacting System-Measurement by Fluorescence Correlation Spectroscopy, Phys. Rev. Lett. 29 (1972) 705–708.

[143] J. Ries, Z. Petráek, A.J. García-Sáez, P. Schwille, A comprehensive framework for fluorescence cross-correlation spectroscopy, New J. Phys. 12 (2010). https://doi.org/10.1088/1367-2630/12/11/113009.

[144] M.A. Digman, R. Dalal, A.F. Horwitz, E. Gratton, Mapping the Number of Molecules and Brightness in the Laser Scanning Microscope, Biophys. J. 94 (2008) 2320–2332. https://doi.org/10.1529/biophysj.107.114645.

[145] M. Digman, E. Gratton, Fluorescence correlation spectroscopy and fluorescence crosscorrelation spectroscopy, Wiley Interdiscip Rev Syst Biol Med. 1 (2009) 273–282. https://doi.org/10.1002/wsbm.5.Fluorescence.

[146] K. Bacia, P. Schwille, Practical guidelines for dual-color fluorescence cross-correlation spectroscopy, Nat. Protoc. 2 (2007) 2842–2856. https://doi.org/10.1038/nprot.2007.410.

[147] J.R. Unruh, E. Gratton, Analysis of molecular concentration and brightness from fluorescence fluctuation data with an electron multiplied CCD camera, Biophys. J. 95 (2008) 5385–5398. https://doi.org/10.1529/biophysj.108.130310.

[148] R. Nolan, M. Iliopoulou, L. Alvarez, S. Padilla-Parra, Detecting protein aggregation and interaction in live cells: A guide to number and brightness, Methods. 140–141 (2018) 172–177. https://doi.org/10.1016/j.ymeth.2017.12.001.

[149] R. Nolan, L.A.J. Alvarez, J. Elegheert, M. Iliopoulou, G.M. Jakobsdottir, M. Rodriguez-Muñoz, A.R. Aricescu, S. Padilla-Parra, nandb—number and brightness in R with a novel automatic detrending algorithm, Bioinformatics. (2017) 1–3. https://doi.org/10.1093/bioinformatics/btx434.

[150] S. Padilla-Parra, N. Audugé, M. Coppey-Moisan, M. Tramier, Dual-color fluorescence lifetime correlation spectroscopy to quantify protein-protein interactions in live cell, Microsc. Res. Tech. 74 (2011) 788–793. https://doi.org/10.1002/jemt.21015.

[151] S. Huet, S. V. Avilov, L. Ferbitz, N. Daigle, S. Cusack, J. Ellenberg, Nuclear Import and Assembly of Influenza A Virus RNA Polymerase Studied in Live Cells by Fluorescence Cross-Correlation Spectroscopy, J. Virol. 84 (2010) 1254–1264. https://doi.org/10.1128/jvi.01533-09.

[152] E. Adu-Gyamfi, M.A. Digman, E. Gratton, R. V. Stahelin, Investigation of Ebola VP40 assembly and oligomerization in live cells using number and brightness analysis, Biophys. J. 102 (2012) 2517–2525. https://doi.org/10.1016/j.bpj.2012.04.022.

[153] M. Ferrer, C. Clerté, C. Chamontin, E. Basyuk, S. Lainé, J. Hottin, E. Bertrand, E. Margeat, M. Mougel, Imaging HIV-1 RNA dimerization in cells by multicolor super-resolution and fluctuation microscopies, Nucleic Acids Res. 44 (2016) 7922–7934. https://doi.org/10.1093/nar/gkw511.

[154] J. Hendrix, V. Baumgärtel, W. Schrimpf, S. Ivanchenko, M.A. Digman, E. Gratton, H.G. Kräusslich, B. Müller, D.C. Lamb, Live-cell observation of cytosolic HIV-1 assembly

onset reveals RNA-interacting Gag oligomers, J. Cell Biol. 210 (2015) 629–646. https://doi.org/10.1083/jcb.201504006.

[155] M. Iliopoulou, R. Nolan, L. Alvarez, Y. Watanabe, C.A. Coomer, G.M. Jakobsdottir, T.A. Bowden, S. Padilla-Parra, A dynamic three-step mechanism drives the HIV-1 pre-fusion reaction, Nat. Struct. Mol. Biol. 25 (2018) 814–822. https://doi.org/10.1038/s41594-018-0113-x.

[156] J. Chojnacki, D. Waithe, P. Carravilla, N. Huarte, S. Galiani, J. Enderlein, C. Eggeling, Envelope glycoprotein mobility on HIV-1 particles depends on the virus maturation state, Nat. Commun. 8 (2017) 545. https://doi.org/10.1038/s41467-017-00515-6.

[157] E. Abbe, Beiträge zur Theorie des Mikroskops und der mikroskopischen Wahrnehmung., Arch. Mikrosk. Anat. 9 (1873) 413–418.

[158] J. Mak, A. De Marco, Recent advances in retroviruses via cryo - electron microscopy, Retrovirology. (2018) 1–10. https://doi.org/10.1186/s12977-018-0405-6.

[159] J. Chojnacki, C. Eggeling, Super - resolution fluorescence microscopy studies of human immunodeficiency virus, Retrovirology. (2018) 1–16. https://doi.org/10.1186/s12977-018-0424-3.

[160] S. Hell, J. Wichmann, Breaking the diffraction resolution limit by stimulated emission: stimulated-emission-depletion fluorescence microscopy, Opt. Lett. 19 (1994) 780–782.

[161] M.J. Rust, M. Bates, X. Zhuang, Sub-diffraction-limit imaging by stochastic optical reconstruction microscopy (STORM), Nat. Methods. 3 (2006) 793–795. https://doi.org/10.1038/nmeth929.

[162] J. Chojnacki, T. Staudt, B. Glass, P. Bingen, J. Engelhardt, M. Anders, J. Schneider, B. Muller, S.W. Hell, H.G. Krausslich, Maturation-dependent HIV-1 surface protein

redistribution revealed by fluorescence nanoscopy, Science (80-.). 338 (2012) 524–528. https://doi.org/10.1126/science.1226359.

[163] C. Favard, J. Chojnacki, P. Merida, N. Yandrapalli, J. Mak, C. Eggeling, D. Muriaux, HIV-1 Gag specifically restricts PI(4,5)P2 and cholesterol mobility in living cells creating a nanodomain platform for virus assembly, Sci. Adv. 5 (2019). https://doi.org/10.1126/sciadv.aaw8651.

[164] M. Kozlov, V. Markin, Possible Mechanism of Membrane Fusion, Biofizika. 28 (1983) 242–247.

[165] L. V Chernomordik, M.M. Kozlov, Mechanics of membrane fusion, Nat. Struct. Mol. Biol. 15 (2008) 675–683. https://doi.org/10.1038/nsmb.1455.Mechanics.

[166] W. Shin, L. Ge, G. Arpino, S.A. Villarreal, E. Hamid, H. Liu, W.D. Zhao, P.J. Wen, H.C. Chiang, L.G. Wu, Visualization of Membrane Pore in Live Cells Reveals a Dynamic-Pore Theory Governing Fusion and Endocytosis, Cell. 173 (2018) 934-945.e12. https://doi.org/10.1016/j.cell.2018.02.062.

[167] A. Sapir, O. Avinoam, B. Podbilewicz, L. V. Chernomordik, Viral and Developmental Cell Fusion Mechanisms: Conservation and Divergence, Dev. Cell. 14 (2008) 11–21. https://doi.org/10.1016/j.devcel.2007.12.008.

[168] B. Podbilewicz, Virus and Cell Fusion Mechanisms, Annu. Rev. Cell Dev. Biol. 30 (2014) 111–139. https://doi.org/10.1146/annurev-cellbio-101512-122422.

[169] F.A. Rey, S.M. Lok, Common Features of Enveloped Viruses and Implications for Immunogen Design for Next-Generation Vaccines, Cell. 172 (2018) 1319–1334. https://doi.org/10.1016/j.cell.2018.02.054.

[170] A.B. Ward, I.A. Wilson, The HIV-1 envelope glycoprotein structure: nailing down a

moving target, Immunol. Rev. 275 (2017) 21–32. https://doi.org/10.1111/imr.12507.

[171] T. Xiao, G. Frey, Q. Fu, C.L. Lavine, D.A. Scott, M.S. Seaman, J.J. Chou, B. Chen, HIV-1 fusion inhibitors targeting the membrane-proximal external region of Env spikes, Nat. Chem. Biol. 16 (2020) 529–537. https://doi.org/10.1038/s41589-020-0496-y.

[172] J.H. Lee, D.P. Leaman, A.S. Kim, A. Torrents, D. Pen, A. Yasmeen, R. Derking, A. Ramos, S.W. De Taeye, G. Ozorowski, F. Klein, D.R. Burton, M.C. Nussenzweig, P. Poignard, J.P. Moore, P.J. Klasse, R.W. Sanders, M.B. Zwick, I.A. Wilson, A.B. Ward, Antibodies to a conformational epitope on gp41, (2015). https://doi.org/10.1038/ncomms9167.

[173] M.A. Churchward, T. Rogasevskaia, D.M. Brandman, H. Khosravani, P. Nava, J.K. Atkinson, J.R. Coorssen, Specific lipids supply critical negative spontaneous curvature-an essential component of native Ca2+-triggered membrane fusion, Biophys. J. 94 (2008) 3976–3986. https://doi.org/10.1529/biophysj.107.123984.

[174] H.T. McMahon, E. Boucrot, Membrane curvature at a glance, J. Cell Sci. 128 (2015) 1065–1070. https://doi.org/10.1242/jcs.114454.

[175] K.N. Liu, S.G. Boxer, Target Membrane Cholesterol Modulates Single Influenza Virus Membrane Fusion Efficiency but Not Rate, Biophys. J. 118 (2020) 2426–2433. https://doi.org/10.1016/j.bpj.2020.03.021.

[176] D.K. Verma, D. Gupta, S.K. Lal, Host lipid rafts play a major role in binding and endocytosis of influenza a virus, Viruses. 10 (2018) 1–11. https://doi.org/10.3390/v10110650.

[177] S. Ray, A. Kassan, A.R. Busija, P. Rangamani, H.H. Patel, The plasma membrane as a capacitor for energy and metabolism, Am. J. Physiol. - Cell Physiol. 310 (2016) C181–

C192. https://doi.org/10.1152/ajpcell.00087.2015.

[178] A. Diz-mu, K. Thurley, S. Chintamen, S.J. Altschuler, L.F. Wu, Membrane Tension Acts Through PLD2 and mTORC2 to Limit Actin Network Assembly During Neutrophil Migration, PLoS Biol. (2016) 1–30. https://doi.org/10.1371/journal.pbio.1002474.

[179] M. Riggi, K. Niewola-staszkowska, N. Chiaruttini, A. Colom, B. Kusmider, V. Mercier, S. Soleimanpour, M. Stahl, S. Matile, A. Roux, R. Loewith, Decrease in plasma membrane tension triggers PtdIns(4,5)P2 phase separation to inactivate TORC2, Nat. Cell Biol. 20 (2018). https://doi.org/10.1038/s41556-018-0150-z.

[180] S.A. Finkenstaedt-Quinn, S.M. Gruba, C.L. Haynes, Variations in Fusion Pore Formation in Cholesterol-Treated Platelets, Biophys. J. 110 (2016) 922–929. https://doi.org/10.1016/j.bpj.2015.12.034.

[181] L. V. Chernomordik, G.B. Melikyan, Y.A. Chizmadzhev, Biomembrane fusion: a new concept derived from model studies using two interacting planar lipid bilayers, BBA - Rev. Biomembr. 906 (1987) 309–352. https://doi.org/10.1016/0304-4157(87)90016-5.

[182] R.M. Markosyan, G.B. Melikyan, F.S. Cohen, Tension of membranes expressing the hemagglutinin of influenza virus inhibits fusion, Biophys. J. 77 (1999) 943–952. https://doi.org/10.1016/S0006-3495(99)76945-6.

[183] M. Bretou, O. Jouannot, I. Fanget, P. Pierobon, N. Larochette, P. Gestraud, M. Guillon, V. Emiliani, S. Gasman, C. Desnos, A.M. Lennon-Duménil, F. Darchen, Cdc42 controls the dilation of the exocytotic fusion pore by regulating membrane tension, Mol. Biol. Cell. 25 (2014) 3195–3209. https://doi.org/10.1091/mbc.E14-07-1229.

[184] G. Meher, H. Chakraborty, Membrane Composition Modulates Fusion by Altering Membrane Properties and Fusion Peptide Structure, J. Membr. Biol. 1 (2019).

https://doi.org/10.1007/s00232-019-00064-7.

[185] D.L. Floyd, J.R. Ragains, J.J. Skehel, S.C. Harrison, A.M. Van Oijen, Single-particle kinetics of influenza virus membrane fusion, Proc. Natl. Acad. Sci. 105 (2008) 15382–15387.

[186] S. Harada, K. Yusa, K. Monde, T. Akaike, Y. Maeda, Influence of membrane fluidity on human immunodeficiency virus type 1 entry, Biochem. Biophys. Res. Commun. 329 (2005) 480–486. https://doi.org/10.1016/j.bbrc.2005.02.007.

[187] S. Harada, K. Monde, Y. Tanaka, T. Kimura, Y. Maeda, K. Yusa, Neutralizing antibodies decrease the envelope fluidity of HIV-1, Virology. 370 (2008) 142–150.

[188] X. Sun, G.R. Whittaker, Role for Influenza Virus Envelope Cholesterol in Virus Entry and Infection, J. Virol. 77 (2003) 12543–12551. https://doi.org/10.1128/jvi.77.23.12543-12551.2003.

[189] A.C. Carro, E.B. Damonte, Requirement of cholesterol in the viral envelope for dengue virus infection, Virus Res. 174 (2013) 78–87. https://doi.org/10.1016/j.virusres.2013.03.005.

[190] D.R.M. Graham, E. Chertova, J.M. Hilburn, L.O. Arthur, J.E.K. Hildreth, Cholesterol Depletion of Human Immunodeficiency Virus Type 1 and Simian Immunodeficiency Virus with β-Cyclodextrin Inactivates and Permeabilizes the Virions: Evidence for Virion-Associated Lipid Rafts, J. Virol. 77 (2003) 8237–8248. https://doi.org/10.1128/jvi.77.15.8237-8248.2003.

[191] G.C. Carter, L. Bernstone, D. Sangani, J.W. Bee, T. Harder, W. James, HIV entry in macrophages is dependent on intact lipid rafts, Virology. 386 (2009) 192–202. https://doi.org/10.1016/j.virol.2008.12.031.

[192] R. Dalgliesh, AG; Beverley, PCL; Clapham, PR: Crawford, DH; Greaves, MF; Weiss, The CD4 (T4) antigen is an essential component of the receptor for the AIDS retrovirus, Nature. 312 (1984) 763–767.

[193] W. Dragic, T; Litwin, V; Allaway, GP; Martin, SR; Huang, Y; Nagashima, KA; Cyanan, C; Maddon, PJ; Koup, RA; Moore, JP; Paxton, HIV-1 entry into CD4+ cells is mediated by the chemokine receptor CC-CKR-5., Nature. 381 (1996) 667–73.

[194] Y. Feng, C.C. Broder, P.E. Kennedy, E.A. Berger, HIV-1 Entry Cofactor : Functional cDNA Cloning of a Seven-Transmembrane , G Protein-Coupled Receptor, Science (80-.). 272 (1996).

[195] S.A. Gallo, C.M. Finnegan, M. Viard, Y. Raviv, A. Dimitrov, S.S. Rawat, A. Puri, S. Durell, R. Blumenthal, The HIV Env-mediated fusion reaction, Biochim. Biophys. Acta - Biomembr. 1614 (2003) 36–50. https://doi.org/10.1016/S0005-2736(03)00161-5.

[196] S.G. Deeks, S.R. Lewin, A.L. Ross, J. Ananworanich, M. Benkirane, P. Cannon, N. Chomont, D. Douek, J.D. Lifson, Y. Lo, D. Kuritzkes, D. Margolis, J. Mellors, D. Persaud, J.D. Tucker, F. Barre-sinoussi, International AIDS Society global scientific strategy : towards an HIV cure 2016, Nat. Med. 22 (2016) 839–850. https://doi.org/10.1038/nm.4108.

[197] M.D. Buck, R.T. Sowell, S.M. Kaech, E.L. Pearce, Metabolic Instruction of Immunity, Cell. 169 (2017) 570–586. https://doi.org/10.1016/j.cell.2017.04.004.

[198] L.J. Pallett, N. Schmidt, A. Schurich, T cell metabolism in chronic viral infection, Clin. Exp. Immunol. 1 (2019) doi: 10.1111/cei.13308. https://doi.org/10.1111/cei.13308.

[199] E.L. Pearce, M.C. Poffenberger, C. Chang, R.G. Jones, Fueling Immunity: Insights into Metabolism and Lymphocyte Function, Science (80-.). 342 (2013) 1–30.

https://doi.org/10.1126/science.1242454.Fueling.

[200] M.D. Buck, D.O. Sullivan, E.L. Pearce, T cell metabolism drives immunity, J. Exp. Med. 212 (2015) 1345–1360. https://doi.org/10.1084/jem.20151159.

[201] S. Liu, R. Aliyari, K. Chikere, G. Li, M.D. Marsden, J.K. Smith, O. Pernet, H. Guo, R. Nusbaum, J.A. Zack, A.N. Freiberg, L. Su, Interferon-inducible cholesterol-25-hydroxylase broadly inhibits viral entry by production of 25-hydroxycholesterol., Immunity. 38 (2013) 92–105. https://doi.org/10.1016/j.immuni.2012.11.005.

[202] A. Biswas, P. Kashyap, S. Datta, T. Sengupta, B. Sinha, Cholesterol Depletion by MBCD Enhances Cell Membrane Tension and Its Variations-Reducing Integrity, Biophys. J. 116 (2019) 1456–1468. https://doi.org/10.1016/j.bpj.2019.03.016.

[203] G. Gruenbacher, M. Thurnher, Mevalonate metabolism in immuno-oncology, Front. Immunol. 8 (2017) 1–8. https://doi.org/10.3389/fimmu.2017.01714.

[204] J.A. Hollenbaugh, J. Munger, B. Kim, Metabolite profiles of human immunodeficiency virus infected CD4+ T cells and macrophages using LC-MS/MS analysis, Virology. 415 (2011) 153–159. https://doi.org/10.1016/j.virol.2011.04.007.

[205] J.A. Hollenbaugh, C. Montero, R.F. Schinazi, J. Munger, B. Kim, Metabolic profiling during HIV-1 and HIV-2 infection of primary human monocyte-derived macrophages, Virology. 491 (2016) 106–114. https://doi.org/10.1016/j.virol.2016.01.023.

[206] A. Hegedus, M. Kavanagh Williamson, H. Huthoff, HIV-1 pathogenicity and virion production are dependent on the metabolic phenotype of activated CD4+ T cells, Retrovirology. 11 (2014) 98. https://doi.org/10.1186/s12977-014-0098-4.

[207] J.C. Valle-Casuso, M. Angin, S. Volant, C. Passaes, V. Monceaux, A. Mikhailova, K. Bourdic, V. Avettand-Fenoel, F. Boufassa, M. Sitbon, O. Lambotte, M.-I. Thoulouze, M.

Müller-Trutwin, N. Chomont, A. Sáez-Cirión, Cellular Metabolism Is a Major Determinant of HIV-1 Reservoir Seeding in CD4+ T Cells and Offers an Opportunity to Tackle Infection, Cell Metab. (2018) 1–16. https://doi.org/10.1016/j.cmet.2018.11.015.

[208] H. Ewers, A. Helenius, Lipid-Mediated Endocytosis, Cold Spring Harb. Perspect. Biol. 3 (2011) a004721.

[209] G.W. Feigenson, Phase behavior of lipid mixtures, Nat. Chem. Biol. 2 (2006) 560–563.

[210] S. Yang, A.J.B. Kreutzberger, J. Lee, V. Kiessling, L.K. Tamm, C. Physiology, B. Physics, The Role of Cholesterol in Membrane Fusion, Chem Phys Lipids. 1999 (2016) 136–143. https://doi.org/10.1016/j.chemphyslip.2016.05.003.The.

[211] S. Yang, V. Kiessling, L.K. Tamm, Line tension at lipid phase boundaries as driving force for HIV fusion peptide-mediated fusion, Nat. Commun. 7 (2016) 1–9. https://doi.org/10.1038/pj.2016.37.

[212] S.T. Yang, A.J.B. Kreutzberger, V. Kiessling, B.K. Ganser-Pornillos, J.M. White, L.K. Tamm, HIV virions sense plasma membrane heterogeneity for cell entry, Sci. Adv. 3 (2017) 1–13. https://doi.org/10.1126/sciadv.1700338.

[213] S.M. Campbell, S.M. Crowe, J. Mak, Lipid rafts and HIV-1 : from viral entry to assembly of progeny virions, J. Clin. Virol. 22 (2001) 217–227.

[214] T. Baumgart, S. Hess, W. Webb, Imaging coexisting fluid domains in biomembrane models coupling curvature and line tension, Nature. 425 (2003) 23–26.

[215] C. Morris, U. Homann, Membrane Biology Cell Surface Area Regulation and Membrane Tension, J. Membr. Biol. 179 (2001) 79–102. https://doi.org/10.1007/s002320010040.

[216] W. Tsai, G.W. Feigenson, Lowering line tension with high cholesterol content induces a transition from macroscopic to nanoscopic phase domains in model biomembranes, BBA -

Biomembr. 1861 (2019) 478–485. https://doi.org/10.1016/j.bbamem.2018.11.010.

[217] G. Rappocciolo, M. Jais, P. Piazza, T.A. Reinhart, S.J. Berendam, L. Garcia-exposito, P. Gupta, R. Rinaldo, Alterations in Cholesterol Metabolism Restrict HIV-1 Trans Infection in Nonprogressors, MBio. 5 (2014) 1–11. https://doi.org/10.1128/mBio.01031-13.Invited.

[218] D.C. Delucia, C.R. Rinaldo, Inefficient HIV-1 trans Infection of CD4+ T Cells by Macrophages from HIV-1 Nonprogressors Is Associated with Altered Membrane Cholesterol and DC-SIGN, J. Virol. 92 (2018) 1–18.

[219] W. Becker, Fluorescence lifetime imaging – techniques and applications, J. Microsc. 247 (2012).

[220] K. Suhling, L.M. Hirvonen, J.A. Levitt, P. Chung, C. Tregidgo, A. Le, D.A. Rusakov, K. Zheng, S. Ameer-beg, S. Poland, S. Coelho, R. Henderson, N. Krstajic, Fluorescence lifetime imaging (FLIM): Basic concepts and some recent developments, Chem. Phys. Lett. 27 (2015) 3–40. https://doi.org/10.1016/j.medpho.2014.12.001.

[221] A. V. Meleshina, V. V. Dudenkova, M. V. Shirmanova, V.I. Shcheslavskiy, W. Becker, A.S. Bystrova, E.I. Cherkasova, E. V. Zagaynova, Probing metabolic states of differentiating stem cells using two-photon FLIM, Sci. Rep. 6 (2016). https://doi.org/10.1038/srep21853.

[222] M.A. Digman, V.R. Caiolfa, M. Zamai, E. Gratton, The phasor approach to fluorescence lifetime imaging analysis, Biophys. J. 94 (2008) L14–L16. https://doi.org/10.1529/biophysj.107.120154.

[223] M. Tantama, Y.P. Hung, G. Yellen, Imaging intracellular pH in live cells with a genetically encoded red fluorescent protein sensor, J. Am. Chem. Soc. 133 (2011) 10034–10037. https://doi.org/10.1021/ja202902d.

[224] J. Berg, Y.P. Hung, G. Yellen, A genetically encoded fluorescent reporter of ATP:ADP ratio, Nat. Methods. 6 (2009) 161–166. https://doi.org/10.1038/nmeth.1288.

[225] A. San Martín, S. Ceballo, I. Ruminot, R. Lerchundi, W.B. Frommer, L.F. Barros, A Genetically Encoded FRET Lactate Sensor and Its Use To Detect the Warburg Effect in Single Cancer Cells, PLoS One. 8 (2013). https://doi.org/10.1371/journal.pone.0057712.

[226] T. Nakabayashi, S. Oshita, R. Sumikawa, F. Sun, M. Kinjo, N. Ohta, PH dependence of the fluorescence lifetime of enhanced yellow fluorescent protein in solution and cells, J. Photochem. Photobiol. A Chem. 235 (2012) 65–71. https://doi.org/10.1016/j.jphotochem.2012.02.016.

[227] P.M. Schaefer, S. Kalinina, A. Rueck, C.A.F. Von Arnim, NADH Autofluorescence — A Marker on its Way to Boost Bioenergetic Research, Cytometry. 95 (2018) 34–46. https://doi.org/10.1002/cyto.a.23597.

[228] S.T. Smale, B-Galactosidase Assay, Cold Spring Harb. Protoc. 5 (2010) doi:10.1101/pdb.prot5423. https://doi.org/10.1101/pdb.prot5423.

[229] D.M. Jones, S. Padilla-Parra, Imaging real-time HIV-1 virion fusion with FRET-based biosensors., Sci. Rep. 5 (2015) 13449. https://doi.org/10.1038/srep13449.

[230] M. De Vega, M. Marin, N. Kondo, K. Miyauchi, Y. Kim, R.F. Epand, R.M. Epand, G.B. Melikyan, Inhibition of HIV-1 endocytosis allows lipid mixing at the plasma membrane , but not complete fusion, Retrovirology. 8 (2011) 1–19.

[231] K. Miyauchi, Y. Kim, O. Latinovic, V. Morozov, G.B. Melikyan, HIV Enters Cells via Endocytosis and Dynamin-Dependent Fusion with Endosomes, Cell. 137 (2009) 433–444. https://doi.org/10.1016/j.cell.2009.02.046.HIV.

[232] R.M. Markosyan, F.S. Cohen, G.B. Melikyan, Time-resolved Imaging of HIV-1 Env-

mediated Lipid and Content Mixing between a Single Virion and Cell Membrane, Mol. Biol. Cell. 16 (2005) 5502–5513. https://doi.org/10.1091/mbc.E05.

[233] U. O'Doherty, W.J. Swiggard, M.H. Malim, Human Immunodeficiency Virus Type 1 Spinoculation Enhances Infection through Virus Binding, J. Virol. 74 (2000) 10074–10080. https://doi.org/10.1128/jvi.74.21.10074-10080.2000.

[234] J. Guo, W. Wang, D. Yu, Y. Wu, Spinoculation Triggers Dynamic Actin and Cofilin Activity That Facilitates HIV-1 Infection of Transformed and Resting CD4 T Cells, J. Virol. 85 (2011) 9824–9833. https://doi.org/10.1128/jvi.05170-11.

[235] M. Hao, S.X. Lin, O.J. Karylowski, D. Wu, T.E. Mcgraw, F.R. Maxfield, Vesicular and Non-vesicular Sterol Transport in Living Cells, J. Biol. Chem. 277 (2002) 609–617. https://doi.org/10.1074/jbc.M108861200.

[236] W. Eid, K. Dauner, K.C. Courtney, A. Gagnon, R.J. Parks, A. Sorisky, mTORC1 activates SREBP-2 by suppressing cholesterol trafficking to lysosomes in mammalian cells, Proc. Natl. Acad. Sci. (2017) 1–6. https://doi.org/10.1073/pnas.1705304114.

[237] K. Habbeger, N. Hoffman, C. Ridenour, J. Brozinick, J. Elmendorf, AMPK Enhances Insulin-Stimulated GLUT4 Regulation via Lowering Membrane Cholesterol, Endocrinology. 153 (2012) 2130–2141.

[238] R. Zidovetzki, I. Levitan, Use of cyclodextrins to manipulate plasma membrane cholesterol content: evidence, misconceptions and control strategies, Biochim. Biophys. Acta. 1768 (2008) 1311–1324.

[239] S.T. Yang, V. Kiessling, J.A. Simmons, J.M. White, L.K. Tamm, HIV gp41-mediated membrane fusion occurs at edges of cholesterol-rich lipid domains, Nat. Chem. Biol. 11 (2015) 424–431. https://doi.org/10.1038/nchembio.1800.

[240] A. Colom, E. Derivery, S. Soleimanpour, C. Tomba, M.D. Molin, N. Sakai, M. González-gaitán, S. Matile, A. Roux, A fluorescent membrane tension probe, Nat. Chem. 10 (2018). https://doi.org/10.1038/s41557-018-0127-3.

[241] S. Soleimanpour, A. Colom, E. Derivery, M. Gonzalez-gaitan, A. Roux, N. Sakai, S. Matile, Headgroup engineering in mechanosensitive membrane probes, Chem. Commun. 52 (2016) 14450–14453. https://doi.org/10.1039/c6cc08771j.

[242] M.D. Molin, Q. Verolet, A. Colom, R. Letrun, E. Derivery, M. Gonzalez-gaitan, E. Vauthey, N. Sakai, S. Matile, Fluorescent Flippers for Mechanosensitive Membrane Probes, J. Am. Chem. Soc. 137 (2015) 8–11. https://doi.org/10.1021/ja5107018.

[243] V. Kilin, O. Glushonkov, L. Herdly, A. Klymchenko, L. Richert, Y. Mely, Article Fluorescence Lifetime Imaging of Membrane Lipid Order with a Ratiometric Fluorescent Probe, Biophys. J. 108 (2015) 2521–2531. https://doi.org/10.1016/j.bpj.2015.04.003.

[244] W. Li, X. Yu, R. Aziz, X. Liao, W. Li, X. Yu, F. Xie, B. Zhang, S. Shao, C. Geng, R. Aziz, Membrane-Bound Biosensor Visualizes Shear Stress-Induced Inhomogeneous Alteration of Cell Membrane Tension A Membrane-Bound Biosensor Visualizes Shear Stress-Induced Inhomogeneous Alteration of Cell Membrane Tension, IScience. 7 (2018) 180–190. https://doi.org/10.1016/j.isci.2018.09.002.

[245] N. Audugé, S. Padilla-Parra, M. Tramier, N. Borghi, M. Coppey-Moisan, Chromatin condensation fluctuations rather than steady-state predict chromatin accessibility, Nucleic Acids Res. 47 (2019) 6184–6194. https://doi.org/10.1093/nar/gkz373.

[246] X. Sun, V.K. Yau, B.J. Briggs, G.R. Whittaker, Role of clathrin-mediated endocytosis during vesicular stomatitis virus entry into host cells, Virology. 338 (2005) 53–60. https://doi.org/10.1016/j.virol.2005.05.006.

[247] G.B. Melikyan, HIV entry : a game of hide-and-fuse ?, Curr. Opin. Virol. 4 (2015) 1–7. https://doi.org/10.1016/j.coviro.2013.09.004.

[248] N. Herold, M. Anders-Osswein, B. Glass, M. Eckhardt, B. Muller, H.-G. Krausslich, HIV-1 Entry in SupT1-R5, CEM-ss, and Primary CD4+ T Cells Occurs at the Plasma Membrane and Does Not Require Endocytosis, J. Virol. 88 (2014) 13956–13970. https://doi.org/10.1128/JVI.01543-14.

[249] N. Kondo, M. Marin, J.H. Kim, T.M. Desai, G.B. Melikyan, Distinct Requirements for HIV-Cell Fusion and HIV-mediated, J. Biol. Chem. 290 (2015) 6558–6573. https://doi.org/10.1074/jbc.M114.623181.

[250] J. Luo, L. Jiang, H. Yang, B.L. Song, Routes and mechanisms of post-endosomal cholesterol trafficking: A story that never ends, Traffic. 18 (2017) 209–217. https://doi.org/10.1111/tra.12471.

[251] K. Jacobson, O.G. Mouritsen, R.G.W. Anderson, Lipid rafts : at a crossroad between cell biology and physics, Nat. Chem. Biol. 9 (2007) 7–14.

[252] L.J. Pike, The challenge of lipid rafts, J. Lipid Res. 50 (2009) 323–328. https://doi.org/10.1194/jlr.R800040-JLR200.

[253] E. Zaitseva, E. Zaitsev, K. Melikov, A. Arakelyan, M. Marin, R. Villasmil, L.B. Margolis, G.B. Melikyan, L. V Chernomordik, Fusion Stage of HIV-1 Entry Depends on Virus-Induced Cell Surface Exposure of Phosphatidylserine, Cell Host Microbe. 22 (2017) 99-110.e7. https://doi.org/10.1016/j.chom.2017.06.012.

[254] N. Yan, Z.J. Chen, Intrinsic antiviral immunity, Nat. Immunol. 13 (2012) 214–222. https://doi.org/10.1038/ni.2229.

[255] A. Kühnl, A. Musiol, N. Heitzig, D. Johnson, C. Ehrhardt, T. Grewal, V. Gerke, S.

Ludwig, U. Reschera, Late Endosomal / Lysosomal Cholesterol Accumulation Is a Host Cell-Protective Mechanism Inhibiting Endosomal Escape of, MBio. 9 (2018) 1–16.

[256] R. Appourchaux, M. Delpeuch, L. Zhong, J. Burlaud-Gaillard, K. Tartour, G. Savidis, A. Brass, L. Etienne, P. Roingeard, A. Cimarelli, Functional Mapping of Regions Involved in the Negative Imprinting of Virion Particle Infectivity and in Target Cell Protection by Interferon-Induced Transmembrane Protein 3 against HIV-1, J. Virol. 93 (2018) 1–18. https://doi.org/10.1128/jvi.01716-18.

[257] M. Poh, G. Shui, X. Xie, P. Shi, M. Wenk, F. Gu, U18666A, an intra-cellular cholesterol transport inhibitor, inhibits dengue virus entry and replication, Antiviral Res. 93 (2012) 191–198.

[258] S. Martens, H.T. McMahon, Mechanisms of membrane fusion: Disparate players and common principles, Nat. Rev. Mol. Cell Biol. 9 (2008) 543–556. https://doi.org/10.1038/nrm2417.

[259] J.F. Meschia, Discovery of a cause of vein of Galen malformations, Brain. 141 (2018) 936–938. https://doi.org/10.1093/brain/awy066.

[260] J. Mo, B. Wang, X. Zhu, X. Wu, Y. Liu, PRRT2 deficiency induces paroxysmal kinesigenic dyskinesia by influencing synaptic function in the primary motor cortex of rats, Neurobiol. Dis. 121 (2019) 274–285. https://doi.org/10.1016/j.nbd.2018.10.011.

[261] Y.T. Liu, F.S. Nian, W.J. Chou, C.Y. Tai, S.Y. Kwan, C. Chen, P.W. Kuo, P.H. Lin, C.Y. Chen, C.W. Huang, Y.C. Lee, B.W. Soong, J.W. Tsai, PRRT2 mutations lead to neuronal dysfunction and neurodevelopmental defects, Oncotarget. 7 (2016) 39184–39196. https://doi.org/10.18632/oncotarget.9258.

[262] P. Valente, E. Castroflorio, P. Rossi, M. Fadda, B. Sterlini, R.I. Cervigni, C. Prestigio, S.

Giovedì, F. Onofri, E. Mura, F.C. Guarnieri, A. Marte, M. Orlando, F. Zara, A. Fassio, F. Valtorta, P. Baldelli, A. Corradi, F. Benfenati, PRRT2 Is a Key Component of the Ca2+-Dependent Neurotransmitter Release Machinery, Cell Rep. 15 (2016) 117–131. https://doi.org/10.1016/j.celrep.2016.03.005.

[263] A. Gardiner, K. Bhatia, M. Stamelou, R. Dale, M. Kurian, S. Schneider, G. Wali, T. Counihan, A. Schapira, S. Spacey, E. Valente, L. Silveira-Moriyama, H. Teive, S. Raskin, J. Sander, A. Lees, T. Warner, D. Kullmann, N. Wood, M. Hanna, H. Houlden, PRRT2 gene mutations From paroxysmal dyskinesia to episodic ataxia and hemiplegic migraine, Neurology. 79 (2012).

[264] R. Van Vliet, G. Breedveld, J. De Rijk-Van Andel, E. Brilstra, N. Verbeek, C. Verschuuren-Bemelmans, M. Boon, J. Samijn, K. Diderich, I. Van De Laar, B. Oostra, V. Bonifati, A. Maat-Kievit, PRRT2 phenotypes and penetrance of paroxysmal kinesigenic dyskinesia and infantile convulsions, Neurology. 79 (2012) 777–784. https://doi.org/10.1212/WNL.0b013e3182661fe3.

[265] Q. Liu, Z. Qi, X.H. Wan, J.Y. Li, L. Shi, Q. Lu, X.Q. Zhou, L. Qiao, L.W. Wu, X.Q. Liu, W. Yang, Y. Liu, L.Y. Cui, X. Zhang, Mutations in PRRT2 result in paroxysmal dyskinesias with marked variability in clinical expression, J. Med. Genet. 49 (2012) 79–82. https://doi.org/10.1136/jmedgenet-2011-100653.

[266] B. Grigorov, J. Rabilloud, P. Lawrence, D. Gerlier, Rapid titration of measles and other viruses: Optimization with determination of replication cycle length, PLoS One. 6 (2011). https://doi.org/10.1371/journal.pone.0024135.

[267] Y. Sun, R.N. Day, A. Periasamy, Investigating protein-protein interactions in living cells using fluorescence lifetime imaging microscopy, Nat. Protoc. 6 (2011) 1324–1340.

[268] S.A. Sanchez, M.A. Tricerri, E. Gratton, Laurdan generalized polarization fluctuations measures membrane packing micro-heterogeneity in vivo, Proc. Natl. Acad. Sci. U. S. A. 109 (2012) 7314–7319. https://doi.org/10.1073/pnas.1118288109.

[269] D.M. Owen, C. Rentero, A. Magenau, A. Abu-Siniyeh, K. Gaus, Quantitative imaging of membrane lipid order in cells and organisms, Nat. Protoc. 7 (2012) 24–35. https://doi.org/10.1038/nprot.2011.419.

[270] P. Rossi, B. Sterlini, E. Castroflorio, A. Marte, F. Onofri, F. Valtorta, L. Maragliano, A. Corradi, F. Benfenati, A novel topology of proline-rich transmembrane protein 2 (PRRT2): Hints for an intracellular function at the synapse, J. Biol. Chem. 291 (2016) 6111–6123. https://doi.org/10.1074/jbc.M115.683888.

[271] U. Omasits, C.H. Ahrens, S. Müller, B. Wollscheid, Protter: Interactive protein feature visualization and integration with experimental proteomic data, Bioinformatics. 30 (2014) 884–886. https://doi.org/10.1093/bioinformatics/btt607.

[272] M.G. Teese, D. Langosch, Role of GxxxG Motifs in Transmembrane Domain Interactions, Biochemistry. 54 (2015) 5125–5135. https://doi.org/10.1021/acs.biochem.5b00495.

[273] M.C. Overton, S.L. Chinault, K.J. Blumer, Oligomerization, biogenesis, and signaling is promoted by a glycophorin A-like dimerization motif in transmembrane domain 1 of a yeast G protein-coupled receptor., J. Biol. Chem. 278 (2003) 49369–49377. https://doi.org/10.1074/jbc.M308654200.

[274] B. Lu, V. Kiessling, L.K. Tamm, D.S. Cafiso, The juxtamembrane linker of full-length synaptotagmin 1 controls oligomerization and calcium-dependent membrane binding, J. Biol. Chem. 289 (2014) 22161–22171. https://doi.org/10.1074/jbc.M114.569327.

[275] Z. Wilson, MR; Kugel, S; Huang, J; Wilson, LJ; Wloszczynski, PA; Ye, J; Matherly, LH; Hou, Structural determinants of human proton-coupled folate transporter oligomerization: role of GXXXG motifs and identification of oligomeric interfaces at transmembrane domains 3 and 6, Biochem. J. 469 (2015) 33–44.

[276] F. Cunningham, P. Achuthan, W. Akanni, J. Allen, M.R. Amode, I.M. Armean, R. Bennett, J. Bhai, K. Billis, S. Boddu, C. Cummins, C. Davidson, K.J. Dodiya, A. Gall, C.G. Girón, L. Gil, T. Grego, L. Haggerty, E. Haskell, T. Hourlier, O.G. Izuogu, S.H. Janacek, T. Juettemann, M. Kay, M.R. Laird, I. Lavidas, Z. Liu, J.E. Loveland, J.C. Marugán, T. Maurel, A.C. McMahon, B. Moore, J. Morales, J.M. Mudge, M. Nuhn, D. Ogeh, A. Parker, A. Parton, M. Patricio, A.I. Abdul Salam, B.M. Schmitt, H. Schuilenburg, D. Sheppard, H. Sparrow, E. Stapleton, M. Szuba, K. Taylor, G. Threadgold, A. Thormann, A. Vullo, B. Walts, A. Winterbottom, A. Zadissa, M. Chakiachvili, A. Frankish, S.E. Hunt, M. Kostadima, N. Langridge, F.J. Martin, M. Muffato, E. Perry, M. Ruffier, D.M. Staines, S.J. Trevanion, B.L. Aken, A.D. Yates, D.R. Zerbino, P. Flicek, Ensembl 2019, Nucleic Acids Res. 47 (2019) D745–D751. https://doi.org/10.1093/nar/gky1113.

[277] S.T. Sherry, M.H. Ward, M. Kholodov, J. Baker, L. Phan, E.M. Smigielski, K. Sirotkin, DbSNP: The NCBI database of genetic variation, Nucleic Acids Res. 29 (2001) 308–311. https://doi.org/10.1093/nar/29.1.308.

[278] A. Sharma, R.N. McLaughlin, R.S. Basom, C. Kikawa, M. OhAinle, J.S. Yount, M. Emerman, J. Overbaugh, Macaque interferon-induced transmembrane proteins limit replication of SHIV strains in an Envelope-dependent manner, PLoS Pathog. 15 (2019) 1–23. https://doi.org/10.1371/journal.ppat.1007925.

[279] R.N. Day, Measuring protein interactions using Förster resonance energy transfer and fluorescence lifetime imaging microscopy, Methods. 66 (2014) 200–207. https://doi.org/10.1016/j.ymeth.2013.06.017.

[280] N.C. Shaner, R.E. Campbell, P.A. Steinbach, B.N.G. Giepmans, A.E. Palmer, R.Y. Tsien, Improved monomeric red, orange and yellow fluorescent proteins derived from Discosoma sp. red fluorescent protein, Nat. Biotechnol. 22 (2004) 1567–1572. https://doi.org/10.1038/nbt1037.

[281] M.G. Teese, D. Langosch, Role of GxxxG Motifs in Transmembrane Domain Interactions, Biochemistry. 54 (2015) 5125–5135. https://doi.org/10.1021/acs.biochem.5b00495.

[282] A. Zani, J.S. Yount, Antiviral Protection by IFITM3 In Vivo, Curr. Clin. Microbiol. Reports. 5 (2018) 229–237. https://doi.org/10.1007/s40588-018-0103-0.

[283] A.D. Kenney, T.M. McMichael, A. Imas, N.M. Chesarino, L. Zhang, L.E. Dorn, Q. Wu, O. Alfaour, F. Amari, M. Chen, A. Zani, M. Chemudupati, F. Accornero, V. Coppola, M.V.S. Rajaram, J.S. Yount, IFITM3 protects the heart during influenza virus infection, Proc. Natl. Acad. Sci. U. S. A. 116 (2019) 18607–18612. https://doi.org/10.1073/pnas.1900784116.

[284] S. Vanni, H. Hirose, H. Barelli, B. Antonny, R. Gautier, A sub-nanometre view of how membrane curvature and composition modulate lipid packing and protein recruitment, Nat. Commun. 5 (2014). https://doi.org/10.1038/ncomms5916.

[285] P. Rangamani, K.K. Mandadap, G. Oster, Protein-induced membrane curvature alters local membrane tension, Biophys. J. 107 (2014) 751–762. https://doi.org/10.1016/j.bpj.2014.06.010.

[286] G. Golani, N. Ariotti, R.G. Parton, M.M. Kozlov, Membrane Curvature and Tension Control the Formation and Collapse of Caveolar Superstructures, Dev. Cell. 48 (2019) 523-538.e4. https://doi.org/10.1016/j.devcel.2018.12.005.

[287] M. Barbot, D.C. Jans, C. Schulz, N. Denkert, B. Kroppen, M. Hoppert, S. Jakobs, M. Meinecke, Mic10 Oligomerizes to Bend Mitochondrial Inner Membranes at Cristae Junctions, Cell Metab. 21 (2015) 756–763. https://doi.org/10.1016/j.cmet.2015.04.006.

[288] O. Faingold, T. Cohen, Y. Shai, A GxxxG-like motif within HIV-1 fusion peptide is critical to its immunosuppressant activity, structure, and interaction with the transmembrane domain of the T-cell receptor, J. Biol. Chem. 287 (2012) 33503–33511. https://doi.org/10.1074/jbc.M112.370817.

[289] B. Fu, L. Wang, S. Li, M.E. Dorf, ZMP STE24 defends against influenza and other pathogenic viruses, J. Exp. Med. 214 (2017) 919–929. https://doi.org/10.1084/jem.20161270.

[290] Y. Okuzaki, S. Kidani, H. Kaneoka, S. Iijima, K.I. Nishijima, Characterization of chicken interferon-inducible transmembrane protein-10, Biosci. Biotechnol. Biochem. 81 (2017) 914–921. https://doi.org/10.1080/09168451.2016.1274639.

[291] A. Patoine, A. Husseini, B. Kasaai, M.H. Gaumond, P. Moffatt, The osteogenic cell surface marker BRIL/IFITM5 is dispensable for bone development and homeostasis in mice, PLoS One. 12 (2017) 1–24. https://doi.org/10.1371/journal.pone.0184568.

[292] O. Semler, L. Garbes, K. Keupp, D. Swan, K. Zimmermann, J. Becker, S. Iden, B. Wirth, P. Eysel, F. Koerber, E. Schoenau, S.K. Bohlander, B. Wollnik, C. Netzer, A mutation in the 5′-UTR of IFITM5 creates an in-frame start codon and causes autosomal-dominant osteogenesis imperfecta type v with hyperplastic callus, Am. J. Hum. Genet. 91 (2012)

349–357. https://doi.org/10.1016/j.ajhg.2012.06.011.

[293] H. Hoyer-Kuhn, O. Semler, L. Garbes, K. Zimmermann, J. Becker, B. Wollnik, E. Schoenau, C. Netzer, A Nonclassical IFITM5 mutation located in the coding region causes severe osteogenesis imperfecta with prenatal onset, J. Bone Miner. Res. 29 (2014) 1387–1391. https://doi.org/10.1002/jbmr.2156.

[294] F. Rauch, P. Moffatt, M. Cheung, P. Roughley, L. Lalic, A.M. Lund, N. Ramirez, S. Fahiminiya, J. Majewski, F.H. Glorieux, Osteogenesis imperfecta type V: Marked phenotypic variability despite the presence of the IFITM5 c.-14C>T mutation in all patients, J. Med. Genet. 50 (2013) 21–24. https://doi.org/10.1136/jmedgenet-2012-101307.

[295] H. Kang, S. Aryal A.C., J.C. Marini, Osteogenesis imperfecta: new genes reveal novel mechanisms in bone dysplasia, Transl. Res. 181 (2017) 27–48. https://doi.org/10.1016/j.trsl.2016.11.005.

[296] N. Hanagata, X. Li, Osteoblast-enriched membrane protein IFITM5 regulates the association of CD9 with an FKBP11-CD81-FPRP complex and stimulates expression of interferon-induced genes, Biochem. Biophys. Res. Commun. 409 (2011) 378–384. https://doi.org/10.1016/j.bbrc.2011.04.136.

[297] A. Takada, C. Robison, H. Goto, A. Sanchez, K.G. Murti, M.A. Whitt, Y. Kawaoka, A system for functional analysis of Ebola virus glycoprotein, Proc. Natl. Acad. Sci. U. S. A. 94 (1997) 14764–14769. https://doi.org/10.1073/pnas.94.26.14764.

[298] J. Yang, R. Yan, A. Roy, D. Xu, J. Poisson, Y. Zhang, The I-TASSER suite: Protein structure and function prediction, Nat. Methods. 12 (2014) 7–8. https://doi.org/10.1038/nmeth.3213.

[299] J. Yang, Y. Zhang, I-TASSER server: New development for protein structure and function predictions, Nucleic Acids Res. 43 (2015) W174–W181. https://doi.org/10.1093/nar/gkv342.

[300] R. Gautier, D. Douguet, B. Antonny, G. Drin, HELIQUEST: A web server to screen sequences with specific α-helical properties, Bioinformatics. 24 (2008) 2101–2102. https://doi.org/10.1093/bioinformatics/btn392.

[301] D.T. Jones, Protein secondary structure prediction based on position-specific scoring matrices, J. Mol. Biol. 292 (1999) 195–202. https://doi.org/10.1006/jmbi.1999.3091.

[302] D.W.A. Buchan, D.T. Jones, The PSIPRED Protein Analysis Workbench: 20 years on, Nucleic Acids Res. 47 (2019) W402–W407. https://doi.org/10.1093/nar/gkz297.

[303] B. Petersen, T.N. Petersen, P. Andersen, M. Nielsen, C. Lundegaard, A generic method for assignment of reliability scores applied to solvent accessibility predictions, BMC Struct. Biol. 9 (2009) 1–10. https://doi.org/10.1186/1472-6807-9-51.

[304] B. Rost, G. Yachdav, J. Liu, The PredictProtein server, Nucleic Acids Res. 32 (2004) 321–326. https://doi.org/10.1093/nar/gkh377.

[305] G. Yachdav, E. Kloppmann, L. Kajan, M. Hecht, T. Goldberg, T. Hamp, P. Hönigschmid, A. Schafferhans, M. Roos, M. Bernhofer, L. Richter, H. Ashkenazy, M. Punta, A. Schlessinger, Y. Bromberg, R. Schneider, G. Vriend, C. Sander, N. Ben-Tal, B. Rost, PredictProtein - An open resource for online prediction of protein structural and functional features, Nucleic Acids Res. 42 (2014) 337–343. https://doi.org/10.1093/nar/gku366.

[306] A.A. Porollo, R. Adamczak, J. Meller, POLYVIEW: A flexible visualization tool for structural and functional annotations of proteins, Bioinformatics. 20 (2004) 2460–2462. https://doi.org/10.1093/bioinformatics/bth248.

[307] P. Thévenet, Y. Shen, J. Maupetit, F. Guyon, P. Derreumaux, P. Tufféry, PEP-FOLD: An updated de novo structure prediction server for both linear and disulfide bonded cyclic peptides, Nucleic Acids Res. 40 (2012) 288–293. https://doi.org/10.1093/nar/gks419.

[308] M. Decock, S. Stanga, J.N. Octave, I. Dewachter, S.O. Smith, S.N. Constantinescu, P. Kienlen-Campard, Glycines from the APP GXXXG/GXXXA transmembrane motifs promote formation of pathogenic Aβ oligomers in cells, Front. Aging Neurosci. 8 (2016) 1–15. https://doi.org/10.3389/fnagi.2016.00107.

[309] N.A. Noordeen, F. Carafoli, E. Hohenester, M.A. Horton, B. Leitinger, A transmembrane leucine zipper is required for activation of the dimeric receptor tyrosine kinase DDR1, J. Biol. Chem. 281 (2006) 22744–22751. https://doi.org/10.1074/jbc.M603233200.

[310] D. Schneider, D.M. Engelman, Motifs of two small residues can assist but are not sufficient to mediate transmembrane helix interactions, J. Mol. Biol. 343 (2004) 799–804. https://doi.org/10.1016/j.jmb.2004.08.083.

[311] A. Senes, M. Gerstein, D.M. Engelman, Statistical analysis of amino acid patterns in transmembrane helices: The GxxxG motif occurs frequently and association with β-branched residues at neighboring positions, J. Mol. Biol. 296 (2000) 921–936. https://doi.org/10.1006/jmbi.1999.3488.

[312] A.O. Stella, S. Turville, All-round manipulation of the actin cytoskeleton by HIV, 2018. https://doi.org/10.3390/v10020063.

[313] S. Iyengar, J.E.K. Hildreth, D.H. Schwartz, Actin-Dependent Receptor Colocalization Required for Human Immunodeficiency Virus Entry into Host Cells, J. Virol. 72 (1998) 5251–5255. https://doi.org/10.1128/jvi.72.6.5251-5255.1998.

[314] I.L. Shytaj, F.A. Procopio, M. Tarek, I. Carlon-andres, H. Tang, Glycolysis

downregulation is a hallmark of HIV-1 latency and sensitizes infected cells to oxidative stress, (2020).

[315] C.M. Finnegan, S.S. Rawat, E.H. Cho, D.L. Guiffre, S. Lockett, A.H. Merrill, R. Blumenthal, Sphingomyelinase Restricts the Lateral Diffusion of CD4 and Inhibits Human Immunodeficiency Virus Fusion, J. Virol. 81 (2007) 5294–5304. https://doi.org/10.1128/jvi.02553-06.

[316] Y. Zhang, Y. Zhang, L. Qin, Y. Zhao, P. Zhang, P. Zhang, B. Xu, K. Li, L. Liang, C. Zhang, Y. Dai, Y. Feng, J. Sun, Z. Hu, H. Xiang, J.C. Knight, J.C. Knight, T. Dong, T. Dong, R. Jin, Interferon-Induced Transmembrane Protein 3 Genetic Variant rs12252-C Associated with Disease Severity in Coronavirus Disease 2019, J. Infect. Dis. 222 (2020) 34–37. https://doi.org/10.1093/infdis/jiaa224.

[317] N. Huarte, P. Carravilla, A. Cruz, M. Lorizate, J.A. Nieto-Garai, H.G. Kräusslich, J. Pérez-Gil, J. Requejo-Isidro, J.L. Nieva, Functional organization of the HIV lipid envelope, Sci. Rep. 6 (2016) 1–14. https://doi.org/10.1038/srep34190.

[318] Y.C. Chen, C. Sood, M. Marin, J. Aaron, E. Gratton, K. Salaita, G.B. Melikyan, Super-Resolution Fluorescence Imaging Reveals That Serine Incorporator Protein 5 Inhibits Human Immunodeficiency Virus Fusion by Disrupting Envelope Glycoprotein Clusters, ACS Nano. 14 (2020) 10929–10943. https://doi.org/10.1021/acsnano.0c02699.

[319] N. Jouvenet, S.M. Simon, P.D. Bieniasz, Visualizing HIV-1 assembly, J. Mol. Biol. 410 (2011) 501–511. https://doi.org/10.1016/j.jmb.2011.04.062.

[320] W. Muranyi, S. Malkusch, B. Müller, M. Heilemann, H.G. Kräusslich, Super-Resolution Microscopy Reveals Specific Recruitment of HIV-1 Envelope Proteins to Viral Assembly Sites Dependent on the Envelope C-Terminal Tail, PLoS Pathog. 9 (2013).

https://doi.org/10.1371/journal.ppat.1003198.

[321] T.A. Stanly, M. Fritzsche, S. Banerji, E. Garcia, J.B. De La Serna, D.G. Jackson, C. Eggeling, Critical importance of appropriate fixation conditions for faithful imaging of receptor microclusters, Biol. Open. 5 (2016) 1343–1350. https://doi.org/10.1242/bio.019943.

[322] S. Campbell, K. Gaus, R. Bittman, W. Jessup, S. Crowe, J. Mak, The Raft-Promoting Property of Virion-Associated Cholesterol, but Not the Presence of Virion-Associated Brij 98 Rafts, Is a Determinant of Human Immunodeficiency Virus Type 1 Infectivity, J. Virol. 78 (2004) 10556–10565. https://doi.org/10.1128/jvi.78.19.10556-10565.2004.

[323] H. Salimi, J. Johnson, M.G. Flores, M.S. Zhang, Y. O'Malley, J.C. Houtman, P.M. Schlievert, H. Haim, The lipid membrane of HIV-1 stabilizes the viral envelope glycoproteins and modulates their sensitivity to antibody neutralization, J. Biol. Chem. 295 (2020) 348–362. https://doi.org/10.1074/jbc.RA119.009481.

[324] J. Chojnacki, T. Staudt, B. Glass, E. Al., Maturation-dependent HIV-1 surface protein redistribution revealed by fluorescence nanoscopy, Science (80-.). 338 (2012) 524–528.

[325] D.M. Owen, D.J. Williamson, A. Magenau, K. Gaus, Sub-resolution lipid domains exist in the plasma membrane and regulate protein diffusion and distribution, Nat. Commun. 3 (2012). https://doi.org/10.1038/ncomms2273.

[326] E. Sezgin, F. Schneider, S. Galiani, I. Urbančič, D. Waithe, B.C. Lagerholm, C. Eggeling, Measuring nanoscale diffusion dynamics in cellular membranes with super-resolution STED–FCS, 2019. https://doi.org/10.1038/s41596-019-0127-9.

[327] L. Matt, L.M. Kirk, G. Chenaux, D.J. Speca, K.R. Puhger, M.C. Pride, M. Qneibi, T. Haham, K.E. Plambeck, Y. Stern-Bach, J.L. Silverman, J.N. Crawley, J.W. Hell, E. Díaz,

SynDIG4/Prrt1 Is Required for Excitatory Synapse Development and Plasticity Underlying Cognitive Function, Cell Rep. 22 (2018) 2246–2253. https://doi.org/10.1016/j.celrep.2018.02.026.

[328] I. Kaur, V. Yarov-Yarovoy, L.M. Kirk, K.E. Plambeck, E. V. Barragan, E.S. Ontiveros, E. Díaz, Activity-dependent palmitoylation controls synDIG1 stability, localization, and function, J. Neurosci. 36 (2016) 7562–7568. https://doi.org/10.1523/JNEUROSCI.4859-14.2016.